NCAR/TN–464+STR
**NCAR TECHNICAL NOTE**
June 2004

# Description of the NCAR Community Atmosphere Model (CAM 3.0)

William D. Collins
Philip J. Rasch
Byron A. Boville
James J. Hack
James R. McCaa
David L. Williamson
Jeffrey T. Kiehl
Bruce Briegleb

Climate And Global Dynamics Division
National Center For Atmospheric Research
Boulder, Colorado, USA

Cecilia Bitz

Polar Science Center
Applied Physics Laboratory
University Of Washington
Seattle, Washington

Shian-Jiann Lin

Geophysical Fluid Dynamics Laboratory
Princeton, New Jersey

Minghua Zhang

Institute For Terrestrial And Planetary Atmospheres
Stony Brook University
Stony Brook, New York

Yongjiu Dai

International Research Institute For Climate Prediction
Columbia University
Palisades, New York

Climate And Global Dynamics Division
National Center For Atmospheric Research
Boulder, Colorado

**NCAR TECHNICAL NOTES**

The Technical Note series provides an outlet for a variety of NCAR manuscripts that contribute in specialized ways to the body of scientific knowledge but which are not suitable for journal, monograph, or book publication. Reports in this series are issued by the NCAR Scientific Divisions; copies may be obtained on request from the Publications Office of NCAR. Designation symbols for the series include:

EDD: *Engineering, Design, or Development Reports*
Equipment descriptions, test results, instrumentation, and operating and maintenance manuals.

IA: *Instructional Aids*
Instruction manuals, bibliographies, film supplements, and other research or instructional aids.

PPR: *Program Progress Reports*
Field program reports, interim and working reports, survey reports, and plans for experiments.

PROC: *Proceedings*
Documentation of symposia, colloquia, conferences, workshops, and lectures. (Distribution may be limited to attendees.)

STR: *Scientific and Technical Reports*
Data compilations, theoretical and numerical investigations, and experimental results.

# Contents

**Appendices**

# List of Figures

# List of Tables

# Acknowledgments

The authors wish to acknowledge members of NCAR's Climate Modeling Section, Computer Software and Engineering Group, and Scientific Computing Division for their contributions to the development of CAM 3.0.

The new model would not exist without the significant input from members of the CCSM Atmospheric Model Working Group (AMWG) too numerous to mention. Bill Collins (NCAR), Leo Donner (GFDL), James Hack (NCAR), David Randall (Colorado State University), and Phil Rasch (NCAR) were the co-chairs of the AMWG during the development of CAM 3.0.

We would like to acknowledge the substantial contributions to the CAM 3.0 effort from the National Science Foundation, Department of Energy, the National Oceanic and Atmospheric Administration, and the National Aeronautics and Space Administration.

Finally, we would like to thank Chris Bretherton, Andrew Gettelman, Steve Ghan, David Randall, Jón-Egill Kristjánsson, and Minghua Zhang for their close reading and thorough critique of this document.

# Chapter 1

# Introduction

This report presents the details of the governing equations, physical parameterizations, and numerical algorithms defining the version of the NCAR Community Atmosphere Model designated CAM 3.0. The material provides an overview of the major model components, and the way in which they interact as the numerical integration proceeds. Details on the coding implementation, along with in-depth information on running the CAM 3.0 code, are given in a separate technical report entitled "User's Guide to NCAR CAM 3.0" [Kluzek et al., 2002]. As before, it is our objective that this model provide NCAR and the university research community with a reliable, well documented atmospheric general circulation model. This version of the CAM 3.0 incorporates significant improvements to the physics package (*e.g.* generalized cloud overlap for radiation calculations), new capabilities such as the incorporation of thermodynamic sea ice, and a number of enhancements to the implementation (*e.g.* clean separation between physics and dynamics). We believe that collectively these improvements provide the research community with a significantly improved atmospheric modeling capability.

## 1.1 Brief History

### 1.1.1 CCM0 and CCM1

Over the last fifteen years, the NCAR Climate and Global Dynamics (CGD) Division has provided a comprehensive, three-dimensional global atmospheric model to university and NCAR scientists for use in the analysis and understanding of global climate. Because of its widespread use, the model was designated a community tool and given the name Community Climate Model (CCM). The original versions of the NCAR Community Climate Model, CCM0A [Washington, 1982] and CCM0B [Williamson, 1983], were based on the Australian spectral model [Bourke et al., 1977; McAvaney et al., 1978] and an adiabatic, inviscid version of the ECMWF spectral model [Baede et al., 1979]. The CCM0B implementation was constructed so that its simulated climate would match the earlier CCM0A model to within natural variability (*e.g.* incorporated the same set of physical parameterizations and numerical approximations), but also provided a more flexible infrastructure for conducting medium– and long–range global forecast studies. The major strength of this latter effort was that all aspects of the model were described in a series of technical notes, which included a Users' Guide [Sato et al., 1983], a subroutine guide which provided a detailed description of the code [Williamson et al., 1983] a detailed description of the algorithms [Williamson, 1983], and a compilation of the simulated circulation statistics [Williamson and Williamson, 1984]. This development activity firmly established NCAR's commitment to provide a versatile, modular, and well–documented atmospheric general circulation model that would be suitable for climate and forecast studies by NCAR and university scientists. A more detailed discussion of the early history and philosophy of the Community Climate Model can be found in Anthes [1986].

The second generation community model, CCM1, was introduced in July of 1987, and included a number of significant changes to the model formulation which were manifested in changes to the simulated climate. Principal changes to the model included major modifications to the parameterization of radiation, a revised vertical finite-differencing technique for the dynamical core, modifications to vertical and horizontal diffusion processes, and modifications to the formulation of surface energy exchange. A number of new modeling capabilities were also introduced, including a seasonal mode in which the specified surface conditions vary with time, and an optional interactive surface hydrology that followed the formulation presented by Manabe [1969]. A detailed series of technical documentation was also made available for this version [Williamson et al., 1987; Bath et al., 1987; Williamson and Williamson, 1987; Hack et al., 1989] and more completely describe this version of the CCM.

### 1.1.2 CCM2

The most ambitious set of model improvements occurred with the introduction of the third generation of the Community Climate Model, CCM2, which was released in October of 1992. This version was the product of a major effort to improve the physical representation of a wide range of key climate processes, including clouds and radiation, moist convection, the planetary boundary layer, and transport. The introduction of this model also marked a new philosophy with respect to implementation. The CCM2 code was entirely restructured so as to satisfy three major objectives: much greater ease of use, which included portability across a wide range of computational platforms; conformance to a plug-compatible physics interface standard; and the incorporation of single-job multitasking capabilities.

The standard CCM2 model configuration was significantly different from its predecessor in almost every way, starting with resolution where the CCM2 employed a horizontal T42 spectral resolution (approximately 2.8 x 2.8 degree transform grid), with 18 vertical levels and a rigid lid at 2.917 mb. Principal algorithmic approaches shared with CCM1 were the use of a semi-implicit, leap frog time integration scheme; the use of the spectral transform method for treating the dry dynamics; and the use of a bi-harmonic horizontal diffusion operator. Major changes to the dynamical formalism included the use of a terrain-following hybrid vertical coordinate, and the incorporation of a shape-preserving semi-Lagrangian transport scheme [Williamson and Olson, 1994] for advecting water vapor, as well as an arbitrary number of other scalar fields (*e.g.* cloud water variables, chemical constituents, etc.). Principal changes to the physics included the use of a $\delta$-Eddington approximation to calculate solar absorption [Briegleb, 1992]; the use of a Voigt line shape to more accurately treat infrared radiative cooling in the stratosphere; the inclusion of a diurnal cycle to properly account for the interactions between the radiative effects of the diurnal cycle and the surface fluxes of sensible and latent heat; the incorporation of a finite heat capacity soil/sea ice model; a more sophisticated cloud fraction parameterization and treatment of cloud optical properties [Kiehl et al., 1994]; the incorporation of a sophisticated non-local treatment of boundary-layer processes [Holtslag and Boville, 1993]; the use of a simple mass flux representation of moist convection [Hack, 1994], and the optional incorporation of the Biosphere-Atmosphere Transfer Scheme (BATS) of Dickinson et al. [1987]. As with previous versions of the model, a User's Guide [Bath et al., 1992] and model description [Hack et al., 1993] were provided to completely document the model formalism and implementation. Control simulation data sets were documented in Williamson [1993].

### 1.1.3 CCM3

The CCM3 was the fourth generation in the series of NCAR's Community Climate Model. Many aspects of the model formulation and implementation were identical to the CCM2, although there were a number of important changes that were incorporated into the collection of parameterized physics, along with some modest changes to the dynamical formalism. Modifications to the physical representation of specific climate processes in the CCM3 were motivated by the need to address the more serious systematic errors apparent in CCM2 simulations, as well as to make the atmospheric model more suitable for coupling to land, ocean, and sea-ice component models. Thus, an important aspect of the changes to the model atmosphere was that they address well known systematic biases in the top-of-atmosphere and surface (to the extent that they were known) energy budgets. When compared to the CCM2, changes to the model formulation fell into five major categories: modifications to the representation of radiative transfer through both clear and cloudy atmospheric columns, modifications to hydrological processes (i.e., in the form of changes to the atmospheric boundary layer, moist convection, and surface energy exchange), the incorporation of a sophisticated land surface model, the incorporation of an optional slab mixed-layer ocean/thermodynamic sea-ice component, and a collection of other changes to the formalism which did not introduce significant changes to the model climate.

Changes to the clear-sky radiation formalism included the incorporation of minor $\mathrm{CO_2}$ bands trace gases ($CH_4$, $N_2O$, $CFC11$, $CFC12$) in the longwave parameterization, and the incorporation of a background aerosol (0.14 optical depth) in the shortwave parameterization. All-sky changes included improvements to the way in which cloud optical properties (effective radius and liquid water path) were diagnosed, the incorporation of the radiative properties of ice clouds, and a number of minor modifications to the diagnosis of convective and layered cloud amount. Collectively these modification substantially reduced systematic biases in the global annually averaged clear-sky and all-sky outgoing longwave radiation and absorbed solar radiation to well within observational uncertainty, while maintaining very good agreement with global observational estimates of cloud forcing. Additionally, the large warm bias in simulated July surface temperature over the Northern Hemisphere, the systematic over-prediction of precipitation over warm land areas, and a large component of the stationary-wave error in CCM2, were also reduced as a result of cloud-radiation improvements.

Modifications to hydrological processes included revisions to the major contributing parameterizations. The formulation of the atmospheric boundary layer parameterization was revised (in collaboration with Dr. A. A. M. Holtslag of KNMI), resulting in significantly improved estimates of boundary layer height, and a substantial reduction in the overall magnitude of the hydrological cycle. Parameterized convection was also modified where this process was represented using the deep moist convection formalism of Zhang and McFarlane [1995] in conjunction with the scheme developed by Hack [1994] for CCM2. This change resulted in an additional reduction in the magnitude of the hydrological cycle and a smoother distribution of tropical precipitation. Surface roughness over oceans was also diagnosed as a function of surface wind speed and stability, resulting in more realistic surface flux estimates for low wind speed conditions. The combination of these changes to hydrological components resulted in a 13% reduction in the annually averaged global latent heat flux and the associated precipitation rate. It should be pointed out that the improvements in the radiative and hydrological cycle characteristics of the model climate were achieved without compromising the quality of the simulated equilibrium thermodynamic structures (one of the major strengths of the CCM2) thanks in part to the incorporation of a Sundqvist [1988] style evaporation of stratiform precipitation.

The CCM3 incorporated version 1 of the Land Surface Model (LSM) developed by Bonan [1996] which provided for the comprehensive treatment of land surface processes. This was a one-dimensional model of energy, momentum, water, and $CO_2$ exchange between the atmosphere and land, accounting for ecological differences among vegetation types, hydraulic and thermal differences among soil types, and allowing for multiple surface types including lakes and wetlands within a grid cell. LSM replaced the prescribed surface wetness, prescribed snow cover, and prescribed surface albedos in CCM2. It also replaced the land surface fluxes in CCM2, using instead flux parameterizations that included hydrological and ecological processes (*e.g.* soil water, phenology, stomatal physiology, interception of water by plants).

The fourth class of changes to the CCM2 included the option to run CCM3 with a simple slab ocean-thermodynamic sea ice model. The model employs a spatially and temporally prescribed ocean heat flux and mixed layer depth, which ensures replication of realistic sea surface temperatures and ice distributions for the present climate. The model allowed for the simplest interactive surface for the ocean and sea ice components of the climate system.

The final class of model modifications included a change to the form of the hydrostatic matrix which ensures consistency between $\omega$ and the discrete continuity equation, and a more generalized form of the gravity wave drag parameterization. In the latter case, the parameterization was configured to behave in the same way as the CCM2 parameterization of wave drag, but included the capability to exploit more sophisticated descriptions of this process.

One of the more significant implementation differences with the earlier model was that CCM3 included an optional message-passing configuration, allowing the model to be executed as a parallel task in distributed-memory environments. This was an example of how the Climate and Global Dynamics Division continued to invest in technical improvements to the CCM in the interest of making it easier to acquire and use in evolving computational environments. As was the case for CCM2, the code was internally documented, obviating the need for a separate technical note that describes each subroutine and common block in the model library. Thus, the Users' Guide, the land surface technical note, the CCM3 technical note [Kiehl et al., 1996], the actual code and a series of reviewed scientific publications (including a special issue of the Journal of Climate, Volume 11, Number 6) were designed to completely document CCM3.

## 1.2 Overview of CAM 3.0

The CAM 3.0 is the fifth generation of the NCAR atmospheric GCM. The name of the model series has been changed from Community Climate Model to Community Atmosphere Model to reflect the role of CAM 3.0 in the fully coupled climate system. In contrast to previous generations of the atmospheric model, CAM 3.0 has been designed through a collaborative process with users and developers in the Atmospheric Model Working Group (AMWG). The AMWG includes scientists from NCAR, the university community, and government laboratories. For CAM 3.0, the AMWG proposed testing a variety of dynamical cores and convective parameterizations. The data from these experiments has been freely shared among the AMWG, particularly with member organizations (*e.g.* PCMDI) with methods for comparing modeled climates against observations. The proposed model configurations have also been extensively evaluated using a new diagnostics package developed by M. Stevens and J. Hack (CMS). The consensus of the AMWG is to retain the spectral Eulerian dynamical core for the first official release of CAM 3.0, although the code includes the option to run with semi-Lagrange dynamics (section 3.2) or with finite-volume dynamics (FV; section 3.3). The addition of FV is a major extension to the model provided through a collaboration between NCAR and NASA Goddard's Data Assimilation Office (DAO). The AMWG also has decided to retain the Zhang and McFarlane [1995] parameterization for deep convection (section 4.1) in CAM 3.0.

The major changes in the physics include:

- Treatment of cloud condensed water using a prognostic treatment (section 4.5): The original formulation is introduced in Rasch and Kristjánsson [1998]. Revisions to the parameterization to deal more realistically with the treatment of the condensation and evaporation under forcing by large scale processes and changing cloud fraction are described in Zhang et al. [2003].The parameterization has two components: 1) a macroscale component that describes the exchange of water substance between the condensate and the vapor phase and the associated temperature change arising from that phase change [Zhang et al., 2003]; and 2) a bulk microphysical component that controls the conversion from condensate to precipitate [Rasch and Kristjánsson, 1998].

- A new thermodynamic package for sea ice (chapter 6): The philosophy behind the design of the sea ice formulation of CAM 3.0 is to use the same physics, where possible, as in the sea ice model within CCSM, which is known as CSIM for Community Sea Ice Model. In the absence of an ocean model, uncoupled simulations with CAM 3.0 require sea ice thickness and concentration to be specified. Hence the primary function of the sea ice formulation in CAM 3.0 is to compute surface fluxes. The new sea ice formulation in CAM 3.0 uses parameterizations from CSIM for predicting snow depth, brine pockets, internal shortwave radiative transfer, surface albedo, ice-atmosphere drag, and surface exchange fluxes.

- Explicit representation of fractional land and sea-ice coverage (section 7.2): Earlier versions of the global atmospheric model (the CCM series) included a simple land-ocean-sea ice mask to define the underlying surface of the model. It is well known that fluxes of fresh water, heat, and momentum between the atmosphere and underlying surface are strongly affected by surface type. The CAM 3.0 provides a much more accurate representation of flux exchanges from coastal boundaries, island regions, and ice edges by including a fractional specification for land, ice, and ocean. That is, the area occupied by these surface types is described as a fractional portion of the atmospheric grid box. This fractional specification provides a mechanism to account for flux differences due to sub-grid inhomogeneity of surface types.

- A new, general, and flexible treatment of geometrical cloud overlap in the radiation calculations (section 4.8.5): The new parameterizations compute the shortwave and longwave fluxes and heating rates for random overlap, maximum overlap, or an arbitrary combination of maximum and random overlap. The specification of the type of overlap is identical for the two bands, and it is completely separated from the radiative parameterizations. In CAM 3.0, adjacent cloud layers are maximally overlapped and groups of clouds separated by cloud-free layers are randomly overlapped. The introduction of the generalized overlap assumptions permits more realistic treatments of cloud-radiative interactions. The parameterizations are based upon representations of the radiative transfer equations which are more accurate than previous approximations in the literature. The methodology has been designed and validated against calculations based upon the independent column approximation (ICA).

- A new parameterization for the longwave absorptivity and emissivity of water vapor (section 4.9.2): This updated treatment preserves the formulation of the radiative transfer equations using the absorptivity/emissivity method. However, the components of the absorptivity and emissivity related to water vapor have been replaced with new terms calculated with the General Line-by-line Atmospheric Transmittance and Radiance Model (GENLN3). Mean absolute differences between the cooling rates from the original method and GENLN3 are typically 0.2 K/day. These differences are reduced by at least a factor of 3 using the updated parameterization. The mean absolute errors in the surface and top-of-atmosphere clear-sky longwave fluxes for standard atmospheres are reduced to less than 1 W/m$^2$. The updated parameterization increases the longwave cooling at 300 mb by 0.3 to 0.6 K/day, and it decreases the cooling near 800 mb by 0.1 to 0.5 K/day. The increased cooling is caused by line absorption and the foreign continuum in the rotation band, and the decreased cooling is caused by the self continuum in the rotation band.

- The near-infrared absorption by water vapor has been updated (section 4.8.2). In the original shortwave parameterization for CAM [Briegleb, 1992], the absorption by water vapor is derived from the LBL calculations by Ramaswamy and Freidenreich [1991]. In turn, these LBL calculations are based upon the 1983 AFGL line data [Rothman et al., 1983]. The original parameterization did not include the effects of the water-vapor continuum in the visible and near-infrared. In the new version of CAM, the parameterization is based upon the HITRAN2k line database [Rothman et al., 2003], and it incorporates the CKD 2.4 prescription for the continuum. The magnitude of errors in flux divergences and heating rates relative to modern LBL calculations have been reduced by approximately seven times compared to the old CAM parameterization.

- The uniform background aerosol has been replaced with a present-day climatology of sulfate, sea-salt, carbonaceous, and soil-dust aerosols (section 4.8.3). The climatology is obtained from a chemical transport model forced with meteorological analysis and constrained by assimilation of satellite aerosol retrievals. These aerosols affect the shortwave energy budget of the atmosphere. CAM 3.0 also includes a mechanism for treating the shortwave and longwave effects of volcanic aerosols. A time history for the mass of stratospheric sulfuric acid for volcanic eruptions in the recent past is included with the standard model.

- Evaporation of convective precipitation (section 4.1) following Sundqvist [1988]: The enhancement of atmospheric moisture through this mechanism offsets the drying introduced by changes in the longwave absorptivity and emissivity.

- A careful formulation of vertical diffusion of dry static energy (section 4.11).

Other major enhancements include:

- A new, extensible sea-surface temperature boundary data set (section 7.2): This dataset prescribes analyzed monthly mid-point mean values of SST and ice concentration for the period 1950 through 2001. The dataset is a blended product, using the global HadISST OI dataset prior to 1981 and the Smith/Reynolds EOF dataset post-1981. In addition to the analyzed time series, a composite of the annual cycle for the period 1981-2001 is also available in the form of a mean "climatological" dataset.

- Clean separation between the physics and dynamics (chapter 2): The dynamical core can be coupled to the parameterization suite in a purely time split manner or in a purely process split one. The distinction is that in the process split approximation the physics and dynamics are both calculated from the same past state, while in the time split approximations the dynamics and physics are calculated sequentially, each based on the state produced by the other.

# Chapter 2

# Coupling of Dynamical Core and Parameterization Suite

The CAM 3.0 cleanly separates the parameterization suite from the dynamical core, and makes it easier to replace or modify each in isolation. The dynamical core can be coupled to the parameterization suite in a purely time split manner or in a purely process split one, as described below.

Consider the general prediction equation for a generic variable $\psi$,

$$\frac{\partial \psi}{\partial t} = D\left(\psi\right) + P\left(\psi\right) \ , \tag{2.1}$$

where $\psi$ denotes a prognostic variable such as temperature or horizontal wind component. The dynamical core component is denoted $D$ and the physical parameterization suite $P$.

A three-time-level notation is employed which is appropriate for the semi-implicit Eulerian spectral transform dynamical core. However, the numerical characteristics of the physical parameterizations are more like those of diffusive processes rather than advective ones. They are therefore approximated with forward or backward differences, rather than centered three-time-level forms.

The *Process Split* coupling is approximated by

$$\psi^{n+1} = \psi^{n-1} + 2\Delta t D(\psi^{n+1}, \psi^{n}, \psi^{n-1}) + 2\Delta t P(\psi^{*}, \psi^{n-1}) \ , \tag{2.2}$$

where $P(\psi^{*}, \psi^{n-1})$ is calculated first from

$$\psi^{*} = \psi^{n-1} + 2\Delta t P(\psi^{*}, \psi^{n-1}) \ . \tag{2.3}$$

The *Time Split* coupling is approximated by

$$\begin{aligned} \psi^{*} &= \psi^{n-1} + 2\Delta t D(\psi^{*}, \psi^{n}, \psi^{n-1}) \ , & (2.4) \\ \psi^{n+1} &= \psi^{*} + 2\Delta t P(\psi^{n+1}, \psi^{*}) \ . & (2.5) \end{aligned}$$

The distinction is that in the *Process Split* approximation the calculations of $D$ and $P$ are both based on the same past state, $\psi^{n-1}$, while in the *Time Split* approximations $D$ and $P$ are calculated sequentially, each based on the state produced by the other.

As mentioned above, the Eulerian core employs the three-time-level notation in (2.2)-(2.5). Eqns. (2.2)-(2.5) also apply to two-time-level semi-Lagrangian and finite volume cores by dropping centered $n$ term dependencies, and replacing $n$-1 by $n$ and $2\Delta t$ by $\Delta t$.

The parameterization package can be applied to produce an updated field as indicated in (2.3) and (2.5). Thus (2.5) can be written with an operator notation

$$\psi^{n+1} = \boldsymbol{P}\left(\psi^{*}\right) \ , \tag{2.6}$$

where only the past state is included in the operator dependency for notational convenience. The implicit predicted state dependency is understood. The *Process Split* equation (2.2) can also be written in operator notation as

$$\psi^{n+1} = \boldsymbol{D}\left(\psi^{n-1}, \frac{\boldsymbol{P}(\psi^{n-1}) - \psi^{n-1}}{2\Delta t}\right) \ , \tag{2.7}$$

where the first argument of $\boldsymbol{D}$ denotes the prognostic variable input to the dynamical core and the second denotes the forcing rate from the parameterization package, e.g. the heating rate in the thermodynamic equation. Again only the past state is included in the operator dependency, with the implicit predicted state dependency left understood. With this notation the *Time Split* system (2.5) and (2.5) can be written

$$\psi^{n+1} = \boldsymbol{P}\left(\boldsymbol{D}\left(\psi^{n-1}, 0\right)\right) \ . \tag{2.8}$$

The total parameterization package in CAM 3.0 consists of a sequence of components, indicated by

$$P = \{M, R, S, T\} \ , \tag{2.9}$$

where $M$ denotes (Moist) precipitation processes, $R$ denotes clouds and Radiation, $S$ denotes the Surface model, and $T$ denotes Turbulent mixing. Each of these in turn is subdivided into various components: $M$ includes an optional dry adiabatic adjustment (normally applied only in the stratosphere), moist penetrative convection, shallow convection, and large-scale stable condensation; $R$ first calculates the cloud parameterization followed by the radiation parameterization; $S$ provides the surface fluxes obtained from land, ocean and sea ice models, or calculates them based on specified surface conditions such as sea surface temperatures and sea ice distribution. These surface fluxes provide lower flux boundary conditions for the turbulent mixing $T$ which is comprised of the planetary boundary layer parameterization, vertical diffusion, and gravity wave drag.

Defining operators following (2.6) for each of the parameterization components, the couplings in CAM 3.0 are summarized as:
TIME SPLIT

$$\psi^{n+1} = \boldsymbol{T}\left(\boldsymbol{S}\left(\boldsymbol{R}\left(\boldsymbol{M}\left(\boldsymbol{D}\left(\psi^{n-1}, 0\right)\right)\right)\right)\right) \tag{2.10}$$

PROCESS SPLIT

$$\psi^{n+1} = \boldsymbol{D}\left(\psi^{n-1}, \frac{\boldsymbol{T}\left(\boldsymbol{S}\left(\boldsymbol{R}\left(\boldsymbol{M}\left(\psi^{n-1}\right)\right)\right)\right) - \psi^{n-1}}{2\Delta t}\right) \tag{2.11}$$

The labels *Time Split* and *Process Split* refer to the coupling of the dynamical core with the complete parameterization suite. The components within the parameterization suite are coupled via time splitting in both forms.

The *Process Split* form is convenient for spectral transform models. With *Time Split* approximations extra spectral transforms are required to convert the updated momentum variables provided by the parameterizations to vorticity and divergence for the Eulerian spectral core, or to recalculate the temperature gradient for the semi-Lagrangian spectral core. The *Time Split* form is convenient for the finite-volume core which adopts a Lagrangian vertical coordinate. Since the scheme is explicit and restricted to small time-steps by its non-advective component, it sub-steps the dynamics multiple times during a longer parameterization time step. With *Process Split* approximations the forcing terms must be interpolated to an evolving Lagrangian vertical coordinate every sub-step of the dynamical core. Besides the expense involved, it is not completely obvious how to interpolate the parameterized forcing, which can have a vertical grid scale component arising from vertical grid scale clouds, to a different vertical grid. [Williamson, 2002] compares simulations with the Eulerian spectral transform dynamical core coupled to the CCM3 parameterization suite via *Process Split* and *Time Split* approximations.

# Chapter 3

# Dynamics

## 3.1 Eulerian Dynamical Core

The hybrid vertical coordinate that has been implemented in CAM 3.0 is described in this section. The hybrid coordinate was developed by Simmons and Strüfing [1981] in order to provide a general framework for a vertical coordinate which is terrain following at the Earth's surface, but reduces to a pressure coordinate at some point above the surface. The hybrid coordinate is more general in concept than the modified $\sigma$ scheme of Sangster [1960], which is used in the GFDL SKYHI model. However, the hybrid coordinate is normally specified in such a way that the two coordinates are identical.

The following description uses the same general development as Simmons and Strüfing [1981], who based their development on the generalized vertical coordinate of Kasahara [1974]. A specific form of the coordinate (the hybrid coordinate) is introduced at the latest possible point. The description here differs from Simmons and Strüfing [1981] in allowing for an upper boundary at finite height (nonzero pressure), as in the original development by Kasahara. Such an upper boundary may be required when the equations are solved using vertical finite differences.

### 3.1.1 Generalized terrain-following vertical coordinates

Deriving the primitive equations in a generalized terrain-following vertical coordinate requires only that certain basic properties of the coordinate be specified. If the surface pressure is $\pi$, then we require the generalized coordinate $\eta(p, \pi)$ to satisfy:

1. $\eta(p, \pi)$ is a monotonic function of $p$.

2. $\eta(\pi, \pi) = 1$

3. $\eta(0, \pi) = 0$

4. $\eta(p_t, \pi) = \eta_t$ where $p_t$ is the top of the model.

The latter requirement provides that the top of the model will be a pressure surface, simplifying the specification of boundary conditions. In the case that $p_t = 0$, the last two requirements are identical and the system reduces to that described in Simmons and Strüfing [1981]. The boundary conditions that are required to close the system are:

$$\dot{\eta}(\pi, \pi) = 0, \tag{3.1}$$

$$\dot{\eta}(p_t, \pi) = \omega(p_t) = 0. \tag{3.2}$$

Given the above description of the coordinate, the continuous system of equations can be written following Kasahara [1974] and Simmons and Strüfing [1981]. The prognostic equations are:

$$\frac{\partial \zeta}{\partial t} = \boldsymbol{k} \cdot \nabla \times (\boldsymbol{n}/\cos\phi) + F_{\zeta_H}, \tag{3.3}$$

$$\frac{\partial \delta}{\partial t} = \nabla \cdot (\boldsymbol{n}/\cos\phi) - \nabla^2 (E + \Phi) + F_{\delta_H}, \tag{3.4}$$

$$\begin{aligned}\frac{\partial T}{\partial t} &= \frac{-1}{a\cos^2\phi}\left[\frac{\partial}{\partial\lambda}(UT) + \cos\phi\frac{\partial}{\partial\phi}(VT)\right] + T\delta - \dot{\eta}\frac{\partial T}{\partial\eta} + \frac{R}{c_p^*}T_v\frac{\omega}{p} \\ &\quad +Q + F_{T_H} + F_{F_H},\end{aligned} \tag{3.5}$$

$$\frac{\partial q}{\partial t} = \frac{-1}{a\cos^2\phi}\left[\frac{\partial}{\partial\lambda}(Uq) + \cos\phi\frac{\partial}{\partial\phi}(Vq)\right] + q\delta - \dot{\eta}\frac{\partial q}{\partial\eta} + S, \tag{3.6}$$

$$\frac{\partial \pi}{\partial t} = \int_1^{\eta_t} \boldsymbol{\nabla}\cdot\left(\frac{\partial p}{\partial\eta}\boldsymbol{V}\right) d\eta. \tag{3.7}$$

The notation follows standard conventions, and the following terms have been introduced with $\boldsymbol{n} = (n_U, n_V)$:

$$n_U = +(\zeta + f)V - \dot{\eta}\frac{\partial U}{\partial\eta}R\frac{T_v}{p}\frac{1}{a} - \frac{\partial p}{\partial\lambda} + F_U\,, \tag{3.8}$$

$$n_V = -(\zeta + f)U - \dot{\eta}\frac{\partial V}{\partial\eta} - R\frac{T_v}{p}\frac{\cos\phi}{a}\frac{\partial p}{\partial\phi} + F_V\,, \tag{3.9}$$

$$E = \frac{U^2 + V^2}{2\cos^2\phi}\,, \tag{3.10}$$

$$(U, V) = (u, v)\cos\phi\,, \tag{3.11}$$

$$T_v = \left[1 + \left(\frac{R_v}{R} - 1\right)q\right]T\,, \tag{3.12}$$

$$c_p^* = \left[1 + \left(\frac{c_{p_v}}{c_p} - 1\right)q\right]c_p\,. \tag{3.13}$$

The terms $F_U, F_V, Q$, and $S$ represent the sources and sinks from the parameterizations for momentum (in terms of $U$ and $V$), temperature, and moisture, respectively. The terms $F_{\zeta_H}$ and $F_{\delta_H}$ represent sources due to horizontal diffusion of momentum, while $F_{T_H}$ and $F_{F_H}$ represent sources attributable to horizontal diffusion of temperature and a contribution from frictional heating (see sections on horizontal diffusion and horizontal diffusion correction).

In addition to the prognostic equations, three diagnostic equations are required:

$$\Phi = \Phi_s + R \int_{p(\eta)}^{p(1)} T_v d \ln p, \tag{3.14}$$

$$\dot{\eta} \frac{\partial p}{\partial \eta} = -\frac{\partial p}{\partial t} - \int_{\eta_t}^{\eta} \boldsymbol{\nabla} \cdot \left( \frac{\partial p}{\partial \eta} \boldsymbol{V} \right) d\eta, \tag{3.15}$$

$$\omega = \boldsymbol{V} \cdot \nabla p - \int_{\eta_t}^{\eta} \boldsymbol{\nabla} \cdot \left( \frac{\partial p}{\partial \eta} \boldsymbol{V} \right) d\eta. \tag{3.16}$$

Note that the bounds on the vertical integrals are specified as values of $\eta$ (*e.g.* $\eta_t$, 1) or as functions of $p$ (*e.g.* $p$ (1), which is the pressure at $\eta = 1$).

### 3.1.2 Conversion to final form

Equations (3.1)-(3.16) are the complete set which must be solved by a GCM. However, in order to solve them, the function $\eta(p, \pi)$ must be specified. In advance of actually specifying $\eta(p, \pi)$, the equations will be cast in a more convenient form. Most of the changes to the equations involve simple applications of the chain rule for derivatives, in order to obtain terms that will be easy to evaluate using the predicted variables in the model. For example, terms involving horizontal derivatives of $p$ must be converted to terms involving only $\partial p/\partial \pi$ and horizontal derivatives of $\pi$. The former can be evaluated once the function $\eta(p, \pi)$ is specified.

The vertical advection terms in (3.5), (3.6), (3.8), and (3.9) may be rewritten as:

$$\dot{\eta} \frac{\partial \psi}{\partial \eta} = \dot{\eta} \frac{\partial p}{\partial \eta} \frac{\partial \psi}{\partial p}\,, \tag{3.17}$$

since $\dot{\eta} \partial p/\partial \eta$ is given by (3.15). Similarly, the first term on the right-hand side of (3.15) can be expanded as

$$\frac{\partial p}{\partial t} = \frac{\partial p}{\partial \pi} \frac{\partial \pi}{\partial t}, \tag{3.18}$$

and (3.7) invoked to specify $\partial \pi/\partial t$.

The integrals which appear in (3.7), (3.15), and (3.16) can be written more conveniently by expanding the kernel as

$$\boldsymbol{\nabla} \cdot \left( \frac{\partial p}{\partial \eta} \boldsymbol{V} \right) = \boldsymbol{V} \cdot \nabla \left( \frac{\partial p}{\partial \eta} \right) + \frac{\partial p}{\partial \eta} \boldsymbol{\nabla} \cdot \boldsymbol{V}\ . \tag{3.19}$$

The second term in (3.19) is easily treated in vertical integrals, since it reduces to an integral in pressure. The first term is expanded to:

$$\begin{aligned} \boldsymbol{V} \cdot \nabla \left( \frac{\partial p}{\partial \eta} \right) &= \boldsymbol{V} \cdot \frac{\partial}{\partial \eta} (\nabla p) \\ &= \boldsymbol{V} \cdot \frac{\partial}{\partial \eta} \left( \frac{\partial p}{\partial \pi} \nabla \pi \right) \\ &= \boldsymbol{V} \cdot \frac{\partial}{\partial \eta} \left( \frac{\partial p}{\partial \pi} \right) \nabla \pi + \boldsymbol{V} \cdot \frac{\partial p}{\partial \pi} \nabla \left( \frac{\partial \pi}{\partial \eta} \right)\ . \end{aligned} \tag{3.20}$$

The second term in (3.20) vanishes because $\partial\pi/\partial\eta = 0$, while the first term is easily treated once $\eta(p,\pi)$ is specified. Substituting (3.20) into (3.19), one obtains:

$$\boldsymbol{\nabla}\cdot\left(\frac{\partial p}{\partial\eta}\boldsymbol{V}\right) = \frac{\partial}{\partial\eta}\left(\frac{\partial p}{\partial\pi}\right)\boldsymbol{V}\cdot\nabla\pi + \frac{\partial p}{\partial\eta}\boldsymbol{\nabla}\cdot V\,. \tag{3.21}$$

Using (3.21) as the kernel of the integral in (3.7), (3.15), and (3.16), one obtains integrals of the form

$$\begin{aligned}\int\boldsymbol{\nabla}\cdot\left(\frac{\partial p}{\partial\eta}\boldsymbol{V}\right)d\eta &= \int\left[\frac{\partial}{\partial\eta}\left(\frac{\partial p}{\partial\pi}\right)\boldsymbol{V}\cdot\nabla\pi + \frac{\partial p}{\partial\eta}\boldsymbol{\nabla}\cdot V\right]d\eta \\ &= \int\boldsymbol{V}\cdot\nabla\pi d\left(\frac{\partial p}{\partial\pi}\right) + \int\delta dp. \end{aligned}\tag{3.22}$$

The original primitive equations (3.3)-(3.7), together with (3.8), (3.9), and (3.14)-(3.16) can now be rewritten with the aid of (3.17), (3.18), and (3.22).

$$\begin{aligned}
\frac{\partial\zeta}{\partial t} &= \boldsymbol{k}\cdot\nabla\times(\boldsymbol{n}/\cos\phi) + F_{\zeta_H}\ , && (3.23)\\
\frac{\partial\delta}{\partial t} &= \boldsymbol{\nabla}\cdot(\boldsymbol{n}/\cos\phi) - \nabla^2(E+\Phi) + F_{\delta_H}\ , && (3.24)\\
\frac{\partial T}{\partial t} &= \frac{-1}{a\cos^2\phi}\left[\frac{\partial}{\partial\lambda}(UT) + \cos\phi\frac{\partial}{\partial\phi}(VT)\right] + T\delta - \dot{\eta}\frac{\partial p}{\partial\eta}\frac{\partial T}{\partial p} + \frac{R}{c_p^*}T_v\frac{\omega}{p} \\
&\quad +Q + F_{T_H} + F_{F_H} && (3.25)\\
\frac{\partial q}{\partial t} &= \frac{-1}{a\cos^2\phi}\left[\frac{\partial}{\partial\lambda}(Uq) + \cos\phi\frac{\partial}{\partial\phi}(Vq)\right] + q\delta - \dot{\eta}\frac{\partial p}{\partial\eta}\frac{\partial q}{\partial p} + S, && (3.26)\\
\frac{\partial\pi}{\partial t} &= -\int_{(\eta_t)}^{(1)}\boldsymbol{V}\cdot\nabla\pi d\left(\frac{\partial p}{\partial\pi}\right) - \int_{p(\eta_t)}^{p(1)}\delta dp, && (3.27)\\
n_U &= +(\zeta+f)V - \dot{\eta}\frac{\partial p}{\partial\eta}\frac{\partial - U}{\partial p} - R\frac{T_v}{a}\frac{1}{p}\frac{\partial p}{\partial\pi}\frac{\partial\pi}{\partial\lambda} + F_U, && (3.28)\\
n_V &= -(\zeta+f)U - \dot{\eta}\frac{\partial p}{\partial\eta}\frac{\partial - V}{\partial p}R\frac{T_v\cos\phi}{a}\frac{1}{p}\frac{\partial p}{\partial\pi}\frac{\partial\pi}{\partial\phi} + F_V, && (3.29)\\
\Phi &= \Phi_s + R\int_{p(\eta)}^{p(1)}T_v d\ln p, && (3.30)\\
\dot{\eta}\frac{\partial p}{\partial\eta} &= \frac{\partial p}{\partial\pi}\left[\int_{(\eta_t)}^{(1)}\boldsymbol{V}\cdot\nabla\pi d\left(\frac{\partial p}{\partial\pi}\right) + \int_{p(\eta_t)}^{p(1)}\delta dp\right] && (3.31)\\
&\quad - \int_{(\eta_t)}^{(\eta)}\boldsymbol{V}\cdot\nabla\pi d\left(\frac{\partial p}{\partial\pi}\right) - \int_{p(\eta_t)}^{p(\eta)}\delta dp, \\
\omega &= \frac{\partial p}{\partial\pi}\boldsymbol{V}\cdot\nabla\pi - \int_{(\eta_t)}^{(\eta)}\boldsymbol{V}\cdot\nabla\pi d\left(\frac{\partial p}{\partial\pi}\right) - \int_{p(\eta_t)}^{p(\eta)}\delta dp. && (3.32)
\end{aligned}$$

Once $\eta(p,\pi)$ is specified, then $\partial p/\partial\pi$ can be determined and (3.23)-(3.32) can be solved in a GCM.

In the actual definition of the hybrid coordinate, it is not necessary to specify $\eta(p, \pi)$ explicitly, since (3.23)-(3.32) only requires that $p$ and $\partial p/\partial \pi$ be determined. It is sufficient to specify $p(\eta, \pi)$ and to let $\eta$ be defined implicitly. This will be done in section 3.1.7. In the case that $p(\eta, \pi) = \sigma\pi$ and $\eta_t = 0$, (3.23)-(3.32) can be reduced to the set of equations solved by CCM1.

### 3.1.3 Continuous equations using $\partial \ln(\pi)/\partial t$

In practice, the solutions generated by solving the above equations are excessively noisy. This problem appears to arise from aliasing problems in the hydrostatic equation (3.30). The $\ln p$ integral introduces a high order nonlinearity which enters directly into the divergence equation (3.24). Large gravity waves are generated in the vicinity of steep orography, such as in the Pacific Ocean west of the Andes.

The noise problem is solved by converting the equations given above, which use $\pi$ as a prognostic variable, to equations using $\Pi = \ln(\pi)$. This results in the hydrostatic equation becoming only quadratically nonlinear except for moisture contributions to virtual temperature. Since the spectral transform method will be used to solve the equations, gradients will be obtained during the transform from wave to grid space. Outside of the prognostic equation for $\Pi$, all terms involving $\nabla\pi$ will then appear as $\pi\nabla\Pi$.

Equations (3.23)-(3.32) become:

$$
\begin{aligned}
\frac{\partial \zeta}{\partial t} &= \boldsymbol{k} \cdot \nabla \times (\boldsymbol{n}/\cos\phi) + F_{\zeta_H}, & (3.33)\\
\frac{\partial \delta}{\partial t} &= \boldsymbol{\nabla} \cdot (\boldsymbol{n}/\cos\phi) - \nabla^2 (E + \Phi) + F_{\delta_H}, & (3.34)\\
\frac{\partial T}{\partial t} &= \frac{-1}{a\cos^2\phi}\left[\frac{\partial}{\partial\lambda}(UT) + \cos\phi\frac{\partial}{\partial\phi}(VT)\right] + T\delta - \dot{\eta}\frac{\partial p}{\partial \eta}\frac{\partial T}{\partial p} + \frac{R}{c_p^*}T_v\frac{\omega}{p} & (3.35)\\
&\quad + Q + F_{T_H} + F_{F_H}, &\\
\frac{\partial q}{\partial t} &= \frac{-1}{a\cos^2\phi}\left[\frac{\partial}{\partial\lambda}(Uq) + \cos\phi\frac{\partial}{\partial\phi}(Vq)\right] + q\delta - \dot{\eta}\frac{\partial p}{\partial \eta}\frac{\partial q}{\partial p} + S, & (3.36)\\
\frac{\partial \Pi}{\partial t} &= -\int_{(\eta_t)}^{(1)} \boldsymbol{V} \cdot \nabla\Pi d\left(\frac{\partial p}{\partial \pi}\right) - \frac{1}{\pi}\int_{p(\eta_t)}^{p(1)} \delta dp, & (3.37)\\
n_U &= +(\zeta + f)V - \dot{\eta}\frac{\partial p}{\partial \eta}\frac{\partial - U}{\partial p} R\frac{T_v}{a}\frac{\pi}{p}\frac{\partial p}{\partial \pi}\frac{\partial \Pi}{\partial \lambda} + F_U, & (3.38)\\
n_V &= -(\zeta + f)U - \dot{\eta}\frac{\partial p}{\partial \eta}\frac{\partial - V}{\partial p} R\frac{T_v\cos\phi}{a}\frac{\pi}{p}\frac{\partial p}{\partial \pi}\frac{\partial \Pi}{\partial \phi} + F_V, & (3.39)\\
\Phi &= \Phi_s + R\int_{p(\eta)}^{p(1)} T_v d\ln p, & (3.40)\\
\dot{\eta}\frac{\partial p}{\partial \eta} &= \frac{\partial p}{\partial \pi}\left[\int_{(\eta_t)}^{(1)} \pi\boldsymbol{V} \cdot \nabla\Pi d\left(\frac{\partial p}{\partial \pi}\right) + \int_{p(\eta_t)}^{p(1)} \delta dp\right] & (3.41)\\
&\quad - \int_{(\eta_t)}^{(\eta)} \pi\boldsymbol{V} \cdot \nabla\Pi d\left(\frac{\partial p}{\partial \pi}\right) - \int_{p(\eta_t)}^{p(\eta)} \delta dp, &\\
\omega &= \frac{\partial p}{\partial \pi}\pi\boldsymbol{V} \cdot \nabla\Pi - \int_{(\eta_t)}^{(\eta)} \pi\boldsymbol{V} \cdot \nabla\Pi d\left(\frac{\partial p}{\partial \pi}\right) - \int_{p(\eta_t)}^{p(\eta)} \delta dp. & (3.42)
\end{aligned}
$$

The above equations reduce to the standard $\sigma$ equations used in CCM1 if $\eta = \sigma$ and $\eta_t = 0$. (Note that in this case $\partial p/\partial \pi = p/\pi = \sigma$.)

### 3.1.4 Semi-implicit formulation

The model described by (3.33)-(3.42), without the horizontal diffusion terms, together with boundary conditions (3.1) and (3.2), is integrated in time using the semi-implicit leapfrog scheme described below. The semi-implicit form of the time differencing will be applied to (3.34) and (3.36) without the horizontal diffusion sources, and to (3.37). In order to derive the semi-implicit form, one must linearize these equations about a reference state. Isolating the terms that will have their linear parts treated implicitly, the prognostic equations (3.33), (3.34), and (3.37) may be rewritten as:

$$\frac{\partial \delta}{\partial t} = -RT_v \nabla^2 \ln p - \nabla^2 \Phi + X_1, \tag{3.43}$$

$$\frac{\partial T}{\partial t} = +\frac{R}{c_p^*} T_v \frac{\omega}{p} - \dot{\eta} \frac{\partial p}{\partial \eta} \frac{\partial T}{\partial p} + Y_1, \tag{3.44}$$

$$\frac{\partial \Pi}{\partial t} = -\frac{1}{\pi} \int_{p(\eta_t)}^{p(1)} \delta dp + Z_1, \tag{3.45}$$

where $X_1, Y_1, Z_1$ are the remaining nonlinear terms not explicitly written in (3.43)-(3.45). The terms involving $\Phi$ and $\omega$ may be expanded into vertical integrals using (3.40) and (3.42), while the $\nabla^2 \ln p$ term can be converted to $\nabla^2 \Pi$, giving:

$$\frac{\partial \delta}{\partial t} = -RT \frac{\pi}{p} \frac{\partial p}{\partial \pi} \nabla^2 \Pi - R \nabla^2 \int_{p(\eta)}^{p(1)} T d \ln p \ + X_2, \tag{3.46}$$

$$\frac{\partial T}{\partial t} = -\frac{R}{c_p} \frac{T}{p} \int_{p(\eta_t)}^{p(\eta)} \delta dp - \left[ \frac{\partial p}{\partial \pi} \int_{p(\eta_t)}^{p(1)} \delta dp - \int_{p(\eta_t)}^{p(\eta)} \delta dp \right] \frac{\partial T}{\partial p} + Y_2, \tag{3.47}$$

$$\frac{\partial \Pi}{\partial t} = -\frac{1}{pi} \int_{p(\eta_t)}^{p(1)} \delta dp + Z_2. \tag{3.48}$$

Once again, only terms that will be linearized have been explicitly represented in (3.46)-(3.48), and the remaining terms are included in $X_2$, $Y_2$, and $Z_2$. Anticipating the linearization, $T_v$ and $c_p^*$ have been replaced by $T$ and $c_p$ in (3.46) and (3.47). Furthermore, the virtual temperature corrections are included with the other nonlinear terms.

In order to linearize (3.46)-(3.48), one specifies a reference state for temperature and pressure, then expands the equations about the reference state:

$$T = T^r + T', \tag{3.49}$$

$$\pi = \pi^r + \pi', \tag{3.50}$$

$$p = p^r(\eta, \pi^r) + p'. \tag{3.51}$$

In the special case that $p(\eta, \pi) = \sigma \pi$, (3.46)-(3.48) can be converted into equations involving only $\Pi = \ln \pi$ instead of $p$, and (3.50) and (3.51) are not required. This is a major difference between the hybrid coordinate scheme being developed here and the $\sigma$ coordinate scheme in CCM1.

Expanding (3.46)-(3.48) about the reference state (3.49)-(3.51) and retaining only the linear terms explicitly, one obtains:

$$\frac{\partial \delta}{\partial t} = -R \nabla^2 \left[ T^r \frac{\pi^r}{p^r} \left( \frac{\partial p}{\partial \pi} \right)^r \Pi + \int_{p^r(\eta)}^{p^r(1)} T' d \ln p^r + \int_{p'(\eta)}^{p'(1)} \frac{T^r}{p^r} dp' \right] + X_3, \tag{3.52}$$

$$\frac{\partial T}{\partial t} = -\frac{R}{c_p} \frac{T^r}{p^r} \int_{p^r(\eta_t)}^{p^r(\eta)} \delta dp^r - \left[ \left( \frac{\partial p}{\partial \pi} \right)^r \int_{p^r(\eta_t)}^{p^r(1)} \delta dp^r - \int_{p^r(\eta_t)}^{p^r(\eta)} \delta dp^r \right] \frac{\partial T^r}{\partial p^r} + Y_3, \tag{3.53}$$

$$\frac{\partial \Pi}{\partial t} = -\frac{1}{\pi^r} \int_{p^r(\eta_t)}^{p^r(1)} \delta dp^r + Z_3. \tag{3.54}$$

The semi-implicit time differencing scheme treats the linear terms in (3.52)-(3.54) by averaging in time. The last integral in (3.52) is reduced to purely linear form by the relation

$$dp' = \pi' d \left( \frac{\partial p}{\partial \pi} \right)^r + x \, . \tag{3.55}$$

In the hybrid coordinate described below, $p$ is a linear function of $\pi$, so $x$ above is zero.

We will assume that centered differences are to be used for the nonlinear terms, and the linear terms are to be treated implicitly by averaging the previous and next time steps. Finite differences are used in the vertical, and are described in the following sections. At this stage only some very general properties of the finite difference representation must be specified. A layering structure is assumed in which field values are predicted on $K$ layer midpoints denoted by an integer index, $\eta_k$ (see Figure 3.1). The interface between $\eta_k$ and $\eta_{k+1}$ is denoted by a half-integer index, $\eta_{k+1/2}$. The model top is at $\eta_{1/2} = \eta_t$, and the Earth's surface is at $\eta_{K+1/2} = 1$. It is further assumed that vertical integrals may be written as a matrix (of order $K$) times a column vector representing the values of a field at the $\eta_k$ grid points in the vertical. The column vectors representing a vertical column of grid points will be denoted by underbars, the matrices will be denoted by bold-faced capital letters, and superscript $T$ will denote the vector transpose. The finite difference forms of (3.52)-(3.54) may then be written down as:

$$\begin{aligned}
\underline{\delta}^{n+1} &= \underline{\delta}^{n-1} + 2\Delta t \underline{X}^n \\
&\quad -2\Delta t R \underline{b}^r \nabla^2 \left( \frac{\Pi^{n-1} + \Pi^{n+1}}{2} - \Pi^n \right) \\
&\quad -2\Delta t R \boldsymbol{H}^r \nabla^2 \left( \frac{(\underline{T}')^{n-1} + (\underline{T}')^{n+1}}{2} - (\underline{T}')^n \right) \\
&\quad -2\Delta t R \underline{h}^r \nabla^2 \left( \frac{\Pi^{n-1} + \Pi^{n+1}}{2} - \Pi^n \right) , 
\end{aligned} \tag{3.56}$$

$$\underline{T}^{n+1} = \underline{T}^{n-1} + 2\Delta t \underline{Y}^n - 2\Delta t \boldsymbol{D}^r \left( \frac{\underline{\delta}^{n-1} + \underline{\delta}^{n+1}}{2} - \underline{\delta}^n \right) , \tag{3.57}$$

$$\Pi^{n+1} = \Pi^{n-1} + 2\Delta t Z^n - 2\Delta t \left( \frac{\underline{\delta}^{n-1} + \underline{\delta}^{n+1}}{2} - \underline{\delta}^n \right)^T \frac{1}{\Pi^r} \underline{\Delta p}^r , \tag{3.58}$$

where $()^n$ denotes a time varying value at time step $n$. The quantities $\underline{X}^n, \underline{Y}^n$, and $Z^n$ are defined so as to complete the right-hand sides of (3.43)-(3.45). The components of $\underline{\Delta p}^r$ are given by $\Delta p^r_k = p^r_{k+\frac{1}{2}} - p^r_{k-\frac{1}{2}}$. This definition of the vertical difference operator $\Delta$ will be used in subsequent equations. The reference matrices $\boldsymbol{H}^r$ and $\boldsymbol{D}^r$, and the reference column vectors $\underline{b}^r$ and $\underline{h}^r$, depend on the precise specification of the vertical coordinate and will be defined later.

### 3.1.5 Energy conservation

We shall impose a requirement on the vertical finite differences of the model that they conserve the global integral of total energy *in the absence of sources and sinks.* We need to derive equations for kinetic and internal energy in order to impose this constraint. The momentum equations (more painfully, the vorticity and divergence equations) without the $F_U, F_V, F_{\zeta_H}$ and

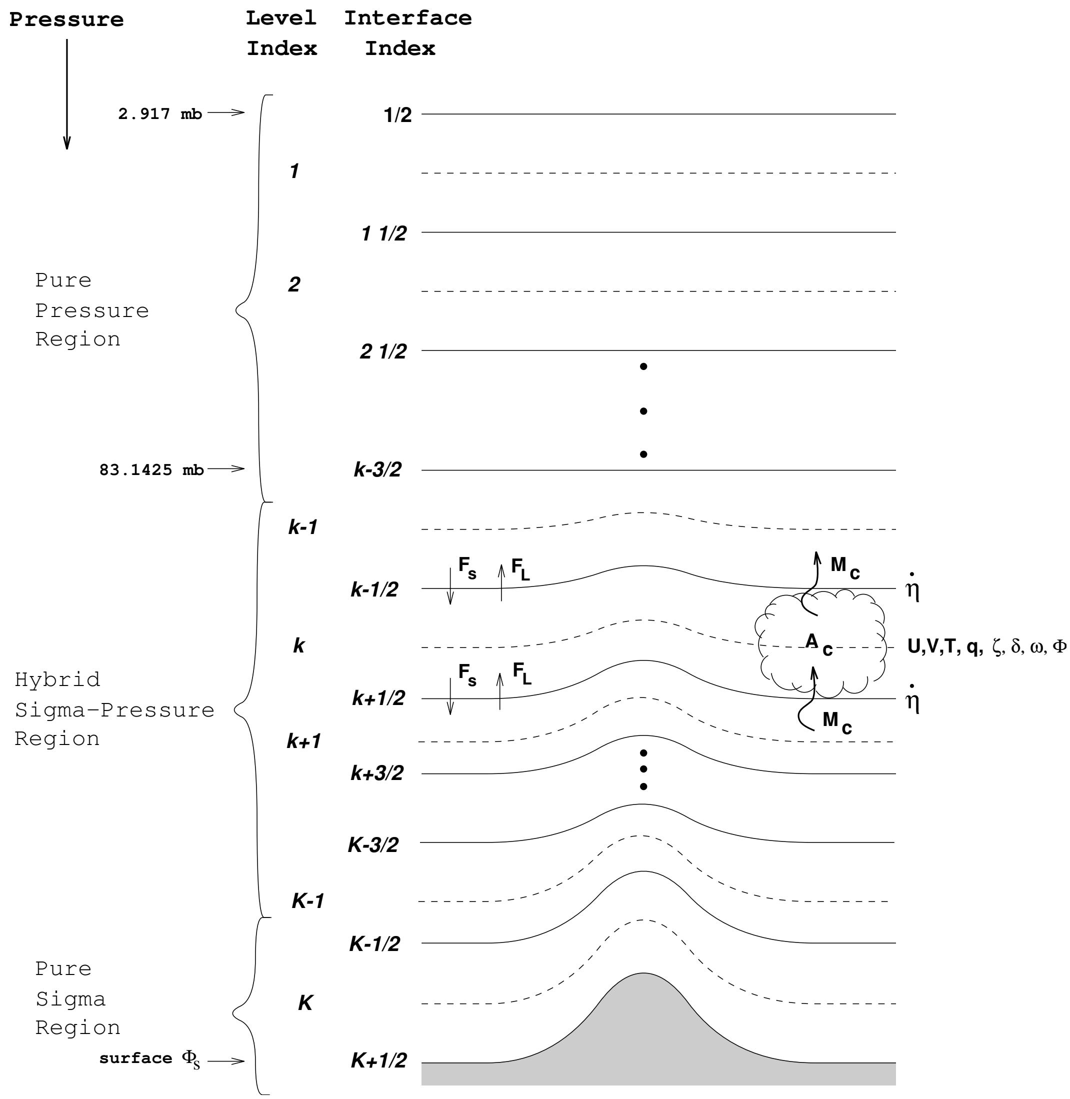


Figure 3.1: Vertical level structure of CAM 3.0

$F_{\delta_H}$ contributions, can be combined with the continuity equation

$$\frac{\partial}{\partial t}\left(\frac{\partial p}{\partial \eta}\right) + \nabla \cdot \left(\frac{\partial p}{\partial \eta}\boldsymbol{V}\right) + \frac{\partial}{\partial \eta}\left(\frac{\partial p}{\partial \eta}\dot{\eta}\right) = 0 \tag{3.59}$$

to give an equation for the rate of change of kinetic energy:

$$\begin{aligned}\frac{\partial}{\partial t}\left(\frac{\partial p}{\partial \eta}E\right) &= -\nabla \cdot \left(\frac{\partial p}{\partial \eta}E\boldsymbol{V}\right) - \frac{\partial}{\partial \eta}\left(\frac{\partial p}{\partial \eta}E\dot{\eta}\right) \\ &\quad -\frac{RT_v}{p}\frac{\partial p}{\partial \eta}\boldsymbol{V}\cdot\nabla p - \frac{\partial p}{\partial \eta}\boldsymbol{V}\cdot\nabla\Phi - . \end{aligned} \tag{3.60}$$

The first two terms on the right-hand side of (3.60) are transport terms. The horizontal integral of the first (horizontal) transport term should be zero, and it is relatively straightforward to construct horizontal finite difference schemes that ensure this. For spectral models, the integral of the horizontal transport term will not vanish in general, but we shall ignore this problem.

The vertical integral of the second (vertical) transport term on the right-hand side of (3.60) should vanish. Since this term is obtained from the vertical advection terms for momentum, which will be finite differenced, we can construct a finite difference operator that will ensure that the vertical integral vanishes.

The vertical advection terms are the product of a vertical velocity ($\dot{\eta}\partial p/\partial\eta$) and the vertical derivative of a field ($\partial\psi/\partial p$). The vertical velocity is defined in terms of vertical integrals of fields (3.42), which are naturally taken to interfaces. The vertical derivatives are also naturally taken to interfaces, so the product is formed there, and then adjacent interface values of the products are averaged to give a midpoint value. It is the definition of the average that must be correct in order to conserve kinetic energy under vertical advection in (3.60). The derivation will be omitted here, the resulting vertical advection terms are of the form:

$$\left(\dot{\eta}\frac{\partial p}{\partial \eta}\frac{\partial \psi}{\partial p}\right)_k = \frac{1}{2\Delta p_k}\left[\left(\dot{\eta}\frac{\partial p}{\partial \eta}\right)_{k+1/2}(\psi_{k+1}-\psi_k) + \left(\dot{\eta}\frac{\partial p}{\partial \eta}\right)_{k-1/2}(\psi_k-\psi_{k-1})\right], \tag{3.61}$$

$$\Delta p_k = p_{k+1/2} - p_{k-1/2}. \tag{3.62}$$

The choice of definitions for the vertical velocity at interfaces is not crucial to the energy conservation (although not completely arbitrary), and we shall defer its definition until later. The vertical advection of temperature is not required to use (3.61) in order to conserve mass or energy. Other constraints can be imposed that result in different forms for temperature advection, but we will simply use (3.61) in the system described below.

The last two terms in (3.60) contain the conversion between kinetic and internal (potential) energy and the form drag. Neglecting the transport terms, under assumption that global integrals will be taken, noting that $\nabla p/p = \frac{\pi}{p}\frac{\partial p}{\partial \pi}\nabla\Pi$, and substituting for the geopotential using (3.40), (3.60) can be written as:

$$\begin{aligned}\frac{\partial}{\partial t}\left(\frac{\partial p}{\partial \eta}E\right) &= -RT_v\frac{\partial p}{\partial \eta}\boldsymbol{V}\cdot\left(\frac{\pi}{p}\frac{\partial p}{\partial \pi}\nabla\Pi\right) \\ &\quad -\frac{\partial p}{\partial \eta}\boldsymbol{V}\cdot\nabla\Phi_s - \frac{\partial p}{\partial \eta}\boldsymbol{V}\cdot\nabla\int_{p(\eta)}^{p(1)} RT_v d\ln p + \ \ldots\end{aligned} \tag{3.63}$$

The second term on the right-hand side of (3.64) is a source (form drag) term that can be neglected as we are only interested in internal conservation properties. The last term on the right-hand side of (3.64) can be rewritten as

$$\frac{\partial p}{\partial \eta}\boldsymbol{V}\cdot\nabla\int_{p(\eta)}^{p(1)} RT_v d\ln p = \nabla\cdot\left\{\frac{\partial p}{\partial \eta}\boldsymbol{V}\int_{p(\eta)}^{p(1)} RT_v d\ln p\right\} - \nabla\cdot\left(\frac{\partial p}{\partial \eta}\boldsymbol{V}\right)\int_{p(\eta)}^{p(1)} RT_v d\ln p\,. \quad (3.64)$$

The global integral of the first term on the right-hand side of (3.64) is obviously zero, so that (3.64) can now be written as:

$$\frac{\partial}{\partial t}\left(\frac{\partial p}{\partial \eta}E\right) = -RT_v\frac{\partial p}{\partial \eta}\boldsymbol{V}\cdot\left(\frac{\pi}{p}\frac{\partial p}{\partial \pi}\nabla\Pi\right) + \nabla\cdot\left(\frac{\partial p}{\partial \eta}\boldsymbol{V}\right)\int_{p(\eta)}^{p(1)} RT_v d\ln p + ... \quad (3.65)$$

We now turn to the internal energy equation, obtained by combining the thermodynamic equation (3.36), without the $Q$, $F_{T_H}$, and $F_{F_H}$ terms, and the continuity equation (3.59):

$$\frac{\partial}{\partial t}\left(\frac{\partial p}{\partial \eta}c_p^*T\right) = -\nabla\cdot\left(\frac{\partial p}{\partial \eta}c_p^*T\boldsymbol{V}\right) - \frac{\partial}{\partial \eta}\left(\frac{\partial p}{\partial \eta}c_p^*T\dot{\eta}\right) + RT_v\frac{\partial p}{\partial \eta}\frac{\omega}{p}\,. \quad (3.66)$$

As in (3.60), the first two terms on the right-hand side are advection terms that can be neglected under global integrals. Using (3.16), (3.66) can be written as:

$$\frac{\partial}{\partial t}\left(\frac{\partial p}{\partial \eta}c_p^*T\right) = RT_v\frac{\partial p}{\partial \eta}\boldsymbol{V}\cdot\left(\frac{\pi}{p}\frac{\partial p}{\partial \pi}\nabla\Pi\right) - RT_v\frac{\partial p}{\partial \eta}\frac{1}{p}\int_{\eta_t}^{\eta}\nabla\cdot\left(\frac{\partial p}{\partial \eta}\boldsymbol{V}\right)d\eta + ... \quad (3.67)$$

The rate of change of total energy due to internal processes is obtained by adding (3.65) and (3.67) and must vanish. The first terms on the right-hand side of (3.65) and (3.67) obviously cancel in the continuous form. When the equations are discretized in the vertical, the terms will still cancel, providing that the same definition is used for $(1/p\ \partial p/\partial \pi)_k$ in the nonlinear terms of the vorticity and divergence equations (3.38) and (3.39), and in the $\omega$ term of (3.36) and (3.42).

The second terms on the right-hand side of (3.65) and (3.67) must also cancel in the global mean. This cancellation is enforced locally in the horizontal on the column integrals of (3.65) and (3.67), so that we require:

$$\int_{\eta_t}^{1}\left\{\nabla\cdot\left(\frac{\partial p}{\partial \eta}\boldsymbol{V}\right)\int_{p(\eta)}^{p(1)} RT_v d\ln p\right\}d\eta = \int_{\eta_t}^{1}\left\{RT_v\frac{\partial p}{\partial \eta}\frac{1}{p}\int_{\eta_t}^{\eta}\nabla\cdot\left(\frac{\partial p}{\partial \eta'}\boldsymbol{V}\right)d\eta'\right\}d\eta. \quad (3.68)$$

The inner integral on the left-hand side of (3.68) is derived from the hydrostatic equation (3.40), which we shall approximate as

$$\Phi_k = \Phi_s + R\sum_{\ell=k}^{K} H_{k\ell}T_{v\ell},$$

$$= \Phi_s + R\sum_{\ell=1}^{K} H_{k\ell}T_{v\ell}, \quad (3.69)$$

$$\underline{\Phi} = \Phi_s\underline{1} + R\boldsymbol{H}\underline{T_v}, \quad (3.70)$$

where $H_{k\ell} = 0$ for $\ell < k$. The quantity $\underline{1}$ is defined to be the unit vector. The inner integral on the right-hand side of (3.68) is derived from the vertical velocity equation (3.42), which we shall approximate as

$$\left(\frac{\omega}{p}\right)_k = \left(\frac{\pi}{p}\frac{\partial p}{\partial \pi}\right)_k \boldsymbol{V}_k \cdot \nabla \Pi - \sum_{\ell=1}^{K} C_{k\ell} \left[\delta_\ell \Delta p_\ell + \pi \left(\boldsymbol{V}_\ell \cdot \nabla \Pi\right) \Delta \left(\frac{\partial p}{\partial \pi}\right)_\ell\right], \tag{3.71}$$

where $C_{k\ell} = 0$ for $\ell > k$, and $C_{k\ell}$ is included as an approximation to $1/p_k$ for $\ell \leq k$ and the symbol $\Delta$ is similarly defined as in (3.62). $C_{k\ell}$ will be determined so that $\omega$ is consistent with the discrete continuity equation following Williamson and Olson [1994]. Using (3.69) and (3.71), the finite difference analog of (3.68) is

$$\begin{aligned}\sum_{k=1}^{K} &\left\{\frac{1}{\Delta \eta_k}\left[\delta_k \Delta p_k + \pi \left(\boldsymbol{V}_k \cdot \nabla \Pi\right) \Delta \left(\frac{\partial p}{\partial \pi}\right)_k\right] R \sum_{\ell=1}^{K} H_{k\ell} T_{v\ell}\right\} \Delta \eta_k \\ &= \sum_{k=1}^{K} \left\{R T_{vk} \frac{\Delta p_k}{\Delta \eta_k} \sum_{\ell=1}^{K} C_{k\ell} \left[\delta_\ell \Delta p_\ell + \pi \left(\boldsymbol{V}_\ell \cdot \nabla \Pi\right) \Delta \left(\frac{\partial p}{\partial \pi}\right)_\ell\right]\right\} \Delta \eta_k,\end{aligned} \tag{3.72}$$

where we have used the relation

$$\nabla \cdot \boldsymbol{V} (\partial p / \partial \eta)_k = [\delta_k \Delta p_k + \pi \left(\boldsymbol{V}_k \cdot \nabla \Pi\right) \Delta \left(\partial p / \partial \pi\right)_k] / \Delta \eta_k \tag{3.73}$$

(see 3.22). We can now combine the sums in (3.72) and simplify to give

$$\begin{aligned}\sum_{k=1}^{K} \sum_{\ell=1}^{K} &\left\{\left[\delta_k \Delta p_k + \pi \left(\boldsymbol{V}_k \cdot \nabla \Pi\right) \Delta \left(\frac{\partial p}{\partial \pi}\right)_k\right] H_{k\ell} T_{v\ell}\right\} \\ &= \sum_{k=1}^{K} \sum_{\ell=1}^{K} \left\{\left[\delta_\ell \Delta p_\ell + \pi \left(\boldsymbol{V}_\ell \cdot \nabla \Pi\right) \Delta \left(\frac{\partial p}{\partial \pi}\right)_\ell\right] \Delta p_k C_{k\ell} T_{vk}\right\}.\end{aligned} \tag{3.74}$$

Interchanging the indexes on the left-hand side of (3.74) will obviously result in identical expressions if we require that

$$H_{k\ell} = C_{\ell k} \Delta p_\ell. \tag{3.75}$$

Given the definitions of vertical integrals in (3.70) and (3.71) and of vertical advection in (3.61) and (3.62) the model will conserve energy as long as we require that $\boldsymbol{C}$ and $\boldsymbol{H}$ satisfy (3.75). We are, of course, still neglecting lack of conservation due to the truncation of the horizontal spherical harmonic expansions.

### 3.1.6 Horizontal diffusion

CAM 3.0 contains a horizontal diffusion term for $T, \zeta$, and $\delta$ to prevent spectral blocking and to provide reasonable kinetic energy spectra. The horizontal diffusion operator in CAM 3.0 is also used to ensure that the CFL condition is not violated in the upper layers of the model. The horizontal diffusion is a linear $\nabla^2$ form on $\eta$ surfaces in the top three levels of the model and a linear $\nabla^4$ form with a partial correction to pressure surfaces for temperature elsewhere.

The $\nabla^2$ diffusion near the model top is used as a simple sponge to absorb vertically propagating planetary wave energy and also to control the strength of the stratospheric winter jets. The $\nabla^2$ diffusion coefficient has a vertical variation which has been tuned to give reasonable Northern and Southern Hemisphere polar night jets.

In the top three model levels, the $\nabla^2$ form of the horizontal diffusion is given by

$$F_{\zeta_H} = K^{(2)} \left[\nabla^2 (\zeta + f) + 2 (\zeta + f) /a^2\right], \tag{3.76}$$

$$F_{\delta_H} = K^{(2)} \left[\nabla^2 \delta + 2(\delta/a^2)\right], \tag{3.77}$$

$$F_{T_H} = K^{(2)} \nabla^2 T. \tag{3.78}$$

Since these terms are linear, they are easily calculated in spectral space. The undifferentiated correction term is added to the vorticity and divergence diffusion operators to prevent damping of uniform ($n = 1$) rotations [Orszag, 1974; Bourke et al., 1977]. The $\nabla^2$ form of the horizontal diffusion is applied *only* to pressure surfaces in the standard model configuration.

The horizontal diffusion operator is better applied to pressure surfaces than to terrain-following surfaces (applying the operator on isentropic surfaces would be still better). Although the governing system of equations derived above is designed to reduce to pressure surfaces above some level, problems can still occur from diffusion along the lower surfaces. Partial correction to pressure surfaces of harmonic horizontal diffusion ($\partial \xi / \partial t = K \nabla^2 \xi$) can be included using the relations:

$$\nabla_p \xi = \nabla_\eta \xi - p \frac{\partial \xi}{\partial p} \nabla_\eta \ln p$$

$$\nabla_p^2 \xi = \nabla_\eta^2 \xi - p \frac{\partial \xi}{\partial p} \nabla_\eta^2 \ln p - 2 \nabla_\eta \left( \frac{\partial \xi}{\partial p} - \right) \cdot \nabla_\eta p + \frac{\partial^2 \xi}{\partial^2 p} \nabla_\eta^2 p \,. \tag{3.79}$$

Retaining only the first two terms above gives a correction to the $\eta$ surface diffusion which involves only a vertical derivative and the Laplacian of log surface pressure,

$$\nabla_p^2 \xi = \nabla_\eta^2 \xi - \pi \frac{\partial \xi}{\partial p} \frac{\partial p}{\partial \pi} \nabla^2 \Pi + \ldots \tag{3.80}$$

Similarly, biharmonic diffusion can be partially corrected to pressure surfaces as:

$$\nabla_p^4 \xi = \nabla_\eta^4 \xi - \pi \frac{\partial \xi}{\partial p} \frac{\partial p}{\partial \pi} \nabla^4 \Pi + \ldots \tag{3.81}$$

The bi-harmonic $\nabla^4$ form of the diffusion operator is applied at all other levels (generally throughout the troposphere) as

$$F_{\zeta_H} = -K^{(4)} \left[\nabla^4 (\zeta + f) - (\zeta + f) \left(2/a^2\right)^2\right], \tag{3.82}$$

$$F_{\delta_H} = -K^{(4)} \left[\nabla^4 \delta - \delta (2/a^2)^2\right], \tag{3.83}$$

$$F_{T_H} = -K^{(4)} \left[\nabla^4 T - \pi \frac{\partial T}{\partial p} \frac{\partial p}{\partial \pi} \nabla^4 \Pi \right]. \tag{3.84}$$

The second term in $F_{T_H}$ consists of the leading term in the transformation of the $\nabla^4$ operator to pressure surfaces. It is included to offset partially a spurious diffusion of $T$ over mountains.

As with the $\nabla^2$ form, the $\nabla^4$ operator can be conveniently calculated in spectral space. The correction term is then completed after transformation of $T$ and $\nabla^4\Pi$ back to grid–point space. As with the $\nabla^2$ form, an undifferentiated term is added to the vorticity and divergence diffusion operators to prevent damping of uniform rotations.

### 3.1.7 Finite difference equations

The governing equations are solved using the spectral method in the horizontal, so that only the vertical and time differences are presented here. The dynamics includes horizontal diffusion of $T, (\zeta + f)$, and $\delta$. Only $T$ has the leading term correction to pressure surfaces. Thus, equations that include the terms in this time split sub-step are of the form

$$\frac{\partial \psi}{\partial t} = \mathrm{Dyn}\,(\psi) - (-1)^i K^{(2i)} \nabla_\eta^{2i} \psi\,, \tag{3.85}$$

for $(\zeta + f)$ and $\delta$, and

$$\frac{\partial T}{\partial t} = \mathrm{Dyn}\,(T) - (-1)^i K^{(2i)} \left\{ \nabla_\eta^{2i} T - \pi \frac{\partial T}{\partial p} \frac{\partial p}{\partial \pi} \nabla^{2i} \Pi \right\}\,, \tag{3.86}$$

where $i = 1$ in the top few model levels and $i = 2$ elsewhere (generally within the troposphere). These equations are further subdivided into time split components:

$$\psi^{n+1} = \psi^{n-1} + 2\Delta t\ \mathrm{Dyn}\left(\psi^{n+1}, \psi^n, \psi^{n-1}\right)\,, \tag{3.87}$$

$$\psi^* = \psi^{n+1} - 2\Delta t\ (-1)^i K^{(2i)} \nabla_\eta^{2i} \left(\psi^{*n+1}\right)\,, \tag{3.88}$$

$$\hat{\psi}^{n+1} = \psi^*\,, \tag{3.89}$$

for $(\zeta + f)$ and $\delta$, and

$$T^{n+1} = T^{n-1} + 2\Delta t\ \mathrm{Dyn}\left(T^{n+1}, T^n, T^{n-1}\right) \tag{3.90}$$

$$T^* = T^{n+1} - 2\Delta t\ \ (-1)^i\, K^{(2i)} \nabla^{2i} \eta\, (T^*)\,, \tag{3.91}$$

$$\hat{T}^{n+1} = T^* + 2\Delta t\ \ (-1)^i\, K^{(2i)} \pi \frac{\partial T^*}{\partial p} \frac{\partial p}{\partial \pi} \nabla^{2i}\,\Pi\,, \tag{3.92}$$

for $T$, where in the standard model $i$ only takes the value 2 in (3.92). The first step from $(\ )^{n-1}$ to $(\ )^{n+1}$ includes the transformation to spectral coefficients. The second step from $(\ )^{n+1}$ to $(\hat{\ })^{n+1}$ for $\delta$ and $\zeta$, or $(\ )^{n+1}$ to $(\ )^*$ for $T$, is done on the spectral coefficients, and the final step from $(\ )^*$ to $(\hat{\ })^{n+1}$ for $T$ is done after the inverse transform to the grid point representation.

The following finite-difference description details only the forecast given by (3.87) and (3.90). The finite-difference form of the forecast equation for water vapor will be presented later in Section 3c. The general structure of the complete finite difference equations is determined by the semi-implicit time differencing and the energy conservation properties described above. In order to complete the specification of the finite differencing, we require a definition of the vertical coordinate. The actual specification of the generalized vertical coordinate takes advantage of the structure of the equations (3.33)-(3.42). The equations can be finite-differenced in the vertical and, in time, without having to know the value of $\eta$ anywhere. The quantities that must be known are $p$ and $\partial p/\partial\pi$ at the grid points. Therefore the coordinate is defined implicitly through the relation:

$$p(\eta,\pi) = A(\eta)p_0 + B(\eta)\pi\,, \tag{3.93}$$

which gives

$$\frac{\partial p}{\partial \pi} = B(\eta)\,. \tag{3.94}$$

A set of levels $\eta_k$ may be specified by specifying $A_k$ and $B_k$, such that $\eta_k \equiv A_k + B_k$, and difference forms of (3.33)-(3.42) may be derived.

The finite difference forms of the Dyn operator (3.33)-(3.42), including semi-implicit time integration are:

$$\begin{aligned}
\underline{\zeta}^{n+1} &= \underline{\zeta}^{n-1} + 2\Delta t\boldsymbol{k}\cdot\nabla\times(\underline{\boldsymbol{n}}^n/\cos\phi)\,, && (3.95)\\
\underline{\delta}^{n+1} &= \underline{\delta}^{n-1} + 2\Delta t\left[\nabla\cdot(\underline{\boldsymbol{n}}^n/\cos\phi) - \nabla^2\left(\underline{E}^n + \Phi_s\underline{1} + R\boldsymbol{H}^n(\underline{T_v}')^n\right)\right]\\
&\quad -2\Delta t R\boldsymbol{H}^r\nabla^2\left(\frac{(\underline{T}')^{n-1}+(\underline{T}')^{n+1}}{2} - (\underline{T}')^n\right)\\
&\quad -2\Delta t R\left(\underline{b}^r + \underline{h}^r\right)\nabla^2\left(\frac{\Pi^{n-1}+\Pi^{n+1}}{2} - \Pi^n\right), && (3.96)\\
(\underline{T}')^{n+1} &= (\underline{T}')^{n-1} - 2\Delta t\left[\frac{1}{a\cos^2\phi}\frac{\partial}{\partial\lambda}(\underline{UT'})^n + \frac{1}{a\cos\phi}\frac{\partial}{\partial\phi}(\underline{VT'})^n - \underline{\Gamma}^n\right] && (3.97)\\
&\quad -2\Delta t\boldsymbol{D}^r\left(\frac{\underline{\delta}^{n-1}+\underline{\delta}^{n+1}}{2} - \underline{\delta}^n\right)\\
\Pi^{n+1} &= \Pi^{n-1} - 2\Delta t\frac{1}{\pi^n}\left((\underline{\delta}^n)^T\,\underline{\Delta p}^n + (\underline{\boldsymbol{V}}^n)^T\cdot\nabla\Pi^n\pi^n\underline{\Delta B}\right)\\
&\quad -2\Delta t\left(\frac{\underline{\delta}^{n-1}+\underline{\delta}^{n+1}}{2} - \underline{\delta}^n\right)^T\frac{1}{\pi^r}\underline{\Delta p}^r, && (3.98)\\
(n_U)_k &= (\zeta_k + f)\,V_k - RT_{vk}\left(\frac{1}{p}\frac{\partial p}{\partial\pi}\right)_k\pi\frac{1}{a}\frac{\partial\Pi}{\partial\lambda}\\
&\quad -\frac{1}{2\Delta p_k}\left[\left(\dot\eta\frac{\partial p}{\partial\eta}\right)_{k+1/2}(U_{k+1}-U_k) + \left(\dot\eta\frac{\partial p}{\partial\eta}\right)_{k-1/2}(U_k-U_{k-1})\right]\\
&\quad +(F_U)_k\ , && (3.99)\\
(n_V)_k &= -(\zeta_k + f)\,U_k - RT_{vk}\left(\frac{1}{p}\frac{\partial p}{\partial\pi}\right)_k\pi\frac{\cos\phi}{a}\frac{\partial\Pi}{\partial\phi}\\
&\quad -\frac{1}{2\Delta p_k}\left[\left(\dot\eta\frac{\partial p}{\partial\eta}\right)_{k+1/2}(V_{k+1}-V_k) + \left(\dot\eta\frac{\partial p}{\partial\eta}\right)_{k-1/2}(V_k-V_{k-1})\right]\\
&\quad +(F_V)_k\ , && (3.100)\\
\Gamma_k &= T'_k\delta_k + \frac{RT_{vk}}{(c_p^*)_k}\left(\frac{\omega}{p}\right)_k - Q\\
&\quad -\frac{1}{2\Delta p_k}\left[\left(\dot\eta\frac{\partial p}{\partial\eta}\right)_{k+1/2}(T_{k+1}-T_k) + \left(\dot\eta\frac{\partial p}{\partial\eta}\right)_{k-1/2}(T_k-T_{k-1})\right], && (3.101)
\end{aligned}$$

$$
\begin{aligned}
E_k &= (u_k)^2 + (v_k)^2, && (3.102)\\
\frac{RT_{vk}}{(c_p^*)_k} &= \frac{R}{c_p}\left(\frac{T_k^r + T_{vk}'}{1+\left(\frac{c_{pv}}{c_p}-1\right)q_k}\right), && (3.103)\\
\left(\dot{\eta}\frac{\partial p}{\partial \eta}\right)_{k+1/2} &= B_{k+1/2}\sum_{\ell=1}^{K}\left[\delta_\ell \Delta p_\ell + \boldsymbol{V}_\ell \cdot \pi \nabla \Pi \Delta B_\ell\right] \\
&\quad -\sum_{\ell=1}^{k}\left[\delta_\ell \Delta p_\ell + \boldsymbol{V}_\ell \cdot \pi \nabla \Pi \Delta B_\ell\right], && (3.104)\\
\left(\frac{\omega}{p}\right)_k &= \left(\frac{1}{p}\frac{\partial p}{\partial \pi}\right)_k \boldsymbol{V}_k \cdot \pi \nabla \Pi - \sum_{\ell=1}^{k} C_{k\ell}\left[\delta_\ell \Delta p_\ell + \boldsymbol{V}_\ell \cdot \pi \nabla \Pi \Delta B_\ell\right], && (3.105)\\
C_{k\ell} &= \begin{cases} \frac{1}{p_k}, & \ell < k \\ \frac{1}{2p_k}, & \ell = k, \end{cases} && (3.106)\\
H_{k\ell} &= C_{\ell k}\Delta p_\ell, && (3.107)\\
D_{k\ell}^r &= \Delta p_\ell^r \frac{R}{c_p} T_k^r C_{\ell k}^r + \frac{\Delta p_\ell^r}{2\Delta p_k^r}\left(T_k^r - T_{k-1}^r\right)\left(\epsilon_{k\ell+1} - B_{k-1/2}\right) \\
&\quad + \frac{\Delta p_\ell^r}{2\Delta p_k^r}\left(T_{k+1}^r - T_k^r\right)\left(\epsilon_{k\ell} - B_{k+1/2}\right), && (3.108)\\
\frac{\epsilon_{k\ell}}{R} &= \begin{cases} 1, & \ell \le k \\ 0, & \ell > k, \end{cases} && (3.109)
\end{aligned}
$$

where notation such as $(\underline{UT'})^n$ denotes a column vector with components $(U_k T_k')^n$. In order to complete the system, it remains to specify the reference vector $\underline{h}^r$, together with the term $(1/p\, \partial p/\partial \pi)$, which results from the pressure gradient terms and also appears in the semi-implicit reference vector $\underline{b}^r$:

$$
\begin{aligned}
\left(\frac{1}{p}\frac{\partial p}{\partial \pi}\right)_k &= \left(\frac{1}{p}\right)_k \left(\frac{\partial p}{\partial \pi}\right)_k = \frac{B_k}{p_k}, && (3.110)\\
\underline{b}^r &= \underline{T}^r, && (3.111)\\
\underline{h}^r &= 0. && (3.112)
\end{aligned}
$$

The matrices $\boldsymbol{C}^n$ and $\boldsymbol{H}^n$ (*i.e.* with components $C_{k\ell}$ and $H_{k\ell}$) must be evaluated at each time step and each point in the horizontal. It is more efficient computationally to substitute the definitions of these matrices into (3.96) and (3.105) at the cost of some loss of generality in the code. The finite difference equations have been written in the form (3.95)-(3.112) because this form is quite general. For example, the equations solved by Simmons and Strüfing [1981] at ECMWF can be obtained by changing only the vectors and hydrostatic matrix defined by (3.109)-(3.112).

### 3.1.8 Time filter

The time step is completed by applying a recursive time filter originally designed by [Robert, 1966] and later studied by [Asselin, 1972].

$$\overline{\psi}^{n} = \psi^{n} + \alpha \left( \overline{\psi}^{n-1} - 2\psi^{n} + \psi^{n+1} \right) \tag{3.113}$$

### 3.1.9 Spectral transform

The spectral transform method is used in the horizontal exactly as in CCM1. As shown earlier, the vertical and temporal aspects of the model are represented by finite–difference approximations. The horizontal aspects are treated by the spectral–transform method, which is described in this section. Thus, at certain points in the integration, the prognostic variables $(\zeta + f), \delta, T$, and $\Pi$ are represented in terms of coefficients of a truncated series of spherical harmonic functions, while at other points they are given by grid–point values on a corresponding Gaussian grid. In general, physical parameterizations and nonlinear operations are carried out in grid–point space. Horizontal derivatives and linear operations are performed in spectral space. Externally, the model appears to the user to be a grid–point model, as far as data required and produced by it. Similarly, since all nonlinear parameterizations are developed and carried out in grid–point space, the model also appears as a grid–point model for the incorporation of physical parameterizations, and the user need not be too concerned with the spectral aspects. For users interested in diagnosing the balance of terms in the evolution equations, however, the details are important and care must be taken to understand which terms have been spectrally truncated and which have not. The algebra involved in the spectral transformations has been presented in several publications [Daley et al., 1976; Bourke et al., 1977; Machenhauer, 1979]. In this report, we present only the details relevant to the model code; for more details and general philosophy, the reader is referred to these earlier papers.

### 3.1.10 Spectral algorithm overview

The horizontal representation of an arbitrary variable $\psi$ consists of a truncated series of spherical harmonic functions,

$$\psi(\lambda, \mu) = \sum_{m=-M}^{M} \sum_{n=|m|}^{\mathcal{N}(m)} \psi_n^m P_n^m(\mu) e^{im\lambda}, \tag{3.114}$$

where $\mu = \sin\phi$, $M$ is the highest Fourier wavenumber included in the east–west representation, and $\mathcal{N}(m)$ is the highest degree of the associated Legendre polynomials for longitudinal wavenumber $m$. The properties of the spherical harmonic functions used in the representation can be found in the review by Machenhauer [1979]. The model is coded for a general pentagonal truncation, illustrated in Figure 3.2, defined by three parameters: $M, K$, and $N$, where $M$ is defined above, $K$ is the highest degree of the associated Legendre polynomials, and $N$ is the highest degree of the Legendre polynomials for $m = 0$. The common truncations are subsets of

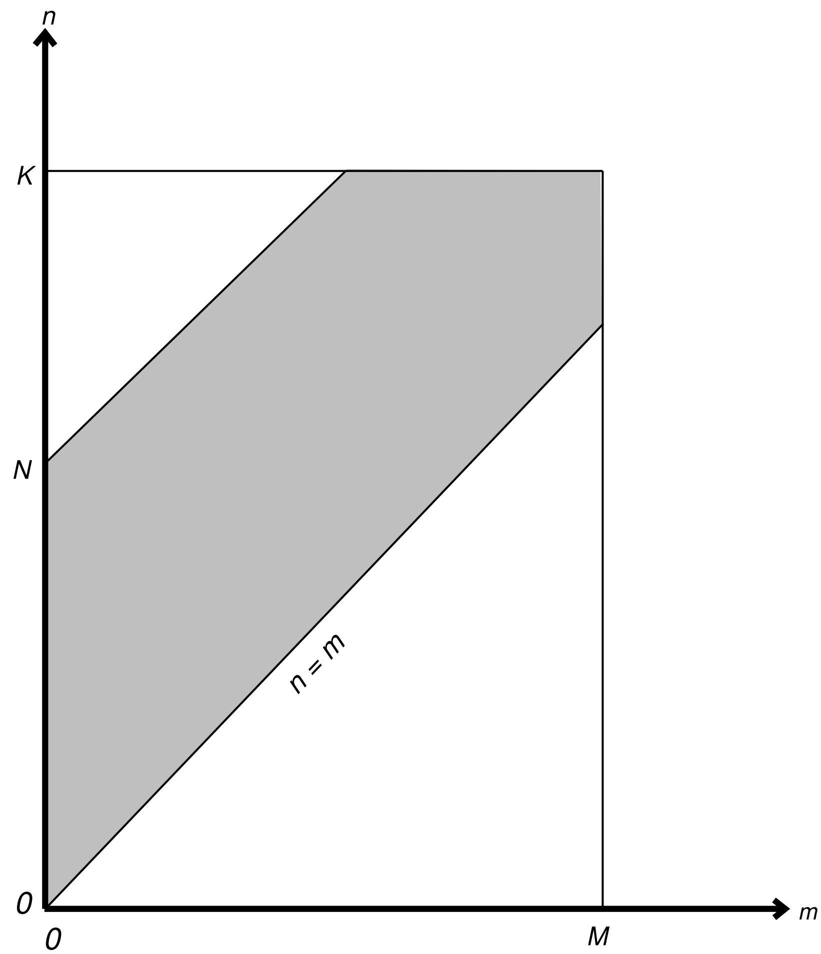


Figure 3.2: Pentagonal truncation parameters

this pentagonal case:

$$\begin{aligned} \text{Triangular}: &\quad M = N = K, \\ \text{Rhomboidal}: &\quad K = N + M, \\ \text{Trapezoidal}: &\quad N = K > M. \end{aligned} \tag{3.115}$$

The quantity $\mathcal{N}(m)$ in (3.114) represents an arbitrary limit on the two-dimensional wavenumber $n$, and for the pentagonal truncation described above is simply given by $\mathcal{N}(m) = \min(N + |m|, K)$.

The associated Legendre polynomials used in the model are normalized such that

$$\int_{-1}^{1} [P_n^m(\mu)]^2 \, d\mu = 1. \tag{3.116}$$

With this normalization, the Coriolis parameter $f$ is

$$f = \frac{\Omega}{\sqrt{0.375}} P_1^o, \tag{3.117}$$

which is required for the absolute vorticity.

The coefficients of the spectral representation (3.114) are given by

$$\psi_n^m = \int_{-1}^{1} \frac{1}{2\pi} \int_0^{2\pi} \psi(\lambda, \mu) e^{-im\lambda} d\lambda P_n^m(\mu) d\mu. \tag{3.118}$$

The inner integral represents a Fourier transform,

$$\psi^m(\mu) = \frac{1}{2\pi} \int_0^{2\pi} \psi(\lambda, \mu) e^{-im\lambda} d\lambda, \tag{3.119}$$

which is performed by a Fast Fourier Transform (FFT) subroutine. The outer integral is performed via Gaussian quadrature,

$$\psi_n^m = \sum_{j=1}^{J} \psi^m(\mu_j) P_n^m(\mu_j) w_j, \tag{3.120}$$

where $\mu_j$ denotes the Gaussian grid points in the meridional direction, $w_j$ the Gaussian weight at point $\mu_j$, and $J$ the number of Gaussian grid points from pole to pole. The Gaussian grid points ($\mu_j$) are given by the roots of the Legendre polynomial $P_J(\mu)$, and the corresponding weights are given by

$$w_j = \frac{2(1-\mu_j^2)}{\left[J\ P_{J-1}(\mu_j)\right]^2}. \tag{3.121}$$

The weights themselves satisfy

$$\sum_{j=1}^{J} w_j = 2.0\ . \tag{3.122}$$

The Gaussian grid used for the north–south transformation is generally chosen to allow unaliased computations of quadratic terms only. In this case, the number of Gaussian latitudes $J$ must satisfy

$$J \geq (2N + K + M + 1)/2 \quad \text{for } M \leq 2(K-N)\ , \tag{3.123}$$

$$J \geq (3K + 1)/2 \quad \text{for } M \geq 2(K-N)\ . \tag{3.124}$$

For the common truncations, these become

$$J \geq (3K + 1)/2 \quad \text{for triangular and trapezoidal,} \tag{3.125}$$

$$J \geq (3N + 2M + 1)/2 \quad \text{for rhomboidal.} \tag{3.126}$$

In order to allow exact Fourier transform of quadratic terms, the number of points $P$ in the east–west direction must satisfy

$$P \geq 3M + 1\ . \tag{3.127}$$

The actual values of $J$ and $P$ are often not set equal to the lower limit in order to allow use of more efficient transform programs.

Although in the next section of this model description, we continue to indicate the Gaussian quadrature as a sum from pole to pole, the code actually deals with the symmetric and antisymmetric components of variables and accumulates the sums from equator to pole only. The model requires an even number of latitudes to easily use the symmetry conditions. This may be slightly inefficient for some spectral resolutions. We define a new index, which goes from $-I$ at the point next to the south pole to $+I$ at the point next to the north pole and not including 0 (there are no points at the equator or pole in the Gaussian grid), *i.e.,* let $I = J/2$ and $i = j - J/2$ for $j \geq J/2 + 1$ and $i = j - J/2 - 1$ for $j \leq J/2$; then the summation in (3.120) can be rewritten as

$$\psi_n^m = \sum_{i=-I,\, i\neq 0}^{I} \psi^m(\mu_i) P_n^m(\mu_i) w_i. \tag{3.128}$$

The symmetric (even) and antisymmetric (odd) components of $\psi^m$ are defined by

$$(\psi_E)_i^m = \frac{1}{2}\left(\psi_i^m + \psi_{-i}^m\right),$$

$$(\psi_O)_i^m = \frac{1}{2}\left(\psi_i^m - \psi_{-i}^m\right). \tag{3.129}$$

Since $w_i$ is symmetric about the equator, (3.128) can be rewritten to give formulas for the coefficients of even and odd spherical harmonics:

$$\psi_n^m = \begin{cases} \sum\limits_{i=1}^{I} (\psi_E)_i^m (\mu_i) P_n^m(\mu_i) 2w_i & \text{for } n-m \text{ even,} \\ \sum\limits_{i=1}^{I} (\psi_O)_i^m (\mu_i) P_n^m(\mu_i) 2w_i & \text{for } n-m \text{ odd.} \end{cases} \tag{3.130}$$

The model uses the spectral transform method [Machenhauer, 1979] for all nonlinear terms. However, the model can be thought of as starting from grid–point values at time $t$ (consistent with the spectral representation) and producing a forecast of the grid–point values at time $t+\Delta t$ (again, consistent with the spectral resolution). The forecast procedure involves computation of the nonlinear terms including physical parameterizations at grid points; transformation via Gaussian quadrature of the nonlinear terms from grid–point space to spectral space; computation of the spectral coefficients of the prognostic variables at time $t + \Delta t$ (with the implied spectral truncation to the model resolution); and transformation back to grid–point space. The details of the equations involved in the various transformations are given in the next section.

### 3.1.11 Combination of terms

In order to describe the transformation to spectral space, for each equation we first group together all undifferentiated explicit terms, all explicit terms with longitudinal derivatives, and all explicit terms with meridional derivatives appearing in the Dyn operator. Thus, the vorticity equation (3.95) is rewritten

$$\underline{(\zeta + f)}^{n+1} = \underline{V} + \frac{1}{a(1-\mu^2)}\left[\frac{\partial}{\partial\lambda}(\underline{V}_\lambda) - (1-\mu^2)\frac{\partial}{\partial\mu}(\underline{V}_\mu)\right], \tag{3.131}$$

where the explicit forms of the vectors $\underline{V}, \underline{V}_\lambda$, and $\underline{V}_\mu$ are given as

$$\begin{aligned}
\underline{V} &= \underline{(\zeta + f)}^{n-1}, & (3.132)\\
\underline{V}_\lambda &= 2\Delta t\, \underline{n}_V^n, & (3.133)\\
\underline{V}_\mu &= 2\Delta t\, \underline{n}_U^n. & (3.134)
\end{aligned}$$

The divergence equation (3.96) is

$$\begin{aligned}
\underline{\delta}^{n+1} &= \underline{D} + \frac{1}{a(1-\mu^2)}\left[\frac{\partial}{\partial\lambda}(\underline{D}_\lambda) + (1-\mu^2)\frac{\partial}{\partial\mu}(\underline{D}_\mu)\right] - \nabla^2 \underline{D}_\nabla \\
&\quad -\Delta t \nabla^2 (R\boldsymbol{H}^r \underline{T}'^{\,n+1} + R\,(\underline{b}^r + \underline{h}^r)\,\Pi^{n+1}). \qquad (3.135)
\end{aligned}$$

The mean component of the temperature is not included in the next–to–last term since the Laplacian of it is zero. The thermodynamic equation (3.98) is

$$\underline{T}'^{\,n+1} = \underline{T} - \frac{1}{a(1-\mu^2)}\left[\frac{\partial}{\partial\lambda}(\underline{T}_\lambda) + (1-\mu^2)\frac{\partial}{\partial\mu}(\underline{T}_\mu) - \right] - \Delta t \boldsymbol{D}^r\ \underline{\delta}^{n+1}. \qquad (3.136)$$

The surface–pressure tendency (3.98) is

$$\Pi^{n+1} = PS - \frac{\Delta t}{\pi^r}\left(\underline{\Delta p}^r\right)^T \underline{\delta}^{n+1}. \qquad (3.137)$$

The grouped explicit terms in (3.135)–(3.137) are given as follows. The terms of (3.135) are

$$\begin{aligned}
\underline{D} &= \underline{\delta}^{n-1}, & (3.138)\\
\underline{D}_\lambda &= 2\Delta t\, \underline{n}_U^n, & (3.139)\\
\underline{D}_\mu &= 2\Delta t\, \underline{n}_V^n, & (3.140)
\end{aligned}$$

$$\begin{aligned}
\underline{D}_\nabla &= 2\Delta t\left[\underline{E}^n + \Phi_s \underline{1} + R\boldsymbol{H}^r \underline{T}'^{n}\right] \\
&\quad + \Delta t\left[R\boldsymbol{H}^r\left((\underline{T}')^{n-1} - 2(\underline{T}')^n\right) + R\,(\underline{b}^r + \underline{h}^r)\left(\Pi^{n-1} - 2\Pi^n\right)\right]. \qquad (3.141)
\end{aligned}$$

The terms of (3.136) are

$$\begin{aligned}
\underline{T} &= (\underline{T}')^{n-1} + 2\Delta t\, \underline{\Gamma}^n - \Delta t \boldsymbol{D}^r\left[\underline{\delta}^{n-1} - 2\underline{\delta}^n\right], & (3.142)\\
\underline{T}_\lambda &= 2\Delta t \underline{(UT')}^n, & (3.143)\\
\underline{T}_\mu &= 2\Delta t \underline{(VT')}^n. & (3.144)
\end{aligned}$$

The nonlinear term in (3.137) is

$$\begin{aligned}
PS &= \Pi^{n-1} - 2\Delta t \tfrac{1}{\pi^n}\left[(\underline{\delta}^n)^T\left(\underline{\Delta p}^n\right) + (\underline{\boldsymbol{V}}^n)^T \nabla\Pi^n \pi^n \underline{\Delta B}\right] \\
&\quad - \Delta t\left[\left(\underline{\Delta p}^r\right)^T \tfrac{1}{\pi^r}\right]\left[\underline{\delta}^{n-1} - 2\underline{\delta}^n\right]. \qquad (3.145)
\end{aligned}$$

### 3.1.12 Transformation to spectral space

Formally, Equations (3.131)-(3.137) are transformed to spectral space by performing the operations indicated in (3.146) to each term. We see that the equations basically contain three types of terms, for example, in the vorticity equation the undifferentiated term $\underline{V}$, the longitudinally differentiated term $\underline{V}_\lambda$, and the meridionally differentiated term $\underline{V}_\mu$. All terms in the original equations were grouped into one of these terms on the Gaussian grid so that they could be transformed at once.

Transformation of the undifferentiated term is obtained by straightforward application of (3.118)-(3.120),

$$\{\underline{V}\}_n^m = \sum_{j=1}^{J} \underline{V}^m(\mu_j) P_n^m(\mu_j) w_j, \tag{3.146}$$

where $\underline{V}^m(\mu_j)$ is the Fourier coefficient of $\underline{V}$ with wavenumber $m$ at the Gaussian grid line $\mu_j$. The longitudinally differentiated term is handled by integration by parts, using the cyclic boundary conditions,

$$\left\{\frac{\partial}{\partial\lambda}(\underline{V}_\lambda)\right\}^m = \frac{1}{2\pi}\int_o^{2\pi} \frac{\partial \underline{V}_\lambda}{\partial\lambda} e^{-im\lambda} d\lambda, \tag{3.147}$$

$$= im\frac{1}{2\pi}\int_o^{2\pi} \underline{V}_\lambda e^{-im\lambda} d\lambda, \tag{3.148}$$

$$\tag{3.149}$$

so that the Fourier transform is performed first, then the differentiation is carried out in spectral space. The transformation to spherical harmonic space then follows (3.152):

$$\left\{\frac{1}{a(1-\mu^2)}\frac{\partial}{\partial\lambda}(\underline{V}_\lambda)\right\}_n^m = im\sum_{j=1}^{J} \underline{V}_\lambda^m(\mu_j)\frac{P_n^m(\mu_j)}{a(1-\mu_j^2)} w_j, \tag{3.150}$$

where $\underline{V}_\lambda^m(\mu_j)$ is the Fourier coefficient of $\underline{V}_\lambda$ with wavenumber $m$ at the Gaussian grid line $\mu_j$.

The latitudinally differentiated term is handled by integration by parts using zero boundary conditions at the poles:

$$\left\{\frac{1}{a(1-\mu^2)}(1-\mu^2)\frac{\partial}{\partial\mu}(\underline{V}_\mu)\right\}_n^m = \int_{-1}^{1} \frac{1}{a(1-\mu^2)}(1-\mu^2)\frac{\partial}{\partial\mu}(\underline{V}_\mu)^m P_n^m d\mu, \tag{3.151}$$

$$= -\int_{-1}^{1} \frac{1}{a(1-\mu^2)}(\underline{V}_\mu)^m (1-\mu^2)\frac{dP_n^m}{d\mu} d\mu. \tag{3.152}$$

Defining the derivative of the associated Legendre polynomial by

$$H_n^m = (1-\mu^2)\frac{dP_n^m}{d\mu}, \tag{3.153}$$

(3.155) can be written

$$\left\{\frac{1}{a(1-\mu^2)}(1-\mu^2)\frac{\partial}{\partial\mu}(\underline{V}_\mu)\right\}_n^m = -\sum_{j=1}^{J} (\underline{V}_\mu)^m \frac{H_n^m(\mu_j)}{a(1-\mu_j^2)} w_j. \tag{3.154}$$

Similarly, the $\nabla^2$ operator in the divergence equation can be converted to spectral space by sequential integration by parts and then application of the relationship

$$\nabla^2 P_n^m(\mu) e^{im\lambda} = \frac{-n(n+1)}{a^2} P_n^m(\mu) e^{im\lambda}, \tag{3.155}$$

to each spherical harmonic function individually so that

$$\left\{\nabla^2 \underline{D}_\nabla\right\}_n^m = \frac{-n(n+1)}{a^2} \sum_{j=1}^{J} \underline{D}_\nabla^m(\mu_j) P_n^m(\mu_j) w_j, \tag{3.156}$$

where $\underline{D}_\nabla^m(\mu)$ is the Fourier coefficient of the original grid variable $\underline{D}_\nabla$.

### 3.1.13 Solution of semi-implicit equations

The prognostic equations can be converted to spectral form by summation over the Gaussian grid using (3.146), (3.150), and (3.154). The resulting equation for absolute vorticity is

$$\underline{(\zeta + f)}_n^m = \underline{VS}_n^m, \tag{3.157}$$

where $\underline{(\zeta + f)}_n^m$ denotes a spherical harmonic coefficient of $\underline{(\zeta + f)}^{n+1}$, and the form of $\underline{VS}_n^m$, as a summation over the Gaussian grid, is given as

$$\underline{VS}_n^m = \sum_{j=1}^{J} \left[ \underline{V}^m(\mu_j) P_n^m(\mu_j) + im \underline{V}_\lambda^m(\mu_j) \frac{P_n^m(\mu_j)}{a(1-\mu_j^2)} + \underline{V}_\mu^m(\mu_j) \frac{H_n^m(\mu_j)}{a(1-\mu_j^2)} \right] w_j. \tag{3.158}$$

The spectral form of the divergence equation (3.135) becomes

$$\underline{\delta}_n^m = \underline{DS}_n^m + \Delta t \frac{n(n+1)}{a^2} \left[ R \boldsymbol{H}^r \underline{T}_n^{\prime m} + R \left( \underline{b}^r + \underline{h}^r \right) \Pi_n^m \right], \tag{3.159}$$

where $\underline{\delta}_n^m$, $\underline{T}_n^{\prime m}$, and $\Pi_n^m$ are spectral coefficients of $\underline{\delta}^{n+1}$, $\underline{T}^{\prime\, n+1}$, and $\Pi^{n+1}$. The Laplacian of the total temperature in (3.135) is replaced by the equivalent Laplacian of the perturbation temperature in (3.159). $\underline{DS}_n^m$ is given by

$$\begin{aligned} \underline{DS}_n^m = \sum_{j=1}^{J} \Bigg\{ & \left[ \underline{D}^m(\mu_j) + \frac{n(n+1)}{a^2} \underline{D}_\nabla^m(\mu_j) \right] P_n^m(\mu_j) \\ & + im \underline{D}_\lambda^m(\mu_j) \frac{P_n^m(\mu_j)}{a(1-\mu_j^2)} - \underline{D}_\mu^m(\mu_j) \frac{H_n^m(\mu_j)}{a(1-\mu_j^2)} \Bigg\} w_j. \end{aligned} \tag{3.160}$$

The spectral thermodynamic equation is

$$\underline{T}_n^{\prime m} = \underline{TS}_n^m - \Delta t \boldsymbol{D}^r \underline{\delta}_n^m, \tag{3.161}$$

with $\underline{TS}_n^m$ defined as

$$\underline{TS}_n^m = \sum_{j=1}^{J} \left[ \underline{T}^m(\mu_j) P_n^m(\mu_j) - im \underline{T}_\lambda^m(\mu_j) \frac{P_n^m(\mu_j)}{a(1-\mu_j^2)} + \underline{T}_\mu^m(\mu_j) \frac{H_n^m(\mu_j)}{a(1-\mu_j^2)} \right] w_j, \tag{3.162}$$

while the surface pressure equation is

$$\Pi_n^m = \mathit{PS}_n^m - \underline{\delta}_n^m \left(\underline{\Delta p}^r\right)^T \frac{\Delta t}{\pi^r}, \tag{3.163}$$

where $\mathit{PS}_n^m$ is given by

$$\mathit{PS}_n^m = \sum_{j=1}^{J} \mathit{PS}^m(\mu_j) P_n^m(\mu_j) w_j. \tag{3.164}$$

Equation (3.157) for vorticity is explicit and complete at this point. However, the remaining equations (3.159)–(3.163) are coupled. They are solved by eliminating all variables except $\underline{\delta}_n^m$:

$$\boldsymbol{A}_n \underline{\delta}_n^m = \underline{\mathit{DS}}_n^m + \Delta t \frac{n(n+1)}{a^2} \left[ R\boldsymbol{H}^r (\underline{\mathit{TS}})_n^m + R\left(\underline{b}^r + \underline{h}^r\right) (\mathit{PS})_n^m \right], \tag{3.165}$$

where

$$\boldsymbol{A}_n = \boldsymbol{I} + \Delta t^2 \frac{n(n+1)}{a^2} \left[ R\boldsymbol{H}^r \boldsymbol{D}^r + R\left(\underline{b}^r + \underline{h}^r\right) \left( \left(\underline{\Delta p}^r\right)^T \frac{1}{\pi^r} \right) \right], \tag{3.166}$$

which is simply a set of $K$ simultaneous equations for the coefficients with given wavenumbers $(m, n)$ at each level and is solved by inverting $\boldsymbol{A}_n$. In order to prevent the accumulation of round–off error in the global mean divergence (which if exactly zero initially, should remain exactly zero) $(\boldsymbol{A}_o)^{-1}$ is set to the null matrix rather than the identity, and the formal application of (3.165) then always guarantees $\underline{\delta}_o^o = 0$. Once $\delta_n^m$ is known, $\underline{T}_n'^m$ and $\Pi_n^m$ can be computed from (3.161) and (3.163), respectively, and all prognostic variables are known at time $n+1$ as spherical harmonic coefficients. Note that the mean component $\underline{T}_o'^o$ is not necessarily zero since the perturbations are taken with respect to a specified $\underline{T}^r$.

### 3.1.14 Horizontal diffusion

As mentioned earlier, the horizontal diffusion in (3.88) and (3.91) is computed implicitly via time splitting after the transformations into spectral space and solution of the semi-implicit equations. In the following, the $\zeta$ and $\delta$ equations have a similar form, so we write only the $\delta$ equation:

$$\begin{aligned} (\delta^*)_n^m &= \left(\delta^{n+1}\right)_n^m - (-1)^i \, 2\Delta t K^{(2i)} \left[ \nabla^{2i} (\delta^*)_n^m - (-1)^i (\delta^*)_n^m \left(2/a^2\right)^i \right], & (3.167) \\ (T^*)_n^m &= \left(T^{n+1}\right)_n^m - (-1)^i \, 2\Delta t K^{(2i)} \left[ \nabla^{2i} (T^*)_n^m \right] . & (3.168) \end{aligned}$$

The extra term is present in (3.167), (3.171) and (3.173) to prevent damping of uniform rotations. The solutions are just

$$(\delta^*)_n^m = K_n^{(2i)}(\delta)\left(\delta^{n+1}\right)_n^m, \tag{3.169}$$

$$(T^*)_n^m = K_n^{(2i)}(T)\left(T^{n+1}\right)_n^m, \tag{3.170}$$

$$K_n^{(2)}(\delta) = \left\{1 + 2\Delta t D_n K^{(2)}\left[\left(\frac{n(n+1)}{a^2}\right) - \frac{2}{a^2}\right]\right\}^{-1}, \tag{3.171}$$

$$K_n^{(2)}(T) = \left\{1 + 2\Delta t D_n K^{(2)}\left(\frac{n(n+1)}{a^2}\right)\right\}^{-1}, \tag{3.172}$$

$$K_n^{(4)}(\delta) = \left\{1 + 2\Delta t D_n K^{(4)}\left[\left(\frac{n(n+1)}{a^2}\right)^2 - \frac{4}{a^4}\right]\right\}^{-1}, \tag{3.173}$$

$$K_n^{(4)}(T) = \left\{1 + 2\Delta t D_n K^{(4)}\left(\frac{n(n+1)}{a^2}\right)^2\right\}^{-1}. \tag{3.174}$$

$K_n^{(2)}(\delta)$ and $K_n^{(4)}(\delta)$ are both set to 1 for $n = 0$. The quantity $D_n$ represents the "Courant number limiter", normally set to 1. However, $D_n$ is modified to ensure that the CFL criterion is not violated in selected upper levels of the model. If the maximum wind speed in any of these upper levels is sufficiently large, then $D_n = 1000$ in that level for all $n > n_c$, where $n_c = a\Delta t / \max|\boldsymbol{V}|$. This condition is applied whenever the wind speed is large enough that $n_c < K$, the truncation parameter in (3.115), and temporarily reduces the effective resolution of the model in the affected levels. The number of levels at which this "Courant number limiter" may be applied is user-selectable, but it is only used in the top level of the 26 level CAM 3.0 control runs.

The diffusion of $T$ is not complete at this stage. In order to make the partial correction from $\eta$ to $p$ in (3.82) local, it is not included until grid–point values are available. This requires that $\nabla^4\Pi$ also be transformed from spectral to grid–point space. The values of the coefficients $K^{(2)}$ and $K^{(4)}$ for the standard T42 resolution are $2.5 \times 10^5 \mathrm{m}^2\mathrm{sec}^{-1}$ and $1.0 \times 10^{16}\mathrm{m}^4\mathrm{sec}^{-1}$, respectively.

### 3.1.15 Initial divergence damping

Occasionally, with poorly balanced initial conditions, the model exhibits numerical instability during the beginning of an integration because of excessive noise in the solution. Therefore, an optional divergence damping is included in the model to be applied over the first few days. The damping has an initial e-folding time of $\Delta t$ and linearly decreases to 0 over a specified number of days, $t_D$, usually set to be 2. The damping is computed implicitly via time splitting after the horizontal diffusion.

$$r = \max\left[\frac{1}{\Delta t}(t_D - t)/t_D,\ 0\right] \tag{3.175}$$

$$(\delta^*)_n^m = \frac{1}{1 + 2\Delta t r}(\delta^*)_n^m \tag{3.176}$$

### 3.1.16 Transformation from spectral to physical space

After the prognostic variables are completed at time $n+1$ in spectral space $\left(\underline{(\zeta+f)^*}\right)_n^m$, $(\underline{\delta^*})_n^m$, $(\underline{T^*})_n^m$, $(\Pi^{n+1})_n^m$ they are transformed to grid space. For a variable $\psi$, the transformation is given by

$$\psi(\lambda,\mu)=\sum_{m=-M}^{M}\left[\sum_{n=|m|}^{\mathcal{N}(m)}\psi_n^m P_n^m(\mu)\right]e^{im\lambda}. \tag{3.177}$$

The inner sum is done essentially as a vector product over $n$, and the outer is again performed by an FFT subroutine. The term needed for the remainder of the diffusion terms, $\nabla^4\Pi$, is calculated from

$$\nabla^4\Pi^{n+1}=\sum_{m=-M}^{M}\left[\sum_{n=|m|}^{\mathcal{N}(m)}\left(\frac{n(n+1)}{a^2}\right)^2\left(\Pi^{n+1}\right)_n^m P_n^m(\mu)\right]e^{im\lambda}. \tag{3.178}$$

In addition, the derivatives of $\Pi$ are needed on the grid for the terms involving $\nabla\Pi$ and $\boldsymbol{V}\cdot\nabla\Pi$,

$$\boldsymbol{V}\cdot\nabla\Pi=\frac{U}{a(1-\mu^2)}\frac{\partial\Pi}{\partial\lambda}+\frac{V}{a(1-\mu^2)}(1-\mu^2)\frac{\partial\Pi}{\partial\mu}. \tag{3.179}$$

These required derivatives are given by

$$\frac{\partial\Pi}{\partial\lambda}=\sum_{m=-M}^{M}im\left[\sum_{n=|m|}^{\mathcal{N}(m)}\Pi_n^m P_n^m(\mu)\right]e^{im\lambda}, \tag{3.180}$$

and using (3.153),

$$(1-\mu^2)\frac{\partial\Pi}{\partial\mu}=\sum_{m=-M}^{M}\left[\sum_{n=|m|}^{\mathcal{N}(m)}\Pi_n^m H_n^m(\mu)\right]e^{im\lambda}, \tag{3.181}$$

which involve basically the same operations as (3.178). The other variables needed on the grid are $U$ and $V$. These can be computed directly from the absolute vorticity and divergence coefficients using the relations

$$(\zeta+f)_n^m = -\frac{n(n+1)}{a^2}\psi_n^m+f_n^m, \tag{3.182}$$

$$\delta_n^m = -\frac{n(n+1)}{a^2}\chi_n^m, \tag{3.183}$$

in which the only nonzero $f_n^m$ is $f_1^o=\Omega/\sqrt{.375}$, and

$$U=\frac{1}{a}\frac{\partial\chi}{\partial\lambda}-\frac{(1-\mu^2)}{a}\frac{\partial\psi}{\partial\mu}, \tag{3.184}$$

$$V=\frac{1}{a}\frac{\partial\psi}{\partial\lambda}+\frac{(1-\mu^2)}{a}\frac{\partial\chi}{\partial\mu}. \tag{3.185}$$

Thus, the direct transformation is

$$
\begin{aligned}
U &= -\sum_{m=-M}^{M} a \sum_{n=|m|}^{\mathcal{N}(m)} \left[ \frac{im}{n(n+1)} \delta_n^m P_n^m(\mu) - \frac{1}{n(n+1)} (\zeta + f)_n^m H_n^m(\mu) \right] e^{im\lambda} \\
&\quad - \frac{a}{2} \frac{\Omega}{\sqrt{0.375}} H_1^o, &(3.186)\\
V &= -\sum_{m=-M}^{M} a \sum_{n=|m|}^{\mathcal{N}(m)} \left[ \frac{im}{n(n+1)} (\zeta + f)_n^m P_n^m(\mu) + \frac{1}{n(n+1)} \delta_n^m H_n^m(\mu) \right] e^{im\lambda}. &(3.187)
\end{aligned}
$$

The horizontal diffusion tendencies are also transformed back to grid space. The spectral coefficients for the horizontal diffusion tendencies follow from (3.167) and (3.168):

$$
\begin{aligned}
F_{T_H}(T^*)_n^m &= (-1)^{i+1} K^{2i} \left[ \nabla^{2i} (T^*) \right]_n^m, &(3.188)\\
F_{\zeta_H}((\zeta + f)^*)_n^m &= (-1)^{i+1} K^{2i} \left\{ \nabla^{2i} (\zeta + f)^* - (-1)^i (\zeta + f)^* \left(2/a^2\right)^i \right\}, &(3.189)\\
F_{\delta_H}(\delta^*)_n^m &= (-1) K^{2i} \left\{ \nabla^{2i} (\delta^*) - (-1)^i \delta^* \left(2/a^2\right)^i \right\}, &(3.190)
\end{aligned}
$$

using $i = 1$ or $2$ as appropriate for the $\nabla^2$ or $\nabla^4$ forms. These coefficients are transformed to grid space following (3.114) for the $T$ term and (3.186) and (3.187) for vorticity and divergence. Thus, the vorticity and divergence diffusion tendencies are converted to equivalent $U$ and $V$ diffusion tendencies.

### 3.1.17 Horizontal diffusion correction

After grid–point values are calculated, frictional heating rates are determined from the momentum diffusion tendencies and are added to the temperature, and the partial correction of the $\nabla^4$ diffusion from $\eta$ to $p$ surfaces is applied to $T$. The frictional heating rate is calculated from the kinetic energy tendency produced by the momentum diffusion

$$F_{F_H} = -u^{n-1} F_{u_H}(u^*)/c_p^* - v^{n-1} F_{v_H}(v^*)/c_p^*, \tag{3.191}$$

where $F_{u_H}$, and $F_{v_H}$ are the momentum equivalent diffusion tendencies, determined from $F_{\zeta_H}$ and $F_{\delta_H}$ just as $U$ and $V$ are determined from $\zeta$ and $\delta$, and

$$c_p^* = c_p \left[ 1 + \left( \frac{c_{p_v}}{c_p} - 1 \right) q^{n+1} \right]. \tag{3.192}$$

These heating rates are then combined with the correction,

$$\hat{T}_k^{n+1} = T_k^* + (2\Delta t F_{F_H})_k + 2\Delta t \left( \pi B \frac{\partial T^*}{\partial p} \right)_k K^{(4)} \nabla^4 \Pi^{n+1}. \tag{3.193}$$

The vertical derivatives of $T^*$ (where the $^*$ notation is dropped for convenience) are defined by

$$\left(\pi B \frac{\partial T}{\partial p}\right)_1 = \frac{\pi}{2\Delta p_1}\left[B_{1+\frac{1}{2}}\left(T_2 - T_1\right)\right] \ , \tag{3.194}$$

$$\left(\pi B \frac{\partial T}{\partial p}\right)_k = \frac{\pi}{2\Delta p_k}\left[B_{k+\frac{1}{2}}\left(T_{k+1} - T_k\right) + B_{k-\frac{1}{2}}\left(T_k - T_{k-1}\right)\right] \ , \tag{3.195}$$

$$\left(\pi B \frac{\partial T}{\partial p}\right)_K = \frac{\pi}{2\Delta p_K}\left[B_{K-\frac{1}{2}}\left(T_K - T_{K-1}\right)\right]. \tag{3.196}$$

The corrections are added to the diffusion tendencies calculated earlier (3.188) to give the total temperature tendency for diagnostic purposes:

$$\hat{F}_{T_H}(T^*)_k = F_{T_H}(T^*)_k + (2\Delta t F_{F_H})_k + 2\Delta t B_k \left(\pi \frac{\partial T^*}{\partial p}\right)_k K^{(4)} \nabla^4 \Pi^{n+1}. \tag{3.197}$$

### 3.1.18 Semi-Lagrangian Tracer Transport

The forecast equation for water vapor specific humidity and constituent mixing ratio in the $\eta$ system is from (3.36) excluding sources and sinks.

$$\frac{dq}{dt} = \frac{\partial q}{\partial t} + \boldsymbol{V} \cdot \nabla q + \dot{\eta} \frac{\partial p}{\partial \eta} \frac{\partial q}{\partial p} = 0 \tag{3.198}$$

or

$$\frac{dq}{dt} = \frac{\partial q}{\partial t} + \boldsymbol{V} \cdot \nabla q + \dot{\eta} \frac{\partial q}{\partial \eta} = 0. \tag{3.199}$$

Equation (3.199) is more economical for the semi-Lagrangian vertical advection, as $\Delta\eta$ does not vary in the horizontal, while $\Delta p$ does. Written in this form, the $\eta$ advection equations look exactly like the $\sigma$ equations.

The parameterizations are time-split in the moisture equation. The tendency sources have already been added to the time level $(n-1)$. The semi-Lagrangian advection step is subdivided into horizontal and vertical advection sub-steps, which, in an Eulerian form, would be written

$$q^* = q^{n-1} + 2\Delta t \left(\boldsymbol{V} \cdot \nabla q\right)^n \tag{3.200}$$

and

$$q^{n+1} = q^* + 2\Delta t \left(\dot{\eta} \frac{\partial q}{\partial n}\right)^n. \tag{3.201}$$

In the semi-Lagrangian form used here, the general form is

$$q^* = \mathrm{L}_{\lambda\varphi}\left(q^{n-1}\right), \tag{3.202}$$

$$q^{n+1} = \mathrm{L}_{\eta}\left(q^*\right). \tag{3.203}$$

Equation (3.202) represents the horizontal interpolation of $q^{n-1}$ at the departure point calculated assuming $\dot{\eta} = 0$. Equation (3.203) represents the vertical interpolation of $q^*$ at the departure point, assuming $\boldsymbol{V} = 0$.

The horizontal departure points are found by first iterating for the mid-point of the trajectory, using winds at time $n$, and a first guess as the location of the mid-point of the previous time step

$$\lambda_M^{k+1} = \lambda_A - \Delta t u^n \left(\lambda_M^k, \varphi_M^k\right) / a \cos \varphi_M^k, \tag{3.204}$$
$$\varphi_M^{k+1} = \varphi_A - \Delta t v^n \left(\lambda_M^k, \varphi_M^k\right) / a, \tag{3.205}$$

where subscript $A$ denotes the arrival (Gaussian grid) point and subscript $M$ the midpoint of the trajectory. The velocity components at $\left(\lambda_M^k, \varphi_M^k\right)$ are determined by Lagrange cubic interpolation. For economic reasons, the equivalent Hermite cubic interpolant with cubic derivative estimates is used at some places in this code. The equations will be presented later.

Once the iteration of (3.204) and (3.205) is complete, the departure point is given by

$$\lambda_D = \lambda_A - 2\Delta t u^n \left(\lambda_M, \varphi_M\right) / a \cos \varphi_M, \tag{3.206}$$
$$\varphi_D = \lambda_A - 2\Delta t v^n \left(\lambda_M, \varphi_M\right) / a, \tag{3.207}$$

where the subscript $D$ denotes the departure point.

The form given by (3.204)-(3.207) is inaccurate near the poles and thus is only used for arrival points equatorward of 70° latitude. Poleward of 70° we transform to a local geodesic coordinate for the calculation at each arrival point. The local geodesic coordinate is essentially a rotated spherical coordinate system whose equator goes through the arrival point. Details are provided in Williamson and Rasch [1989]. The transformed system is rotated about the axis through $\left(\lambda_A - \frac{\pi}{2}, 0\right)$ and $\left(\lambda_A + \frac{\pi}{2}, 0\right)$, by an angle $\varphi_A$ so the equator goes through $(\lambda_A, \varphi_A)$. The longitude of the transformed system is chosen to be zero at the arrival point. If the local geodesic system is denoted by $(\lambda', \varphi')$, with velocities $(u', v')$, the two systems are related by

$$
\begin{aligned}
\sin \phi' &= \sin \phi \cos \phi_A - \cos \phi \sin \phi_A \cos \left(\lambda_A - \lambda\right), & (3.208)\\
\sin \phi &= \sin \phi' \cos \phi_A + \cos \phi' \sin {\prime}_A \cos \lambda' \ , & (3.209)\\
\sin \lambda' \cos \phi' &= -\sin \left(\lambda_A - \lambda\right) \cos \phi \ , & (3.210)\\
v' \cos \phi' &= v \left[\cos \phi \cos \phi_A + \sin \phi \sin \phi_A \cos \left(\lambda_A - \lambda\right)\right] & \\
&\quad -u \sin \phi_A \sin \left(\lambda_A - \lambda\right), & (3.211)\\
u' \cos \lambda' - v' \sin \lambda' \sin \phi' &= u \cos \left(\lambda_A - \lambda\right) + v \sin \phi \sin \left(\lambda_A - \lambda\right) \ . & (3.212)
\end{aligned}
$$

The calculation of the departure point in the local geodesic system is identical to (3.204)-(3.207) with all variables carrying a prime. The equations can be simplified by noting that $(\lambda'_A, \varphi'_A) = (0, 0)$ by design and $u'(\lambda'_A, \varphi'_A) = u(\lambda_A, \varphi_A)$ and $v'(\lambda'_A, \varphi'_A) = v(\lambda_A, \varphi_A)$. The interpolations are always done in global spherical coordinates.

The interpolants are most easily defined on the interval $0 \leq \theta \leq 1$. Define

$$\theta = \left(x_D - x_i\right) / \left(x_{i+1} - x_i\right), \tag{3.213}$$

where $x$ is either $\lambda$ or $\varphi$ and the departure point $x_D$ falls within the interval $(x_i, x_{i+1})$. Following (23) of [Rasch and Williamson, 1990] with $r_i = 3$ the Hermite cubic interpolant is given by

$$
\begin{aligned}
q_D = \; & q_{i+1} \left[3 - 2\theta\right] \theta^2 - d_{i+1} \left[h_i \theta^2 \left(1 - \theta\right)\right] \\
& + q_i \left[3 - 2\left(1 - \theta\right)\right] \left(1 - \theta\right)^2 + d_i \left[h_i \theta \left(1 - \theta\right)^2\right]
\end{aligned} \tag{3.214}
$$

where $q_i$ is the value at the grid point $x_i$, $d_i$ is the derivative estimate given below, and $h_i = x_{i+1} - x_i$.

Following (3.2.12) and (3.2.13) of Hildebrand [1956], the Lagrangian cubic polynomial interpolant used for the velocity interpolation, is given by

$$f_D = \sum_{j=-1}^{2} \ell_j(x_D) f_{i+j} \tag{3.215}$$

where

$$\ell_j(x_D) = \frac{(x_D - x_{i-1})\dots(x_D - x_{i+j-1})(x_D - x_{i+j+1})\dots(x_D - x_{i+2})}{(x_{i+j} - x_{i-1})\dots(x_{i+j} - x_{i+j-1})(x_{i+j} - x_{i+j+1})\dots(x_{i+j} - x_{i+2})} \tag{3.216}$$

where $f$ can represent either $u$ or $v$, or their counterparts in the geodesic coordinate system.

The derivative approximations used in (3.214) for $q$ are obtained by differentiating (3.215) with respect to $x_D$, replacing $f$ by $q$ and evaluating the result at $x_D$ equal $x_i$ and $x_{i+1}$. With these derivative estimates, the Hermite cubic interpolant (3.214) is equivalent to the Lagrangian (3.215). If we denote the four point stencil $(x_{i-1}, x_i, x_{i+1}, x_{i+2})$ by $(x_1, x_2, x_3, x_4, )$ the cubic derivative estimates are

$$d_2 = \left[\frac{(x_2 - x_3)(x_2 - x_4)}{(x_1 - x_2)(x_1 - x_3)(x_1 - x_4)}\right] q_1 \tag{3.217}$$

$$- \left[\frac{1}{(x_1 - x_2)} - \frac{1}{(x_2 - x_3)} - \frac{1}{(x_2 - x_4)}\right] q_2 \tag{3.218}$$

$$+ \left[\frac{(x_2 - x_1)(x_2 - x_4)}{(x_1 - x_3)(x_2 - x_3)(x_3 - x_4)}\right] q_3 \tag{3.219}$$

$$- \left[\frac{(x_2 - x_1)(x_2 - x_3)}{(x_1 - x_4)(x_2 - x_4)(x_3 - x_4)}\right] q_4 \tag{3.220}$$

and

$$d_3 = \left[\frac{(x_3 - x_2)(x_3 - x_4)}{(x_1 - x_2)(x_1 - x_3)(x_1 - x_4)}\right] q_1 \tag{3.221}$$

$$- \left[\frac{(x_3 - x_1)(x_3 - x_4)}{(x_1 - x_2)(x_2 - x_3)(x_2 - x_4)}\right] q_2 \tag{3.222}$$

$$- \left[\frac{1}{(x_1 - x_3)} + \frac{1}{(x_2 - x_3)} - \frac{1}{(x_3 - x_4)}\right] q_3 \tag{3.223}$$

$$- \left[\frac{(x_3 - x_1)(x_3 - x_2)}{(x_1 - x_4)(x_2 - x_4)(x_3 - x_4)}\right] q_4 \tag{3.224}$$

The two dimensional $(\lambda, \varphi)$ interpolant is obtained as a tensor product application of the one-dimensional interpolants, with $\lambda$ interpolations done first. Assume the departure point falls in the grid box $(\lambda_i, \lambda_{i+1})$ and $(\varphi_i, \varphi_{i+1})$. Four $\lambda$ interpolations are performed to find $q$ values at $(\lambda_D, \varphi_{j-1})$, $(\lambda_D, \varphi_j)$, $(\lambda_D, \varphi_{j+1})$, and $(\lambda_D, \varphi_{j+2})$. This is followed by one interpolation in $\varphi$ using these four values to obtain the value at $(\lambda_D, \varphi_D)$. Cyclic continuity is used in longitude. In latitude, the grid is extended to include a pole point (row) and one row across the pole. The pole row is set equal to the average of the row next to the pole for $q$ and to wavenumber 1 components for $u$ and $v$. The row across the pole is filled with the values from the first row below the pole shifted $\pi$ in longitude for $q$ and minus the value shifted by $\pi$ in longitude for $u$ and $v$.

Once the departure point is known, the constituent value of $q^* = q_D^{n-1}$ is obtained as indicated in (3.202) by Hermite cubic interpolation (3.214), with cubic derivative estimates (3.215) and (3.216) modified to satisfy the Sufficient Condition for Monotonicity with C° continuity (SCMO) described below. Define $\Delta_i q$ by

$$\Delta_i q = \frac{q_{i+1} - q_i}{x_{i+1} - x_i} \ . \tag{3.225}$$

First, if $\Delta_i q = 0$ then

$$d_i = d_{i+1} = 0 \ . \tag{3.226}$$

Then, if either

$$0 \leq \frac{d_i}{\Delta_i q} \leq 3 \tag{3.227}$$

or

$$0 \leq \frac{d_{i+1}}{\Delta_i q} \leq 3 \tag{3.228}$$

is violated, $d_i$ or $d_{i+1}$ is brought to the appropriate bound of the relationship. These conditions ensure that the Hermite cubic interpolant is monotonic in the interval $[x_i, x_{i+1}]$.

The horizontal semi-Lagrangian sub-step (3.202) is followed by the vertical step (3.203). The vertical velocity $\dot{\eta}$ is obtained from that diagnosed in the dynamical calculations (3.94) by

$$(\dot{\eta})_{k+\frac{1}{2}} = \left(\dot{\eta}\,\frac{\partial p}{\partial \eta}\right)_{k+\frac{1}{2}} \Big/ \left(\frac{p_{k+1} - p_k}{\eta_{k+1} - \eta_k}\right) , \tag{3.229}$$

with $\eta_k = A_k + B_k$. Note, this is the only place that the model actually requires an explicit specification of $\eta$. The mid-point of the vertical trajectory is found by iteration

$$\eta_M^{k+1} = \eta_A - \Delta t \dot{\eta}^n \left(\eta_M^k\right) . \tag{3.230}$$

Note, the arrival point $\eta_A$ is a mid-level point where $q$ is carried, while the $\dot{\eta}$ used for the interpolation to mid-points is at interfaces. We restrict $\eta_M$ by

$$\eta_1 \leq \eta_M \leq \eta_K , \tag{3.231}$$

which is equivalent to assuming that $q$ is constant from the surface to the first model level and above the top $q$ level. Once the mid-point is determined, the departure point is calculated from

$$\eta_D = \eta_A - 2\Delta t \dot{\eta}^n \left(\eta_M\right) , \tag{3.232}$$

with the restriction

$$\eta_1 \leq \eta_D \leq \eta_K . \tag{3.233}$$

The appropriate values of $\dot{\eta}$ and $q$ are determined by interpolation (3.214), with the derivative estimates given by (3.215) and (3.216) for $i = 2$ to $K - 1$. At the top and bottom we assume a zero derivative (which is consistent with (3.231) and (3.233)), $d_i = 0$ for the interval $k = 1$, and $\delta_{i+1} = 0$ for the interval $k = K - 1$. The estimate at the interior end of the first and last grid intervals is determined from an uncentered cubic approximation; that is $d_{i+1}$ at the $k = 1$ interval is equal to $d_i$ from the $k = 2$ interval, and $d_i$ at the $k = K - 1$ interval is equal to $d_{i+1}$ at the $k = K - 2$ interval. The monotonic conditions (3.227) to (3.228) are applied to the $q$ derivative estimates.

### 3.1.19 Mass fixers

This section describes original and modified fixers used for the Eulerian and semi-Lagrangian dynamical cores.

Let $\pi^0$, $\Delta p^0$ and $q^0$ denote the values of air mass, pressure intervals, and water vapor specific humidity at the beginning of the time step (which are the same as the values at the end of the previous time step.)

$\pi^+$, $\Delta p^+$ and $q^+$ are the values after fixers are applied at the end of the time step.

$\pi^-$, $\Delta p^-$ and $q^-$ are the values after the parameterizations have updated the moisture field and tracers.

Since the physics parameterizations do not change the surface pressure, $\pi^-$ and $\Delta p^-$ are also the values at the beginning of the time step.

The fixers which ensure conservation are applied to the dry atmospheric mass, water vapor specific humidity and constituent mixing ratios. For water vapor and atmospheric mass the desired discrete relations, following Williamson and Olson [1994] are

$$\int\limits_2 \pi^+ - \int\limits_3 q^+ \Delta p^+ = \boldsymbol{P}, \tag{3.234}$$

$$\int\limits_3 q^+ \Delta p^+ = \int\limits_3 q^- \Delta p^-, \tag{3.235}$$

where $\boldsymbol{P}$ is the dry mass of the atmosphere. From the definition of the vertical coordinate,

$$\Delta p = p_0 \Delta A + \pi \Delta B, \tag{3.236}$$

and the integral $\int\limits_2$ denotes the normal Gaussian quadrature while $\int\limits_3$ includes a vertical sum followed by Gaussian quadrature. The actual fixers are chosen to have the form

$$\pi^+ (\lambda, \varphi) = \boldsymbol{M} \hat{\pi}^+ (\lambda, \varphi), \tag{3.237}$$

preserving the horizontal gradient of $\Pi$, which was calculated earlier during the inverse spectral transform, and

$$q^+ (\lambda, \varphi, \eta) = \hat{q}^+ + \alpha \eta \hat{q}^+ |\hat{q}^+ - q^-|. \tag{3.238}$$

In (3.237) and (3.238) the $(\hat{\ })$ denotes the provisional value before adjustment. The form (3.238) forces the arbitrary corrections to be small when the mixing ratio is small and when the change made to the mixing ratio by the advection is small. In addition, the $\eta$ factor is included to make the changes approximately proportional to mass per unit volume [Rasch et al., 1995]. Satisfying

(3.234) and (3.235) gives

$$\alpha = \frac{\int\limits_3 q^- \Delta p^- - \int\limits_3 \hat{q}^+ p_0 \Delta A - M \int\limits_3 \hat{q}^+ \hat{\pi}^+ \Delta B}{\int\limits_3 \eta \hat{q}^+ |\hat{q}^+ - q^-| \, p_0 \Delta A + M \int\limits_3 \eta \hat{q}^+ |\hat{q}^+ - q^-| \hat{\pi}^+ \Delta B} \tag{3.239}$$

and

$$\boldsymbol{M} = \left( \boldsymbol{P} + \int\limits_3 q^- \Delta p^- \right) \Bigg/ \int\limits_2 \hat{\pi}^+ \ . \tag{3.240}$$

Note that water vapor and dry mass are corrected simultaneously. Additional advected constituents are treated as mixing ratios normalized by the mass of dry air. This choice was made so that as the water vapor of a parcel changed, the constituent mixing ratios would not change. Thus the fixers which ensure conservation involve the dry mass of the atmosphere rather than the moist mass as in the case of the specific humidity above. Let $\chi$ denote the mixing ratio of constituents. Historically we have used the following relationship for conservation:

$$\int\limits_3 \chi^+ (1 - q^+) \Delta p^+ = \int\limits_3 \chi^- (1 - q^-) \Delta p^- \ . \tag{3.241}$$

The term $(1 - q)\Delta p$ defines the dry air mass in a layer. Following Rasch et al. [1995] the change made by the fixer has the same form as (3.238)

$$\chi^+ (\lambda, \varphi, \eta) = \hat{\chi}^+ + \alpha_\chi \eta \hat{\chi}^+ |\hat{\chi}^+ - \chi^-| \ . \tag{3.242}$$

Substituting (3.242) into (3.241) and using (3.237) through (3.240) gives

$$\alpha_\chi = \frac{\int\limits_3 \chi^- (1 - q^-) \Delta p^- - \int\limits_{A,B} \hat{\chi}^+ (1 - \hat{q}^+) \Delta \hat{p}^+ + \alpha \int\limits_{A,B} \hat{\chi}^+ \eta \hat{q}^+ |\hat{q}^+ - q^-| \Delta p}{\int\limits_{A,B} \eta \hat{\chi}^+ |\hat{\chi}^+ - \chi^-| (1 - \hat{q}^+) \Delta p - \alpha \int\limits_{A,B} \eta \hat{\chi}^+ |\hat{\chi}^+ - \chi^-| \eta \hat{q}^+ |\hat{q}^+ - q^-| \Delta p} \ , \tag{3.243}$$

where the following shorthand notation is adopted:

$$\int\limits_{A,B} (\ \ ) \Delta p = \int\limits_3 (\ \ ) p_0 \Delta A + M \int\limits_3 (\ \ ) p_s \Delta B \ . \tag{3.244}$$

We note that there is a small error in (3.241). Consider a situation in which moisture is transported by a physical parameterization, but there is no source or sink of moisture. Under this circumstance $q^- \neq q^0$, but the surface pressure is not allowed to change. Since $(1 - q^-)\Delta p^- \neq (1 - q^0)\Delta p^0$, there is an implied change of dry mass of dry air in the layer, and even in circumstances where there is no change of dry mixing ratio $\chi$ there would be an implied change in mass of the tracer. The solution to this inconsistency is to define a dry air mass *only once* within the model time step, and use it consistently throughout the model. In this revision, we have chosen to fix the dry air mass in the model time step where the surface pressure is updated, e.g. at the end of the model time step. Therefore, we now replace (3.241) with

$$\int\limits_3 \chi^+ (1 - q^+) \Delta p^+ = \int\limits_3 \chi^- (1 - q^0) \Delta p^0 \ . \tag{3.245}$$

There is a corresponding change in the first term of the numerator of (3.243) in which $q^-$ is replace by $q^0$. CAM 3.0uses (3.243) for water substances and constituents affecting the temperature field to prevent changes to the IPCC simulations. In the future, constituent fields may use a *corrected* version of (3.243).

### 3.1.20 Energy Fixer

Following notation in section 3.1.19, the total energy integrals are

$$\int_3 \frac{1}{g}\left[c_p T^+ + \Phi_s + \frac{1}{2}\left({u^+}^2 + {v^+}^2\right)\right]\Delta p^+ = \boldsymbol{E} \tag{3.246}$$

$$\boldsymbol{E} = \int_3 \frac{1}{g}\left[c_p T^- + \Phi_s + \frac{1}{2}\left({u^-}^2 + {v^-}^2\right)\right]\Delta p^- + \boldsymbol{S} \tag{3.247}$$

$$\boldsymbol{S} = \int_2 \left[(FSNT - FLNT) - (FSNS - FLNS - SHFLX - \rho_{H_2O} L_v PRECT) -\right]\Delta t \tag{3.248}$$

where $\boldsymbol{S}$ is the net source of energy from the parameterizations. $FSNT$ is the net downward solar flux at the model top, $FLNT$ is the net upward longwave flux at the model top, $FSNS$ is the net downward solar flux at the surface, $FLNS$ is the net upward longwave flux at the surface, $SHFLX$ is the surface sensible heat flux, and $PRECT$ is the total precipitation during the time step. From equation (3.237)

$$\pi^+(\lambda,\varphi) = \boldsymbol{M}\hat{\pi}^+(\lambda,\varphi) \tag{3.249}$$

and from (3.236)

$$\Delta p = p_0 \Delta A + \pi \Delta B \tag{3.250}$$

The energy fixer is chosen to have the form

$$\begin{aligned} T^+(\lambda,\varphi,\eta) &= \hat{T}^+ + \beta && (3.251)\\ u^+(\lambda,\varphi,\eta) &= \hat{u}^+ && (3.252)\\ v^+(\lambda,\varphi,\eta) &= \hat{v}^+ && (3.253) \end{aligned}$$

Then

$$\beta = \frac{g\boldsymbol{E} - \int_3 \left[c_p\hat{T}^+ + \Phi_s + \frac{1}{2}\left({\hat{u}^+}{}^2 + {\hat{v}^+}{}^2\right)\right] p_0\Delta A - \boldsymbol{M}\int_3 \left[c_p\hat{T}^+ + \Phi_s + \frac{1}{2}\left({\hat{u}^+}{}^2 + {\hat{v}^+}{}^2\right)\right]\hat{\pi}^+\Delta B}{\int_3 c_p\, p_0 \Delta A + \boldsymbol{M}\int_3 c_p \hat{\pi}^+ \Delta B} \tag{3.254}$$

### 3.1.21 Statistics Calculations

At each time step, selected global average statistics are computed for diagnostic purposes when the model is integrated with the Eulerian and semi-Lagrangian dynamical cores. Let $\int_3$ denote a global and vertical average and $\int_2$ a horizontal global average. For an arbitrary variable $\psi$, these are defined by

$$\int_3 \psi dV = \sum_{k=1}^{K} \sum_{j=1}^{J} \sum_{i=1}^{I} \psi_{ijk} w_j \left( \frac{\Delta p_k}{\pi} \right) \Big/ 2I, \tag{3.255}$$

and

$$\int_2 \psi dA = \sum_{j=1}^{J} \sum_{i=1}^{I} \psi_{ijk} w_j / 2I, \tag{3.256}$$

where recall that

$$\sum_{j=1}^{J} w_j = 2. \tag{3.257}$$

The quantities monitored are:

$$\text{global rms } (\zeta + f)(\text{s}^{-1}) = \left[ \int_3 (\zeta^n + f)^2 dV \right]^{1/2}, \tag{3.258}$$

$$\text{global rms } \delta(\text{s}^{-1}) = \left[ \int_3 (\delta^n)^2 dV \right]^{1/2}, \tag{3.259}$$

$$\text{global rms } T \text{ (K)} = \left[ \int_3 (T^r + T'^n)^2 dV \right]^{1/2}, \tag{3.260}$$

$$\text{global average mass times } g \text{ (Pa)} = \int_2 \pi^n dA, \tag{3.261}$$

$$\text{global average mass of moisture (kg m}^{-2}) = \int_3 \pi^n q^n / g dV. \tag{3.262}$$

### 3.1.22 Reduced grid

The Eulerian core and semi-Lagrangian tracer transport can be run on reduced grids. The term reduced grid generally refers to a grid based on latitude and longitude circles in which the longitudinal grid increment increases at latitudes approaching the poles so that the longitudinal distance between grid points is reasonably constant. Details are provided in [Williamson and Rosinski, 2000]. This option provides a saving of computer time of up to 25%.

## 3.2 Semi-Lagrangian Dynamical Core

### 3.2.1 Introduction

The two-time-level semi-implicit semi-Lagrangian spectral transform dynamical core in CAM 3.0 evolved from the three-time-level CCM2 semi-Lagrangian version detailed in Williamson and Olson [1994] hereafter referred to as W&O94. As a first approximation, to convert from a three-time-level scheme to a two-time-level scheme, the time level index n-1 becomes n, the time level index n becomes n+$\frac{1}{2}$, and $2\Delta t$ becomes $\Delta t$. Terms needed at n+$\frac{1}{2}$ are extrapolated in time using time n and n-1 terms, except the Coriolis term which is implicit as the average of time n and n+1. This leads to a more complex semi-implicit equation to solve. Additional changes have been made in the scheme to incorporate advances in semi-Lagrangian methods developed since W&O94. In the following, reference is made to changes from the scheme developed in W&O94. The reader is referred to that paper for additional details of the derivation of basic aspects of the semi-Lagrangian approximations. Only the details of the two-time-level approximations are provided here.

### 3.2.2 Vertical coordinate and hydrostatic equation

The semi-Lagrangian dynamical core adopts the same hybrid vertical coordinate ($\eta$) as the Eulerian core defined by

$$p(\eta, p_s) = A(\eta)p_o + B(\eta)p_s \ , \tag{3.263}$$

where $p$ is pressure, $p_s$ is surface pressure, and $p_o$ is a specified constant reference pressure. The coefficients $A$ and $B$ specify the actual coordinate used. As mentioned by Simmons and Burridge [1981] and implemented by Simmons and Strüfing [1981] and Simmons and Strüfing [1983], the coefficients $A$ and $B$ are defined only at the discrete model levels. This has implications in the continuity equation development which follows.

In the $\eta$ system the hydrostatic equation is approximated in a general way by

$$\Phi_k = \Phi_s + R \sum_{l=k}^{K} H_{kl}\left(p\right) T_{vl} \tag{3.264}$$

where k is the vertical grid index running from 1 at the top of the model to $K$ at the first model level above the surface, $\Phi_k$ is the geopotential at level $k$, $\Phi_s$ is the surface geopotential, $T_v$ is the virtual temperature, and R is the gas constant. The matrix $H$, referred to as the hydrostatic matrix, represents the discrete approximation to the hydrostatic integral and is left unspecified for now. It depends on pressure, which varies from horizontal point to point.

### 3.2.3 Semi-implicit reference state

The semi-implicit equations are linearized about a reference state with constant $T^r$ and $p_s^r$. We choose

$$T^r = 350\text{K}, \qquad p_s^r = 10^5\text{Pa} \tag{3.265}$$

### 3.2.4 Perturbation surface pressure prognostic variable

To ameliorate the mountain resonance problem, Ritchie and Tanguay [1996] introduce a perturbation $\ln p_s$ surface pressure prognostic variable

$$\ln p_s' = \ln p_s - \ln p_s^* \tag{3.266}$$

$$\ln p_s^* = -\frac{\Phi_s}{RT^r} \tag{3.267}$$

The perturbation surface pressure, $\ln p'_s$, is never actually used as a grid point variable in the CAM 3.0 code. It is only used for the semi-implicit development and solution. The total $\ln p_s$ is reclaimed in spectral space from the spectral coefficients of $\Phi_s$ immediately after the semi-implicit equations are solved, and transformed back to spectral space along with its derivatives. This is in part because $\nabla^4 \ln p_s$ is needed for the horizontal diffusion correction to pressure surfaces. However the semi-Lagrangian CAM 3.0 default is to run with no horizontal diffusion.

### 3.2.5 Extrapolated variables

Variables needed at time $(n+\frac{1}{2})$ are obtained by extrapolation

$$( \quad )^{n+\frac{1}{2}} = \frac{3}{2}( \quad )^n - \frac{1}{2}( \quad )^{n-1} \tag{3.268}$$

### 3.2.6 Interpolants

Lagrangian polynomial quasi-cubic interpolation is used in the prognostic equations for the dynamical core. Monotonic Hermite quasi-cubic interpolation is used for tracers. Details are provided in the Eulerian Dynamical Core description. The trajectory calculation uses tri-linear interpolation of the wind field.

### 3.2.7 Continuity Equation

The discrete semi-Lagrangian, semi-implicit continuity equation is obtained from (16) of W&O94 modified to be spatially uncentered by a fraction $\epsilon$, and to predict $\ln p'_s$

$$\begin{aligned}
\Delta B_l \left\{ \left(\ln p'_{s_l}\right)^{n+1}_A - \left[ (\ln p_{s_l})^n + \frac{\Phi_s}{RT^r} \right]_{D_2} \right\} \Big/ \Delta t = \\
-\frac{1}{2} \left\{ \left[ (1+\epsilon)\,\Delta \left( \frac{1}{p_s} \dot{\eta} \frac{\partial p}{\partial \eta} \right)_l \right]^{n+1}_A + \left[ (1-\epsilon)\,\Delta \left( \frac{1}{p_s} \dot{\eta} \frac{\partial p}{\partial \eta} \right)_l \right]^{n}_{D_2} \right\} \\
-\left( \frac{1}{p_s} \delta_l \Delta p_l \right)^{n+\frac{1}{2}}_{M_2} + \frac{\Delta B_l}{RT^r} \left( \boldsymbol{V}_l \cdot \nabla\, \Phi_s \right)^{n+\frac{1}{2}}_{M_2} \\
-\left\{ \frac{1}{2} \left[ (1+\epsilon) \left( \frac{1}{p^r_s} \delta_l \Delta p^r_l \right)^{n+1}_A + (1-\epsilon) \left( \frac{1}{p^r_s} \delta_l \Delta p^r_l \right)^{n}_{D_2} \right] - \left( \frac{1}{p^r_s} \delta_l \Delta p^r_l \right)^{n+\frac{1}{2}}_{M_2} \right\}
\end{aligned} \tag{3.269}$$

where

$$\Delta( \quad )_l = ( \quad )_{l+\frac{1}{2}} - ( \quad )_{l-\frac{1}{2}} \tag{3.270}$$

and

$$( \quad )^{n+\frac{1}{2}}_{M_2} = \frac{1}{2}\left[ (1+\epsilon)( \quad )^{n+\frac{1}{2}}_A + (1-\epsilon)( \quad )^{n+\frac{1}{2}}_{D_2} \right] \tag{3.271}$$

$\Delta( \quad )_l$ denotes a vertical difference, $l$ denotes the vertical level, $A$ denotes the arrival point, $D_2$ the departure point from horizontal (two-dimensional) advection, and $M_2$ the midpoint of that trajectory.

The surface pressure forecast equation is obtained by summing over all levels and is related to (18) of W&O94 but is spatially uncentered and uses $\ln p'_s$

$$
\begin{aligned}
(\ln p'_s)^{n+1}_{A} = & \sum_{l=1}^{K} \Delta B_l \left[ (\ln p_{s_l})^n + \frac{\Phi_s}{RT^r} \right]_{D_2} - \frac{1}{2}\Delta t \sum_{l=1}^{K} \left[ (1-\epsilon)\, \Delta \left( \frac{1}{p_s} \dot{\eta} \frac{\partial p}{\partial \eta} \right)_l \right]^n_{D_2} \\
& - \Delta t \sum_{l=1}^{K} \left( \frac{1}{p_s} \delta_l \Delta p_l \right)^{n+\frac{1}{2}}_{M_2} + \Delta t \sum_{l=1}^{K} \frac{\Delta B_l}{RT^r} \left( \boldsymbol{V}_l \cdot \nabla \, \Phi_s \right)^{n+\frac{1}{2}}_{M_2} \\
& - \Delta t \sum_{l=1}^{K} \frac{1}{p^r_s} \left\{ \frac{1}{2} \left[ (1+\epsilon)\, (\delta_l)^{n+1}_{A} + (1-\epsilon)\, (\delta_l)^{n}_{D_2} \right] - (\delta_l)^{n+\frac{1}{2}}_{M_2} \right\} \Delta p^r_l
\end{aligned}
\tag{3.272}
$$

The corresponding $\left( \frac{1}{p_s} \dot{\eta} \frac{\partial p}{\partial \eta} \right)$ equation for the semi-implicit development follows and is related to (19) of W&O94, again spatially uncentered and using $ln\, p'_s$.

$$
\begin{aligned}
(1+\epsilon) \left( \frac{1}{p_s} \dot{\eta} \frac{\partial p}{\partial \eta} \right)^{n+1}_{k+\frac{1}{2}} = & - \frac{2}{\Delta t} \left\{ B_{k+\frac{1}{2}} \left( \ln\, p'_s \right)^{n+1}_{A} - \sum_{l=1}^{k} \Delta B_l \left[ (\ln\, p_{s_l})^n + \frac{\Phi_s}{RT^r} \right]_{D_2} \right\} \\
& - \sum_{l=1}^{k} \left[ (1-\epsilon)\, \Delta \left( \frac{1}{p_s} \dot{\eta} \frac{\partial p}{\partial \eta} \right)_l \right]^n_{D_2} \\
& - 2 \sum_{l=1}^{k} \left( \frac{1}{p_s} \delta_l \Delta p_l \right)^{n+\frac{1}{2}}_{M_2} + 2 \sum_{l=1}^{k} \frac{\Delta B_l}{RT^r} \left( \boldsymbol{V}_l \cdot \nabla \, \Phi_s \right)^{n+\frac{1}{2}}_{M_2} \\
& - 2 \sum_{l=1}^{k} \frac{1}{p^r_s} \left\{ \frac{1}{2} \left[ (1+\epsilon)\, (\delta_l)^{n+1}_{A} + (1-\epsilon)\, (\delta_l)^{n}_{D_2} \right] - (\delta_l)^{n+\frac{1}{2}}_{M_2} \right\} \Delta p^r_l
\end{aligned}
\tag{3.273}
$$

This is not the actual equation used to determine $\left( \frac{1}{p_s} \dot{\eta} \frac{\partial p}{\partial \eta} \right)$ in the code. The equation actually used in the code to calculate $\left( \frac{1}{p_s} \dot{\eta} \frac{\partial p}{\partial \eta} \right)$ involves only the divergence at time $(n+1)$ with $(\ln\, p'_s)^{n+1}$ eliminated.

$$
\begin{aligned}
&(1+\epsilon)\left(\frac{1}{p_s}\dot{\eta}\frac{\partial p}{\partial \eta}\right)^{n+1}_{k+\frac{1}{2}} = \\
&\quad \frac{2}{\Delta t}\left[\sum_{l=1}^{k} \; - \; B_{k+\frac{1}{2}}\sum_{l=1}^{K}\right]\Delta B_l\left[(\ln p_{s_l})^n + \frac{\Phi_s}{RT^r}\right]_{D_2} \\
&\quad -\left[\sum_{l=1}^{k} \; - \; B_{k+\frac{1}{2}}\sum_{l=1}^{K}\right]\left[(1-\epsilon)\,\Delta\left(\frac{1}{p_s}\dot{\eta}\frac{\partial p}{\partial \eta}\right)_l\right]^n_{D_2} \\
&\quad -2\left[\sum_{l=1}^{k} \; - \; B_{k+\frac{1}{2}}\sum_{l=1}^{K}\right]\left(\frac{1}{p_s}\delta_l\Delta p_l\right)^{n+\frac{1}{2}}_{M_2} \qquad (3.274) \\
&\quad +2\left[\sum_{l=1}^{k} \; - \; B_{k+\frac{1}{2}}\sum_{l=1}^{K}\right]\frac{\Delta B_l}{RT^r}\left(\boldsymbol{V}_l\cdot\nabla\,\Phi_s\right)^{n+\frac{1}{2}}_{M_2} \\
&\quad -2\left[\sum_{l=1}^{k} \; - \; B_{k+\frac{1}{2}}\sum_{l=1}^{K}\right]\frac{1}{p_s^r}\left\{\frac{1}{2}\left[(1+\epsilon)\,(\delta_l)^{n+1}_A + (1-\epsilon)\,(\delta_l)^n_{D_2}\right] - (\delta_l)^{n+\frac{1}{2}}_{M_2}\right\}\Delta p_l^r
\end{aligned}
$$

The combination $\left[(\ln p_{s_l})^n + \frac{\Phi_s}{RT^r} + \frac{1}{2}\frac{\Delta t}{RT^r}\left(\boldsymbol{V}\cdot\nabla\,\Phi_s\right)^{n+\frac{1}{2}}\right]_{D_2}$ is treated as a unit, and follows from (3.271).

### 3.2.8 Thermodynamic Equation

The thermodynamic equation is obtained from (25) of W&O94 modified to be spatially uncentered and to use $\ln p_s'$. In addition Hortal's modification [Temperton et al., 2001] is included, in which

$$
\frac{d}{dt}\left[-\left(p_s B\frac{\partial T}{\partial p}\right)_{ref}\frac{\Phi_s}{RT^r}\right] \qquad (3.275)
$$

is subtracted from both sides of the temperature equation. This is akin to horizontal diffusion which includes the first order term converting horizontal derivatives from eta to pressure coordinates, with $(\ln p_s)$ replaced by $-\frac{\Phi_s}{RT^r}$, and $\left(p_s B\frac{\partial T}{\partial p}\right)_{ref}$ taken as a global average so it is invariant with time and can commute with the differential operators.

$$
\begin{aligned}
\frac{T_A^{n+1} - T_D^{n}}{\Delta t} \quad = \quad & \left\{ \left\{ \left[ - \left( p_s B(\eta) \frac{\partial T}{\partial p} \right)_{ref} \frac{\Phi_s}{RT^r} \right]_A^{n+1} - \left[ - \left( p_s B(\eta) \frac{\partial T}{\partial p} \right)_{ref} \frac{\Phi_s}{RT^r} \right]_D^{n} \right\} \Big/ \Delta t \right. \\
& \left. + \frac{1}{RT^r} \left[ \left( p_s B(\eta) \frac{\partial T}{\partial p} \right)_{ref} \boldsymbol{V} \cdot \nabla \, \Phi_s + \Phi_s \dot{\eta} \frac{\partial}{\partial \eta} \left( p_s B(\eta) \frac{\partial T}{\partial p} \right)_{ref} \right]_M^{n+\frac{1}{2}} \right\} \\
& + \left( \frac{RT_v}{c_p^*} \frac{\omega}{p} \right)_M^{n+\frac{1}{2}} + Q_M^n \\
& + \frac{RT^r}{c_p} \frac{p_s^r}{p^r} \left[ B(\eta) \frac{d_2 \ln p_s'}{dt} + \overline{\left( \frac{1}{p_s} \dot{\eta} \frac{\partial p}{\partial \eta} \right)}^{t} \right] \\
& - \frac{RT^r}{c_p} \frac{p_s^r}{p^r} \left[ \left( \frac{p}{p_s} \right) \left( \frac{\omega}{p} \right) \right]_M^{n+\frac{1}{2}} \\
& - \frac{RT^r}{c_p} \frac{p_s^r}{p^r} B(\eta) \left[ \frac{1}{RT^r} \boldsymbol{V} \cdot \nabla \, \Phi_s \right]_{M_2}^{n+\frac{1}{2}}
\end{aligned}
\tag{3.276}
$$

Note that $Q^n$ represents the heating calculated to advance from time $n$ to time $n+1$ and is valid over the interval.

The calculation of $\left( p_s B \frac{\partial T}{\partial p} \right)_{ref}$ follows that of the ECMWF (Research Manual 3, ECMWF Forecast Model, Adiabatic Part, ECMWF Research Department, 2nd edition, 1/88, pp 2.25-2.26) Consider a constant lapse rate atmosphere

$$
\begin{aligned}
T &= T_0 \left(\frac{p}{p_0}\right)^{R\gamma/g} && (3.277) \\
\frac{\partial T}{\partial p} &= \frac{1}{p}\frac{R\gamma}{g} T_0 \left(\frac{p}{p_0}\right)^{R\gamma/g} && (3.278) \\
p_s B \frac{\partial T}{\partial p} &= B \frac{p_s}{p}\frac{R\gamma}{g} T && (3.279) \\
\left(p_s B \frac{\partial T}{\partial p}\right)_{ref} &= B_k \frac{(p_s)_{ref}}{(p_k)_{ref}}\frac{R\gamma}{g}(T_k)_{ref} \quad \text{for} \quad (T_k)_{ref} > T_C && (3.280) \\
\left(p_s B \frac{\partial T}{\partial p}\right)_{ref} &= 0 \quad for \quad (T_k)_{ref} \leq T_C && (3.281) \\
(p_k)_{ref} &= A_k p_0 + B_k (p_s)_{ref} && (3.282) \\
(T_k)_{ref} &= T_0 \left(\frac{(p_k)_{ref}}{(p_s)_{ref}}\right)^{R\gamma/g} && (3.283) \\
(p_s)_{ref} &= 1013.25\text{mb} && (3.284) \\
T_0 &= 288\text{K} && (3.285) \\
p_0 &= 1000\text{mb} && (3.286) \\
\gamma &= 6.5\text{K/km} && (3.287) \\
T_C &= 216.5\text{K} && (3.288)
\end{aligned}
$$

### 3.2.9 Momentum equations

The momentum equations follow from (3) of W&O94 modified to be spatially uncentered, to use $\ln p'_s$, and with the Coriolis term implicit following Côté and Staniforth [1988] and Temperton [1997]. The semi-implicit, semi-Lagrangian momentum equation at level $k$ (but with the level subscript $k$ suppressed) is

$$
\begin{aligned}
\frac{\boldsymbol{V}_A^{n+1} - \boldsymbol{V}_D^n}{\Delta t} \quad = \quad & -\frac{1}{2}\Big\{ (1+\epsilon)\left[f\hat{\boldsymbol{k}} \times \boldsymbol{V}\right]_A^{n+1} + (1-\epsilon)\left[f\hat{\boldsymbol{k}} \times \boldsymbol{V}\right]_D^n \Big\} + \boldsymbol{F}_M^n \\
& -\frac{1}{2}\Big\{ (1+\epsilon)\left[\nabla\left(\Phi_s + R\boldsymbol{H}_k \cdot \boldsymbol{T}_v\right) + RT_v\frac{B}{p}p_s\nabla\ln p_s\right]_A^{n+\frac{1}{2}} \\
& \quad + (1-\epsilon)\left[\nabla\left(\Phi_s + R\boldsymbol{H}_k \cdot \boldsymbol{T}_v\right) + RT_v\frac{B}{p}p_s\nabla\ln p_s\right]_D^{n+\frac{1}{2}} \Big\} \\
& -\frac{1}{2}\Big\{ (1+\epsilon)\nabla\left[R\boldsymbol{H}_k^r \cdot \boldsymbol{T} + RT^r \ln p_s'\right]_A^{n+1} \\
& \quad - (1+\epsilon)\nabla\left[\Phi_s + R\boldsymbol{H}_k^r \cdot \boldsymbol{T} + RT^r \ln p_s\right]_A^{n+\frac{1}{2}} \\
& \quad + (1-\epsilon)\nabla\left[\Phi_s + R\boldsymbol{H}_k^r \cdot \boldsymbol{T} + RT^r \ln p_s\right]_D^{n} \\
& \quad - (1-\epsilon)\nabla\left[\Phi_s + R\boldsymbol{H}_k^r \cdot \boldsymbol{T} + RT^r \ln p_s\right]_D^{n+\frac{1}{2}} \Big\}
\end{aligned} \tag{3.289}
$$

The gradient of the geopotential is more complex than in the $\sigma$ system because the hydrostatic matrix $\boldsymbol{H}$ depends on the local pressure:

$$
\nabla\left(\boldsymbol{H}_k \cdot \boldsymbol{T}_v\right) = \boldsymbol{H}_k \cdot \left[\left(1 + \epsilon_v \boldsymbol{q}\right)\nabla\boldsymbol{T} + \epsilon_v \boldsymbol{T}\nabla\boldsymbol{q}\right] + \boldsymbol{T}_v \cdot \nabla\boldsymbol{H}_k \tag{3.290}
$$

where $\epsilon_v$ is $(R_v/R - 1)$ and $R_v$ is the gas constant for water vapor. The gradient of $T$ is calculated from the spectral representation and that of $q$ from a discrete cubic approximation that is consistent with the interpolation used in the semi-Lagrangian water vapor advection. In general, the elements of $\boldsymbol{H}$ are functions of pressure at adjacent discrete model levels

$$
H_{kl} = f_{kl}(p_{l+1/2}, p_l, p_{l-1/2}) \tag{3.291}
$$

The gradient is then a function of pressure and the pressure gradient

$$
\nabla H_{kl} = g_{kl}(p_{l+1/2},\ p_l,\ p_{l-1/2}, \nabla p_{l+1/2}, \nabla p_l, \nabla p_{l-1/2}) \tag{3.292}
$$

The pressure gradient is available from (3.263) and the surface pressure gradient calculated from the spectral representation

$$
\nabla p_l = B_l \nabla p_s = B_l p_s \nabla \ln p_s \tag{3.293}
$$

### 3.2.10 Development of semi-implicit system equations

The momentum equation can be written as

$$
\begin{aligned}
\frac{\boldsymbol{V}_A^{n+1} - \boldsymbol{V}_D^n}{\Delta t} = & -\frac{1}{2}\Big\{ (1+\epsilon)\left[f\hat{\boldsymbol{k}} \times \boldsymbol{V}\right]_A^{n+1} + (1-\epsilon)\left[f\hat{\boldsymbol{k}} \times \boldsymbol{V}\right]_D^n \Big\} \\
& -\frac{1}{2}\Big\{ (1+\epsilon)\nabla\left[R\boldsymbol{H}_k^r \cdot \boldsymbol{T} + RT^r \ln p_s'\right]_A^{n+1} \Big\} + RHS_{\boldsymbol{V}}\ ,
\end{aligned} \tag{3.294}
$$

where $RHS_{\boldsymbol{V}}$ contains known terms at times $(n+\frac{1}{2})$ and $(n)$.

By combining terms, 3.294 can be written in general as

$$\mathcal{U}_{A}^{n+1}\hat{\mathbf{i}}_{A}+\mathcal{V}_{A}^{n+1}\hat{\mathbf{j}}_{A}=\mathcal{U}_{A}\hat{\mathbf{i}}_{A}+\mathcal{V}_{A}\hat{\mathbf{j}}_{A}+\mathcal{U}_{D}\hat{\mathbf{i}}_{D}+\mathcal{V}_{D}\hat{\mathbf{j}}_{D}\ , \tag{3.295}$$

where $\hat{\mathbf{i}}$ and $\hat{\mathbf{j}}$ denote the spherical unit vectors in the longitudinal and latitudinal directions, respectively, at the points indicated by the subscripts, and $\mathcal{U}$ and $\mathcal{V}$ denote the appropriate combinations of terms in 3.294. Note that $\mathcal{U}_{A}^{n+1}$ is distinct from the $\mathcal{U}_{A}$. Following Bates et al. [1990], equations for the individual components are obtained by relating the unit vectors at the departure points $(\hat{\mathbf{i}}_{D},\hat{\mathbf{j}}_{D})$ to those at the arrival points $(\hat{\mathbf{i}}_{A},\hat{\mathbf{j}}_{A})$:

$$\hat{\mathbf{i}}_{D}=\alpha_{A}^{u}\hat{\mathbf{i}}_{A}+\beta_{A}^{u}\hat{\mathbf{j}}_{A} \tag{3.296}$$

$$\hat{\mathbf{j}}_{D}=\alpha_{A}^{v}\hat{\mathbf{i}}_{A}+\beta_{A}^{v}\hat{\mathbf{j}}_{A}\ , \tag{3.297}$$

in which the vertical components $(\hat{\mathbf{k}})$ are ignored. The dependence of $\alpha$'s and $\beta$'s on the latitudes and longitudes of the arrival and departure points is given in the Appendix of Bates et al. [1990].

W&O94 followed Bates et al. [1990] which ignored rotating the vector to remain parallel to the earth's surface during translation. We include that factor by keeping the length of the vector written in terms of $\left(\hat{\boldsymbol{i}}_{A},\hat{\boldsymbol{j}}_{A}\right)$ the same as the length of the vector written in terms of $\left(\hat{\boldsymbol{i}}_{D},\hat{\boldsymbol{j}}_{D}\right)$. Thus, (10) of W&O94 becomes

$$\begin{aligned}\mathcal{U}_{A}^{n+1}&=\mathcal{U}_{A}+\gamma\alpha_{A}^{u}\mathcal{U}_{D}+\gamma\alpha_{A}^{v}\mathcal{V}_{D}\\ \mathcal{V}_{A}^{n+1}&=\mathcal{V}_{A}+\gamma\beta_{A}^{u}\mathcal{U}_{D}+\gamma\beta_{A}^{v}\mathcal{V}_{D}\end{aligned} \tag{3.298}$$

where

$$\gamma=\left[\frac{\mathcal{U}_{D}^{2}+\mathcal{V}_{D}^{2}}{\left(\mathcal{U}_{D}\alpha_{A}^{u}+\mathcal{V}_{D}\alpha_{A}^{v}\right)^{2}+\left(\mathcal{U}_{D}\beta_{A}^{u}+\mathcal{V}_{D}\beta_{A}^{v}\right)^{2}}\right]^{\frac{1}{2}} \tag{3.299}$$

After the momentum equation is written in a common set of unit vectors

$$\boldsymbol{V}_{A}^{n+1}+\left(\frac{1+\epsilon}{2}\right)\Delta t\left[f\hat{\boldsymbol{k}}\times\boldsymbol{V}\right]_{A}^{n+1}+\left(\frac{1+\epsilon}{2}\right)\Delta t\nabla\left[R\boldsymbol{H}_{k}^{r}\cdot\boldsymbol{T}+RT^{r}\ln p_{s}'\right]_{A}^{n+1}=\mathcal{R}_{\boldsymbol{V}}^{*} \tag{3.300}$$

Drop the $(\quad)_{A}^{n+1}$ from the notation, define

$$\alpha=(1+\epsilon)\,\Delta t\Omega \tag{3.301}$$

and transform to vorticity and divergence

$$\zeta+\alpha\sin\varphi\delta+\frac{\alpha}{a}v\cos\varphi\ =\ \frac{1}{a\cos\varphi}\left[\frac{\partial\mathcal{R}_{v}^{*}}{\partial\lambda}-\frac{\partial}{\partial\varphi}\left(\mathcal{R}_{u}^{*}\cos\varphi\right)\right] \tag{3.302}$$

$$\begin{aligned}\delta-\alpha\sin\varphi\zeta+\frac{\alpha}{a}u\cos\varphi\ &+\ \left(\frac{1+\epsilon}{2}\right)\Delta t\nabla^{2}\left[R\boldsymbol{H}_{k}^{r}\cdot\boldsymbol{T}+RT^{r}\ln p_{s}'\right]_{A}^{n+1}\\ &=\ \frac{1}{a\cos\varphi}\left[\frac{\partial\mathcal{R}_{u}^{*}}{\partial\lambda}+\frac{\partial}{\partial\varphi}\left(\mathcal{R}_{v}^{*}\cos\varphi\right)\right]\end{aligned} \tag{3.303}$$

Note that

$$u\cos\varphi = \frac{1}{a}\frac{\partial}{\partial\lambda}\left(\nabla^{-2}\delta\right) - \frac{\cos\varphi}{a}\frac{\partial}{\partial\varphi}\left(\nabla^{-2}\zeta\right) \tag{3.304}$$

$$v\cos\varphi = \frac{1}{a}\frac{\partial}{\partial\lambda}\left(\nabla^{-2}\zeta\right) + \frac{\cos\varphi}{a}\frac{\partial}{\partial\varphi}\left(\nabla^{-2}\delta\right) \tag{3.305}$$

Then the vorticity and divergence equations become

$$\begin{aligned}\zeta + \alpha\sin\varphi\delta + \frac{\alpha}{a^2}\frac{\partial}{\partial\lambda}\left(\nabla^{-2}\zeta\right) &+ \frac{\alpha\cos\varphi}{a^2}\frac{\partial}{\partial\varphi}\left(\nabla^{-2}\delta\right)\\ &= \frac{1}{a\cos\varphi}\left[\frac{\partial\mathcal{R}_v^*}{\partial\lambda} - \frac{\partial}{\partial\varphi}\left(\mathcal{R}_u^*\cos\varphi\right)\right] = \mathcal{L}\end{aligned} \tag{3.306}$$

$$\begin{aligned}\delta - \alpha\sin\varphi\zeta + \frac{\alpha}{a^2}\frac{\partial}{\partial\lambda}\left(\nabla^{-2}\delta\right) &- \frac{\alpha\cos\varphi}{a^2}\frac{\partial}{\partial\varphi}\left(\nabla^{-2}\zeta\right) + \left(\frac{1+\epsilon}{2}\right)\Delta t\nabla^2\left[R\boldsymbol{H}_k^r\cdot\boldsymbol{T} + RT^r\ln p_s'\right]_A^{n+1}\\ &= \frac{1}{a\cos\varphi}\left[\frac{\partial\mathcal{R}_u^*}{\partial\lambda} + \frac{\partial}{\partial\varphi}\left(\mathcal{R}_v^*\cos\varphi\right)\right] = \mathcal{M}\end{aligned} \tag{3.307}$$

Transform to spectral space as described in the description of the Eulerian spectral transform dynamical core. Note, from (4.5b) and (4.6) on page 177 of Machenhauer [1979]

$$\mu P_n^m = D_{n+1}^m P_{n+1}^m + D_n^m P_{n-1}^m \tag{3.308}$$

$$D_n^m = \left(\frac{n^2-m^2}{4n^2-1}\right)^{\frac{1}{2}} \tag{3.309}$$

and from (4.5a) on page 177 of Machenhauer [1979]

$$\left(1-\mu^2\right)\frac{\partial}{\partial\mu}P_n^m = -nD_{n+1}^m P_{n+1}^m + (n+1)\,D_n^m P_{n-1}^m \tag{3.310}$$

Then the equations for the spectral coefficients at time $n+1$ at each vertical level are

$$\zeta_n^m\left(1-\frac{im\alpha}{n\,(n+1)}\right) + \delta_{n+1}^m\alpha\left(\frac{n}{n+1}\right)D_{n+1}^m + \delta_{n-1}^m\alpha\left(\frac{n+1}{n}\right)D_n^m = \mathcal{L}_n^m \tag{3.311}$$

$$\begin{aligned}\delta_n^m\left(1-\frac{im\alpha}{n\,(n+1)}\right) - \zeta_{n+1}^m\alpha\left(\frac{n}{n+1}\right)D_{n+1}^m - \zeta_{n-1}^m\alpha\left(\frac{n+1}{n}\right)D_n^m&\\ - \left(\frac{1+\epsilon}{2}\right)\Delta t\frac{n\,(n+1)}{a^2}\left[R\boldsymbol{H}_k^r\cdot\boldsymbol{T}_n^m + RT^r\ln {p'}_{sn}^{m}\right] &= \mathcal{M}_n^m\end{aligned} \tag{3.312}$$

$$\ln {p'}_{sn}^{m} = \mathrm{PS}_n^m - \left(\frac{1+\epsilon}{2}\right)\frac{\Delta t}{p_s^r}\left(\underline{\Delta p^r}\right)^T\underline{\delta}_n^m \tag{3.313}$$

$$\underline{T}_n^m = \underline{\mathrm{TS}}_n^m - \left(\frac{1+\epsilon}{2}\right)\Delta t\boldsymbol{D}^r\underline{\delta}_n^m \tag{3.314}$$

The underbar denotes a vector over vertical levels. Rewrite the vorticity and divergence equations in terms of vectors over vertical levels.

$$\begin{aligned} \underline{\delta}_n^m \left(1 - \frac{im\alpha}{n(n+1)}\right) - \underline{\zeta}_{n+1}^m \alpha \left(\frac{n}{n+1}\right) - D_{n+1}^m \underline{\zeta}_{n-1}^m \alpha \left(\frac{n+1}{-n}\right) D_n^m & \\ - \left(\frac{1+\epsilon}{2}\right) \Delta t \frac{n(n+1)}{a^2} \left[R\boldsymbol{H}^r \underline{T}_n^m + R\underline{T}^r \ln p_{sn}^{\prime\, m}\right] &= \underline{DS}_n^m \end{aligned} \tag{3.315}$$

$$\underline{\zeta}_n^m \left(1 - \frac{im\alpha}{n(n+1)}\right) + \underline{\delta}_{n+1}^m \alpha \left(\frac{n}{n+1}\right) D_{n+1}^m + \underline{\delta}_{n-1}^m \alpha \left(\frac{n+1}{n}\right) D_n^m = \underline{VS}_n^m \tag{3.316}$$

Define $\underline{h}_n^m$ by

$$g\underline{h}_n^m = R\boldsymbol{H}^r T_n^m + R\underline{T}^r \ln p_{sn}^{\prime\, m} \tag{3.317}$$

and

$$\mathcal{A}_n^m = 1 - \frac{im\alpha}{n(n+1)} \tag{3.318}$$

$$\mathcal{B}^{+}{}_n^m = \alpha \left(\frac{n}{n+1}\right) D_{n+1}^m \tag{3.319}$$

$$\mathcal{B}^{-}{}_n^m = \alpha \left(\frac{n+1}{n}\right) D_n^m \tag{3.320}$$

Then the vorticity and divergence equations are

$$\mathcal{A}_n^m \underline{\zeta}_n^m + \mathcal{B}^{+}{}_n^m \underline{\delta}_{n+1}^m + \mathcal{B}^{-}{}_n^m \underline{\delta}_{n-1}^m = \underline{VS}_n^m \tag{3.321}$$

$$\mathcal{A}_n^m \underline{\delta}_n^m - \mathcal{B}^{+}{}_n^m \underline{\zeta}_{n+1}^m \mathcal{B}^{-}{}_n^m - \underline{\zeta}_{n-1}^m - \left(\frac{1+\epsilon}{2}\right) \Delta t \frac{n(n+1)}{a^2} g\underline{h}_n^m = \underline{DS}_n^m \tag{3.322}$$

Note that these equations are uncoupled in the vertical, i.e. each vertical level involves variables at that level only. The equation for $\underline{h}_n^m$ however couples all levels.

$$g\underline{h}_n^m = -\left(\frac{1+\epsilon}{2}\right) \Delta t \left[R\boldsymbol{H}^r \boldsymbol{D}^r + R\underline{T}^r \frac{\left(\underline{\Delta p}^r\right)^T}{p_s^r}\right] \underline{\delta}_n^m + R\boldsymbol{H}^r \underline{TS}_n^m + R\underline{T}^r \mathrm{PS}_n^m \tag{3.323}$$

Define $\boldsymbol{C}^r$ and $\underline{HS}_n^m$ so that

$$g\underline{h}_n^m = -\left(\frac{1+\epsilon}{2}\right) \Delta t \boldsymbol{C}^r \underline{\delta}_n^m + \underline{HS}_n^m \tag{3.324}$$

Let $g\mathrm{D}_\ell$ denote the eigenvalues of $\boldsymbol{C}^r$ with corresponding eigenvectors $\underline{\Phi}_\ell$ and $\boldsymbol{\Phi}$ is the matrix with columns $\underline{\Phi}_\ell$

$$\boldsymbol{\Phi} = \left(\ \underline{\Phi}_1\ \underline{\Phi}_2 \ldots \underline{\Phi}_L\ \right) \tag{3.325}$$

and $g\boldsymbol{D}$ the diagonal matrix of corresponding eigenvalues

$$
\begin{aligned}
g\boldsymbol{D} &= g\begin{pmatrix} \mathrm{D}_1 & 0 & \cdots & 0 \\ 0 & \mathrm{D}_2 & \cdots & 0 \\ \vdots & \vdots & \ddots & \vdots \\ 0 & 0 & \cdots & \mathrm{D}_L \end{pmatrix} && (3.326)\\
\boldsymbol{C}^r\boldsymbol{\Phi} &= \boldsymbol{\Phi} g\boldsymbol{D} && (3.327)\\
\boldsymbol{\Phi}^{-1}\boldsymbol{C}^r\boldsymbol{\Phi} &= g\boldsymbol{D} && (3.328)
\end{aligned}
$$

Then transform

$$
\begin{aligned}
&\tilde{\underline{\zeta}}_n^m = \boldsymbol{\Phi}^{-1}\underline{\zeta}_n^m \quad , \quad \widetilde{\underline{\mathsf{VS}}}_n^m = \boldsymbol{\Phi}^{-1}\underline{\mathsf{VS}}_n^m && (3.329)\\
&\tilde{\underline{\delta}}_n^m = \boldsymbol{\Phi}^{-1}\underline{\delta}_n^m \quad , \quad \widetilde{\underline{\mathsf{DS}}}_n^m = \boldsymbol{\Phi}^{-1}\underline{\mathsf{DS}}_n^m && (3.330)\\
&\tilde{\underline{h}}_n^m = \boldsymbol{\Phi}^{-1}\underline{h}_n^m \quad , \quad \widetilde{\underline{\mathsf{HS}}}_n^m = \boldsymbol{\Phi}^{-1}\underline{\mathsf{HS}}_n^m && (3.331)
\end{aligned}
$$

$$
\begin{aligned}
\mathcal{A}_n^m\tilde{\underline{\zeta}}_n^m + \mathcal{B}^{+}{}_n^m\tilde{\underline{\delta}}_{n+1}^m + \mathcal{B}^{-}{}_n^m\tilde{\underline{\delta}}_{n-1}^m &= \widetilde{\underline{\mathsf{VS}}}_n^m && (3.332)\\
\mathcal{A}_n^m\tilde{\underline{\delta}}_n^m - \mathcal{B}^{+}{}_n^m\tilde{\underline{\zeta}}_{n+1}^m\mathcal{B}^{-}{}_n^m - \tilde{\underline{\zeta}}_{n-1}^m - \left(\frac{1+\epsilon}{2}\right)\Delta t\frac{n\,(n+1)}{a^2}g\tilde{\underline{h}}_n^m &= \widetilde{\underline{\mathsf{DS}}}_n^m && (3.333)\\
g\tilde{\underline{h}}_n^m + \left(\frac{1+\epsilon}{2}\right)\Delta t\boldsymbol{\Phi}^{-1}\boldsymbol{C}^r\boldsymbol{\Phi}\boldsymbol{\Phi}^{-1}\underline{\delta}_n^m &= \widetilde{\underline{\mathsf{HS}}}_n^m && (3.334)\\
\tilde{\underline{h}}_n^m + \left(\frac{1+\epsilon}{2}\right)\Delta t\boldsymbol{D}\tilde{\underline{\delta}}_n^m &= \frac{1}{g}\widetilde{\underline{\mathsf{HS}}}_n^m && (3.335)
\end{aligned}
$$

Since $\boldsymbol{D}$ is diagonal, all equations are now uncoupled in the vertical.

For each vertical mode, i.e. element of $(\tilde{\underline{\ \ }})_n^m$, and for each Fourier wavenumber $m$ we have a system of equations in $n$ to solve. In following we drop the Fourier index $m$ and the modal element index $(\ \ )_\ell$ from the notation.

$$
\begin{aligned}
\mathcal{A}_n\tilde{\zeta}_n + \mathcal{B}^{+}{}_n\tilde{\delta}_{n+1} + \mathcal{B}^{-}{}_n\tilde{\delta}_{n-1} &= \widetilde{\mathsf{VS}}_n && (3.336)\\
\mathcal{A}_n\tilde{\delta}_n - \mathcal{B}^{+}{}_n\tilde{\zeta}_{n+1}\mathcal{B}^{-}{}_n\tilde{\zeta}_{n-1} - \left(\frac{1+\epsilon}{2}\right)\Delta t\frac{n\,(n+1)}{a^2}g\tilde{h}_n &= \widetilde{\mathsf{DS}}_n && (3.337)\\
\tilde{h}_n + \left(\frac{1+\epsilon}{2}\right)\Delta t\mathrm{D}_\ell\tilde{\delta}_n &= \frac{1}{g}\widetilde{\mathsf{HS}}_n && (3.338)
\end{aligned}
$$

The modal index $(\ \ )_\ell$ was included in the above equation on D only as a reminder, but will also be dropped in the following.

Substitute $\tilde{\zeta}$ and $\tilde{h}$ into the $\tilde{\delta}$ equation.

$$
\begin{aligned}
&\left[\mathcal{A}_n + \left(\frac{1+\epsilon}{2}\right)^2(\Delta t)^2\frac{n\,(n+1)}{a^2}g\mathrm{D} + \mathcal{B}^{+}{}_n\mathcal{A}_{n+1}^{-1}\mathcal{B}^{-}{}_{n+1} + \mathcal{B}^{-}{}_n\mathcal{A}_{n-1}^{-1}\mathcal{B}^{+}{}_{n-1}\right]\tilde{\delta}_n\\
&\qquad + \left(\mathcal{B}^{+}{}_n\mathcal{A}_{n+1}^{-1}\mathcal{B}^{+}{}_{n+1}\right)\tilde{\delta}_{n+2} \quad + \quad \left(\mathcal{B}^{-}{}_n\mathcal{A}_{n-1}^{-1}\mathcal{B}^{-}{}_{n-1}\right)\tilde{\delta}_{n-2} && (3.339)\\
&= \widetilde{\mathsf{DS}}_n + \left(\frac{1+\epsilon}{2}\right)\Delta t\frac{n\,(n+1)}{a^2}\widetilde{\mathsf{HS}}_n + \mathcal{B}^{+}{}_n\mathcal{A}_{n+1}^{-1}\widetilde{\mathsf{VS}}_{n+1} + \mathcal{B}^{-}{}_n\mathcal{A}_{n-1}^{-1}\widetilde{\mathsf{VS}}_{n-1}
\end{aligned}
$$

which is just two tri-diagonal systems of equations, one for the even and one for the odd $n$'s, and $m \leq n \leq N$

At the end of the system, the boundary conditions are

$$\begin{aligned} n = m, &\qquad \mathcal{B}^{-}{}_{n} = \mathcal{B}^{-}{}^{m}_{m} = 0 \\ n = m+1, &\quad \mathcal{B}^{-}{}_{n-1} = \mathcal{B}^{-}{}^{m}_{m} = \mathcal{B}^{-}{}^{m}_{(m+1)-1} = 0 \end{aligned} \tag{3.340}$$

the $\tilde{\delta}_{n-2}$ term is not present, and from the underlying truncation

$$\tilde{\delta}^{m}_{N+1} = \tilde{\delta}^{m}_{N+2} = 0 \tag{3.341}$$

For each $m$ and $\ell$ we have the general systems of equations

$$-A_n\tilde{\delta}_{n+2} + B_n\tilde{\delta}_n - C_n - \tilde{\delta}_{n-2} = D_n \ , \begin{cases} n = m, m+2, ..., \begin{cases} N+1 \\ \text{or} \\ N+2 \end{cases} \\ n = m+1, m+3, ..., \begin{cases} N+1 \\ \text{or} \\ N+2 \end{cases} \end{cases} \tag{3.342}$$

$$C_m = C_{m+1} = 0 \tag{3.343}$$

$$\tilde{\delta}_{N+1} = \tilde{\delta}_{N+2} = 0 \tag{3.344}$$

Assume solutions of the form

$$\tilde{\delta}_n = E_n\tilde{\delta}_{n+2} + F_n \tag{3.345}$$

then

$$E_m = \frac{A_m}{B_m} \tag{3.346}$$

$$F_M = \frac{D_m}{B_m} \tag{3.347}$$

$$E_n = \frac{A_n}{B_n - C_nE_{n-2}} \quad , \quad n = m+2, m+4, ..., \begin{cases} N-2 \\ \text{or} \\ N-3 \end{cases} \tag{3.348}$$

$$F_n = \frac{D_n + C_nF_{n-2}}{B_n - C_nE_{n-2}} \quad , \quad n = m+2, m+4, ..., \begin{cases} N \\ \text{or} \\ N-1 \end{cases} \tag{3.349}$$

$$\tilde{\delta}_N = F_N \quad \text{or} \quad \tilde{\delta}_{N-1} = F_{N-1} \ , \tag{3.350}$$

$$\tilde{\delta}_n = E_n\tilde{\delta}_{n+2} + F_n \ , \quad \begin{cases} n = N-2, N-4, ..., \begin{cases} m \\ \text{or} \\ m+1 \end{cases} \\ n = N-3, N-5, ..., \begin{cases} m+1 \\ \text{or} \\ m \end{cases} \end{cases} \tag{3.351}$$

Divergence in physical space is obtained from the vertical mode coefficients by

$$\underline{\delta}_n^m = \mathbf{\Phi}\underline{\tilde{\delta}}_n^m \tag{3.352}$$

The remaining variables are obtained in physical space by

$$\begin{aligned}
\zeta_n^m\left(1-\frac{im\alpha}{n\,(n+1)}\right) &= \mathcal{L}_n^m - \delta_{n+1}^m\alpha\left(\frac{n}{n+1}\right)D_{n+1}^m - \delta_{n-1}^m\alpha\left(\frac{n+1}{n}\right)D_n^m && (3.353)\\
\underline{T}_n^m &= \underline{\mathrm{TS}}_n^m - \left(\frac{1+\epsilon}{2}\right)\Delta t\boldsymbol{D}^r\underline{\delta}_n^m && (3.354)\\
\ln p_{sn}'^{\,m} &= \mathrm{PS}_n^m - \left(\frac{1+\epsilon}{2}\right)\frac{\Delta t}{p_s^r}\left(\underline{\Delta p^r}\right)^T\underline{\delta}_n^m && (3.355)
\end{aligned}$$

### 3.2.11 Trajectory Calculation

The trajectory calculation follows Hortal [1999] Let $\boldsymbol{R}$ denote the position vector of the parcel,

$$\frac{d\boldsymbol{R}}{dt} = \boldsymbol{V} \tag{3.356}$$

which can be approximated in general by

$$\boldsymbol{R}_D^n = \boldsymbol{R}_A^{n+1} - \Delta t\boldsymbol{V}_M^{n+\frac{1}{2}} \tag{3.357}$$

Hortal's method is based on a Taylor's series expansion

$$\boldsymbol{R}_A^{n+1} = \boldsymbol{R}_D^n + \Delta t\left(\frac{d\boldsymbol{R}}{dt}\right)_D^n + \frac{\Delta t^2}{2}\left(\frac{d^2\boldsymbol{R}}{dt^2}\right)_D^n + \ldots \tag{3.358}$$

or substituting for $d\boldsymbol{R}/dt$

$$\boldsymbol{R}_A^{n+1} = \boldsymbol{R}_D^n + \Delta t\boldsymbol{V}_D^n + \frac{\Delta t^2}{2}\left(\frac{d\boldsymbol{V}}{dt}\right)_D^n + \ldots \tag{3.359}$$

Approximate

$$\left(\frac{d\boldsymbol{V}}{dt}\right)_D^n \approx \frac{\boldsymbol{V}_A^n - \boldsymbol{V}_D^{n-1}}{\Delta t} \tag{3.360}$$

giving

$$\boldsymbol{V}_M^{n+\frac{1}{2}} = \frac{1}{2}\left[\left(2\boldsymbol{V}^n - \boldsymbol{V}^{n-1}\right)_D + \boldsymbol{V}_A^n\right] \tag{3.361}$$

for the trajectory equation.

### 3.2.12 Mass and energy fixers and statistics calculations

The semi-Lagrangian dynamical core applies the same mass and energy fixers and statistical calculations as the Eulerian dynamical core. These are described in sections 3.1.19, 3.1.20, and 3.1.21.

## 3.3 Finite Volume Dynamical Core

### 3.3.1 Overview

This document describes the Finite-Volume (FV) dynamical core that was initially developed and used at the NASA Data Assimilation Office (DAO) for data assimilation, numerical weather predictions, and climate simulations. The finite-volume discretization is local and entirely in physical space. The horizontal discretization is based on a conservative "*flux-form semi-Lagrangian*" scheme described by Lin and Rood [1996] (hereafter LR96) and Lin and Rood [1997] (hereafter LR97). The vertical discretization can be best described as *Lagrangian* with a conservative re-mapping, which essentially makes it *quasi-Lagrangian*. The *quasi-Lagrangian* aspect of the vertical coordinate is transparent to model users or physical parameterization developers, and it functions exactly like the $\eta - coordinate$ (a hybrid $\sigma - p$ coordinate) used by other dynamical cores within CAM.

In the current implementation for use in CAM, the FV dynamics and physics are "time split" in the sense that all prognostic variables are updated sequentially by the "dynamics" and then the "physics". The time integration within the FV dynamics is fully explicit, with sub-cycling within the 2D Lagrangian dynamics to stabilize the fastest wave (see section 3.3.4). The transport for tracers, however, can take a much larger time step (*e.g.*, 30 minutes as for the physics).

### 3.3.2 The governing equations for the hydrostatic atmosphere

For reference purposes, we present the continuous differential equations for the hydrostatic 3D atmospheric flow on the sphere for a general vertical coordinate $\zeta$ (*e.g.*, Kasahara [1974]). Using standard notations, the hydrostatic balance equation is given as follows:

$$\frac{1}{\rho}\frac{\partial p}{\partial z} + g = 0, \tag{3.362}$$

where $\rho$ is the density of the air, $p$ the pressure, and $g$ the gravitational constant. Introducing the "*pseudo-density*" $\pi = \frac{\partial p}{\partial \zeta}$ (*i.e.*, the vertical pressure gradient in the general coordinate), from the hydrostatic balance equation the *pseudo-density* and the true density are related as follows:

$$\pi = -\frac{\partial \Phi}{\partial \zeta}\rho, \tag{3.363}$$

where $\Phi = gz$ is the geopotential. Note that $\pi$ reduces to the "true density" if $\zeta = -gz$, and the "surface pressure" $P_s$ if $\zeta = \sigma$ ($\sigma = \frac{p}{P_s}$). The conservation of total air mass using $\pi$ as the prognostic variable can be written as

$$\frac{\partial}{\partial t}\pi + \nabla \cdot \left(\overrightarrow{V}\pi\right) = 0, \tag{3.364}$$

where $\overrightarrow{V} = (u, v, \frac{d\zeta}{dt})$. Similarly, the mass conservation law for tracer species (or water vapor) can be written as

$$\frac{\partial}{\partial t}(\pi q) + \nabla \cdot \left(\overrightarrow{V}\pi q\right) = 0, \tag{3.365}$$

where $q$ is the mass mixing ratio (or specific humidity) of the tracers (or water vapor).

Choosing the (virtual) potential temperature $\Theta$ as the thermodynamic variable, the first law of thermodynamics is written as

$$\frac{\partial}{\partial t}(\pi\Theta) + \nabla \cdot \left(\overrightarrow{V}\pi\Theta\right) = 0. \tag{3.366}$$

Letting $(\lambda, \theta)$ denote the (longitude, latitude) coordinate, the momentum equations can be written in the "vector-invariant form" as follows:

$$\frac{\partial}{\partial t}u = \Omega v - \frac{1}{Acos\theta}\left[\frac{\partial}{\partial \lambda}\left(\kappa + \Phi - \nu D\right) + \frac{1}{\rho}\frac{\partial}{\partial \lambda}p\right] - \frac{d\zeta}{dt}\frac{\partial u}{\partial \zeta}, \tag{3.367}$$

$$\frac{\partial}{\partial t}v = -\Omega u - \frac{1}{A}\left[\frac{\partial}{\partial \theta}\left(\kappa + \Phi - \nu D\right) + \frac{1}{\rho}\frac{\partial}{\partial \theta}p\right] - \frac{d\zeta}{dt}\frac{\partial v}{\partial \zeta}, \tag{3.368}$$

where $A$ is the radius of the earth, $\nu$ is the coefficient for the optional divergence damping, $D$ is the horizontal divergence

$$D = \frac{1}{Acos\theta}\left[\frac{\partial}{\partial \lambda}(u) + \frac{\partial}{\partial \theta}(v\, cos\theta)\right],$$

$$\kappa = \frac{1}{2}\left(u^2 + v^2\right),$$

and $\Omega$, the vertical component of the absolute vorticity, is defined as follows:

$$\Omega = 2\omega\, sin\theta + \frac{1}{A\, cos\theta}\left[\frac{\partial}{\partial \lambda}v - \frac{\partial}{\partial \theta}(u\, cos\theta)\right],$$

where $\omega$ is the angular velocity of the earth. Note that the last term in (3.367) and (3.368) vanishes if the vertical coordinate $\zeta$ is a conservative quantity (*e.g.*, entropy under adiabatic conditions [Hsu and Arakawa, 1990] or an imaginary conservative tracer), and the 3D divergence operator becomes 2D along constant $\zeta$ surfaces. The discretization of the 2D horizontal transport process is described in section 3.3.3. The complete dynamical system using the Lagrangian control-volume vertical discretization is described in section 3.3.4. A mass, momentum, and total energy conservative mapping algorithm is described in section 3.3.5.

### 3.3.3 Horizontal discretization of the transport process on the sphere

Since the vertical transport term would vanish after the introduction of the vertical Lagrangian control-volume discretization (see section 3.3.4), we shall present here only the 2D (horizontal) forms of the FFSL transport algorithm for the transport of density (3.364) and mixing ratio-like quantities (3.365) on the sphere. The governing equation for the pseudo-density (3.364) becomes

$$\frac{\partial}{\partial t}\pi + \frac{1}{Acos\theta}\left[\frac{\partial}{\partial \lambda}(u\pi) + \frac{\partial}{\partial \theta}(v\pi\, cos\theta)\right] = 0. \tag{3.369}$$

The finite-volume (*integral*) representation of the continuous $\pi$ field is defined as follows:

$$\widetilde{\pi}(t) \equiv \frac{1}{A^2 \Delta\theta \Delta\lambda cos\theta} \iint \pi(t;\lambda,\theta) A^2 cos\theta \, d\theta d\lambda. \tag{3.370}$$

Given the *exact* 2D wind field $\overrightarrow{V}(t;\lambda,\theta) = (U,V)$ the 2D integral representation of the conservation law for $\widetilde{\pi}$ can be obtained by integrating (3.369) in time and in space

$$\widetilde{\pi}^{n+1} = \widetilde{\pi}^n - \frac{1}{A^2 \Delta\theta \Delta\lambda cos\theta} \int_t^{t+\Delta t} \left[ \oint \pi(t;\lambda,\theta) \overrightarrow{V} \cdot \overrightarrow{n} \, dl \right] dt. \tag{3.371}$$

The above 2D transport equation is still *exact for the finite-volume under consideration.* To carry out the contour integral, certain approximations must be made. LR96 essentially decomposed the flux integral using two orthogonal 1D flux-form transport operators. Introducing the following difference operator

$$\delta_x q = q(x + \frac{\Delta x}{2}) - q(x - \frac{\Delta x}{2}),$$

and assuming $(u^*, v^*)$ is the time-averaged (from time $t$ to time $t + \Delta t$) $\overrightarrow{V}$ on the C-grid (*e.g.*, Fig. 1 in LR96), the 1-D finite-volume flux-form transport operator $F$ in the $\lambda$-direction is

$$F(u^*, \Delta t, \widetilde{\pi}) = -\frac{1}{A \Delta\lambda cos\theta} \delta_\lambda \left[ \int_t^{t+\Delta t} \pi U \, dt \right] = -\frac{\Delta t}{A \Delta\lambda cos\theta} \delta_\lambda \left[ \chi(u^*, \Delta t; \pi) \right], \tag{3.372}$$

where $\chi$ , the time-accumulated (from $t$ to $t$+$\Delta t$) mass flux across the cell wall, is defined as follows,

$$\chi(u^*, \Delta t; \pi) = \frac{1}{\Delta t} \int_t^{t+\Delta t} \pi U \, dt \equiv u^* \pi^*(u^*, \Delta t, \widetilde{\pi}), \tag{3.373}$$

and

$$\pi^*(u^*, \Delta t; \widetilde{\pi}) \approx \frac{1}{\Delta t} \int_t^{t+\Delta t} \pi \, dt \tag{3.374}$$

can be interpreted as a time mean (from time $t$ to time $t + \Delta t$) pseudo-density value of all material that passed through the cell edge from the upwind direction.

Note that the above *time integration* is to be carried out along the *backward-in-time* trajectory of the cell edge position from $t = t + \Delta t$ (the arrival point; (*e.g.*, point B in Fig. 3 of LR96) back to time $t$ (the departure point; *e.g.*, point B' in Fig. 3 of LR96). The very essence of the 1D finite-volume algorithm is to construct, based on the given initial cell-mean values of $\widetilde{\pi}$, an approximated subgrid distribution of the true $\pi$ field, to enable an analytic integration of (3.374). Assuming there is no error in obtaining the time-mean wind ($u^*$), the only error produced by the 1D transport scheme would be solely due to the approximation to the continuous distribution of $\pi$ within the subgrid under consideration. From this perspective, it can be said that the 1D finite-volume transport algorithm combines the time-space discretization in the approximation of the time-mean cell-edge values $\pi^*$. The physically correct way of approximating the integral (3.374) must be "upwind", in the sense that it is integrated along the backward trajectory of the cell edges. For example, a center difference approximation to (3.374) would be physically incorrect, and consequently numerically unstable unless artificial numerical diffusion is added.

Central to the accuracy and computational efficiency of the finite-volume algorithms is the degrees of freedom that describe the subgrid distribution. The first order upwind scheme, for example, has zero degrees of freedom within the volume as it is assumed that the subgrid distribution is piecewise constant having the same value as the given volume-mean. The second order finite-volume scheme (*e.g.*, Lin et al. [1994]) assumes a piece-wise linear subgrid distribution, which allows one degree of freedom for the specification of the "slope" of the linear distribution to improve the accuracy of integrating (3.374). The Piecewise Parabolic Method (PPM, Colella and Woodward [1984]) has two degrees of freedom in the construction of the second order polynomial within the volume, and as a result, the accuracy is significantly enhanced. The PPM appears to strike a good balance between computational efficiency and accuracy. Therefore, the PPM is the basic 1D scheme we chose. (An extension of the standard PPM by S.-J. Lin has also been documented in Machenhauer [1998]). Note that the subgrid PPM distributions are compact, and do not extend beyond the volume under consideration. The accuracy is therefore significantly better than the order of the chosen polynomials implies. While the PPM scheme possesses all the desirable attributes (mass conserving, monotonicity preserving, and high-order accuracy) in 1D, it is important that a solution be found to avoid the directional splitting in the multi-dimensional problem of modeling the dynamics and transport processes of the Earth's atmosphere.

The first step for reducing the splitting error is to apply the two orthogonal 1D flux-form operators in a directionally symmetric way. After symmetry is achieved, the "inner operators" are then replaced with corresponding advective-form operators. A consistent advective-form operator in the $\lambda-$direction can be derived from its flux-form counterpart ($F$) as follows:

$$f(u^*, \Delta t, \widetilde{\pi}) = F(u^*, \Delta t, \widetilde{\pi}) + \widetilde{\rho}\, F(u^*, \Delta t, \widetilde{\pi} \equiv 1) = F(u^*, \Delta t, \widetilde{\pi}) + \widetilde{\pi}\, C^{\lambda}_{def}, \tag{3.375}$$

$$C^{\lambda}_{def} = \frac{\Delta t\, \delta_\lambda u^*}{A \Delta \lambda cos\theta}, \tag{3.376}$$

where $C^{\lambda}_{def}$ is a dimensionless number indicating the degree of the flow deformation in the $\lambda$-direction. The above derivation of $f$ is slightly different from LR96's approach, which adopted the traditional 1D advective-form semi-Lagrangian scheme. The advantage of using (3.375) is that computation of winds at cell centers (Eq. 2.25 in LR96) are avoided.

Analogously, the 1D flux-form transport operator $G$ in the latitudinal ($\theta$) direction is derived as follows:

$$G(v^*, \Delta t, \widetilde{\pi}) = -\frac{1}{A \Delta \theta cos\theta}\, \delta_\theta \left[ \int_t^{t+\Delta t} \pi V cos\theta\, dt \right] = -\frac{\Delta t}{A \Delta \theta cos\theta}\, \delta_\theta \left[ v^* cos\theta\, \pi^* \right], \tag{3.377}$$

and likewise the advective-form operator,

$$g(v^*, \Delta t, \widetilde{\pi}) = G(v^*, \Delta t, \widetilde{\pi}) + \widetilde{\pi}\, C^{\theta}_{def}, \tag{3.378}$$

where

$$C^{\theta}_{def} = \frac{\Delta t\, \delta_\theta \left[ v^* cos\theta \right]}{A \Delta \theta cos\theta}. \tag{3.379}$$

To complete the construction of the 2D algorithm on the sphere, we introduce the following short hand notations:

$$(\,)^\theta = (\,)^n + \frac{1}{2} g \left[ v^*, \Delta t, \, (\,)^n \right], \tag{3.380}$$

$$( )^{\lambda} = ( )^{n} + \frac{1}{2} f\left[u^{*}, \Delta t, ( )^{n}\right]. \tag{3.381}$$

The 2D transport algorithm (*cf*, Eq. 2.24 in LR96) can then be written as

$$\widetilde{\pi}^{n+1} = \widetilde{\pi}^{n} + F\left[u^{*}, \Delta t, \widetilde{\pi}^{\theta}\right] + G\left[v^{*}, \Delta t, \widetilde{\pi}^{\lambda}\right]. \tag{3.382}$$

Using explicitly the mass fluxes $(\chi, Y)$, (3.382) is rewritten as

$$\widetilde{\pi}^{n+1} = \widetilde{\pi}^{n} - \frac{\Delta t}{A cos\theta}\left\{\frac{1}{\Delta\lambda}\delta_{\lambda}\left[\chi(u^{*}, \Delta t; \widetilde{\pi}^{\theta})\right] + \frac{1}{\Delta\theta}\delta_{\theta}\left[cos\theta\, Y(v^{*}, \Delta t; \widetilde{\pi}^{\lambda})\right]\right\}, \tag{3.383}$$

where $Y$, the mass flux in the meridional direction, is defined in a similar fashion as $\chi$ (3.373). It can be verified that in the special case of constant density flow ($\widetilde{\pi} = constant$) the above equation degenerates to the finite-difference representation of the *incompressibility condition* of the "time mean" wind field $(u^{*}, v^{*})$, *i.e.*,

$$\frac{1}{\Delta\lambda}\delta_{\lambda} u^{*} + \frac{1}{\Delta\theta}\delta_{\theta}\left(v^{*} cos\theta\right) = 0. \tag{3.384}$$

The fulfillment of the above *incompressibility condition* for constant density flows is crucial to the accuracy of the 2D flux-form formulation. For transport of volume mean mixing ratio-like quantities ($\widetilde{q}$) the mass fluxes $(\chi, Y)$ as defined previously should be used as follows

$$\widetilde{q}^{n+1} = \frac{1}{\widetilde{\pi}^{n+1}}\left[\widetilde{\pi}^{n}\widetilde{q}^{n} + F(\chi, \Delta t, \widetilde{q}^{\theta}) + G(Y, \Delta t, \widetilde{q}^{\lambda})\right]. \tag{3.385}$$

Note that the above form of the tracer transport equation consistently degenerates to (3.382) if $\widetilde{q} \equiv 1$ (*i.e.*, the tracer density equals to the background air density), which is another important condition for a flux-form transport algorithm to be able to avoid generation of noise (*e.g.*, creation of artificial gradients) and to maintain mass conservation.

### 3.3.4 A *vertically Lagrangian* and *horizontally Eulerian* control-volume discretization of the hydrodynamics

The very idea of using Lagrangian vertical coordinate for formulating governing equations for the atmosphere is not entirely new. Starr [1945]) is likely the first to have formulated, in the *continuous differential form*, the governing equations using a Lagrangian coordinate. Starr did not make use of the *discrete* Lagrangian control-volume concept for discretization nor did he present a solution to the problem of computing the pressure gradient forces. In the *finite-volume discretization* to be described here, the Lagrangian surfaces are treated as the bounding material surfaces of the Lagrangian control-volumes within which the finite-volume algorithms developed in LR96, LR97, and L97 will be directly applied.

To use a vertical Lagrangian coordinate system to reduce the 3D governing equations to the 2D forms, one must first address the issue of whether it is an inertial coordinate or not. For hydrostatic flows, it is. This is because both the right-hand-side and the left-hand-side of the vertical momentum equation vanish for purely hydrostatic flows.

Realizing that the earth's surface, for all practical modeling purposes, can be regarded as a non-penetrable material surface, it becomes straightforward to construct a terrain-following

Lagrangian control-volume coordinate system. In fact, any commonly used terrain-following coordinates can be used as the starting reference (*i.e.*, fixed, Eulerian coordinate) of the floating Lagrangian coordinate system. To close the coordinate system, the model top (at a prescribed constant pressure) is also assumed to be a Lagrangian surface, which is the same assumption being used by practically all global hydrostatic models.

The basic idea is to start the time marching from the chosen terrain-following Eulerian coordinate (*e.g.*, pure $\sigma$ or hybrid $\sigma$-p), *treating the initial coordinate surfaces as material surfaces*, the finite-volumes bounded by two coordinate surfaces, *i.e.*, the Lagrangian control-volumes, are free vertically, to float, compress, or expand with the flow as dictated by the hydrostatic dynamics.

By choosing an imaginary conservative tracer $\zeta$ that is a monotonic function of height and constant on the initial reference coordinate surfaces (*e.g.*, the value of "$\eta$" in the hybrid $\sigma - p$ coordinate used in CAM), the 3D governing equations written for the general vertical coordinate in section 1.2 can be reduced to 2D forms. After factoring out the constant $\delta\zeta$, (3.364), the conservation law for the pseudo-density ($\pi = \frac{\delta p}{\delta \zeta}$), becomes

$$\frac{\partial}{\partial t}\delta p + \frac{1}{Acos\theta}\left[\frac{\partial}{\partial \lambda}(u\delta p) + \frac{\partial}{\partial \theta}(v\delta p\, cos\theta)\right] = 0, \tag{3.386}$$

where the symbol $\delta$ represents the vertical difference between the two neighboring Lagrangian surfaces that bound the finite control-volume. From (3.362), the pressure thickness $\delta p$ of that control-volume is proportional to the total mass, *i.e.*, $\delta p = -\rho g \delta z$. Therefore, it can be said that the Lagrangian control-volume vertical discretization has the hydrostatic balance built-in, and $\delta p$ can be regarded as the "pseudo-density" for the discretized Lagrangian vertical coordinate system.

Similarly, (3.365), the mass conservation law for all tracer species, is

$$\frac{\partial}{\partial t}(q\delta p) + \frac{1}{Acos\theta}\left[\frac{\partial}{\partial \lambda}(uq\delta p) + \frac{\partial}{\partial \theta}(vq\delta p\, cos\theta)\right] = 0, \tag{3.387}$$

the thermodynamic equation, (3.366), becomes

$$\frac{\partial}{\partial t}(\Theta\delta p) + \frac{1}{Acos\theta}\left[\frac{\partial}{\partial \lambda}(u\Theta\delta p) + \frac{\partial}{\partial \theta}(v\Theta\delta p\, cos\theta)\right] = 0, \tag{3.388}$$

and (3.367) and (3.368), the momentum equations, are reduced to

$$\frac{\partial}{\partial t}u = \Omega v - \frac{1}{Acos\theta}\left[\frac{\partial}{\partial \lambda}\left(\kappa + \Phi - \nu D\right) + \frac{1}{\rho}\frac{\partial}{\partial \lambda}p\right], \tag{3.389}$$

$$\frac{\partial}{\partial t}v = -\Omega u - \frac{1}{A}\left[\frac{\partial}{\partial \theta}\left(\kappa + \Phi - \nu D\right) + \frac{1}{\rho}\frac{\partial}{\partial \theta}p\right]. \tag{3.390}$$

Given the prescribed pressure at the model top $P_\infty$, the position of each Lagrangian surface $P_l$ (horizontal subscripts omitted) is determined in terms of the hydrostatic pressure as follows:

$$P_l = P_\infty + \sum_{k=1}^{l}\delta P_k, \quad (for\, l = 1,\, 2,\, 3,\, ...,\, N), \tag{3.391}$$

where the subscript $l$ is the vertical index ranging from 1 at the lower bounding Lagrangian surface of the first (the highest) layer to $N$ at the Earth's surface. There are $N+1$ Lagrangian surfaces to define a total number of $N$ Lagrangian layers. The surface pressure, which is the pressure at the lowest Lagrangian surface, is easily computed as $P_N$ using (3.391). The surface pressure is needed for the physical parameterizations and to define the reference Eulerian coordinate for the mapping procedure (to be described in section 3.3.5).

With the exception of the pressure-gradient terms and the addition of a thermodynamic equation, the above 2D Lagrangian dynamical system is the same as the shallow water system described in LR97. The conservation law for the depth of fluid $h$ in the shallow water system of LR97 is replaced by (3.386) for the pressure thickness $\delta p$. The ideal gas law, the mass conservation law for air mass, the conservation law for the potential temperature (3.388), together with the modified momentum equations (3.389) and (3.390) close the 2D Lagrangian dynamical system, which are vertically coupled only by the hydrostatic relation (see (3.406), section 3.3.5).

The time marching procedure for the 2D Lagrangian dynamics follows closely that of the shallow water dynamics fully described in LR97. For computational efficiency, we shall take advantage of the stability of the FFSL transport algorithm by using a much larger time step ($\Delta t$) for the transport of all tracer species (including water vapor). As in the shallow water system, the Lagrangian dynamics uses a relatively small time step, $\Delta\tau = \Delta t/m$, where $m$ is the number of the sub-cycling needed to stabilize the fastest wave in the system. We shall describe here this time-split procedure for the *prognostic variables* $[\delta p, \Theta, u, v; q]$ on the D-grid. Discretization on the C-grid for obtaining the *diagnostic variables*, the time-averaged winds $(u^*, v^*)$, is analogous to that of the D-grid (see also LR97).

Introducing the following short hand notations (*cf*, (3.380) and (3.381)):

$$(\,)_i^\theta = (\,)^{n+\frac{i-1}{m}} + \frac{1}{2} g[v_i^*, \Delta\tau, (\,)^{n+\frac{i-1}{m}}],$$

$$(\,)_i^\lambda = (\,)^{n+\frac{i-1}{m}} + \frac{1}{2} f[u_i^*, \Delta\tau, (\,)^{n+\frac{i-1}{m}}],$$

and applying directly (3.383), the update of "pressure thickness" $\delta p$, using the fractional time step $\Delta\tau = \Delta t/m$, can be written as

$$\delta p^{n+\frac{i}{m}} = \delta p^{n+\frac{i-1}{m}} - \frac{\Delta\tau}{A cos\theta}\left\{\frac{1}{\Delta\lambda}\delta_\lambda\left[x_i^*(u_i^*, \Delta\tau; \delta p_i^\theta)\right] + \frac{1}{\Delta\theta}\delta_\theta\left[cos\theta\, y_i^*(v_i^*, \Delta\tau; \delta p_i^\lambda)\right]\right\} \quad (3.392)$$

$$(for\, i = 1, ..., m),$$

where $[x_i^*, y_i^*]$ are the background air mass fluxes, which are then used as input to Eq. 24 for transport of the potential temperature $\Theta$:

$$\Theta^{n+\frac{i}{m}} = \frac{1}{\delta p^{n+\frac{i}{m}}}\left[\delta p^{n+\frac{i-1}{m}}\Theta^{n+\frac{i-1}{m}} + F(x_i^*, \Delta\tau; \Theta_i^\theta) + G(y_i^*, \Delta\tau, \Theta_i^\lambda)\right]. \quad (3.393)$$

The discretized momentum equations for the shallow water system (*cf*, Eq. 16 and Eq. 17 in LR97) are modified for the pressure gradient terms as follows:

$$u^{n+\frac{i}{m}} = u^{n+\frac{i-1}{m}} + \Delta\tau\left[y_i^*\left(v_i^*, \Delta\tau; \Omega^\lambda\right) - \frac{1}{A\Delta\lambda cos\theta}\delta_\lambda(\kappa^* - \nu D^*) + \widehat{P_\lambda}\right], \quad (3.394)$$

$$v^{n+\frac{i}{m}} = v^{n+\frac{i-1}{m}} - \Delta\tau \left[ x_i^* \left( u_i^*, \Delta\tau; \Omega^\theta \right) + \frac{1}{A\Delta\theta} \delta_\theta (\kappa^* - \nu D^*) - \widehat{P_\theta} \right], \tag{3.395}$$

where $\kappa^*$ is the upwind-biased "kinetic energy" (as defined by Eq. 18 in LR97), and $D^*$, the horizontal divergence on the D-grid, is discretized as follows:

$$D^* = \frac{1}{Acos\theta} \left[ \frac{1}{\Delta\lambda} \delta_\lambda u^{n+\frac{i-1}{m}} + \frac{1}{\Delta\theta} \delta_\theta \left( v^{n+\frac{i-1}{m}} cos\theta \right) \right].$$

The finite-volume mean pressure-gradient terms in (3.394) and (3.395) are computed as follows:

$$\widehat{P_\lambda} = \frac{\oint_{\Pi \rightleftharpoons \lambda} \phi d\Pi}{Acos\theta \oint_{\Pi \rightleftharpoons \lambda} \Pi d\lambda}, \tag{3.396}$$

$$\widehat{P_\theta} = \frac{\oint_{\Pi \rightleftharpoons \theta} \phi d\Pi}{A \oint_{\Pi \rightleftharpoons \theta} \Pi d\theta}, \tag{3.397}$$

where $\Pi = p^\kappa$ ($\kappa = R/C_p$), and the symbols "$\Pi \rightleftharpoons \lambda$" and "$\Pi \rightleftharpoons \theta$" indicate that the contour integrations are to be carried out, using the finite-volume algorithm described in L97, in the $(\Pi, \lambda)$ and $(\Pi, \theta)$ space, respectively.

To complete one time step, equations (3.392-3.395), together with their counterparts on the C-grid are cycled $m$ times using the fractional time step $\Delta\tau$, which are followed by the tracer transport using (3.387) with the large-time-step $\Delta t$.

Mass fluxes $(x^*, y^*)$ and the winds $(u^*, v^*)$ on the C-grid are accumulated for the large-time-step transport of tracer species (including water vapor) $q$ as

$$q^{n+1} = \frac{1}{\delta p^{n+1}} \left[ q^n \delta p^n + F(X^*, \Delta t, q^\theta) + G(Y^*, \Delta t, q^\lambda) \right], \tag{3.398}$$

where the time-accumulated mass fluxes $(X^*, Y^*)$ are computed as

$$X^* = \sum_{i=1}^{m} x_i^*(u_i^*,\, \Delta\tau,\, \delta p_i^\theta), \tag{3.399}$$

$$Y^* = \sum_{i=1}^{m} y_i^*(v_i^*,\, \Delta\tau,\, \delta p_i^\lambda). \tag{3.400}$$

The time-averaged winds $(U^*, V^*)$, defined as follows, are to be used as input for the computations of $q^\lambda$ and $q^\theta$ :

$$U^* = \frac{1}{m} \sum_{i=1}^{m} u_i^*, \tag{3.401}$$

$$V^* = \frac{1}{m} \sum_{i=1}^{m} v_i^*. \tag{3.402}$$

The use of the time accumulated mass fluxes and the time-averaged winds for the large-time-step tracer transport in the manner described above ensures the conservation of the tracer mass and maintains the highest degree of consistency possible given the time split integration procedure.

The algorithm described here can be readily applied to a regional model if appropriate boundary conditions are supplied. There is formally no Courant number related time step restriction associated with the transport processes. There is, however, a stability condition imposed by the gravity-wave processes. For application on the whole sphere, it is computationally advantageous to apply a polar filter to allow a dramatic increase of the size of the small time step $\Delta\tau$. The effect of the polar filter is to stabilize the short-in-wavelength (and high-in-frequency) gravity waves that are being unnecessarily and unidirectionally resolved at very high latitudes in the zonal direction. To minimize the impact to meteorologically significant larger scale waves, the polar filter is highly scale selective and is applied only to the diagnostic variables on the auxiliary C-grid and the tendency terms in the D-grid momentum equations. No polar filter is applied directly to any of the prognostic variables.

The design of the polar filter follows closely that of Suarez and Takacs [1995] for the C-grid Arakawa type dynamical core (*e.g.*, Arakawa and Lamb [1981]). Because our prognostic variables are computed on the D-grid and the fact that the FFSL transport scheme is stable for Courant number greater than one, in realistic test cases the maximum size of the time step is about two to three times larger than a model based on Arakawa and Lamb's C-grid differencing scheme. It is possible to avoid the use of the polar filter if, for example, the "Cubed grid" is chosen, instead of the current latitude-longitude grid. However, this would require a significant rewrite of the rest of the model codes including physics parameterizations, the land model, and most of the post processing packages.

The size of the small time step for the Lagrangian dynamics is only a function of the horizontal resolution. Applying the polar filter, for the 2-degree horizontal resolution, a small-time-step size of 450 seconds can be used for the Lagrangian dynamics. From the large-time-step transport perspective, the small-time-step integration of the 2D Lagrangian dynamics can be regarded as a very accurate iterative solver, with $m$ iterations, for computing the time mean winds and the mass fluxes, analogous in functionality to a semi-implicit algorithm's elliptic solver (*e.g.*, Ringler et al. [2000]). Besides accuracy, the merit of an "explicit" versus "semi-implicit" algorithm ultimately depends on the computational efficiency of each approach. In light of the advantage of the explicit algorithm in parallelization, we do not regard the explicit algorithm for the Lagrangian dynamics as an impedance to computational efficiency, particularly on modern parallel computing platforms. Furthermore, it may be possible to further increase the size of the small time step via vertical mode decomposition. This approach is one of the algorithm design issues we plan to revisit.

### 3.3.5 A mass, momentum, and total energy conserving mapping algorithm

The Lagrangian surfaces that bound the finite-volume will eventually deform, particularly in the presence of persistent diabatic heating/cooling, in a time scale of a few hours to a day depending on the strength of the heating and cooling, to a degree that it will negatively impact the accuracy of the horizontal-to-Lagrangian-coordinate transport and the computation of the pressure gradient forces. Therefore, a key to the success of the Lagrangian control-volume discretization is an accurate and conservative algorithm for mapping the deformed Lagrangian coordinate back to a fixed reference Eulerian coordinate.

There are some degrees of freedom in the design of the vertical mapping algorithm. To ensure conservation, our current (and recommended) mapping algorithm is based on the reconstruction of the "mass" (pressure thickness $\delta p$), zonal and meridional "winds", "tracer mixing ratios", and "total energy" (volume integrated sum of the internal, potential, and kinetic energy), using the monotonic Piecewise Parabolic sub-grid distributions with the hydrostatic pressure (as defined by (3.391)) as the mapping coordinate. We outline the mapping procedure as follows.

**Step 1**: Define a suitable Eulerian reference coordinate. The mass in each layer ($\delta p$) is then distributed vertically according to the chosen Eulerian coordinate. The surface pressure typically plays an "anchoring" role in defining the terrain following Eulerian vertical coordinate. The hybrid $\eta - coordinate$ used in the NCAR CCM3 [Kiehl et al., 1996] is adopted in the current model setup.

**Step 2**: Construct the piece-wise continuous vertical subgrid profiles of tracer mixing ratios ($q$), zonal and meridional winds ($u$ and $v$), and total energy ($\Gamma$) in the Lagrangian control-volume coordinate based on the Piece-wise Parabolic Method (PPM, Colella and Woodward [1984]). The total energy $\Gamma$ is computed as the sum of the finite-volume integrated geopotential $\phi$, internal energy ($C_v T$), and the kinetic energy ($K$) as follows:

$$\Gamma = \frac{1}{\delta p} \int \left[ C_v T + \phi + \frac{1}{2} \left( u^2 + v^2 \right) \right] dp. \tag{3.403}$$

Applying integration by parts and the ideal gas law, the above integral can be rewritten as

$$\Gamma = C_p \overline{T} + \frac{1}{\delta p} \delta \left( p\phi \right) + K, \tag{3.404}$$

where $\overline{T}$ is the layer mean temperature, $K$ is the kinetic energy, $p$ is the pressure at layer edges, and $C_v$ and $C_p$ are the specific heat of the air at constant volume and at constant pressure, respectively. Layer mean values of $q$, ($u$, $v$), and $\Gamma$ in the Eulerian coordinate system are obtained by integrating analytically the sub-grid distributions, in the vertical direction, from model top to the surface, layer by layer. Since the hydrostatic pressure is chosen as the mapping coordinate, tracer mass, momentum, and total energy are locally and globally conserved.

**Step 3**: Compute kinetic energy in the Eulerian coordinate system for each layer. Substituting kinetic energy and the hydrostatic relationship into (3.404), the layer mean temperature $\overline{T}_k$ for layer $k$ in the Eulerian coordinate is then retrieved from the reconstructed total energy (done in Step 2) by a fully explicit integration procedure starting from the surface up to the model top as follows:

$$\overline{T}_k = \frac{\Gamma_k - K_k - \phi_{k+\frac{1}{2}}}{C_p \left[ 1 - \kappa \, p_{k-\frac{1}{2}} \frac{ln\, p_{k+\frac{1}{2}} - ln\, p_{k-\frac{1}{2}}}{p_{k+\frac{1}{2}} - p_{k-\frac{1}{2}}} \right]}. \tag{3.405}$$

To convert the potential temperature $\Theta$ to the layer mean temperature the conversion factor is obtained by equating the following two equivalent forms of the hydrostatic relation for $\Theta$ and $\overline{T}$ :

$$\delta\phi = -C_p \Theta \, \delta\Pi, \tag{3.406}$$

$$\delta\phi = -R\overline{T} \, \delta ln \, \Pi, \tag{3.407}$$

where $\Pi = p^{\kappa}$. The conversion formula between layer mean temperature and layer mean potential temperature is obtained as follows:

$$\Theta = \kappa \frac{\delta ln \Pi}{\delta \Pi} \overline{T}. \tag{3.408}$$

The physical implication of retrieving the layer mean temperature from the total energy as described in Step 3 is that the dissipated kinetic energy, if any, is locally converted into internal energy via the vertically sub-grid mixing (dissipation) processes. Due to the monotonicity preserving nature of the sub-grid reconstruction the column-integrated kinetic energy inevitably decreases (dissipates), which leads to local frictional heating. The frictional heating is a physical process that maintains the conservation of the total energy in a closed system.

As viewed by an observer riding on the Lagrangian surfaces, the mapping procedure essentially performs the physical function of the relative-to-the-Eulerian-coordinate vertical transport, by vertically redistributing (air and tracer) mass, momentum, and total energy from the Lagrangian control-volume back to the Eulerian framework.

As described in section 3.3.4, the model time integration cycle consists of $m$ small time steps for the 2D Lagrangian dynamics and one large time step for tracer transport. The mapping time step can be much larger than that used for the large-time-step tracer transport. In tests using the Held-Suarez forcing [Held and Suarez, 1994], a three-hour mapping time interval is found to be adequate. In the full model integration, one may choose the same time step used for the physical parameterizations so as to ensure the input state variables to physical parameterizations are in the usual "Eulerian" vertical coordinate.

### 3.3.6 Adjustment of specific humidity to conserve water

The physics parameterizations operate on a model state provided by the dynamics, and are allowed to update specific humidity. However, the surface pressure remains fixed throughout the physics updates, and since there is an explicit relationship between the surface pressure and the air mass within each layer, the total air mass must remain fixed as well. This implies a change of dry air mass at the end of the physics updates. We impose a restriction that dry air mass and water mass be conserved as follows:

The total pressure $p$ is

$$p = d + e. \tag{3.409}$$

with dry pressure $d$, water vapor pressure $e$. The specific humidity is

$$q = \frac{e}{p} = \frac{e}{d+e}, \qquad d = (1-q)p. \tag{3.410}$$

We define a layer thickness as $\delta^k p \equiv p^{k+1/2} - p^{k-1/2}$, so

$$\delta^k d = (1 - q^k)\delta^k p. \tag{3.411}$$

We are concerned about 3 time levels: $q_n$ is input to physics, $q_{n*}$ is output from physics, $q_{n+1}$ is the adjusted value for dynamics.

Dry mass is the same at $n$ and $n+1$ but not at $n*$. To conserve dry mass, we require that

$$\delta^k d_n = \delta^k d_{n+1} \tag{3.412}$$

or

$$(1 - q_n^k)\delta^k p_n = (1 - q_{n+1}^k)\delta^k p_{n+1}. \tag{3.413}$$

Water mass is the same at $n*$ and $n+1$, but not at $n$. To conserve water mass, we require that

$$q_{n*}^k \delta^k p_n = q_{n+1}^k \delta^k p_{n+1}. \tag{3.414}$$

Substituting (3.414) into (3.413),

$$(1 - q_n^k)\delta^k p_n = \delta^k p_{n+1} - q_{n*}^k \delta^k p_n \tag{3.415}$$

$$\delta^k p_{n+1} = (1 - q_n^k + q_{n*}^k)\delta^k p_n \tag{3.416}$$

which yields a modified specific humidity for the dynamics:

$$q_{n+1}^k = q_n^k \frac{\delta^k p_n}{\delta^k p_{n+1}} = \frac{q_{n*}^k}{1 - q_n^k + q_{n*}^k}. \tag{3.417}$$

### 3.3.7 Further discussion

There are still aspects of the numerical formulation in the finite volume dynamical core that can be further improved. For example, the choice of the horizontal grid, the computational efficiency of the split-explicit time marching scheme, the choice of the various monotonicity constraints, and how the conservation of total energy is achieved.

The impact of the non-linear diffusion associated with the monotonicity constraint is difficult to assess. All discrete schemes must address the problem of subgrid-scale mixing. The finite-volume algorithm contains a non-linear diffusion that mixes strongly when monotonicity principles are locally violated. However, the effect of nonlinear diffusion due to the imposed monotonicity constraint diminishes quickly as the resolution matches better to the spatial structure of the flow. In other numerical schemes, however, an explicit (and tunable) linear diffusion is often added to the equations to provide the subgrid-scale mixing as well as to smooth and/or stabilize the time marching.

The finite-volume dynamical core as implemented in CAM and described here conserves the dry air and all other tracer mass exactly without a “mass fixer”. The vertical Lagrangian discretization and the associated remapping conserves the total energy exactly. The only remaining issue regarding conservation of the total energy is the horizontal discretization and the use of the “diffusive” transport scheme with monotonicity constraint. To compensate for the loss of total energy due to horizontal discretization, we apply a global fixer to add the loss in kinetic energy due to "diffusion" back to the thermodynamic equation so that the total energy is conserved. However, it should be noted that even without the "energy fixer" the loss in total energy (in flux unit) is found to be less than 2 ($W/m^2$) with the 2 degrees resolution, and much smaller with higher resolution. In the future, we may consider using the total energy as a transported prognostic variable so that the total energy could be automatically conserved.

# Chapter 4

# Model Physics

As stated in chapter 2, the total parameterization package in CAM 3.0 consists of a sequence of components, indicated by

$$P = \{M, R, S, T\} \ , \tag{4.1}$$

where $M$ denotes (Moist) precipitation processes, $R$ denotes clouds and Radiation, $S$ denotes the Surface model, and $T$ denotes Turbulent mixing. Each of these in turn is subdivided into various components: $M$ includes an optional dry adiabatic adjustment normally applied only in the stratosphere, moist penetrative convection, shallow convection, and large-scale stable condensation; $R$ first calculates the cloud parameterization followed by the radiation parameterization; $S$ provides the surface fluxes obtained from land, ocean and sea ice models, or calculates them based on specified surface conditions such as sea surface temperatures and sea ice distribution. These surface fluxes provide lower flux boundary conditions for the turbulent mixing $T$ which is comprised of the planetary boundary layer parameterization, vertical diffusion, and gravity wave drag.

## 4.1 Deep Convection

The process of deep convection is treated with a parameterization scheme developed by Zhang and McFarlane [1995]. The scheme is based on a plume ensemble approach where it is assumed that an ensemble of convective scale updrafts (and the associated saturated downdrafts) may exist whenever the atmosphere is conditionally unstable in the lower troposphere. The updraft ensemble is comprised of plumes sufficiently buoyant so as to penetrate the unstable layer, where all plumes have the same upward mass flux at the bottom of the convective layer. Moist convection occurs only when there is convective available potential energy (CAPE) for which parcel ascent from the sub-cloud layer acts to destroy the CAPE at an exponential rate using a specified adjustment time scale. For the convenience of the reader we will review some aspects of the formulation, but refer the interested reader to Zhang and McFarlane [1995] for additional detail, including behavioral characteristics of the parameterization scheme. Evaporation of convective precipitation is computed following the procedure described in section 4.3.

The large-scale budget equations distinguish between a cloud and sub-cloud layer where temperature and moisture response to convection in the cloud layer is written in terms of bulk convective fluxes as

$$c_p\left(\frac{\partial T}{\partial t}\right)_{cu} = -\frac{1}{\rho}\frac{\partial}{\partial z}\left(M_u S_u + M_d S_d - M_c S\right) + L(C-E) \tag{4.2}$$

$$\left(\frac{\partial q}{\partial t}\right)_{cu} = -\frac{1}{\rho}\frac{\partial}{\partial z}\left(M_u q_u + M_d q_d - M_c q\right) + E - C\ , \tag{4.3}$$

for $z \geq z_b$, where $z_b$ is the height of the cloud base. For $z_s < z < z_b$, where $z_s$ is the surface height, the sub-cloud layer response is written as

$$c_p\left(\rho\frac{\partial T}{\partial t}\right)_m = -\frac{1}{z_b - z_s}\left(M_b[S(z_b) - S_u(z_b)] + M_d[S(z_b) - S_d(z_b)]\right) \tag{4.4}$$

$$\left(\rho\frac{\partial q}{\partial t}\right)_m = -\frac{1}{z_b - z_s}\left(M_b[q(z_b) - q_u(z_b)] + M_d[q(z_b) - q_d(z_b)]\right)\ , \tag{4.5}$$

where the net vertical mass flux in the convective region, $M_c$, is comprised of upward, $M_u$, and downward, $M_d$, components, $C$ and $E$ are the large-scale condensation and evaporation rates, $S$, $S_u$, $S_d$, $q$, $q_u$, $q_d$, are the corresponding values of the dry static energy and specific humidity, and $M_b$ is the cloud base mass flux.

### 4.1.1 Updraft Ensemble

The updraft ensemble is represented as a collection of entraining plumes, each with a characteristic fractional entrainment rate $\lambda$. The moist static energy in each plume $h_c$ is given by

$$\frac{\partial h_c}{\partial z} = \lambda(h - h_c), \quad z_b < z < z_D\ . \tag{4.6}$$

Mass carried upward by the plumes is detrained into the environment in a thin layer at the top of the plume, $z_D$, where the detrained air is assumed to have the same thermal properties as in the environment ($S_c = S$). Plumes with smaller $\lambda$ penetrate to larger $z_D$. The entrainment rate $\lambda_D$ for the plume which detrains at height $z$ is then determined by solving (4.6), with lower boundary condition $h_c(z_b) = h_b$:

$$\frac{\partial h_c}{\partial (z - z_b)} = \lambda_D(h - h_b) - \lambda_D(h_c - h_b) \tag{4.7}$$

$$\frac{\partial (h_c - h_b)}{\partial (z - z_b)} - \lambda_D(h_c - h_b) = \lambda_D(h - h_b) \tag{4.8}$$

$$\frac{\partial (h_c - h_b)e^{\lambda_D(z-z_b)}}{\partial (z - z_b)} = \lambda_D(h - h_b)e^{\lambda_D(z-z_b)} \tag{4.9}$$

$$(h_c - h_b)e^{\lambda_D(z-z_b)} = \int_{z_b}^{z} \lambda_D(h - h_b)e^{\lambda_D(z'-z_b)}dz' \tag{4.10}$$

$$(h_c - h_b) = \lambda_D \int_{z_b}^{z} (h - h_b)e^{\lambda_D(z'-z)}dz'\ . \tag{4.11}$$

Since the plume is saturated, the detraining air must have $h_c = h^*$, so that

$$(h_b - h^*) = \lambda_D \int_{z_b}^{z} (h_b - h) e^{\lambda_D (z'-z)} dz' \; . \tag{4.12}$$

Then, $\lambda_D$ is determined by solving (4.12) iteratively at each $z$.

The top of the shallowest of the convective plumes, $z_0$ is assumed to be no lower than the mid-tropospheric minimum in saturated moist static energy, $h^*$, ensuring that the cloud top detrainment is confined to the conditionally stable portion of the atmospheric column. All condensation is assumed to occur within the updraft plumes, so that $C = C_u$. Each plume is assumed to have the same value for the cloud base mass flux $M_b$, which is specified below. The vertical distribution of the cloud updraft mass flux is given by

$$M_u = M_b \int_0^{\lambda_D} \frac{1}{\lambda_0} e^{\lambda (z-z_b)} d\lambda = M_b \frac{e^{\lambda_D (z-z_b)} - 1}{\lambda_0 (z - z_b)} \; , \tag{4.13}$$

where $\lambda_0$ is the maximum detrainment rate, which occurs for the plume detraining at height $z_0$, and $\lambda_D$ is the entrainment rate for the updraft that detrains at height $z$. Detrainment is confined to regions where $\lambda_D$ decreases with height, so that the total detrainment $D_u = 0$ for $z < z_0$. Above $z_0$,

$$D_u = -\frac{M_b}{\lambda_0} \frac{\partial \lambda_D}{\partial z} \; . \tag{4.14}$$

The total entrainment rate is then just given by the change in mass flux and the total detrainment,

$$E_u = \frac{\partial M_u}{\partial z} - D_u \; . \tag{4.15}$$

The updraft budget equations for dry static energy, water vapor mixing ratio, moist static energy, and cloud liquid water, $\ell$, are:

$$\frac{\partial}{\partial z}(M_u S_u) = (E_u - D_u) S + \rho L C_u \tag{4.16}$$

$$\frac{\partial}{\partial z}(M_u q_u) = E_u q - D_u q^* + \rho C_u \tag{4.17}$$

$$\frac{\partial}{\partial z}(M_u h_u) = E_u h - D_u h^* \tag{4.18}$$

$$\frac{\partial}{\partial z}(M_u \ell) = -D_u \ell_d + \rho C_u - \rho R_u \; , \tag{4.19}$$

where (4.18) is formed from (4.16) and (4.17) and detraining air has been assumed to be saturated ($q = q^*$ and $h = h^*$). It is also assumed that the liquid content of the detrained air is the same as the ensemble mean cloud water ($\ell_d = \ell$). The conversion from cloud water to rain water is given by

$$\rho R_u = c_0 M_u \ell \; , \tag{4.20}$$

following Lord et al. [1982], with $c_0 = 2 \times 10^{-3}$ m$^{-1}$.

Since $M_u$, $E_u$ and $D_u$ are given by (4.13-4.15), and $h$ and $h^*$ are environmental profiles, (4.18) can be solved for $h_u$, given a lower boundary condition. The lower boundary condition is obtained by adding a 0.5 K temperature perturbation to the dry (and moist) static energy at cloud base, or $h_u = h + c_p \times 0.5$ at $z = z_b$. Below the lifting condensation level (LCL), $S_u$ and $q_u$ are given by (4.16) and (4.17). Above the LCL, $q_u$ is reduced by condensation and $S_u$ is increased by the latent heat of vaporization. In order to obtain to obtain a saturated updraft at the temperature implied by $S_u$, we define $\Delta T$ as the temperature perturbation in the updraft, then:

$$\begin{aligned} h_u &= S_u + Lq_u & (4.21) \\ S_u &= S + c_p \Delta T & (4.22) \\ q_u &= q^* + \frac{dq^*}{dT}\Delta T \ . & (4.23) \end{aligned}$$

Substituting (4.22) and (4.23) into (4.21),

$$\begin{aligned} h_u &= S + Lq^* + c_p\left(1 + \frac{L}{c_p}\frac{dq^*}{dT}\right)\Delta T & (4.24) \\ &= h^* + c_p\left(1+\gamma\right)\Delta T & (4.25) \\ \gamma &\equiv \frac{L}{c_p}\frac{dq^*}{dT} & (4.26) \\ \Delta T &= \frac{1}{c_p}\frac{h_u - h^*}{1+\gamma} \ . & (4.27) \end{aligned}$$

The required updraft quantities are then

$$\begin{aligned} S_u &= S + \frac{h_u - h^*}{1+\gamma} & (4.28) \\ q_u &= q^* + \frac{\gamma}{L}\frac{h_u - h^*}{1+\gamma} \ . & (4.29) \end{aligned}$$

With $S_u$ given by (4.28), (4.16) can be solved for $C_u$, then (4.19) and (4.20) can be solved for $\ell$ and $R_u$.

The expressions above require both the saturation specific humidity to be

$$q^* = \frac{\epsilon e^*}{p - e^*}, \qquad e^* < p \ , \qquad (4.30)$$

where $e^*$ is the saturation vapor pressure, and its dependence on temperature (in order to maintain saturation as the temperature varies) to be

$$\begin{aligned} \frac{dq^*}{dT} &= \frac{\epsilon}{p - e^*}\frac{de^*}{dT} - \frac{\epsilon e^*}{(p-e^*)^2}\frac{d(p-e^*)}{dT} & (4.31) \\ &= \frac{\epsilon}{p-e^*}\left(1 + \frac{1}{p-e^*}\right)\frac{de^*}{dT} & (4.32) \\ &= \frac{\epsilon}{p-e^*}\left(1 + \frac{q^*}{\epsilon e^*}\right)\frac{de^*}{dT} \ . & (4.33) \end{aligned}$$

The deep convection scheme does not use the same approximation for the saturation vapor pressure $e^*$ as is used in the rest of the model. Instead,

$$e^* = c_1 \exp\left[\frac{c_2(T - T_f)}{(T - T_f + c_3)}\right] \ , \tag{4.34}$$

where $c_1 = 6.112$, $c_2 = 17.67$, $c_3 = 243.5$ K and $T_f = 273.16$ K is the freezing point. For this approximation,

$$\frac{de^*}{dT} = e^* \frac{d}{dT}\left[\frac{c_2(T - T_f)}{(T - T_f + c_3)}\right] \tag{4.35}$$

$$= e^* \left[\frac{c_2}{(T - T_f + c_3)} - \frac{c_2(T - T_f)}{(T - T_f + c_3)^2}\right] \tag{4.36}$$

$$= e^* \frac{c_2 c_3}{(T - T_f + c_3)^2} \tag{4.37}$$

$$\frac{dq^*}{dT} = q^* \left(1 + \frac{q^*}{\epsilon e^*}\right) \frac{c_2 c_3}{(T - T_f + c_3)^2} \ . \tag{4.38}$$

We note that the expression for $\gamma$ in the code gives

$$\frac{dq^*}{dT} = \frac{c_p}{L}\gamma = q^* \left(1 + \frac{q^*}{\epsilon}\right) \frac{\epsilon L}{RT^2} \ . \tag{4.39}$$

The expressions for $dq^*/dT$ in (4.38) and (4.39) are not identical. Also, $T - T_f + c_3 \neq T$ and $c_2 c_3 \neq \epsilon L/R$.

### 4.1.2 Downdraft Ensemble

Downdrafts are assumed to exist whenever there is precipitation production in the updraft ensemble where the downdrafts start at or below the bottom of the updraft detrainment layer. Detrainment from the downdrafts is confined to the sub-cloud layer, where all downdrafts have the same mass flux at the top of the downdraft region. Accordingly, the ensemble downdraft mass flux takes a similar form to (4.13) but includes a "proportionality factor" to ensure that the downdraft strength is physically consistent with precipitation availability. This coefficient takes the form

$$\alpha = \mu \left[\frac{P}{P + E_d}\right] \ , \tag{4.40}$$

where $P$ is the total precipitation in the convective layer and $E_d$ is the rain water evaporation required to maintain the downdraft in a saturated state. This formalism ensures that the downdraft mass flux vanishes in the absence of precipitation, and that evaporation cannot exceed some fraction, $\mu$, of the precipitation, where $\mu = 0.2$.

### 4.1.3 Closure

The parameterization is closed, i.e., the cloud base mass fluxes are determined, as a function of the rate at which the cumulus consume convective available potential energy (CAPE). Since the large-scale temperature and moisture changes in both the cloud and sub-cloud layer are linearly proportional to the cloud base updraft mass flux (*e.g.* see eq. 4.2 – 4.5), the CAPE change due to convective activity can be written as

$$\left(\frac{\partial A}{\partial t}\right)_{cu} = -M_b F \ , \tag{4.41}$$

where $F$ is the CAPE consumption rate per unit cloud base mass flux. The closure condition is that the CAPE is consumed at an exponential rate by cumulus convection with characteristic adjustment time scale $\tau = 7200$ s:

$$M_b = \frac{A}{\tau F} \ . \tag{4.42}$$

### 4.1.4 Numerical Approximations

The quantities $M_{u,d}$, $\ell$, $S_{u,d}$, $q_{u,d}$, $h_{u,d}$ are defined on layer interfaces, while $D_u$, $C_u$, $R_u$ are defined on layer midpoints. $S$, $q$, $h$, $\gamma$ are required on both midpoints and interfaces and the interface values $\psi^{k\pm}$ are determined from the midpoint values $\psi^k$ as

$$\psi^{k-} = \log\left(\frac{\psi^{k-1}}{\psi^k}\right)\frac{\psi^{k-1}\psi^k}{\psi^{k-1}-\psi^k} \ . \tag{4.43}$$

All of the differencing within the deep convection is in height coordinates. The differences are naturally taken as

$$\frac{\partial \psi}{\partial z} = \frac{\psi^{k-}-\psi^{k+}}{z^{k-}-z^{k+}} \ , \tag{4.44}$$

where $\psi^{k-}$ and $\psi^{k+}$ represent values on the upper and lower interfaces, respectively for layer $k$. The convention elsewhere in this note (and elsewhere in the code) is $\delta^k\psi = \psi^{k+} - \psi^{k-}$. Therefore, we avoid using the compact $\delta^k$ notation, except for height, and define

$$d^k z \equiv z^{k-} - z^{k+} = -\delta^k z \ , \tag{4.45}$$

so that $d^k z$ corresponds to the variable dz(k) in the deep convection code.

Although differences are in height coordinates, the equations are cast in flux form and the tendencies are computed in units kg m$^{-3}$ s$^{-1}$. The expected units are recovered at the end by multiplying by $g\delta z/\delta p$.

The environmental profiles at midpoints are

$$\begin{aligned}
S^k &= c_p T^k + g z^k && (4.46)\\
h^k &= S^k + L q^k && (4.47)\\
h^{*k} &= S^k + L q^{*k} && (4.48)\\
q^{*k} &= \epsilon e^{*k}/(p^k - e^{*k}) && (4.49)\\
e^{*k} &= c_1 \exp\left[\frac{c_2(T^k - T_f)}{(T^k - T_f + c_3)}\right] && (4.50)\\
\gamma^k &= q^{*k}\left(1+\frac{q^{*k}}{\epsilon}\right)\frac{\epsilon L^2}{c_p R {T^k}^2} \ . && (4.51)
\end{aligned}$$

The environmental profiles at interfaces of $S$, $q$, $q^*$, and $\gamma$ are determined using (4.43) if $|\psi^{k-1} - \psi^k|$ is large enough. **However, there are inconsistencies in what happens if $|\psi^{k-1} - \psi^k|$ is not large enough**. For $S$ and $q$ the condition is

$$\psi^{k-} = (\psi^{k-1} + \psi^k)/2, \quad \frac{|\psi^{k-1} - \psi^k|}{\max(\psi^{k-1} - \psi^k)} \leq 10^{-6} \ . \tag{4.52}$$

For $q^*$ and $\gamma$ the condition is

$$\psi^{k-} = \psi^k, \quad |\psi^{k-1} - \psi^k| \leq 10^{-6} \ . \tag{4.53}$$

Interface values of $h$ are not needed and interface values of $h^*$ are given by

$$h^{*k-} \ = \ S^{k-} + Lq^{*k-} \ . \tag{4.54}$$

The unitless updraft mass flux (scaled by the inverse of the cloud base mass flux) is given by differencing (4.13) as

$$M_u^{k-} = \frac{1}{\lambda_0(z^{k-} - z_b)} \left( e^{\lambda_D^k (z^{k-} - z_b)} - 1 \right) \ , \tag{4.55}$$

with the boundary condition that $M_u^{M+} = 1$. The entrainment and detrainment are calculated using

$$\begin{aligned} m_u^{k-} &= \frac{1}{\lambda_0(z^{k-} - z_b)} \left( e^{\lambda_D^{k+1} (z^{k-} - z_b)} - 1 \right) && (4.56) \\ E_u^k &= \frac{m_u^{k-} - M_u^{k+}}{d^k z} && (4.57) \\ D_u^k &= \frac{m_u^{k-} - M_u^{k-}}{d^k z} \ . && (4.58) \end{aligned}$$

Note that $M_u^{k-}$ and $m_u^{k-}$ differ only by the value of $\lambda_D$.

The updraft moist static energy is determined by differencing (4.18)

$$\frac{M_u^{k-} h_u^{k-} - M_u^{k+} h_u^{k+}}{d^k z} = E_u^k h^k - D_u^k h^{*k} \tag{4.59}$$

$$h_u^{k-} = \frac{1}{M_u^{k-}} \left[ M_u^{k+} h_u^{k+} + d^k z \left( E_u^k h^k - D_u^k h^{*k} \right) \right] \ , \tag{4.60}$$

with $h_u^{M-} = h^M + c_p/2$, where $M$ is the layer of maximum $h$.

Once $h_u$ is determined, the lifting condensation level is found by differencing (4.16) and (4.17) similarly to (4.18):

$$\begin{aligned} S_u^{k-} &= \frac{1}{M_u^{k-}} \left[ M_u^{k+} S_u^{k+} + d^k z \left( E_u^k S^k - D_u^k S^k \right) \right] && (4.61) \\ q_u^{k-} &= \frac{1}{M_u^{k-}} \left[ M_u^{k+} q_u^{k+} + d^k z \left( E_u^k q^k - D_u^k q^{*k} \right) \right] \ . && (4.62) \end{aligned}$$

The detrainment of $S_u$ is given by $D_u^k S^k$ not by $D_u^k S_u^k$, since detrainment occurs at the environmental value of $S$. The detrainment of $q_u$ is given by $D_u^k q^{*k}$, even though the updraft is not yet saturated. The LCL will usually occur below $z_0$, the level at which detrainment begins, but this is not guaranteed.

The lower boundary conditions, $S_u^{M-} = S^M + c_p/2$ and $q_u^{M-} = q^M$, are determined from the first midpoint values in the plume, rather than from the interface values of $S$ and $q$. The solution of (4.61) and (4.62) continues upward until the updraft is saturated according to the condition

$$q_u^{k-} > q^*(T_u^{k-}), \tag{4.63}$$

$$T_u^{k-} = \frac{1}{c_p}\left(S_u^{k-} - gz^{k-}\right) \ . \tag{4.64}$$

The condensation (in units of m$^{-1}$) is determined by a centered differencing of (4.16):

$$\frac{M_u^{k-}S_u^{k-} - M_u^{k+}S_u^{k+}}{d^k z} = (E_u^k - D_u^k)S^k + LC_u^k \tag{4.65}$$

$$C_u^k = \frac{1}{L}\left[\frac{M_u^{k-}S_u^{k-} - M_u^{k+}S_u^{k+}}{d^k z} - (E_u^k - D_u^k)S^k\right] \ . \tag{4.66}$$

The rain production (in units of m$^{-1}$) and condensed liquid are then determined by differencing (4.19) as

$$\frac{M_u^{k-}\ell^{k-} - M_u^{k+}\ell^{k+}}{d^k z} = -D_u^k \ell^{k+} + C_u^k - R_u^k \ , \tag{4.67}$$

and (4.20) as

$$R_u^k = c_0 M_u^{k-}\ell^{k-} \ . \tag{4.68}$$

Then

$$M_u^{k-}\ell^{k-} = M_u^{k+}\ell^{k+} - d^k z\left(D_u^k \ell^{k+} - C_u^k + c_0 M_u^{k-}\ell^{k-}\right) \tag{4.69}$$

$$M_u^{k-}\ell^{k-}\left(1 + c_0 d^k z\right) = M_u^{k+}\ell^{k+} + d^k z\left(D_u^k \ell^{k+} - C_u^k\right) \tag{4.70}$$

$$\ell^{k-} = \frac{1}{M_u^{k-}\left(1 + c_0 d^k z\right)}\left[M_u^{k+}\ell^{k+} - d^k z\left(D_u^k \ell^{k+} - C_u^k\right)\right] \ . \tag{4.71}$$

### 4.1.5 Deep Convective Tracer Transport

The CAM 3.0 provides the ability to transport constituents via convection. The method used for constituent transport by deep convection is a modification of the formulation described in Zhang and McFarlane [1995].

We assume the updrafts and downdrafts are described by a steady state mass continuity equation for a "bulk" updraft or downdraft

$$\frac{\partial(M_x q_x)}{\partial p} = E_x q_e - D_x q_x \ . \tag{4.72}$$

The subscript $x$ is used to denote the updraft ($u$) or downdraft ($d$) quantity. $M_x$ here is the mass flux in units of Pa/s defined at the layer interfaces, $q_x$ is the mixing ratio of the updraft or downdraft. $q_e$ is the mixing ratio of the quantity in the environment (that part of the grid volume not occupied by the up and downdrafts). $E_x$ and $D_x$ are the entrainment and detrainment rates (units of $s^{-1}$) for the up- and down-drafts. Updrafts are allowed to entrain or detrain in any layer. Downdrafts are assumed to entrain only, and all of the mass is assumed to be deposited into the surface layer.

Equation 4.72 is first solved for up and downdraft mixing ratios $q_u$ and $q_d$, assuming the environmental mixing ratio $q_e$ is the same as the gridbox averaged mixing ratio $\bar{q}$.

Given the up- and down-draft mixing ratios, the mass continuity equation used to solve for the gridbox averaged mixing ratio $\bar{q}$ is

$$\frac{\partial \bar{q}}{\partial t} = \frac{\partial}{\partial p}(M_u(q_u - \bar{q}) + M_d(q_d - \bar{q})) \ . \tag{4.73}$$

These equations are solved for in subroutine `CONVTRAN`. There are a few numerical details employed in `CONVTRAN` that are worth mentioning here as well.

- mixing quantities needed at interfaces are calculated using the geometric mean of the layer mean values.
- simple first order upstream biased finite differences are used to solve 4.72 and 4.73.
- fluxes calculated at the interfaces are constrained so that the resulting mixing ratios are positive definite. *This means that this parameterization is not suitable for moving mixing ratios of quantities meant to represent perturbations of a trace constituent about a mean value* (in which case the quantity can meaningfully take on positive and negative mixing ratios). The algorithm can be modified in a straightforward fashion to remove this constraint, and provide meaningful transport of perturbation quantities if necessary. *the reader is warned however that there are other places in the model code where similar modifications are required because the model assumes that all mixing ratios should be positive definite quantities.*

## 4.2 Shallow/Middle Tropospheric Moist Convection

To characterize the convective forcing associated with shallow and middle-level convection (i.e., convective activity not treated by the primary convective parameterization scheme) we write the large-scale budget equations for dry static energy and total water as

$$\begin{aligned} \frac{\partial \overline{s}}{\partial t} &= -\nabla \cdot \overline{\boldsymbol{V}}\,\overline{s} - \frac{\partial \overline{\omega}\,\overline{s}}{\partial p} - \frac{\partial}{\partial p}\left(\overline{\omega' s'_\ell}\right) + L\mathcal{R} + c_p Q_R \\ &= \left.\frac{\partial \overline{s}}{\partial t}\right|_{R.S.} - \frac{\partial}{\partial p}\left(\overline{\omega' s'_\ell}\right) + L\mathcal{R} \end{aligned} \tag{4.74}$$

and

$$
\begin{aligned}
\frac{\partial \overline{q}}{\partial t} &= -\nabla \cdot \overline{\boldsymbol{V}}\,\overline{q} - \frac{\partial \overline{\omega}\,\overline{q}}{\partial p} - \frac{\partial}{\partial p}\left(\overline{\omega' - (q' + \ell')}\right) - \mathcal{R} \\
&= \left.\frac{\partial \overline{q}}{\partial t}\right|_{R.S.} - \frac{\partial}{\partial p}\left(\overline{\omega'\,(q' + \ell')}\right) - \mathcal{R}\ ,
\end{aligned}
\tag{4.75}
$$

where $s \equiv c_p T + gz$ is the dry static energy; $\ell$ represents liquid water; $s_\ell \equiv s - L\ell$ is the static energy analogue of the liquid water potential temperature introduced by Betts [1975]; $\mathcal{R}$ is the "convective-scale" liquid water sink (sometimes denoted by $C - E$); and $Q_R$ is the net radiative heating rate. The subscript $R.S.$ denotes the resolvable-scale contributions to the large-scale budget. Note that variations of the mean liquid water on the large scale have been neglected. The barred quantities represent horizontal averages over an area large enough to contain a collection of cloud elements, but small enough so as to cover only a fraction of a large-scale disturbance. By writing the mean thermodynamic variables in terms of their average cloud and environment properties, and assuming that the convection occupies only a small fraction of the averaging area, the vertical eddy transports $\overline{\omega' s'_\ell}$ and $\overline{\omega'\,(q' + \ell')}$ can be approximated by the difference between the upward flux inside a typical convective element and the downward flux (*i.e.* induced subsidence) in the environment (cf. Yanai et al. [1973]). Mathematically, this approximation takes the form

$$
F_{s_\ell}(p) = -\frac{1}{g}\left(\overline{\omega' s'_\ell}\right) \approx -M_c\,(p)\,(\overline{s}\,(p) - s_c\,(p) + L\ell\,(p))
\tag{4.76}
$$

and

$$
F_{q+\ell}(p) = -\frac{1}{g}\left(\overline{\omega'\,(q' + \ell')}\right) \approx -M_c\,(p)\,(\overline{q}\,(p) - q_c\,(p) - \ell\,(p))\ \ ,
\tag{4.77}
$$

where $M_c$ is a convective mass flux, and $s_c$, $q_c$, and $\ell$ represent cloud-scale properties. Thus, (4.74) and (4.75) can be written as

$$
\frac{\partial \overline{s}}{\partial t} = \left.\frac{\partial \overline{s}}{\partial t}\right|_{R.S.} + g\,\frac{\partial}{\partial p}\,F_{s_\ell} + L\mathcal{R}\ ,
\tag{4.78}
$$

and

$$
\frac{\partial \overline{q}}{\partial t} = \left.\frac{\partial \overline{q}}{\partial t}\right|_{R.S.} + g\frac{\partial}{\partial p}F_{q+\ell} - \mathcal{R}\ \ .
\tag{4.79}
$$

Let us now turn our attention to a vertically discrete model atmosphere and consider the case where layers $k$ and $k+1$ are moist adiabatically unstable, *i.e.* a non-entraining parcel of air at level $k+1$ (with moist static energy $h_c$) would be unstable if raised to level $k$. We assume the existence of a non-entraining convective element with roots in level $k+1$, condensation and rainout processes in level $k$, and limited detrainment in level $k-1$ (see Figure 4.1). In accordance with (4.78) and (4.79), the discrete dry static energy and specific humidity budget equations for these three layers can be written as

$$\hat{\bar{s}}_{k-1} = \bar{s}_{k-1} + \frac{2\Delta tg}{\Delta p_{k-1}} \left\{ \beta m_c \left( s_c - \bar{s}_{k-\frac{1}{2}} - L\ell_k \right) \right\} , \tag{4.80}$$

$$\hat{\bar{s}}_k = \bar{s}_k + \frac{2\Delta tg}{\Delta p_k} \left\{ m_c \left( s_c - \bar{s}_{k+\frac{1}{2}} \right) - \beta m_c \left( s_c - L\ell_k - \bar{s}_{k-\frac{1}{2}} \right) + LR_k \right\} , \tag{4.81}$$

$$\hat{\bar{s}}_{k+1} = \bar{s}_{k+1} + \frac{2\Delta tg}{\Delta p_{k+1}} \left\{ m_c \left( \bar{s}_{k+\frac{1}{2}} - s_c \right) \right\} , \tag{4.82}$$

$$\hat{\bar{q}}_{k-1} = \bar{q}_{k-1} + \frac{2\Delta tg}{\Delta p_{k-1}} \left\{ \beta m_c \left( q_c - \bar{q}_{k-\frac{1}{2}} \right) \right\} , \tag{4.83}$$

$$\hat{\bar{q}}_k = \bar{q}_k + \frac{2\Delta tg}{\Delta p_k} \left\{ m_c \left( q_c - \bar{q}_{k+\frac{1}{2}} \right) - \beta m_c \left( q_c - \bar{q}_{k-\frac{1}{2}} - \right) R_k \right\} , \tag{4.84}$$

$$\hat{\bar{q}}_{k+1} = \bar{q}_{k+1} + \frac{2\Delta tg}{\Delta p_{k+1}} \left\{ m_c \left( \bar{q}_{k+\frac{1}{2}} - q_c \right) \right\} , \tag{4.85}$$

where the subscript $c$ denotes cloud properties in the ascent region, $m_c$ is a convective mass flux at the bottom of the condensation layer (level $k + \frac{1}{2}$, "cloud base"), and $\beta$ is a yet to be determined "detrainment parameter" at level $k - \frac{1}{2}$ that will take a value between zero and one. Note that the convective-scale liquid water sink $\mathcal{R}$ has been redefined in terms of mass per unit area per unit time (denoted by $R$), and the resolvable-scale components have been dropped for the convenience of the following discussion. In the general case, the thermodynamic properties of the updraft region can be assumed to be equal to their large-scale values in the sub-cloud layer, level $k + 1$, plus some arbitrary thermodynamic perturbation; *i.e.*

$$s_c = \bar{s}_{k+1} + s', \tag{4.86}$$

$$q_c = \bar{q}_{k+1} + q', \tag{4.87}$$

and

$$h_c = s_c + Lq_c \; . \tag{4.88}$$

In the CAM 3.0 implementation of this scheme, when a sub-cloud layer lies within the diagnosed atmospheric boundary layer, the perturbation quantities $q'$ and $s'$ are assumed to be equal to $b \, \frac{\overline{(w'q')}_s}{w_m}$ (*e.g.* see 4.470 and the atmospheric boundary layer discussion) and zero.
The liquid water generation rate at level $k$ is given by

$$m_c \ell_k = m_c \left[ q_c - (q_c)_k \right] . \tag{4.89}$$

Using the saturation relation

$$(q_c)_k = \bar{q}_k^* + \frac{\gamma_k}{1 + \gamma_k} \, \frac{1}{L} \left( h_c - \bar{h}_k^* \right) , \tag{4.90}$$

where $\bar{q}^*$ denotes the saturated specific humidity

$$\bar{q}^* = \epsilon \, \frac{e_s}{p - (1 - \epsilon) e_s} , \tag{4.91}$$

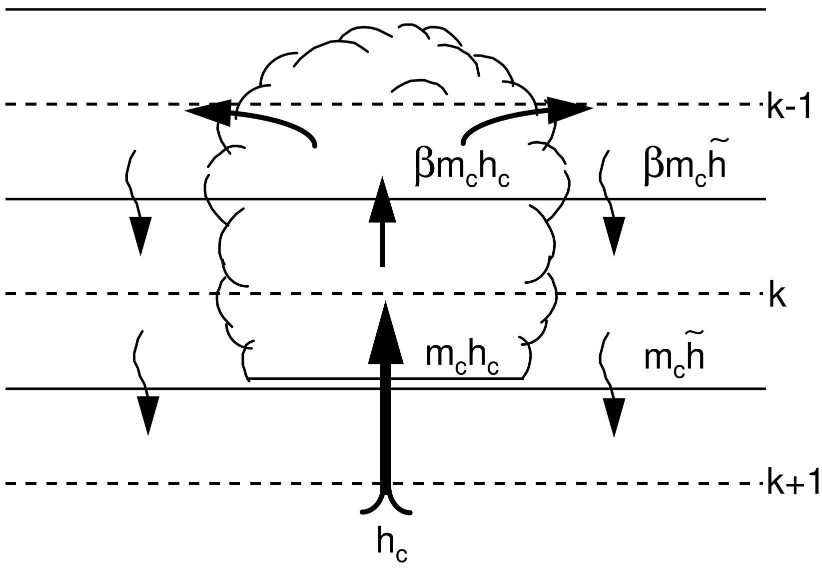


Figure 4.1: Conceptual three-level non-entraining cloud model

$h^*$ denotes the saturated moist state energy, $e_s$ is the saturation vapor pressure (determined from a precomputed table), and $\gamma \equiv (L/c_p)(\partial\overline{q}^*/\partial\overline{T})_p$, and assuming that the large-scale liquid water divergence in layer $k$ is zero, (4.89) can be manipulated to give the rainout term in layer $k$ as

$$LR_k \equiv L(1-\beta)m_c\ell_k = (1-\beta)m_c \left\{\overline{s}_k - s_c + \frac{1}{1+\gamma_{_k}}\left(h_c - \overline{h}^*_k\right)\right\}, \tag{4.92}$$

and the liquid water flux into layer $k-1$ as

$$\beta m_c L\ell_k = \beta m_c \left\{\overline{s}_k - s_c + \frac{1}{1+\gamma_{_k}}\left(h_c - \overline{h}^*_k\right)\right\}. \tag{4.93}$$

Equations (4.82) and (4.85) can be combined to give an equation for moist static energy in layer $k+1$

$$\frac{\partial\overline{h}_{k+1}}{\partial t} = \frac{g}{\Delta p_{k+1}} m_c \left(\overline{h}_{k+\frac{1}{2}} - h_c\right) \approx \frac{\partial h_c}{\partial t}, \tag{4.94}$$

where the approximation follows from the assumption that $\partial h'/\partial t$ can be neglected. Using the relation $(1+\gamma_{_k})\frac{\partial\overline{s}_k}{\partial t} = \partial\overline{h}^*_k\partial t$, (4.81) can be manipulated to give an expression for the time rate of change of saturated moist static energy in layer $k$

$$\frac{\partial\overline{h}^*_k}{\partial t} = \frac{gm_c}{\Delta p_k}(1+\gamma_{_k})\left\{\left(s_c - \overline{s}_{k+\frac{1}{2}} + L\ell_k\right) - \beta\left(s_c - \overline{s}_{k-\frac{1}{2}}\right)\right\}. \tag{4.95}$$

Subtracting (4.95) from (4.94) results in

$$\begin{aligned}\frac{\partial\left(h_c - \overline{h}^*_k\right)}{\partial t} \quad = \quad & m_c\Big\{\frac{g}{\Delta p_{k+1}}\left(\overline{h}_{k+\frac{1}{2}} - h_c\right) \\ & -\frac{g}{\Delta p_k}(1+\gamma_{_k})\left[\left(\overline{s}_k - \overline{s}_{k+\frac{1}{2}}\right) - \beta\left(s_c - \overline{s}_{k-\frac{1}{2}}\right)\right]\Big\},\end{aligned} \tag{4.96}$$

from which the convective mass flux $m_c$ can be written as

$$m_c = \frac{h_c - \overline{h}_k^*}{g\tau \left\{ \frac{(1+\gamma_k)}{\Delta p_k} \left[ \left( s_c - \overline{s}_{k+\frac{1}{2}} + L\ell_k \right) - \beta \left( s_c - \overline{s}_{k-\frac{1}{2}} \right) \right] - \frac{1}{\Delta p_{k+1}} \left[ \overline{h}_{k+\frac{1}{2}} - h_c \right] \right\}} \tag{4.97}$$

where $\tau$ is a characteristic convective adjustment time scale.

Physically realistic solutions require that the convective mass flux $m_c$ be positive, implying the following constraint on the detrainment parameter $\beta$

$$\beta\,(1+\gamma_k)\left(s_c - \overline{s}_{k-\frac{1}{2}}\right) < (1+\gamma_k)\left(s_c - \overline{s}_{k+\frac{1}{2}} + L\ell_k\right) - \frac{\Delta p_k}{\Delta p_{k+1}}\left(\overline{h}_{k+\frac{1}{2}} - h_c\right)\ . \tag{4.98}$$

A second physical constraint is imposed to ensure that the adjustment process does not supersaturate the "detrainment layer", $k-1$, which leads to the following constraint on the detrainment parameter, $\beta$:

$$\begin{aligned}
&\frac{1}{\Delta p_k}\Big[ (1+\gamma_k)\left(s_c - \overline{s}_{k+\frac{1}{2}} + L\ell_k\right)\Big] - \frac{1}{\Delta p_{k+1}}\left[\overline{h}_{k+\frac{1}{2}} - h_c\right] > \\
&\beta \Bigg\{ \left(\frac{2\Delta t}{\tau}\right) \frac{h_c - \overline{h}_k^*}{\left(\overline{h}_{k-1}^* - \overline{h}_{k-1}\right)\Delta p_{k-1}} \Bigg[ \gamma_{k-1} \left\{ \overline{s}_{k-\frac{1}{2}} - s_c + L\ell_k \right\} \\
&\qquad + h_c - \overline{h}_{k-\frac{1}{2}} - s_c + \overline{s}_{k-\frac{1}{2}} \Bigg] + \frac{1}{\Delta p_k}(1+\gamma_k)\left(s_c - \overline{s}_{k-\frac{1}{2}}\right) \Bigg\}.
\end{aligned} \tag{4.99}$$

A final constraint on the adjustment process attempts to minimize the introduction of $2\Delta\eta$ computational structures in the thermodynamic field by not allowing the procedure to increase the vertical gradient of $h$ when $\frac{\partial h}{\partial p} < 0$ in the upper pair of layers. Mathematically this constraint is formulated by discretizing in time the moist static energy equations in layers $k$ and $k-1$, leading to the following constraint on $\beta$

$$\begin{aligned}
&\frac{\overline{h}_k - \overline{h}_{k-1} - G}{(h_c - \overline{h}_k^*)}\left(\frac{\tau}{2\Delta t}\right)\left(\frac{1}{\Delta p_h}\left[(1+\gamma_k)(s_c - \overline{s}_{k+\frac{1}{2}} + L\ell_k)\right] - \frac{1}{\Delta p_{k+\frac{1}{2}}}\left[\overline{h}_{k+\frac{1}{2}} - h_c\right]\right) \\
&\qquad + \frac{1}{\Delta p_k}\left[h_c - \overline{h}_{k+\frac{1}{2}}\right] \geq \beta \Bigg\{ \frac{\overline{h}_k - \overline{h}_{k-1} - G}{h_c - \overline{h}_k^*}\left(\frac{\tau}{2\Delta t}\right)\left(\frac{1+\gamma_k}{\Delta p_k}\right)\left(s_c - \overline{s}_{k-\frac{1}{2}}\right) \\
&\qquad\qquad + \left(h_c - \overline{h}_{k-\frac{1}{2}} - L\ell_k\right)\left(\frac{1}{\Delta p_k} + \frac{1}{\Delta p_{k+1}}\right) \Bigg\}\ .
\end{aligned} \tag{4.100}$$

where $G$ is an arbitrary vertical difference in the adjusted moist static energy profile (cf. Hack et al. [1993]).

The first guess for the detrainment parameter, $\beta$, comes from a crude buoyancy argument where

$$\beta = \max \begin{cases} \beta_{\min} \\ \min \begin{cases} \beta_{\max} \\ 1 + \frac{(h_c - \overline{h}_{k-1}^*)\Delta p_{k-1}}{(h_c - \overline{h}_k^*)\Delta p_k} \end{cases} \end{cases} \tag{4.101}$$

and $\beta_{\min}$ is assumed to be 0.10 (i.e., 10% detrainment). Since $\beta$ effectively determines the actual autoconversion from cloud water to rainwater, $\beta_{\max}$ is determined from a minimum autoconversion requirement which is mathematically written as

$$\beta_{\max} = \max \begin{cases} \beta_{\min} \\ 1 - c_0(\delta z - \delta z_{\min}) \end{cases} \tag{4.102}$$

where $c_0$ is a constant autoconversion coefficient assumed to be equal to $1.0\times10^{-4}$ m$^{-1}$, $\delta z$ is the depth of contiguous convective activity (*i.e.* layers in which condensation and rainout takes place) including and below layer $k$, and $\delta z_{\min}$ is a minimum depth for precipitating convection. The physical constraints on the adjustment process are then applied to determine the actual value of $\beta$ appropriate to the stabilization of levels $k$ and $k+1$.

In summary, the adjustment procedure is applied as follows. A first guess at $\beta$ is determined from (4.101) and (4.102), and further refined using (4.98), (4.99), and (4.100). The convective mass flux, $m_c$, is then determined from (4.97), followed by application of budget equations (4.80)-(4.85) to complete the thermodynamic adjustment in layers $k-1$ through $k+1$. By repeated application of this procedure from the bottom of the model to the top, the thermodynamic structure is locally stabilized, and a vertical profile of the total cloud mass flux associated with shallow and mid-level convection, $M_c$ (where $M_{c_{k+\frac{1}{2}}} = m_{c_{k+\frac{1}{2}}} + \beta\, m_{c_{k+\frac{3}{2}}}$) can be constructed. This mass flux profile can also be used to estimate the convective-scale transport of arbitrary passive scalars. The production rate of convective precipitation $R_k$ is supplied to the parameterization of evaporation of convective precipitation described in section 4.3. The free parameters for the convection scheme consist of a minimum convective detrainment, $\beta_{\min}$, a characteristic adjustment time scale for the convection, $\tau$, a cloud-water to rain-water autoconversion coefficient $c_0$, and a minimum depth for precipitating convection $\delta z_{\min}$.

## 4.3 Evaporation of convective precipitation

The CAM 3.0 employs a Sundqvist [1988] style evaporation of the convective precipitation as it makes its way to the surface. This scheme relates the rate at which raindrops evaporate to the local large-scale subsaturation, and the rate at which convective rainwater is made available to the subsaturated model layer

$$E_{r_k} = K_E \, (1 - \mathrm{RH}_k) \, (\hat{R}_{r_k})^{1/2} \; . \tag{4.103}$$

where $\mathrm{RH}_k$ is the relative humidity at level $k$, $\hat{R}_{r_k}$ denotes the total rainwater flux at level $k$ (which can be different from the locally diagnosed rainwater flux from the convective parameterization, as will be shown below), the coefficient $K_E$ takes the value $0.2 \cdot 10^{-5}$ (kg m$^{-2}$ s$^{-1}$)$^{-1/2}$s$^{-1}$, and the variable $E_{r_k}$ has units of s$^{-1}$. The evaporation rate $E_{r_k}$ is used to determine a local change in $q_k$ and $T_k$, associated with an evaporative reduction of $\hat{R}_{r_k}$. Conceptually, the evaporation process is invoked after a vertical profile of $R_{r_k}$ has been evaluated. An evaporation rate is then computed for the uppermost level of the model for which $R_{r_k} \neq 0$ using (4.103), where in this case $R_{r_k} \equiv \hat{R}_{r_k}$. This rate is used to evaluate an evaporative reduction in $R_{r_k}$

which is then accumulated with the previously diagnosed rainwater flux in the layer below,

$$\hat{R}_{r_{k+1}} = \hat{R}_{r_k} - \left(\frac{\Delta p_k}{g}\right)\ E_{r_k} + R_{r_{k+1}}\ . \tag{4.104}$$

A local increase in the specific humidity $q_k$ and a local reduction of $T_k$ are also calculated in accordance with the net evaporation

$$q_k = q_k + E_{r_k}\ 2\Delta t\ \ , \tag{4.105}$$

and

$$T_k = T_k - \left(\frac{L}{c_p}\right) E_{r_k}\ 2\Delta t\ \ . \tag{4.106}$$

The procedure, (4.103)-(4.106), is then successively repeated for each model level in a downward direction where the final convective precipitation rate is that portion of the condensed rainwater in the column to survive the evaporation process

$$P_s = \left(\hat{R}_{r_K} - \left(\frac{\Delta p_K}{g}\right)\ E_{r_K}\right)/\rho_{H_20}\ . \tag{4.107}$$

In global annually averaged terms, this evaporation procedure produces a very small reduction in the convective precipitation rate where the evaporated condensate acts to moisten the middle and lower troposphere.

## 4.4 Conversion to and from dry and wet mixing ratios for trace constituents in the model

There are trade offs in the various options for the representation of trace constituents $\chi$ in any general circulation model:

1. When the air mass in a model layer is defined to include the water vapor, it is frequently convenient to represent the quantity of trace constituent as a “moist” mixing ratio $\chi^m$, that is, the mass of tracer per mass of moist air in the layer. The advantage of the representation is that one need only multiply the moist mixing ratio by the moist air mass to determine the tracer air mass. It has the disadvantage of implicitly requiring a change in $\chi^m$ whenever the water vapor $q$ changes within the layer, even if the mass of the trace constituent does not.

2. One can also utilize a “dry” mixing ratio $\chi^d$ to define the amount of constituent in a volume of air. This variable does not have the implicit dependence on water vapor, but does require that the mass of water vapor be factored out of the air mass itself in order to calculate the mass of tracer in a cell.

NCAR atmospheric models have historically used a combination of dry and moist mixing ratios. Physical parameterizations (including convective transport) have utilized moist mixing ratios. The resolved scale transport performed in the Eulerian (spectral), and semi-Lagrangian dynamics use dry mixing ratios, specifically to prevent oscillations associated with variations in water vapor requiring changes in tracer mixing ratios. The finite volume dynamics module utilizes moist mixing ratios, with an attempt to maintain internal consistency between transport of water vapor and other constituents.

There is no "right" way to resolve the requirements associated with the simultaneous treatment of water vapor, air mass in a layer and tracer mixing ratios. But the historical treatment significantly complicates the interpretation of model simulations, and in the latest version of CAM we have also provided an "alternate" representation. That is, we allow the user to specify whether any given trace constituent is interpreted as a "dry" or "wet" mixing ratio through the specification of an "attribute" to the constituent in the physics state structure. The details of the specification are described in the users manual, but we do identify the interaction between state quantities here.

At the end of the dynamics update to the model state, the surface pressure, specific humidity, and tracer mixing ratios are returned to the model. The physics update then is allowed to update specific humidity and tracer mixing ratios through a sequence of operator splitting updates *but the surface pressure is not allowed to evolve.* Because there is an explicit relationship between the surface pressure and the air mass within each layer we assume that water mass can change within the layer by physical parameterizations *but dry air mass cannot.* We have chosen to define the dry air mass in each layer at the beginning of the physics update as

$$\delta p^d_{i,k} = (1 - q^0_{i,k})\delta^m_{i,k}$$

for column $i$, level $k$. Note that the specific humidity used is the value defined at the beginning of the physics update. We define the transformation between dry and wet mixing ratios to be

$$\chi^d_{i,k} = (\delta p^d_{i,k}/\delta p^m_{i,k})\chi^m_{i,k}$$

We note that the various physical parameterizations that operate on tracers on the model (convection, turbulent transport, scavenging, chemistry) will require a specification of the air mass within each cell as well as the value of the mixing ratio in the cell. We have modified the model so that it will use the correct value of $\delta p$ depending on the attribute of the tracer, that is, we use couplets of $(\chi^m, \delta p^m)$ or $(\chi^d, \delta p^d)$ in order to assure that the process conserves mass appropriately.

We note further that there are a number of parameterizations (*e.g.* convection, vertical diffusion) that transport species using a continuity equation in a flux form that can be written generically as

$$\frac{\partial \chi}{\partial t} = \frac{\partial F(\chi)}{\partial p} \tag{4.108}$$

where $F$ indicates a flux of $\chi$. For example, in convective transports $F(\chi)$ might correspond to $M_u\chi$ where $M_u$ is an updraft mass flux. In principle one should adjust $M_u$ to reflect the fact that it may be moving a mass of dry air or a mass of moist air. We assume these differences are small, and well below the errors required to produce equation 4.108 in the first place. The same is true for the diffusion coefficients involved in turbulent transport. All processes using equations of such a form still satisfy a conservation relationship

$$\frac{\partial}{\partial t}\sum_k \chi_k \delta p_k = F_{kbot} - F_{ktop}$$

provided the appropriate $\delta p$ is used in the summation.

## 4.5 Prognostic Condensate and Precipitation Parameterization

### 4.5.1 Introductory comments

The parameterization of non-convective cloud processes in CAM 3.0 is described in Rasch and Kristjánsson [1998] and Zhang et al. [2003]. The original formulation is introduced in Rasch and Kristjánsson [1998]. Revisions to the parameterization to deal more realistically with the treatment of the condensation and evaporation under forcing by large scale processes and changing cloud fraction are described in Zhang et al. [2003]. The equations used in the formulation are discussed here. The papers contain a more thorough description of the formulation and a discussion of the impact on the model simulation.

The formulation for cloud condensate combines a representation for condensation and evaporation with a bulk microphysical parameterization closer to that used in cloud resolving models. The parameterization replaces the diagnosed liquid water path of CCM3 with evolution equations for two additional predicted variables: liquid and ice phase condensate. At one point during each time step, these are combined into a total condensate and partitioned according to temperature (as described in section 4.5.3), but elsewhere function as independent quantities. They are affected by both resolved (*e.g.* advective) and unresolved (*e.g.* convective, turbulent) processes. Condensate can evaporate back into the environment or be converted to a precipitating form depending upon its in-cloud value and the forcing by other atmospheric processes. The precipitate may be a mixture of rain and snow, and is treated in diagnostic form, *i.e.* its time derivative has been neglected.

The parameterization calculates the condensation rate more consistently with the change in fractional cloudiness and in-cloud condensate than the previous CCM3 formulation. Changes in water vapor and heat in a grid volume are treated consistently with changes to cloud fraction and in-cloud condensate. Condensate can form prior to the onset of grid-box saturation and can require a significant length of time to convert (via the cloud microphysics) to a precipitable form. Thus a substantially wider range of variation in condensate amount than in the CCM3 is possible.

The new parameterization adds significantly to the flexibility in the model and to the range of scientific problems that can be studied. This type of scheme is needed for quantitative treatment of scavenging of atmospheric trace constituents and cloud aqueous and surface chemistry. The addition of a more realistic condensate parameterization closely links the radiative properties of the clouds and their formation and dissipation. These processes must be treated for many problems of interest today (e.g. anthropogenic aerosol-climate interactions).

The parameterization has two components: 1) a macroscale component that describes the exchange of water substance between the condensate and the vapor phase and the associated temperature change arising from that phase change Zhang et al. [2003]; and 2) a bulk microphysical component that controls the conversion from condensate to precipitate [Rasch and Kristjánsson, 1998]. These components are discussed in the following two sections.

### 4.5.2 Description of the macroscale component

As in Sundqvist [1988] and Rasch and Kristjánsson [1998], the controlling equations for the water vapor mixing ratio, temperature, and total cloud condensate are written as

$$\frac{\partial q}{\partial t} = A_q - Q + E_r \tag{4.109}$$

$$\frac{\partial T}{\partial t} = A_T + \frac{L}{c_p}(Q - E_r) \tag{4.110}$$

$$\frac{\partial l}{\partial t} = A_l + Q - R_l \ , \tag{4.111}$$

where $A_q$, $A_T$, and $A_l$ are tendencies of water vapor, temperature, and cloud water from processes other than large-scale condensation and evaporation of cloud and rain water. $A_q$, $A_T$ and $A_l$ include advective, expansive, radiative, turbulent, and convective tendencies. The convective tendencies include evaporation of convective cloud and convective precipitation. For simplicity, all these processes are collectively called advective tendencies. They are assumed to be uniform across the whole model grid cell, although this assumption can be relaxed as discussed in Zhang et al. [2003]. $Q$ is the grid-averaged net stratiform condensation of cloud meteors (condensation minus evaporation). $E_r$ is the grid-averaged evaporative rate of rain and snow. $R_l$ is the conversion rate of cloud water to rain and snow. This section is devoted to the determination of the term $Q$ in equations (4.109)–(4.111).

The controlling equation of relative humidity $U$, when written on a pressure surface, can be derived from (4.109) and (4.110) as

$$\frac{\partial U}{\partial t} = \alpha\frac{\partial q}{\partial t} - \beta\frac{\partial T}{\partial t} \tag{4.112}$$

$$= \alpha A_q - \beta A_T - \gamma(Q - E_r) \tag{4.113}$$

where

$$\alpha = \frac{1}{q_s}, \tag{4.114}$$

$$\beta = \frac{q}{q_s^2}\frac{\partial q_s}{\partial T}, \tag{4.115}$$

$$\gamma = \alpha + \frac{L}{c_p}\beta \ . \tag{4.116}$$

Note that $\alpha$, $\beta$, and $\gamma$ are all positive. They can be viewed as the efficiencies of moisture advection, cold advection, and net evaporation in changing the relative humidity $U$. Changing $U$ can alter the fractional cloud cover. As in Sundqvist [1988] and Rasch and Kristjánsson [1998], ice saturation is not separately considered here; rather, it is approximated by a weighted average $q_s(T)$ of the saturation mixing ratios over ice and water. The dependence of $q_s$ on pressure is not made explicit since pressure enters into the calculation only as a parameter.

Equations (4.109)–(4.113) are applicable on both the grid scale and sub-grid scale as long as $Q$, $E_r$, and $R_l$ are appropriately defined. In the following, a hat denotes variables in the cloudy portion of a grid box to distinguish them from variables of the whole grid box, and $\mathcal{C}$

denotes the fractional cloud coverage. For the portion of the grid box that is cloudy before and after the calculation of fractional condensation (i.e., the cloudy area that does not experience clear-cloudy conversion), equation (4.113) becomes

$$\alpha \hat{A}_q - \hat{\beta}\hat{A}_T - \hat{\gamma}\hat{Q} = 0.$$

This follows from the assumption that $E_r = 0$ and $U = 1$ in the saturated cloud interior. Thus the condensation rate in this portion of the grid box is

$$\hat{Q} = \frac{\alpha \hat{A}_q - \hat{\beta}\hat{A}_T}{\hat{\gamma}} \tag{4.117}$$

and the in-cloud condensate equation becomes

$$\frac{\partial \hat{l}}{\partial t} = \hat{A}_l + \frac{\alpha \hat{A}_q - \hat{\beta}\hat{A}_T}{\hat{\gamma}} - \hat{R}_l. \tag{4.118}$$

Since the total cloud water can be written as $l = \mathcal{C}\hat{l}$, it follows that

$$\frac{\partial l}{\partial t} = \mathcal{C}\frac{\partial \hat{l}}{\partial t} + \hat{l}^* \frac{\partial \mathcal{C}}{\partial t} \tag{4.119}$$

The symbol $\hat{l}^*$ denotes the mean cloud condensate of the newly formed or dissipated clouds within a time step. The first term on the right hand side of the above equation represents the evolution of cloud water within existing clouds, and the second term represents the change in cloud water associated with expansion and contraction of cloud boundaries. Theoretically, newly formed or dissipated clouds should have zero cloud water content, except for detrained cloud from cumulus. However, because of the finite time step in the integration of the cloud water equation, the second term may be nonzero. Rasch and Kristjánsson [1998] set $\hat{l}^* = \hat{l}$, and the same closure is used in CAM 3.0. Inserting (4.118) and the relations $R_l = \mathcal{C}\hat{R}_l$ as well as $A_T = \hat{A}_T$, $A_q = \hat{A}_q$, and $A_l = \hat{A}_l$ into (4.111) yields:

$$\hat{l}^* \frac{\partial \mathcal{C}}{\partial t} = (1 - \mathcal{C})A_l + Q - \mathcal{C}(\frac{\alpha A_q - \hat{\beta}A_T}{\hat{\gamma}}) \tag{4.120}$$

This equation states that the condensation rate is linked with fractional cloudiness change as required by the total water budget. Equation (4.120) is not integrated in the present formulation. Instead, it is used to calculate the condensation rate as follows.

The fractional cloud cover and grid-scale relative humidity are related by

$$\mathcal{C} = \mathcal{C}(U, b) \tag{4.121}$$

where $b$ denotes a generic variable describing vertical stability, local Richardson number, cumulus mass flux, etc. The term $b$ varies with space and time. This equation is assumed to be valid when the relative humidity $U$ is larger than a threshold value $U_{00}$, which is the minimum grid-scale relative humidity at which clouds are present.

Taking partial derivatives of the equation (4.121) with respect to time gives

$$\frac{\partial \mathcal{C}}{\partial t} = \frac{\partial \mathcal{C}}{\partial U}\frac{\partial U}{\partial t} + \frac{\partial \mathcal{C}}{\partial b}\frac{\partial b}{\partial t}$$

With the definitions

$$F_a = \frac{\partial \mathcal{C}}{\partial U} \tag{4.122}$$

and

$$F_b = [(\frac{\partial \mathcal{C}}{\partial b})/(\frac{\partial \mathcal{C}}{\partial U})]\frac{\partial b}{\partial t} \ , \tag{4.123}$$

the time derivative of cloud amount becomes

$$F_a^{-1}\frac{\partial \mathcal{C}}{\partial t} = \frac{\partial U}{\partial t} + F_b \tag{4.124}$$

It is assumed that $F_a$ and $F_b$ can be calculated without the knowledge of the condensation rate. Substituting the relative humidity equation (4.113) into equation (4.124) yields

$$F_a^{-1}\frac{\partial \mathcal{C}}{\partial t} = \alpha A_q - \beta A_T - \gamma(Q - E_r) + F_b \tag{4.125}$$

Eliminating $\partial\mathcal{C}/\partial t$ between (4.120) and (4.125) gives

$$Q = c_q A_q - c_T A_T - c_l A_l + c_r E_r + \sigma \hat{l}^* F_b \tag{4.126}$$

with

$$c_q = \frac{\alpha}{\hat{\gamma}}\mathcal{C} + \left(1 - \frac{\gamma}{\hat{\gamma}}\mathcal{C}\right)\sigma\alpha\hat{l}^* \tag{4.127}$$

$$c_T = \frac{\hat{\beta}}{\hat{\gamma}}\mathcal{C} + \left(1 - \frac{\gamma}{\hat{\gamma}}\frac{\hat{\beta}}{\beta}\mathcal{C}\right)\sigma\beta\hat{l}^* \tag{4.128}$$

$$c_l = (1 - \mathcal{C})\,\sigma F_a^{-1} \tag{4.129}$$

$$c_r = \sigma\gamma\hat{l}^* \tag{4.130}$$

where

$$\sigma = \frac{1}{F_a^{-1} + \gamma\hat{l}^*} \ . \tag{4.131}$$

All coefficient variables are positive, and all are non-dimensional except for $C_T$ and $\beta$ which have units of 1/K. Equation (4.126) is valid when $U \geq U_{00}$. The terms in the equation have the following physical interpretation. Moist advection (positive $A_q$) and cold advection (negative $A_T$) produce condensation. Evaporation of rain/snow water (positive $E_r$) also produces cloud condensation because it changes the mean relative humidity, thus increasing cloud amount and cloud water. Import of cloud water (positive $A_l$) leads to evaporation. The reason is that it increases cloud fraction, thus requiring a higher clear-sky relative humidity which has to be generated by evaporation. The increase of cloud fraction from a non-water source through $F_b$, however, requires condensation.

To evaluate $F_a$, the cloud routine is called twice each time step with relative humidity perturbed by one percent (indicated by a $*$ superscript) while holding all other variables in the model fixed. Thus,

$$F_a \approx \frac{\Delta\mathcal{C}}{\Delta U} = \frac{\mathcal{C}^* - \mathcal{C}}{U^* - U}.$$

In this implementation, all $b$ variables are assumed fixed in the stratiform condensation calculation, and therefore $F_b = 0$. Since a top-hat distribution is adopted for the cloud water distribution, $\hat{l}^* = \hat{l}$.

The effects of convection on cloud cover are introduced through the convective tendencies. Detrainment of cloud water from the Zhang and McFarlane [1995] convection scheme is used as input in the calculation of $A_l$, $A_T$ and $A_q$. In the original version of the Zhang and McFarlane [1995] parameterization, the detrained cloud water from convection was assumed to evaporate.

The calculation is carried out by categorizing each model grid into one of four cases:

- If $U = 1$, $Q$ is calculated from (4.117);
- if $1 > U \geq U_{00}$, $Q$ calculated from (4.126);
- if $U < U_{00}$ but $l > 0$, $Q = -l$; and
- if $U < U_{00}$ and $l = 0$, $Q = 0$.

The use of the threshold relative humidity follows from equation (4.121).

### 4.5.3 Description of the microscale component

The condensation process has been determined by forcing terms and closure assumptions described in the previous subsection rather than an approach in which a supersaturation is calculated and CCN can nucleate and grow. Therefore the whole microphysical calculation reduces to modeling the process of conversion of cloud condensate to precipitation. The microscale component of the parameterization determines the evaporation $E_R$ and conversion of condensate to precipitate $R_l$.

The formulation follows closely the bulk microphysical formulations used in smaller scale cloud resolving models rather than those of Sundqvist [1988]. A method based upon cloud resolving models makes an explicit connection between the formation of precipitate and individual physical quantities like droplet or crystal number, shape of size distribution of precipitate, etc. It also separates the various processes contributing to precipitation more strongly, and makes diagnosis more straightforward. Because these quantities must represent an ensemble of cloud types in any given region (or grid volume) the new formulation still involves gross approximations, but it is much easier to control the parameterizations and understand their individual impact when the processes are isolated from each other.

As in Sundqvist [1988], the parameterization is expressed in terms of a single predicted variable representing total suspended condensate. Within the parameterization, however, there are four types of condensate expressed as mixing ratios: a liquid and ice phase for suspended condensate with minimal fall speed ($q_l$ and $q_i$) and a liquid and ice phase for falling condensate, i.e. precipitation ($q_r$ and $q_s$). Currently, only the suspended condensates ($q_l$ and $q_i$) are integrated in time; the other quantities are diagnosed as described below.

Before beginning the microphysical calculation, the total condensate is decomposed into liquid and ice phases assuming the fraction of ice is

$$f_i = \frac{T - T_{max}}{T_{min} - T_{max}}, \quad T_{min} \leq T \leq T_{max} \tag{4.132}$$

with $f_i(T < T_{min}) = 1$ and $f_i(T > T_{max}) = 0$. $T$ is the grid volume temperature. The bounds are adjustable constants with current settings $T_{min} = -40°$ C and $T_{max} = -10°$ C. Observations and more detailed microphysical models show a broad range of ratios of liquid to ice in clouds, and it is difficult to be certain of an appropriate range for this parameter.

Liquid and ice mass mixing ratios ($\ell$ and $I$) are independently advected, diffused, and transported by convection. The detrained liquid from the ZM convection is all added to the cloud liquid, since the ZM scheme does not have an ice phase. After the convection and sedimentation (see below), the liquid and ice are recalculated from the total cloud condensate

$$\ell_{n\prime} = (\ell_n + I_n)(1 - f_i) \tag{4.133}$$

$$I_{n\prime} = (\ell_n + I_n)f_i \ . \tag{4.134}$$

The heating due to the change in cloud ice is

$$Q^k = L_f \frac{I_n - I_{n\prime}}{\delta t}. \tag{4.135}$$

The stratiform cloud condensate tendency is computed and partitioned according to $f_i$. The excess heating due to cloud ice production instead of cloud liquid production is included with the evaporation and freezing of precipitation below.

The *in-cloud* liquid water mixing ratio is

$$\hat{q}_l = (1 - f_i)q_c/\mathcal{C} \tag{4.136}$$

and the *in-cloud* ice water mixing ratio is assumed to be

$$\hat{q}_i = (f_i)q_c/\mathcal{C}. \tag{4.137}$$

The grid volume mean quantities have been converted to in-cloud quantities by dividing the mean mixing ratios by the cloud fraction.

The evaporation of precipitation is computed for each source of precipitation using the same expressions, following Sundqvist [1988]. The precipitate falling from above can be a mixture of snow and rain. The flux of total precipitation $F^{k+}$ on each interface is

$$F^{k+} = F^{k-} + \frac{\delta^k p}{g}(P^k - E^k) \tag{4.138}$$

where $P^k$ and $E^k$ are precipitation production and evaporation, respectively. $P^k$ is determined by the convection or stratiform microphysics routines and

$$E^k = k_e(1 - c^k)\left(1 - \min(1, \frac{q^k}{q^k_*})\right)(F^{k-})^{1/2} \tag{4.139}$$

where $k_e$ is an adjustable constant and $c^k$ is the fractional cloud area. The $(1 - c^k)$ factor represents a random overlap assumption; precipitation falling into the existing cloud in a layer does not evaporate. For stratiform precipitation, $k_e = 1 \times 10^{-5}$, while for convective precipitation, $k_e$ is considered to be an adjustable parameter and is specified according to the table in appendix C.

Two bounds are applied to $E^k$:

1. $E^k \leq \frac{q_*^k - q^k}{\delta t}$, to prevent supersaturation;

2. $E^k \leq F^{k-} \frac{g}{\delta^k p}$, to prevent $F^{k+} < 0$. Note that precipitation is not permitted to evaporate in the layer in which it forms;

Exactly the same procedure is applied to snow,

$$F_s^{k+} = F_s^{k-} + \frac{\delta^k p}{g}(P_s^k - E_s^k - M^k) \tag{4.140}$$

where $P_s^k = f_s P^k$ is the snow production, $f_s(T)$ is the snow production fraction, $M^k$ is the melting rate and

$$E_s^k = E^k F_s^{k-} / F^{k-} \tag{4.141}$$

so snow evaporates in proportion to the fraction of snow in the precipitation flux on the upper interface.

The snow production fraction is simple function of temperature

$$f_s = \frac{T - T_{s,max}}{T_{s,min} - T_{s,max}}, \quad T_{min} \leq T \leq T_{max} \tag{4.142}$$

with $f_s(T < T_{s,min}) = 1$ and $f_s(T > T_{s,max}) = 0$. $T$ is the grid volume temperature. The bounds are adjustable constants with current settings $T_{min} = -5^\circ$ C and $T_{max} = 0^\circ$ C.

Falling precipitation is not permitted to freeze. Snow is produced only by the assumed snow fraction $f_s$ in the production term. Snow does not melt unless it it falls into a layer with $T^k > 0$ C, in which case $M^k = F_s^k \frac{g}{\delta^k p}$ so that all the snow melts.

The net heating rate due to freezing, melting and evaporation of precipitation is

$$Q^k = -L_v E^k + L_f(P_i^k - E_s^k - M^k) \tag{4.143}$$

This is the method by which the heating due to $L_f$ is included for all condensation processes. For convective precipitation, $P_i^k \equiv P_s^k$, while for stratiform precipitation, $P_i = f_i C^k$ where $C^k$ is the net condensation rate in the cloud. Both the cloud ice fraction and the snow production fractions are determined by $f_i$, with $P_s^k$ coming from the cloud ice. For stratiform precipitation, the above equations are iterated once to allow the first estimate of the heating to change $T$ and consequently $q_*$ (but not $f_i$) for the 2nd iteration.

Cloud liquid and ice particles are allowed to sediment using independent settling velocities, similar to the form described by Lawrence and Crutzen [1998]. The liquid and ice settling fluxes are computed at interfaces, from velocities and concentrations at midpoints, using a *SPITFIRE* solver [Rasch and Lawrence, 1998]. The resulting flux at each interface is constrained to be smaller than the mass of liquid or ice in the layer above. This constraint does not allow for particles falling into the layer from above.

Sedimenting particles evaporate if they fall into the cloud free portion of a layer. No bound is applied to prevent supersaturation of the layer. This will be accounted for in the subsequent cloud condensate tendency calculation. Maximum overlap is assumed for stratiform clouds, so particles only evaporate if the cloud fraction is larger in the layer above. The overlapped fraction is

$$f_o = \min\left(\frac{f_c^k}{f_c^{k-1}}, 1\right) \tag{4.144}$$

The ice velocity $v_i$ is a function only of the effective radius $R_e$ (see Section 4.8.4 for more information and a plot), which itself is a function only of $T$. For $R_e < 40 \times 10^{-6}$ m, the Stokes terminal velocity equation for a falling sphere is used

$$v_i = \frac{2}{9}\frac{\rho_w g R_e^2}{\eta} \tag{4.145}$$

where $\eta = 1.7 \times 10^{-5}$ kg m/s is the viscosity of air and the density of air has been neglected compared to the density of water.

For $R_e > 40 \times 10^{-6}$ m, the Stokes formula is no longer valid and we use a linear dependence of $v_i$ on $r = 10^{-6} \times R_e$

$$v_i(r) = v_i(40) + (r - 40)\frac{v_{400} - v_i(40)}{400 - 40} \tag{4.146}$$

where $v_{400} = 1.0$ m/s is the assumed velocity of a 400 micron sphere, close to the value suggested by Locatelli and Hobbs [1974].

The liquid particle velocity depends only on whether the cloud is over land or ocean, as is true of the liquid effective radius. The net liquid velocity $v_l$ is

$$v_l = v_l^{land} f^{land} + v_l^{ocean} f^{ocean} \tag{4.147}$$

where $f^{land}$ and $f^{ocean}$ are the land and ocean fractional areas of the cell, respectively. The ocean fraction may contain sea ice. The velocities are $v_l^{land} = 1.5$ and $v_l^{ocean} = 2.8$ cm/s.

It is assumed that there are five processes that convert condensate to precipitate:

• The conversion of liquid water to rain (PWAUT) follows a formulation originally suggested by Chen and Cotton [1987]:

$$PWAUT = C_{l,aut}\hat{q}_l^2\rho_a/\rho_w(\hat{q}_l\rho_a/\rho_w N)^{1/3}H(r_{3l} - r_{3lc}). \tag{4.148}$$

Here $\rho_a$ and $\rho_w$ are the local densities of air and water respectively, and $N$ is the assumed number density of cloud droplets. $C_{l,aut} = 0.55\pi^{1/3}k(3/4)^{4/3}(1.1)^4$, and $k = 1.18 \times 10^6$ cm$^{-1}$ sec$^{-1}$ is the Stokes constant.

$N$ is set to $400/cm^3$ over land near the surface, $150/cm^3$ over ocean, and $75/cm^3$ over sea ice. The number density also varies with distance from land by a factor equal to the distance to the nearest land point divided by 1000 km and multiplied by the cosine of latitude. The provides a sharper transition from land properties to ocean properties near the poles.

The terms $r_{3l}$ and $r_{3lc}$ are the mean volume radii of the droplets and a critical value below which no auto-conversion is allowed to take place, respectively. $H$ is the Heaviside function with the definition $H(x) = (0, 1)$ for $x(<, \geq)0$. The volume radius $r_{3l} = [(3\rho_a q_l)/(4\pi N\rho_w)]^{1/3}$. The standard value for the critical mean volume radius at which conversion begins is $15\mu$m. Baker [1993] has shown that this parameterization results in collection rates that far exceed those calculated in more realistic stochastic collection models. This is because the parameterization is based upon a collection efficiency corresponding to a cloud droplet distribution that has already been substantially modified by precipitation. Austin et al. [1995] suggest that a much smaller choice is appropriate prior to precipitation onset. Therefore the parameterization is adjusted by making $C_{l,aut} \rightarrow 0.1C_{l,aut}$ when the precipitation flux leaving the grid box is below 0.5 mm/day.

• The collection of cloud water by rain from above (PRACW) follows Tripoli and Cotton [1980]

$$PRACW = C_{racw}\rho^{3/2}\hat{q}_l q_r \tag{4.149}$$

where $C_{racw} = 0.884(g/(\rho_w\ 2.7\times10^{-4}))^{1/2}s^{-1}$ is derived by assuming a Marshall-Palmer distribution of rainwater falling through a uniformly distributed cloud water field, and $q_r$ is determined iteratively.

• The auto-conversion of ice to snow (PSAUT) is similar in form to that originally proposed by Kessler [1969] for liquid processes and Lin et al. [1983] for ice. However, it includes a temperature dependence similar to that proposed in Sundqvist [1988]

$$PSAUT = C_{i,aut}H(\hat{q}_i - q_{ic}). \tag{4.150}$$

The rate of conversion of ice ($C_{i,aut}$) to snow is set to $10^{-3}s^{-1}$ when the ice mixing ratio exceeds a critical threshold $q_{ic}$. The threshold is set to $q_{ic,warm}$ at $T = 0°C$ and $q_{ic,cold}$ at $T = -20°C$. Values for $q_{ic,warm}$ and $q_{ic,cold}$ are given in Appendix C. The threshold varies linearly in temperature between these two limits.

• The collection of ice by snow (PSACI) follows Lin et al. [1983], although it has been rewritten in the form:

$$PSACI = C_{sac}e_i\hat{q}_i. \tag{4.151}$$

where $e_i$ (= 1) is an ice collection efficiency. The coefficient of collection is

$$C_{sac} = c_7\rho_a^{c_8}\tilde{P}^{c_5} \tag{4.152}$$

Here, $c_5$, $c_7$ and $c_8$ are constants arising from the assumed shape of the snow distribution.

The coefficients of the equation (4.152) arise from some algebraic manipulation of the expressions appearing in Lin et al. [1983]. They in turn depend upon the specification for parameters describing an exponential size distribution for graupel-like snow. The parameter values used in Lin et al. [1983] are adopted in the CAM 3.0 implementation. The parameters are a slope parameter $d = 0.25$; an empirical parameter $c = 152.93$ controlling the fall speed of graupel-like snow; and the assumed integrated number density of snow $N_s = 3. \times 10^{-2}$. The constants appearing in equation (4.152) can be expressed as

$$c_1 = \pi N_s c\Gamma(3+d)/4 \tag{4.153}$$

$$c_2 = 6(\pi\rho_s N_s)^{d+4}/\left[c\Gamma(4+d)\rho_0^{0.5}\right] \tag{4.154}$$

$$c_5 = (3+d)/(4+d) \tag{4.155}$$

$$c_6 = (3+d)/4 \tag{4.156}$$

$$c_7 = c_1\rho_0^{0.5}c_2^{c_5}/(\rho_s N_s)^{c_6} \tag{4.157}$$

and

$$c_8 = -0.5/(4+d)\ . \tag{4.158}$$

Here $\Gamma$ is the Gamma function, $\rho_s = 0.1$ is the density of snow, and $\rho_0 = 1.275 \times 10^{-3}$ is a reference air density at the surface. All constants have been expressed in CGS units. The constants follow from integrating the geometric collection of a uniform distribution of suspended cloud liquid or ice over the size distribution of snow.

The collection of liquid by snow (PSACW) also follows Lin et al. [1983]:

$$PSACW = C_{sac}e_w\hat{q}_l. \tag{4.159}$$

where $e_w$ is the water collection efficiency. Lohmann and Roeckner [1996] note that the work by Levkov et al. [1992] suggests that the riming process is too efficient using the standard values. There the collection efficiency is reduced by an order of magnitude to $e_w = 0.1$.

## 4.6 Dry Adiabatic Adjustment

If a layer is unstable with respect to the dry adiabatic lapse rate, dry adiabatic adjustment is performed. The layer is stable if

$$\frac{\partial T}{\partial p} < \frac{\kappa T}{p}. \tag{4.160}$$

In finite–difference form, this becomes

$$T_{k+1} - T_k < C1_{k+1}(T_{k+1} + T_k) + \delta, \tag{4.161}$$

where

$$C1_{k+1} = \frac{\kappa(p_{k+1} - p_k)}{2p_{k+1/2}}\ . \tag{4.162}$$

If there are any unstable layers in the top three model layers, the temperature is adjusted so that (4.161) is satisfied everywhere in the column. The variable $\delta$ represents a convergence criterion. The adjustment is done so that sensible heat is conserved,

$$c_p(\hat{T}_k \Delta p_k + \hat{T}_{k+1}\Delta p_{k+1}) = c_p(T_k \Delta p_k + T_{k+1}\Delta p_{k+1}), \tag{4.163}$$

and so that the layer has neutral stability:

$$\hat{T}_{k+1} - \hat{T}_k = C1_{k+1}(\hat{T}_{k+1} + \hat{T}_k)\,. \tag{4.164}$$

As mentioned above, the hats denote the variables after adjustment. Thus, the adjusted temperatures are given by

$$\hat{T}_{k+1} = \frac{\Delta p_k}{\Delta p_{k+1} + \Delta p_k C2_{k+1}} T_k + \frac{\Delta p_{k+1}}{\Delta p_{k+1} + \Delta p_k C2_{k+1}} T_{k+1}, \tag{4.165}$$

and

$$\hat{T}_k = C2_{k+1}\hat{T}_{k+1}, \tag{4.166}$$

where

$$C2_{k+1} = \frac{1 - C1_{k+1}}{1 + C1_{k+1}}\ . \tag{4.167}$$

Whenever the two layers undergo dry adjustment, the moisture is assumed to be completely mixed by the process as well. Thus, the specific humidity is changed in the two layers in a conserving manner to be the average value of the original values,

$$\hat{q}_{k+1} = \hat{q}_k = (q_{k+1}\Delta p_{k+1} + q_k \Delta p_k)/(\Delta p_{k+1} + \Delta p_k). \tag{4.168}$$

The layers are adjusted iteratively. Initially, $\delta = 0.01$ in the stability check (4.161). The column is passed through from $k = 1$ to a user-specifiable lower level (set to 3 in the standard model configuration) up to 15 times; each time unstable layers are adjusted until the entire column is stable. If convergence is not reached by the 15th pass, the convergence criterion is doubled, a message is printed, and the entire process is repeated. If $\delta$ exceeds 0.1 and the column is still not stable, the model stops.

As indicated above, the dry convective adjustment is only applied to the top three levels of the standard model. The vertical diffusion provides the stabilizing vertical mixing at other levels. Thus, in practice, momentum is mixed as well as moisture and potential temperature in the unstable case.

## 4.7 Parameterization of Cloud Fraction

Cloud amount (or cloud fraction), and the associated optical properties, are evaluated via a diagnostic method in CAM 3.0. The basic approach is similar to that employed in the CCM2 and CCM3. The diagnosis of cloud fraction is a generalization of the scheme introduced by Slingo [1987], with variations described in Hack et al. [1993]; Kiehl et al. [1998], and Rasch and Kristjánsson [1998]. Cloud fraction depends on relative humidity, atmospheric stability and convective mass fluxes. Three types of cloud are diagnosed by the scheme: low-level marine stratus ($\mathcal{C}_{st}$), convective cloud ($\mathcal{C}_{cir}$), and layered cloud ($\mathcal{C}_c$). Layered clouds form when the relative humidity exceeds a threshold value which varies according to pressure. The diagnoses of these cloud types are described in more detail in the following paragraphs.

Marine stratocumulus clouds are diagnosed using an empirical relationship between marine stratocumulus cloud fraction and the stratification between the surface and 700mb derived by Klein and Hartmann [1993]. The CCM3 parameterization for stratus cloud fraction over oceans has been replaced with

$$\mathcal{C}_{st} = \min\Big\{1., \max\big[0., (\theta_{700} - \theta_s) * .057 - .5573\big]\Big\} \tag{4.169}$$

$\theta_{700}$ and $\theta_s$ are the potential temperatures at 700 mb and the surface, respectively. The cloud is assumed to be located in the model layer below the strongest stability jump between 750 mb and the surface. If no two layers present a stability in excess of -0.125 K/mb, no cloud is diagnosed. In areas where terrain filtering has produced non-zero ocean elevations, the sea surface temperature used for this computation is reduced from the true sea surface elevation to the model surface elevation according to the lapse rate of the U.S. Standard Atmosphere (-6.5 °C/km).

Convective cloud fraction in the model is related to updraft mass flux in the deep and shallow cumulus schemes according to a functional form suggested by Xu and Krueger [1991]:

$$\mathcal{C}_{shallow} = k_{1,shallow} ln(1.0 + k_2 M_{c,shallow}) \tag{4.170}$$

$$\mathcal{C}_{deep} = k_{1_{deep}} ln(1.0 + k_2 M_{c,deep}) \tag{4.171}$$

where $k_{1,shallow}$ and $k_{1_{deep}}$ are adjustable parameters given in Appendix C, $k_2 = 500$, and $M_c$ is the convective mass flux at the given model level.

The remaining cloud types are diagnosed on the basis of relative humidity, according to

$$\mathcal{C}_c = \left(\frac{RH - RH_{\min}}{1 - RH_{\min}}\right)^2 \tag{4.172}$$

The threshold relative humidity $RH_{\min}$ is set according to pressure $p$ as

$$RH_{\min} = \begin{cases} RH_{\min}^{low} & p > 750mb \\ RH_{\min}^{low} + (RH_{\min}^{high} - RH_{\min}^{low})\frac{p-750mb}{p_{mid}-750mb} & p_{mid} < p < 750mb \\ RH_{\min}^{high} & p < p_{mid} \end{cases} \tag{4.173}$$

where $p_{mid}$ in an adjustable parameter denoting the minimum pressure for a linear ramp from the low cloud threshold to the high cloud threshold. At present this ramp is implemented only in one configuration of the model; other versions have a step function achieved by setting $p_{mid} = 750$ mb. $RH_{\min}^{low}$, $RH_{\min}^{high}$, and $p_{mid}$ are specified as in Appendix C. Also, the parameter $RH_{\min}^{low}$ is adjusted over land by $-0.10$. This distinction is made to account for the increased sub-grid-scale variability of the water vapor field due to inhomogeneities in the land surface properties and subgrid orographic effects.

The total cloud $\mathcal{C}_{tot}$ within each volume is then diagnosed as

$$\mathcal{C}_{tot} = \max(\mathcal{C}_c, \mathcal{C}_{cir}, \mathcal{C}_{st}),$$

This is equivalent to a maximum overlap assumption of cloud types within each gridbox. The condensate value is assumed uniform within any and all types of cloud within each grid box.

## 4.8 Parameterization of Shortwave Radiation

### 4.8.1 Diurnal cycle

With standard name-list settings, both the longwave and shortwave heating rates are evaluated every model hour. Between hourly evaluations, the longwave and shortwave fluxes and flux divergences are held constant.

In CAM 3.0, insolation is computed using the method of Berger [1978]. Using this formulation, the insolation can be determined for any time within $10^6$ years of 1950 AD. This facilitates using CAM 3.0 for paleoclimate simulations. The insolation at the top of the model atmosphere is given by

$$S_I = S_0\, \rho^{-2} \cos \mu, \tag{4.174}$$

where $S_0$ is the solar constant, $\mu$ is the solar zenith angle, and $\rho^{-2}$ is the distance factor (square of the ratio of mean to actual distance that depends on the time of year). In the standard configuration, $S_0 = 1367.0$ W/m$^2$. CAM 3.0 includes a mechanism for treating the slow variations in the solar constant over the 11-year cycle and during longer secular trends. A time series of $S_0$ for 1870-2100 based upon Lean et al. [1995] is included with the standard model.

We represent the annual and diurnal cycle of solar insolation with a repeatable solar year of exactly 365 days and with a mean solar day of exactly 24 hours, respectively. The repeatable solar year does not allow for leap years. The expressions defining the annual and diurnal variation of solar insolation are:

$$\cos \mu = \sin \phi \sin \delta - \cos \phi \cos \delta \cos(H) \tag{4.175}$$

$$\delta = \arcsin(\sin \epsilon \sin \lambda) \tag{4.176}$$

$$\rho = \frac{1 - e^2}{1 + e\, \cos(\lambda - \tilde{\omega})} \tag{4.177}$$

$$\tilde{\omega} = \Pi + \psi \tag{4.178}$$

where

$$
\begin{aligned}
\phi &= \text{latitude in radians} \\
\delta &= \text{solar declination in radians} \\
H &= \text{hour angle of sun during the day} \\
\epsilon &= \text{obliquity} \\
\lambda &= \text{true longitude of the earth relative to vernal equinox} \\
e &= \text{eccentricity factor} \\
\tilde{\omega} &= \text{longitude of the perihelion} + 180^\circ \\
\Pi &= \text{longitude of perihelion based on the fixed equinox} \\
\psi &= \text{general precession} .
\end{aligned}
\tag{4.179}
$$

Note that $\Pi$ is denoted by $\pi$ in Berger [1978].

The hour angle $H$ in the expression for $\cos\mu$ depends on the calendar day $d$ as well as model longitude:

$$
H = 2\,\pi \left( d + \frac{\theta}{360^\circ} \right) , \tag{4.180}
$$

where $\theta =$ model longitude in degrees starting from Greenwich running eastward. Note that the calendar day $d$ varies continuously throughout the repeatable year and is updated every model time step. The values of $d$ at 0 GMT for January 1 and December 31 are 0 and 364, respectively. This would mean, for example, that a model calendar day $d$ having no fraction (such as 182.00) would refer to local midnight at Greenwich, and to local noon at the date line (180° longitude).

The obliquity $\epsilon$ may be approximated by an empirical series expansion of solutions for the Earth's orbit

$$
\epsilon = \epsilon^* + \sum_{j=1}^{47} A_j \, \cos \left( f_j \, t + \delta_j \right) \tag{4.181}
$$

where $A_j$, $f_j$, and $\delta_j$ are determined by numerical fitting. The term $\epsilon^* = 23.320556^\circ$, and $t$ is the time (in years) relative to 1950 AD.

Since the series expansion for the eccentricity $e$ is slowly convergent, it is computed using

$$
e = \sqrt{\left( e \cos \Pi \right)^2 + \left( e \sin \Pi \right)^2} \tag{4.182}
$$

The terms on the right-hand side may also be written as empirical series expansions:

$$
e \left\{ \begin{array}{c} \cos \\ \sin \end{array} \right\} \Pi = \sum_{j=1}^{19} M_j \, \left\{ \begin{array}{c} \cos \\ \sin \end{array} \right\} \left( g_j \, t + \beta_j \right) \tag{4.183}
$$

where $M_j$, $g_j$, and $\beta_j$ are estimated from numerical fitting. Once these series have been computed, the longitude of perihelion $\Pi$ is calculated using

$$
\Pi = \arctan \left( \frac{e \, \sin \Pi}{e \, \cos \Pi} \right) \tag{4.184}
$$

The general precession is given by another empirical series expansion

$$\psi = \tilde{\psi}\, t + \zeta + \sum_{j=1}^{78} F_j \, \sin\left(f'_j\, t + \delta'_j\right) \tag{4.185}$$

where $\tilde{\psi} = 50.439273''$, $\zeta = 3.392506°$, and $F_j$, $f'_j$, and $\delta'_j$ are estimated from the numerical solution for the Earth's orbit.

The calculation of $\lambda$ requires first determining two mean longitudes for the orbit. The mean longitude $\lambda_{m0}$ at the time of the vernal equinox is :

$$\begin{aligned} \lambda_{m0} \quad = \quad & 2 \left\{ \left(\frac{e}{2} + \frac{e^3}{8}\right) (1+\beta) \sin(\tilde{\omega}) \right. \\ & \quad - \frac{e^2}{4} \left(\frac{1}{2} + \beta\right) \sin(2\,\tilde{\omega}) \\ & \quad \left. + \frac{e^3}{8} \left(\frac{1}{3} + \beta\right) \sin(3\,\tilde{\omega}) \right\} \end{aligned} \tag{4.186}$$

where $\beta = \sqrt{1-e^2}$. The mean longitude is

$$\lambda_m = \lambda_{m0} + \frac{2\,\pi\,(d - d_{ve})}{365} \tag{4.187}$$

where $d_{ve} = 80.5$ is the calendar day for the vernal equinox at noon on March 21. The true longitude $\lambda$ is then given by:

$$\begin{aligned} \lambda = \lambda_m \quad & + \quad \left(2\,e - \frac{e^3}{4}\right) \sin(\lambda_m - \tilde{\omega}) \\ & + \quad \frac{5\,e^2}{4} \sin\left[2(\lambda_m - \tilde{\omega})\right] \\ & + \quad \frac{13\,e^3}{12} \sin\left[3(\lambda_m - \tilde{\omega})\right] \end{aligned} \tag{4.188}$$

The orbital state used to calculate the insolation is held fixed over the length of the model integration. This state may be specified in one of two ways. The first method is to specify a year for computing $t$. The value of the year is held constant for the entire length of the integration. The year must fall within the range of $1950 \pm 10^6$. The second method is to specify the eccentricity factor $e$, longitude of perihelion $\tilde{\omega} - 180°$, and obliquity $\epsilon$. This set of values is sufficient to specify the complete orbital state. Settings for AMIP II style integrations under 1995 AD conditions are $\epsilon = 23.4441$, $e = 0.016715$, and $\tilde{\omega} - 180 = 102.7$.

### 4.8.2 Formulation of shortwave solution

The $\delta$-Eddington approximation of Joseph et al. [1976] and Coakley et al. [1983] has been adopted and is described in Briegleb [1992]. This approximation has been shown to simulate quite well the effects of multiple scattering. The major differences between the shortwave parameterizations in CCM3 and CAM 3.0 are

1. the new treatment of cloud vertical overlap [Collins, 2001];
2. updated parameterization for near-infrared absorption by water vapor; and
3. inclusion of prescribed aerosol data sets for computing shortwave aerosol radiative forcing.

The solar spectrum is divided into 19 discrete spectral and pseudo-spectral intervals (7 for $O_3$, 1 for the visible, 7 for $H_2O$, 3 for $CO_2$, and 1 for the near-infrared following Collins [1998]). The CAM 3.0 model atmosphere consists of a discrete vertical set of horizontally homogeneous layers within which radiative heating rates are to be specified (see Figure 3.1). Each of these layers is considered to be a homogeneous combination of several radiatively active constituents. Solar irradiance, surface reflectivity for direct and diffuse radiation in each spectral interval, and the cosine of the solar zenith angle are specified. The surface albedo is specified in two wavebands (0.2-0.7 $\mu$m, and 0.7-5.0 $\mu$m) and distinguishes albedos for direct and diffuse incident radiation. Albedos for ocean surfaces, geographically varying land surfaces, and sea ice surfaces are distinguished.

The method involves evaluating the $\delta$-Eddington solution for the reflectivity and transmissivity for each layer in the vertical under clear and overcast conditions. The layers are then combined together, accounting for multiple scattering between layers, which allows evaluation of upward and downward spectral fluxes at each interface boundary between layers. This procedure is repeated for each spectral or pseudo-spectral interval and binary cloud configuration (see "Cloud vertical overlap" below) to accumulate broad band fluxes, from which the heating rate can be evaluated from flux differences across each layer. The $\delta$-Eddington scheme is implemented so that the solar radiation is evaluated once every model hour (in the standard configuration) over the sunlit portions of the model earth.

The $\delta$-Eddington approximation allows for gaseous absorption by $O_3$, $CO_2$, $O_2$, and $H_2O$. Molecular scattering and scattering/absorption by cloud droplets and aerosols are included. With the exception of $H_2O$, a summary of the spectral intervals and the absorption/scattering data used in the formulation are given in Briegleb [1992] and Collins [1998]. Diagnostic cloud amount is evaluated every model hour just prior to the solar radiation calculation.

The absorption by water vapor of sunlight between 1000 and 18000 cm$^{-1}$ is treated using seven pseudo-spectral intervals. A constant specific extinction is specified for each interval. These extinctions have been adjusted to minimize errors in heating rates and flux divergences relative to line-by-line (LBL) calculations for reference atmospheres [Anderson et al., 1986] using GENLN3 [Edwards, 1992] combined with the radiative transfer solver DISORT2 [Stamnes et al., 1988]. The coefficients and weights have the same properties as a k-distribution method [Lacis and Oinas, 1991], but this parameterization is essentially an exponential sum fit (e.g., Wiscombe and Evans [1977]). LBL calculations are performed with the HITRAN2k line database [Rothman et al., 2003] and the Clough, Kneizys, and Davies (CKD) model version 2.4.1 [Clough et al., 1989]. The Rayleigh scattering optical depths in the seven pseudo-spectral intervals have been changed for consistency with LBL calculations of the variation of water-vapor absorption with wavelength. The updated parameterization increases the absorption of solar radiation by water vapor relative to the treatment used in CCM and CAM since its introduction by Briegleb [1992].

For some diagnostic purposes, such as estimating cloud radiative forcing [Kiehl and Ramanathan, 1990] a clear-sky absorbed solar flux is required. In CAM 3.0, the clear-sky fluxes and heating rates are computed using the same vertical grid as the all-sky fluxes. This replaces the 2-layer diagnostic grid used in CCM3.

### 4.8.3 Aerosol properties and optics

#### Introduction

The treatment of aerosols in CAM 3.0 replaces the uniform background boundary-layer aerosol used in previous versions of CAM and CCM. The optics for the globally uniform aerosol were identical to the sulfate aerosols described by Kiehl and Briegleb [1993]. In the visible, the uniform aerosol was essentially a conservative scatterer. The new treatment introduces five chemical species of aerosol, including sea salt, soil dust, black and organic carbonaceous aerosols, sulfate, and volcanic sulfuric acid. The new aerosols include two species, the soil dust and carbonaceous types, which are strongly absorbing in visible wavelengths and hence increase the shortwave diabatic heating of the atmosphere.

The three-dimensional time-dependent distributions of the five aerosol species and the optics for each species are loaded into CAM 3.0 during the initialization process. This provides considerable flexibility to:

- Change the speciated aerosol climatology / time-series as aerosol modeling improves;
- Vary the aerosol distributions for climates different from present-day conditions;
- Examine the effects of individual aerosol species and arbitrary combinations of aerosol species; and
- Change aerosol optical properties.

In its present configuration, CAM includes the direct and semi-direct effects of tropospheric aerosols on shortwave fluxes and heating rates. The first indirect effect, or Twomey et al. [1984] effect, is not included in the standard version of CAM 3.0.

#### Description of aerosol climatologies and data sets

The data sets for the tropospheric and stratospheric aerosols are treated separately in the model.

The annually-cyclic tropospheric aerosol climatology consists of three-dimensional, monthly-mean distributions of aerosol mass for:

- sulfate from natural and anthropogenic sources;
- sea salt;
- black and organic carbon derived from natural and anthropogenic sources; and

- soil dust

There are four size categories of dust spanning diameters from 0.01 to 10 $\mu$m, and the black and organic carbon are represented by two tracers each for the hydrophobic (new) and hydrophilic (aged) components. The climatology therefore contains ten types of aerosol: sea salt, four size bins of soil dust, sulfate, new and aged black carbon, and hydrophobic and hydrophilic organic carbon.

The climatology is produced using an aerosol assimilation system [Collins et al., 2001, 2002*b*] integrated for present-day conditions. The system consists of the Model for Atmospheric Chemistry and Transport (MATCH) [Rasch et al., 1997] and an assimilation of satellite retrievals of aerosol optical depth. MATCH version 4 is integrated using the National Centers for Environmental Prediction (NCEP) meteorological reanalysis at T63 triangular truncation [Kalnay et al., 1996]. The satellite estimates of aerosol optical depth are from the NOAA Pathfinder II data set [Stowe et al., 1997].

The formulation of the sulfur cycle is described in Barth et al. [2000] and Rasch et al. [2000]. The emissions inventory for $SO_2$ is from Smith et al. [2001]. The sources for mineral dust are based upon the approach of Zender et al. [2003] and Mahowald et al. [2003]. The emissions of carbonaceous aerosols include contributions from biomass burning [Liousse et al., 1996], fossil fuel burning [Cooke et al., 1999], and a source of natural organic aerosols resulting from terpene emissions. The vertical profiles of sea salt are computed from the 10m wind speed [Blanchard and Woodcock, 1980].

The monthly-mean mass path for each aerosol species in each layer is computed in units of kg/m$^2$. During the initialization of CAM 3.0, the climatology is temporally interpolated from monthly-mean to mid-month values. At each CAM 3.0 time step, the mid-month values bounding the current time step are vertically interpolated onto the pressure grid of CAM 3.0 and then time interpolated to the current time step. The interpolation scheme in CAM 3.0 preserves the aerosol masses for each species to 1 part in $10^7$ relative to the climatology, and it is guaranteed to yield positive definite mass-mixing ratios for all aerosols.

The stratospheric volcanic aerosols are treated using a single species in the standard model. Zonal variations in the stratospheric mass loading are omitted. The volcanic input consists of the monthly-mean masses in units of kg/m$^2$ on an arbitrary meridional and vertical grid. The time series for the recent past is based upon Ammann et al. [2003] following Stenchikov et al. [1998].

**Calculation of aerosol optical properties**

The three intrinsic optical properties stored for each of the eleven aerosol types are specific extinction, single scattering albedo, and asymmetry parameter. These properties are computed on the band structure of CAM 3.0 using Chandrasekhar weighting with spectral solar insolation. The aerosol types affected by hygroscopic growth are sulfate, sea salt, and hydrophilic organic carbon. In previous versions of CCM and CAM 3.0, the relative humidity was held constant in calculations of hygroscopic growth at 80%. In CAM 3.0, the actual profiles of relative humidity computed from the model state each radiation time step are used in the calculation.

The optics for black and organic carbon are identical to the optics for soot and water-soluble aerosols in the Optical Properties of Aerosols and Clouds (OPAC) data set [Hess et al., 1998]. The optics for dust are derived from Mie calculations for the size distribution represented by each size bin [Zender et al., 2003]. The Mie calculations for sulfate assume that it is comprised of ammonium sulfate with a log-normal size distribution. The dry size parameters are a median radius of 0.05 $\mu$m and a geometric standard deviation of 2.0. The optical properties in the seven $H_2O$ pseudo-spectral intervals are averaged consistently with LBL calculations of the variation of water-vapor absorption with wavelength. This averaging technique preserves the cross correlations among the spectral variation of solar insolation, water vapor absorption, and the aerosol optical properties. The volcanic stratospheric aerosols are assumed to be comprised of 75% sulfuric acid and 25% water. The log-normal size distribution has an effective radius of 0.426 $\mu$m and a standard deviation of 1.25.

The bulk formulae of Cess [1985] are used to combine the optical properties of the individual aerosol species into a single set of bulk aerosol extinctions, single-scattering albedos, and asymmetry parameters for each layer.

#### Calculation of aerosol shortwave effects and radiative forcing

CAM 3.0 includes a mechanism to scale the masses of each aerosol species by user-selectable factors at runtime. These factors are global, time-independent constants. This provides the flexibility to consider the climate effects of an arbitrary combination of the aerosol species in the climatology. It also facilitates simulation of climates different from present-day conditions for which the only information available is the ratio of globally averaged aerosol emissions or atmospheric loadings. A mechanism to scale the carbonaceous aerosols with a time-dependent unitless factor has been included to facilitate realistic simulations of the recent past.

CAM 3.0 also includes a run-time option for computing a diagnostic set of shortwave fluxes with an arbitrary combination of aerosols multiplied with a separate set of user-selectable scale factors. This option can be used to compute, for example, the aerosol radiative forcing relative to an atmosphere containing no aerosols.

The diagnostic fields produced the aerosol calculation include the column-integrated optical depth and column-averaged single-scattering albedo, asymmetry parameter, and forward scattering parameter (in the $\delta$-Eddington approximation) for each aerosol species and spectral interval. These fields are only computed for illuminated grid points, and for non-illuminated points the fields are set to zero. The fraction of the time that a given grid point is illuminated is also recorded. Time averages of, for example, the optical depth can be obtained by dividing the time-averaged optical depths in the history files by the corresponding daylit fractions.

#### Globally uniform background sulfate aerosol

The option of introducing a globally uniform background sulfate aerosol is retained, although by default the optical depth of this aerosol is set to zero. Its optical properties are computed using the same sulfate optics as are used for the aerosol climatology. However, for consistency with the uniform aerosol in previous versions of CAM 3.0 and CCM3, the relative humidity used to compute hygroscopic growth is set to 80%.

### 4.8.4 Cloud Optical Properties

**Parameterization of effective radius**

Observational studies have shown a distinct difference between maritime, polar, and continental effective cloud drop size, $r_e$, for warm clouds. For this reason, CAM 3.0 differentiates between the cloud drop effective radius for clouds diagnosed over maritime and continental regimes [Kiehl et al., 1994], and over pristine surfaces (sea ice, snow covered land). Over the ocean, the cloud drop effective radius for liquid water clouds, $r_{el}$, is specified to be 14$\mu$m. Over sea ice, where we presume pristine conditions, $r_{el}$ is also specified to be 14$\mu$m. Over land masses $r_{el}$ is determined using

$$r_{el} = \begin{cases} 8\ \mu\text{m} & -10°C < T \\ 8 - 6(\left(\frac{10°+T}{20°}\right)\ \mu\text{m} & -30°C \leq T \leq -10°C \\ 14\ \mu\text{m} & -30°C > T \end{cases} \tag{4.189}$$

This does not necessarily correspond to the range over which the cloud ice fraction increases from 0 to 1. In addition, $r_{el}$ ramps linearly toward the pristine value of 14$\mu$m as water equivalent snow depth over land goes from 0 to 0.1 m.

An ice particle effective radius, $r_{ei}$, is also diagnosed by CAM 3.0. Following Kristjánsson and Kristiansen [2000], the effective radius for ice clouds is now a function only of temperature, as shown in Figure 4.2.

**Dependencies involving effective radius**

For cloud scattering and absorption, the radiative parameterization of Slingo [1989] for liquid water droplet clouds is employed. In this parameterization, the optical properties of the cloud droplets are represented in terms of the prognosed cloud water path (CWP, in units of kg m$^{-2}$) and effective radius $r_e = \int r^3 n(r) dr / \int r^2 n(r) dr$, where $n(r)$ is the cloud drop size distribution as a function of radius $r$.

Cloud radiative properties explicitly account for the phase of water. For shortwave radiation we use the following generalization of the expression used by Slingo [1989] for liquid water clouds. The cloud liquid optical properties (extinction optical depth, single scattering albedo, asymmetry parameter and forward scattering parameter) for each spectral interval are defined as

$$\tau_l^c = CWP \left[ a_l^i + \frac{b_l^i}{r_{el}} \right] (1 - f_{ice}) \tag{4.190}$$

$$\omega_l^c = 1 - c_l^i - d_l^i r_{el} \tag{4.191}$$

$$g_l^c = e_l^i + f_l^i r_{el} \tag{4.192}$$

$$f_l^c = (g_l^c)^2 \tag{4.193}$$

where superscript $i$ denotes spectral interval. The spectral intervals and coefficients for liquid water are defined in Slingo [1989].

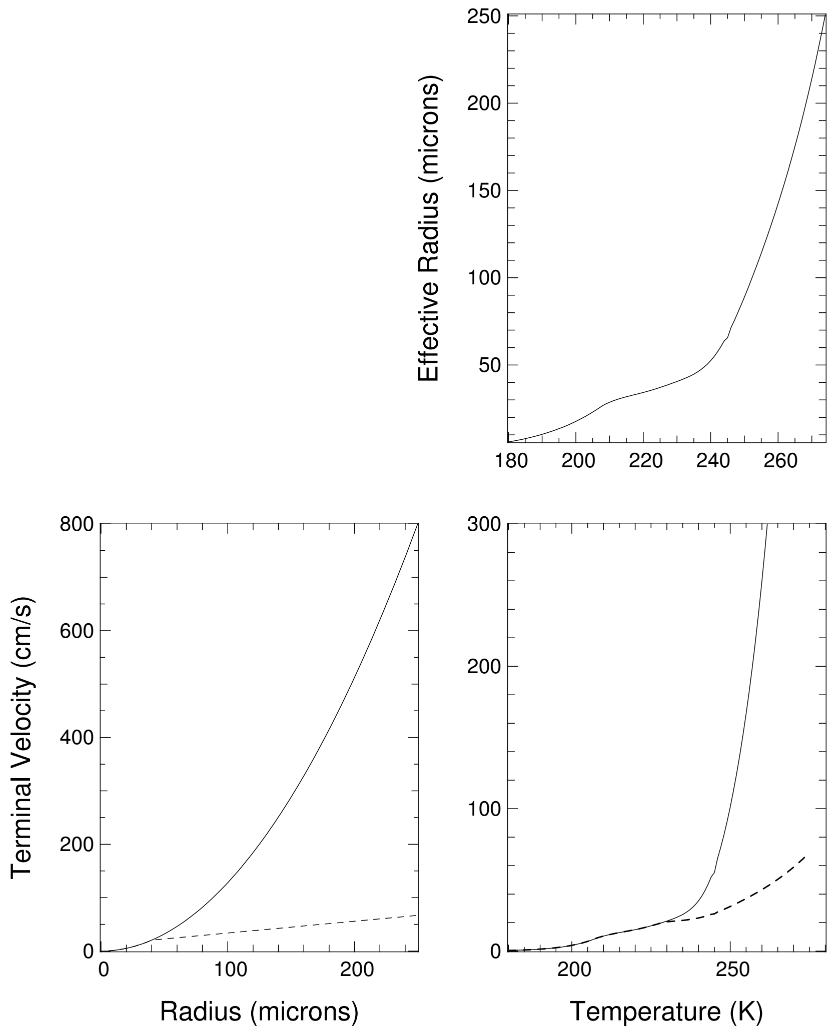


Figure 4.2: Ice effective radius and terminal velocity. Top, ice effective radius versus temperature. Bottom, ice velocity versus radius (left) and temperature (right); the Stokes terminal velocity is solid and the actual velocity is dashed.

The radiative properties of ice cloud are defined by

$$\tau_i^c = CWP \left[ a_i^i + \frac{b_i^i}{r_{ei}} \right] f_{ice} \quad (4.194)$$

$$\omega_i^c = 1 - c_i^i - d_i^i r_{ei} \quad (4.195)$$

$$g_i^c = e_i^i + f_i^i r_{ei} \quad (4.196)$$

$$f_i^c = (g_i^c)^2 \quad (4.197)$$

where the subscript $i$ denotes ice radiative properties. The values for the coefficients $a_i - f_i$ are based on the results of Ebert and Curry [1992] for the four pseudo-spectral intervals (.25-.69 $\mu$m, .69-1.19 $\mu$m, 1.19-2.38 $\mu$m, and 2.38-4.00 $\mu$m) employed in the CAM 3.0 shortwave radiation model. Note that when $0 < f_{ice} < 1$, then the combination of these expressions in (4.204 - 4.207) represent the radiative properties for a mixed phase cloud.

### 4.8.5 Cloud vertical overlap

The treatment of cloud vertical overlap follows Collins [2001]. The overlap parameterization is designed to reproduce calculations based upon the independent column approximation (ICA). The differences between the results from the new parameterization and ICA are governed by a set of parameters in the shortwave code (Table 4.1 on page 116 and section 4.8.9). The differences can be made arbitrarily small with appropriate settings of these parameters. The current parameter settings represent a compromise between computational cost and accuracy.

The new parameterizations can treat random, maximum, or an arbitrary combination of maximum and random overlap between clouds. The type of overlap is specified with the same two variables for the longwave and shortwave calculations. These variables are the number of random-overlap interfaces between adjacent groups of maximally-overlapped layers and a vector of the pressures at each of the interfaces. The specification of the overlap is completely separated from the radiative calculations, and if necessary the type of overlap can change at each grid cell or time step.

**Conversion of cloud amounts to binary cloud profiles**

The algorithm for cloud overlap first converts the vertical profile of partial cloudiness into an equivalent collection of binary cloud configurations. Let $\mathcal{C}(i)$ be the fractional amount of cloud in layer $i$ in a profile with $K$ layers. The index $i = 1$ corresponds to the top of the model atmosphere and $i = K$ corresponds to the layer adjacent to the surface. Let $N_m$ be the number of maximally-overlapped regions in the column separated by random-overlap boundaries. If the entire column is maximally overlapped, then $N_m = 1$, and if the entire column is randomly overlapped, then $N_m = K$. Each region $j$ includes all layers $i$ between $i_{j,\min}$ and $i_{j,\max}$. Within each region, identify the $n_j$ unique, non-zero cloud amounts and sort them into a descending list $\mathcal{C}_{j,k_j}$ with $1 \leq k_j \leq n_j$. Note than in CAM 3.0, cloud amounts are not allowed to be identically equal to 1. It is convenient to define $\mathcal{C}_{j,0} = 1$ and $\mathcal{C}_{j,n_j+1} = 0$. By construction $\mathcal{C}_{j,k_j-1} > \mathcal{C}_{j,k_j}$ for $1 \leq k_j \leq n_j + 1$.

The binary cloud configurations are defined in terms of the sorted cloud amounts. The number of unique cloud binary configurations in region $j$ is $n_j + 1$. The $k_j^{\text{th}}$ binary cloud configuration $\tilde{\mathcal{C}}_{j,k_j}$ in region $j$ is given by

$$\tilde{\mathcal{C}}_{j,k_j}(i) = \begin{cases} 1 & \text{if } i_{j,\min} \leq i \leq i_{j,\max} \text{ and } \mathcal{C}(i) \geq \mathcal{C}_{j,k_j-1} \\ 0 & \text{otherwise} \end{cases} \tag{4.198}$$

with $1 \leq k_j \leq n_j + 1$. The fractional area of this configuration is

$$\tilde{A}_{j,k_j} = \mathcal{C}_{j,k_j-1} - \mathcal{C}_{j,k_j} \tag{4.199}$$

The binary cloud configurations for each maximum-overlap region can be combined into cloud configurations for the entire column. Because of the random overlap boundaries between regions, the number of column configurations is

$$N_c = \prod_{j'=1}^{N_m} (n_{j'} + 1) \tag{4.200}$$

Let $\tilde{\mathcal{C}}[k_1, \ldots, k_{N_m}]$ represent the column configuration with $\tilde{\mathcal{C}}_{1,k_1}$ in region 1, $\tilde{\mathcal{C}}_{2,k_2}$ in region 2, etc. The vertical profile of binary cloud elements is given by:

$$\tilde{\mathcal{C}}[k_1, \ldots, k_{N_m}](i) = \sum_{j'=1}^{N_m} \tilde{\mathcal{C}}_{j',k_{j'}}(i) \tag{4.201}$$

The area of this configuration is

$$\tilde{A}[k_1, \ldots, k_{N_m}] = \prod_{j'=1}^{N_m} \tilde{A}_{j',k_{j'}} \tag{4.202}$$

**Maximum-random overlap assumption**

The cloud overlap for radiative calculations in CAM 3.0 is maximum-random (M/R). Clouds in adjacent layers are maximally overlapped, and groups of clouds separated by one or more clear layers are randomly overlapped. The two overlap parameters input to the radiative calculations are the number of random-overlap interfaces, which equals $N_m$, and a vector of pressures $\vec{p}$ at each random-overlap interface. These parameters are determined for each grid cell at each radiation time step. Suppose there are $M \geq 0$ groups of vertically contiguous clouds in a given grid cell. The first parameter $N_m = \max(M, 1)$. Let $p_j$ represent the pressure at the bottom interface of each group of contiguous clouds, and let $p_s$ denote the surface pressure. Both $j$ and $p_j$ increase from the top of the model downward. Then

$$\vec{p} = \begin{cases} [p_s] & \text{if } M \leq 1 \\ [p_1,\ \ldots\ , p_{M-1}, p_s] & \text{if } M \geq 2 \end{cases} \tag{4.203}$$

**Low, medium and high cloud overlap assumptions (diagnostics)**

For diagnostic purposes, the CAM 3.0 calculates three levels of cloud fraction assuming the same maximum-random overlap as in the radiative calculations. These diagnostics, denoted as low, middle, and high cloud, are bounded by the pressure levels $p_s$ to 700 mb, 700 mb to 400 mb, and 400 mb to the model top.

### Computation of fluxes and heating rates with overlap

The solution for the shortwave fluxes is calculated by determining all possible arrangements of binary clouds which are consistent with the vertical profile of partial cloudiness, the overlap assumption, and the parameters for accelerating the solution (Table 4.1 and section 4.8.9). The shortwave radiation within each of these configurations is calculated using the same $\delta$-Eddington solver introduced in CCM3 [Briegleb, 1992]. The all-sky fluxes and heating rates for the original profile of partial cloudiness are calculated as weighted sums of the corresponding quantities from each configuration. The weights are equal to the horizontal fractional area occupied by each configuration. The number of configurations is given by eqn. (4.200), and the area of each configuration is given by eqn. (4.202). There are two steps in the calculations: first, the calculation of the cloud-free and overcast radiative properties for each layer, and second the combination of these properties using the adding method to calculate fluxes. These two processes are described below.

## 4.8.6 $\delta$-Eddington solution for a single layer

Details of the implementation are as follows. The CAM 3.0 model atmosphere is divided into $K + 1$ layers in the vertical; an extra top layer (with index 0, above the $K$ layers specified by CAM 3.0) is added. This extra layer prevents excessive heating in the top layer when the top pressure is not very low; also, as the model does not specify absorber properties above its top layer, the optical properties of the top layer must be used for the extra layer. In CAM 3.0, clear-sky and all-sky solar fluxes are calculated and output for the top of model (TOM) at layer 1 and the top of atmosphere (TOA) corresponding to layer 0. The TOM fluxes are used to compute the model energetic balance, and the TOA fluxes are output for diagnostic comparison against satellite measurements. The provision of both sets of fluxes is new in CAM 3.0. Layers are assumed to be horizontally and vertically homogeneous for each model grid point and are bounded vertically by layer interfaces. For each spectral band, upward and downward fluxes are computed on the layer interfaces (which include the surface and top interface). The spectral fluxes are summed and differenced across layers to evaluate the solar heating rate. The following discussion refers to each of the spectral intervals.

In general, several constituents absorb and/or scatter in each homogeneous layer (e.g. cloud, aerosol, gases...). Every constituent is defined in terms of a layer extinction optical depth $\tau$, single scattering albedo $\omega$, asymmetry parameter $g$, and the forward scattering fraction $f$. To define bulk layer properties, the combination formulas of Cess [1985] are used:

$$\tau = \sum_i \tau_i, \tag{4.204}$$

$$\omega = \sum_i \omega_i \tau_i \tau, \tag{4.205}$$

$$g = \frac{\sum_i g_i \omega_i \tau_i}{\omega \tau}, \tag{4.206}$$

$$f = \frac{\sum_i f_i \omega_i \tau_i}{\omega \tau}, \tag{4.207}$$

where the sums are over all constituents.

The $\delta$-Eddington solution for each layer requires scaled properties for $\tau$, $\omega$, $g$, given by the expressions:

$$\tau^* = \tau(1-\omega f), \tag{4.208}$$

$$\omega^* = \omega\left(\frac{1-f}{1-\omega f}\right), \tag{4.209}$$

$$g^* = \frac{g-f}{1-f}. \tag{4.210}$$

The scaling accounts for the scattering effects of the strong forward peak in particle scattering. The $\delta$-Eddington nonconservative ($\omega < 1$) solutions for each layer for direct radiation at cosine zenith angle $\mu_0$ are (following the notation of Coakley et al. [1983]:

$$R(\mu_0) = (\alpha-\gamma)\overline{T}e^{-\tau^*/\mu_0} + (\alpha+\gamma)\overline{R} - (\alpha-\gamma), \tag{4.211}$$

$$T(\mu_0) = (\alpha+\gamma)\overline{T} + (\alpha-\gamma)\overline{R}e^{-\tau^*/\mu_0} - (\alpha+\gamma-1)e^{-\tau^*/\mu_0}, \tag{4.212}$$

$$\overline{R} = (u+1)(u-1)(e^{\lambda\tau^*} - e^{-\lambda\tau^*})N^{-1}, \tag{4.213}$$

$$\overline{T} = 4uN^{-1}, \tag{4.214}$$

where

$$\alpha = \frac{3}{4}\omega^*\mu_0\left(\frac{1+g^*(1-\omega^*)}{1-\lambda^2\mu_0^2}\right), \tag{4.215}$$

$$\gamma = \frac{1}{2}\omega^*\left(\frac{1+3g^*(1-\omega^*)\mu_0^2}{1-\lambda^2\mu_0^2}\right), \tag{4.216}$$

$$N = (u+1)^2e^{\lambda\tau^*} - (u-1)^2e^{-\lambda\tau^*}, \tag{4.217}$$

$$u = \frac{3}{2}\left(1-\omega^*g^*\lambda\right), \tag{4.218}$$

$$\lambda = \sqrt{3(1-\omega^*)(1-\omega^*g^*)}, \tag{4.219}$$

where $R(\mu_0)$, $T(\mu_0)$ are the layer reflectivity and transmissivity to direct radiation respectively, and $\overline{R}$, $\overline{T}$ are the layer reflectivity and transmissivity to diffuse radiation respectively. It should be noted that in some cases of small but nonzero $\omega$, the diffuse reflectivity can be negative. For these cases, $\overline{R}$ is set to 0, which produces negligible impact on fluxes and the heating rate. Note that in the new overlap scheme, these properties are computed separately for the clear and cloud-filled portions of each layer [Collins, 2001].

### 4.8.7 Combination of layers

To combine layers, it is assumed that radiation, once scattered, is diffuse and isotropic (including from the surface). For an arbitrary layer 1 (or combination of layers with radiative properties $R_1(\mu_0)$, $T_1(\mu_0)$,$\overline{R}_1$,$\overline{T}_1$) overlaying layer 2 (or combination of layers with radiative properties $R_2(\mu_0)$, $T_2(\mu_0)$, and $\overline{R}_2$, $\overline{T}_2$), the combination formulas for direct and diffuse radiation incident from above are:

$$
\begin{aligned}
R_{12}(\mu_0) &= R_1(\mu_0) + \frac{\overline{T}_1\{(T_1(\mu_0) - e^{-\tau_1^*/\mu_0})\overline{R}_2 + e^{-\tau_1^*/\mu_0} R_2(\mu_0)\}}{1 - \overline{R}_1\overline{R}_2}, && (4.220)\\
T_{12}(\mu_0) &= e^{-\tau_1^*/\mu_0} T_2(\mu_0) + \frac{\overline{T}_2\{(T_1(\mu_0) - e^{-\tau_1^*/\mu_0}) + e^{-\tau_1^*/\mu_0} R_2(\mu_0)\overline{R}_1\}}{1 - \overline{R}_1\overline{R}_2}, && (4.221)\\
\overline{R}_{12} &= \overline{R}_1 + \frac{\overline{T}_1\overline{R}_2\overline{T}_1}{1 - \overline{R}_1\overline{R}_2}, && (4.222)\\
\overline{T}_{12} &= \frac{\overline{T}_1\overline{T}_2}{1 - \overline{R}_1\overline{R}_2}. && (4.223)
\end{aligned}
$$

Note that the transmissions for each layer $(T_1(\mu_0), T_2(\mu_0))$ and for the combined layers $(T_{12}(\mu_0))$ are total transmissions, containing both direct and diffuse transmission. Note also that the two layers (or combination of layers), once combined, are no longer a homogeneous system.

To combine the layers over the entire column, two passes are made through the layers, one starting from the top and proceeding downward, the other starting from the surface and proceeding upward. The result is that for every interface, the following combined reflectivities and transmissivities are available:

$e^{-\tau^*/\mu_0}$ = direct beam transmission from top-of-atmosphere to the interface ($\tau^*$ is the scaled optical depth from top-of-atmosphere to the interface),

$R_{up}(\mu_0)$ = reflectivity to direct solar radiation of entire atmosphere *below* the interface,

$T_{dn}(\mu_0)$ = total transmission to direct solar radiation incident from above to entire atmosphere *above* the interface,

$\overline{R}_{up}$ = reflectivity of atmosphere *below* the interface to diffuse radiation from above,

$\overline{R}_{dn}$ = reflectivity of atmosphere *above* the interface to diffuse radiation from below.

With these quantities, the upward and downward fluxes at every interface can be computed. For example, the upward flux would be the directly transmitted flux ($e^{-\tau*/\mu_0}$) times the reflection of the entire column below the interface to direct radiation ($R_{up}(\mu_0)$), plus the diffusely transmitted radiation from above that reaches the interface ($T_{dn}(\mu_0) - e^{-\tau*/\mu_0}$) times the reflectivity of the entire atmosphere below the interface to diffuse radiation from above ($\overline{R}_{up}$), all times a factor that accounts for multiple reflections at the interface. A similar derivation of the downward flux is straightforward. The resulting expressions for the upward and downward flux

Table 4.1: Parameters for Decreasing Number of SW Calculations.

| Parameter | Symbol | Definition | Value in CAM 3.0 |
|---|---|---|---|
| **cldmin** | $\mathcal{C}_{\min}$ | Minimum cloud area | 0. |
| **cldeps** | $\mathcal{C}_{eps}$ | Minimum cloud area difference | 0. |
| **areamin** | $\tilde{A}_{\min}$ | Minimum configuration area | 0.01 |
| **nconfgmax** | $N_{c,\max}$ | Maximum # of configurations | 15. |

are:

$$F_{up} = \frac{e^{-\tau^*/\mu_0} R_{up}(\mu_0) + (T_{dn}(\mu_0) - e^{-\tau^*/\mu_0})\overline{R}_{up}}{1 - \overline{R}_{dn}\overline{R}_{up}}, \tag{4.224}$$

$$F_{dn} = e^{-\tau^*/\mu_0} + \frac{(T_{dn}(\mu_0) - e^{-\tau^*/\mu_0}) + e^{-\tau^*/\mu_0} R_{up}(\mu_0)\overline{R}_{dn}}{1 - \overline{R}_{dn}\overline{R}_{up}}. \tag{4.225}$$

Note that in the new overlap scheme, the calculation of the combined reflectivities, transmissions, and fluxes at layer interfaces are computed for each binary cloud configuration, subject to techniques for significantly accelerating these calculations (below) [Collins, 2001].

### 4.8.8 Acceleration of the adding method in all-sky calculations

If two or more configurations of binary clouds are identical between TOA and a particular interface, then $T_{dir} = e^{-\tau^*/\mu_0}$, $T_{dn}$, and $\bar{R}_{dn}$ are also identical at that interface. The adding method is applied once and the three radiative quantities are copied to all the identical configurations. This process is applied at each interface by constructing a binary tree of identical cloud configurations starting at TOA down to the surface. A similar method is used for $R_{up}$ and $\bar{R}_{up}$, which are calculated using the adding method starting the surface and continuing up to a particular interface. The copying of identical radiative properties reduces the number of calculations of $T_{dir}$, $T_{dn}$, and $\bar{R}_{dn}$ by 62% and the number of calculations of $R_{up}$ and $\bar{R}_{up}$ by 21% in CAM 3.0 with M/R overlap.

### 4.8.9 Methods for reducing the number of binary cloud configurations

The computational cost of the shortwave code has two components: a fixed cost for computing the radiative properties of each layer under clear and overcast conditions, and a variable cost for applying the adding method for each column configuration $\tilde{\mathcal{C}}[k_1, \ldots, k_{N_m}]$. The variable component can be reduced by omitting configurations which contribute small terms in the shortwave fluxes. Several mechanisms for selecting configurations for omission have been included in the parameterization. The parameters that govern the selection process are described in Table 4.1.

Any combination of the selection conditions may be imposed. If the parameter $\mathcal{C}_{\min} > 0$, cloud layers with $\mathcal{C}(i) \leq \mathcal{C}_{\min}$ are identified as cloud-free layers. The configurations including these clouds are excluded from the flux calculations. If the parameter $\mathcal{C}_{eps} > 0$, the cloud amounts are discretized by

$$\mathcal{C}(i) \rightarrow \left[\frac{\mathcal{C}(i)}{\mathcal{C}_{eps}}\right] \mathcal{C}_{eps} \tag{4.226}$$

where $[x]$ represents rounding to the nearest integer less than $x$. This reduces the number of unique, non-zero cloud amounts $n_j$ in each maximum-overlap region $j$. For example, if $\mathcal{C}_{eps} = 0.01$, then two cloud amounts are distinguished only if they differ by more than 0.01. If the parameter $\tilde{A}_{\min} > 0$, only configurations with $\tilde{A}[k_1, \ldots, k_{N_m}] \geq \tilde{A}_{\min}$ are retained in the calculation. The fluxes and heating rates are normalized by the area of these configurations:

$$\tilde{A}_{tot} = \sum_{k_1=1}^{n_1+1} \cdots \sum_{k_{N_m}=1}^{n_{N_m}+1} \tilde{A}[k_1, \ldots, k_{N_m}] \;\; \theta\left(\tilde{A}[k_1, \ldots, k_{N_m}] - \tilde{A}_{\min}\right) \tag{4.227}$$

where $\theta$ is the Heaviside function. In CAM 3.0, $\tilde{A}_{\min} = 0.01$. Finally, if the number of configurations $N_c > N_{c,\max}$, then only the $N_{c,\max}$ configurations with the largest values of $\tilde{A}[k_1, \ldots, k_{N_m}]$ are retained. This is equivalent to setting $\tilde{A}_{\min}$ so that the largest $N_{c,\max}$ configurations are selected. The fluxes and heating rates are normalized by $\tilde{A}_{tot}$ calculated with this value of $\tilde{A}_{\min}$. With the current cloud parameterizations in CAM 3.0 and with $\tilde{A}_{\min} = 0.01$, the mean and RMS $N_c$ are approximately 5. $N_{c,\max}$ is set to 15, or 2 standard deviations above the mean $N_c$. Only 5% of cloud configurations in CAM 3.0 have $N_c \geq N_{c,\max}$. The errors of the solutions relative to ICA are relatively insensitive to $\tilde{A}_{tot}$ [Collins, 2001].

### 4.8.10 Computation of shortwave fluxes and heating rates

The upward and downward spectral fluxes at each interface are summed to evaluate the spectrally integrated fluxes, then differenced to produce the solar heating rate,

$$Q_{\text{sol}} = \frac{g}{c_p} \frac{F_{dn}(p_{k+1}) - F_{up}(p_{k+1}) - F_{dn}(p_k) + F_{up}(p_k)}{p_{k+1} - p_k} \tag{4.228}$$

which is added to the nonlinear term $(Q)$ in the thermodynamic equation.

## 4.9 Parameterization of Longwave Radiation

The method employed in the CAM 3.0 to represent longwave radiative transfer is based on an absorptivity/emissivity formulation [Ramanathan and Downey, 1986]

$$F^{\downarrow}(p) \;\; = \;\; B(p_t)\varepsilon(p_t, p) + \int_{p_t}^{p} \alpha(p, p')dB(p') \tag{4.229}$$

$$F^{\uparrow}(p) \;\; = \;\; B(p_s) - \int_{p}^{p_s} \alpha(p, p')dB(p') \;, \tag{4.230}$$

where $B(p) = \sigma T(p)^4$ is the Stefan-Boltzmann relation. The pressures $p_t$ and $p_s$ refer to the top of the model and the surface, respectively. $\alpha$ and $\epsilon$ are the absorptivity and emissivity

$$\alpha(p, p') = \frac{\int_0^\infty \{dB_\nu(p')/dT(p')\} (1 - \mathcal{T}_\nu(p, p'))\, d\nu}{dB(p)/dT(p)} \tag{4.231}$$

$$\varepsilon(p_t, p) = \frac{\int_0^\infty B_\nu(p_t)(1 - \mathcal{T}_\nu(p_t, p))\, d\nu}{B(p_t)}, \tag{4.232}$$

where the integration is over wavenumber $\nu$. $B_\nu(p) = B_\nu(T(p))$ is the Planck function, and $\mathcal{T}_\nu$ is the atmospheric transmission. Thus, to solve for fluxes at each model layer we need solutions to the following:

$$\int_0^\infty (1 - \mathcal{T}_\nu) F(B_\nu) d\nu, \tag{4.233}$$

where $F(B_\nu)$ is the Planck function for the emissivity, or the derivative of the Planck function with respect to temperature for the absorptivity.

The general method employed for the solution of (4.233) for a given gas is based on the broad band model approach described by Kiehl and Briegleb [1991] and Kiehl and Ramanathan [1983]. This approach is based on the earlier work of Ramanathan [1976]. The broad band approach assumes that the spectral range of absorption by a gas is limited to a relatively small range in wavenumber $\nu$, and hence can be evaluated at the band center, i.e.

$$\int_{\nu_1}^{\nu_2} (1 - \mathcal{T}_\nu) F(B_\nu)\, d\nu \approx F(B_{\bar{\nu}}) \int_{\nu_1}^{\nu_2} (1 - \mathcal{T}_\nu) d\nu = F(B_{\bar{\nu}}) A, \tag{4.234}$$

where $A$ is the band absorptance (or equivalent width) in units of $\mathrm{cm}^{-1}$. Note that $A$, in general, is a function of the absorber amount, the local emitting temperature, and the pressure. Thus, the broad band model is based on finding analytic expressions for the band absorptance. Ramanathan [1976] proposed the following functional form for $A$:

$$A(u, T, P) = 2A_0 \ln \left\{ 1 + \frac{u}{\sqrt{4 + u(1 + 1/\beta)}} \right\}, \tag{4.235}$$

where $A_0$ is an empirical constant. $u$ is the scaled dimensionless path length

$$u = \int \frac{S(T)}{A_0(T)} \mu \rho_a dz, \tag{4.236}$$

where $S(T)$ is the band strength, $\mu$ is the mass mixing ratio of the absorber, and $\rho_a$ is the density of air. $\beta$ is a line width factor,

$$\beta = \frac{4}{ud} \int \gamma(T) \left( \frac{P}{P_0} \right) du, \tag{4.237}$$

where $\gamma(T)$ is the mean line halfwidth for the band, $P$ is the atmospheric pressure, $P_0$ is a reference pressure, and $d$ is the mean line spacing for the band. The determination of $\gamma$, $d$,

$S$ from spectroscopic line databases, such as the FASCODE database, is described in detail in Kiehl and Ramanathan [1983]. Kiehl and Briegleb [1991] describe how (4.235) can be extended to account for sub-bands within a spectral region. Essentially, the argument in the log function is replaced by a summation over the sub-bands. This broad band formalism is employed for $CO_2$, $O_3$, $CH_4$, $N_2O$, and minor absorption bands of $CO_2$, while for the CFCs and stratospheric aerosols we employ the exponential transmission approximation discussed by Ramanathan et al. [1985]

$$T = \exp\left[-D\left(S(T)/\Delta\nu\right)W\right], \tag{4.238}$$

where $\Delta\nu$ is the band width, and $W$ is the absorber path length

$$W = \int \mu\rho_a dz, \tag{4.239}$$

and $D$ is a diffusivity factor. The final problem that must be incorporated into the broad band method is the overlap of one or more absorbers within the same spectral region. Thus, for the wavenumber range of interest, namely 500 to 1500 cm$^{-1}$, the radiative flux is determined in part by the integral

$$\int_{500}^{1500} (1 - \mathcal{T}_\nu)F(B_\nu)d\nu, \tag{4.240}$$

which can be re-formulated for given sub intervals in wavenumber as

$$\begin{aligned}
\int_{500}^{1500} (1 - \mathcal{T}_\nu)F(B_\nu)d\nu = & \int_{500}^{750} (1 - \mathcal{T}^1_{CO_2}\mathcal{T}^1_{N_2O}\mathcal{T}_{H_2O}\mathcal{T}^1_{H_2SO_4})F(B_\nu)d\nu \\
& + \int_{750}^{820} (1 - \mathcal{T}^1_{CFC11}\mathcal{T}_{H_2O}\mathcal{T}^*_{H_2SO_4})F(B_\nu)d\nu \\
& + \int_{820}^{880} (1 - \mathcal{T}^2_{CFC11}\mathcal{T}_{H_2O}\mathcal{T}^3_{H_2SO_4})F(B_\nu)d\nu \\
& + \int_{880}^{900} (1 - \mathcal{T}^1_{CFC12}\mathcal{T}_{H_2O}\mathcal{T}^3_{H_2SO_4})F(B_\nu)d\nu \\
& + \int_{900}^{1000} (1 - \mathcal{T}^2_{CO_2}\mathcal{T}_{H_2O}\mathcal{T}^3_{H_2SO_4}\mathcal{T}^3_{CFC11}\mathcal{T}^2_{CFC12})F(B_\nu)d\nu \\
& + \int_{1000}^{1120} (1 - \mathcal{T}^3_{CO_2}\mathcal{T}_{O_3}\mathcal{T}_{H_2O}\mathcal{T}^4_{H_2SO_4}\mathcal{T}^4_{CFC11}\mathcal{T}^3_{CFC12})F(B_\nu)d\nu \\
& + \int_{1120}^{1170} (1 - \mathcal{T}^4_{CFC12}\mathcal{T}_{H_2O}\mathcal{T}^4_{H_2SO_4}\mathcal{T}^2_{N_2O})F(B_\nu)d\nu \\
& + \int_{1170}^{1500} (1 - \mathcal{T}_{CH_4}\mathcal{T}^3_{N_2O}\mathcal{T}_{H_2O}\mathcal{T}^5_{H_2SO_4})F(B_\nu)d\nu
\end{aligned} \tag{4.241}$$

The factors $\mathcal{T}^i_{H_2SO_4}$ represent the transmissions through stratospheric volcanic aerosols. The transmissions in each band are replaced by effective transmissions $\bar{T}^i_{H_2SO_4}$ given by:

$$\bar{T}^i_{H_2SO_4} = \exp\left(-D\,\kappa_{i,volc}\,W_{volc}\right) \tag{4.242}$$

Table 4.2: Wavenumber Intervals for Volcanic Specific Extinctions

| Index | $\nu_1 - \nu_2$ |
|---|---|
| 1 | 500 - 650 |
| 2 | 650 - 800 |
| 3 | 800 - 1000 |
| 4 | 1000 - 1200 |
| 5 | 1200 - 2000 |

where $D = 1.66$ is the diffusivity factor, $\kappa_{i,volc}$ is an effective specific extinction for the band, and $W_{volc}$ is the mass path of the volcanic aerosols. For computing overlap with minor absorbers, methane, and carbon dioxide, the volcanic extinctions are computed for five wavenumber intervals given in table 4.2. The transmissions for overlap with the broadband absorption by water vapor are defined in equation 4.275. The volcanic transmission for the 798 cm$^{-1}$ band of $N_2O$ is

$$\bar{T}^*_{H_2SO_4} = 0.7\bar{T}^2_{H_2SO_4} + 0.3\bar{T}^3_{H_2SO_4} \tag{4.243}$$

The sub-intervals in equation 4.241, in turn, can be reformulated in terms of the absorptance for a given gas and the "overlap" transmission factors that multiply this transmission. Note that in the broad band formulation there is an explicit assumption that these two are uncorrelated (see Kiehl and Ramanathan [1983]). The specific parameterizations for each of these sub-intervals depends on spectroscopic data particular to a given gas and absorption band for that absorber.

### 4.9.1 Major absorbers

Details of the parameterization for the three major absorbers, $H_2O$, $CO_2$ and $O_3$, are given in Collins et al. [2002*a*], Kiehl and Briegleb [1991], and Ramanathan and Dickinson [1979], respectively. Therefore, we only provide a brief description of how these gases are treated in the CAM 3.0. Note that the original parameterization for $H_2O$ by Ramanathan and Downey [1986] has been replaced a new formulation in CAM 3.0.

For $CO_2$

$$\alpha_{CO_2}(p, p') = \frac{1}{4\sigma T^3(p')}\frac{dB_{CO_2}}{dT'}(p')A_{CO_2}(p', p). \tag{4.244}$$

$B_{CO_2}$ is evaluated for $\tilde{\nu} = 667$ cm$^{-1}$, where $A_{CO_2}(p', p)$ is the broad–band absorptance from Kiehl and Briegleb [1991]. Similarly,

$$\epsilon_{CO_2}(0, p) = \frac{1}{\sigma T^4(0)}B_{CO_2}(0)A_{CO_2}(0, p). \tag{4.245}$$

For ozone,

$$\alpha_{O_3}(p, p') = \frac{1}{4\sigma T^3(p')}\frac{dB_{O_3}}{dT'}(p')A_{O_3}(p', p), \tag{4.246}$$

and

$$\epsilon_{O_3}(0,p) = \frac{1}{\sigma T^4(0)} B_{O_3}(0) A_{O_3}(0,p), \tag{4.247}$$

where $A_{O_3}$ is the ozone broad–band absorptance from Ramanathan and Dickinson [1979]. The longwave absorptance formulation includes a Voigt line profile effects for $CO_2$ and $O_3$. For the mid-to-upper stratosphere ($p \lesssim$ 10mb), spectral absorption lines are no longer Lorentzian in shape. To account for the transition to Voigt lines a method described in Kiehl and Briegleb [1991] is employed. Essentially the pressure appearing in the mean line width parameter, $\gamma$,

$$\gamma = \gamma_o \frac{p}{p_0} \tag{4.248}$$

is replaced with

$$\gamma = \gamma_0 \left[ \frac{p}{p_0} + \delta \sqrt{\frac{T}{250}} \right], \tag{4.249}$$

where $\delta = 5.0 \times 10^{-3}$ for $CO_2$ and $\delta = 2.5 \times 10^{-3}$ for $O_3$. These values insure agreement with line-by-line cooling rate calculations up to $p \approx 0.3$ mb.

### 4.9.2 Water vapor

Water vapor cannot employ the broad–band absorptance method since $H_2O$ absorption extends throughout the entire longwave region. Thus, we cannot factor out the Planck function dependence as in (4.234). The method of Collins et al. [2002*a*] is used for water–vapor absorptivities and emissivities. This parameterization replaces the scheme developed by Ramanathan and Downey [1986] used in previous versions of the model. The new formulation uses the line-by-line radiative transfer model GENLN3 [Edwards, 1992] to generate the absorptivities and emissivities for $H_2O$. In this version of GENLN3, the parameters for $H_2O$ lines have been obtained from the HITRAN2k data base [Rothman et al., 2003], and the continuum is treated with the Clough, Kneizys, and Davies (CKD) model version 2.4.1 [Clough et al., 1989]. To generate the absorptivity and emissivity, GENLN is used to calculate the transmission through homogeneous atmospheres for $H_2O$ lines alone and for $H_2O$ lines and continuum. The calculation is done for a five dimensional parameter space with coordinates equaling the emission temperature, path temperature, precipitable water, effective relative humidity, and pressure. The limits for each coordinate span the entire range of instantaneous values for the corresponding variable from a 1-year control integration of CAM 3.0. The resulting tables of absorptivity and emissivity are then read into the model for use in the longwave calculations. The overlap treatment between water vapor and other gases is described in Ramanathan and Downey [1986].

The absorptivity and emissivity can be split into terms for the window and non-window portions of the infrared spectrum. The window is defined as 800-1200 $cm^{-1}$, and the non-window is the remainder of the spectrum between 20 to 2200 $cm^{-1}$. Outside the mid-infrared window (the so-called non-window region), the $H_2O$ continuum is dominated by the foreign component [Clough et al., 1992]. The foreign continuum absorption has the same linear scaling with water vapor path as line absorption, and thus in the non-window region the line and continuum absorption are combined in a single expression. In the window region, where the self-broadened component of the continuum is dominant, the line and continuum absorption have different scalings with the amount of water vapor and must be treated separately. The formalism is identical for the absorptivity and emissivity, and for brevity only the absorptivity is discussed in detail. The absorptivity is decomposed into two terms:

$$A(p_1,p_2) \simeq A_w(p_1,p_2) + A_{nw}(p_1,p_2), \tag{4.250}$$

where $A_w(p_1,p_2)$ is the window component and $A_{nw}(p_1,p_2)$ is the non-window component for the portion of the atmosphere bounded by pressures $p_1$ and $p_2$.

Let $\widetilde{A}_{nw}(i)$ represent the total non-window absorption for a homogeneous atmosphere characterized by a set of scaling parameters $i$. Scaling theory is a relationship between an inhomogeneous path and an equivalent homogeneous path with nearly identical line absorption for the spectral band under consideration [Goody and Yung, 1989]. Scaling theory is used to reduce the parameter space of atmospheric conditions that have to be evaluated. The equivalent pressure, temperature, and absorber amount are calculated using the standard Curtis-Godson scaling theory for absorption lines [Curtis, 1952; Godson, 1953]. In addition, we retain explicit dependence on the emission temperature of the radiation following Ramanathan and Downey [1986], and we introduce dependence on an equivalent relative humidity. It follows from Curtis-Godson scaling theory that

$$A_{nw}(p_1,p_2) \simeq \widetilde{A}_{nw}(l_{nw}). \tag{4.251}$$

In the following expressions, a tilde denotes a parameter derived using scaling theory for the equivalence between homogeneous and inhomogeneous atmospheres. The subscript $b$ denotes a parameter which depends upon the spectral band under consideration. The set of scaling parameters that determine the total non-window absorption are labeled:

$$l_{nw} = \left[\widetilde{U_{nw}}, \widetilde{P_{nw}}, T_e, \widetilde{T}_p, \widetilde{\rho}\right]. \tag{4.252}$$

Here $\widetilde{U_{nw}}$ is the pressure-weighted precipitable water, $\widetilde{P_{nw}}$ is the scaled atmospheric pressure, $T_e$ is the emission temperature of radiation, $\widetilde{T}_p$ is the absorber weighted path temperature, and $\widetilde{\rho}$ is the scaled relative humidity. The subscript $(b =)nw$ indicates that the quantities are evaluated for the non-window.

The absorber-weighted path temperature is:

$$\widetilde{T}_p = \frac{1}{W} \int_{p_1}^{p_2} T(p)\, dW(p), \tag{4.253}$$

where $T(p)$ is the thermodynamic temperature of the atmosphere at pressure $p$. The $H_2O$ path or precipitable water is:

$$\begin{aligned} W &= \int_{p_1}^{p_2} dW(p) \qquad [g/cm^2] \\ dW(p) &= q(p)\, dp/g, \end{aligned} \tag{4.254}$$

where $q(p)$ is the specific humidity at pressure $p$ and $g$ is the acceleration of gravity. The $H_2O$ path and pressure for a homogeneous atmosphere with equivalent line absorption are [Goody and Yung, 1989]

$$\widetilde{W}_b = \int_{p_1}^{p_2} \frac{\phi_b(T)}{\phi_b\left(\widetilde{T}_p\right)} \, dW(p) \tag{4.255}$$

$$\widetilde{P}_b = \frac{1}{\widetilde{W}_b} \int_{p_1}^{p_2} \frac{\psi_b(T)}{\psi_b\left(\widetilde{T}_p\right)} \, p \, dW(p), \tag{4.256}$$

where

$$\phi_b(T) = \sum_{k=1}^{N} S_k(T) \tag{4.257}$$

$$\psi_b(T) = \left\{ \sum_{k=1}^{N} [S_k(T)\alpha_k(T)]^{1/2} \right\}^2 . \tag{4.258}$$

The factor $S_k(T)$ is the line strength for each line $k$ in the spectral interval under consideration. The characteristic width of each line at a reference pressure $p_0$ and specific humidity $q_0$ is $\alpha_k(T)$. It is convenient to calculate the absorptance in terms of a pressure-weighted $H_2O$ path

$$U = \int_{p_1}^{p_2} \frac{p}{p_0} \, dW(p) \tag{4.259}$$

The equivalent pressure-weighted $H_2O$ path is simply

$$\widetilde{U}_b = \frac{\widetilde{P}_b}{p_0} \widetilde{W}_b \tag{4.260}$$

Although the relative humidity (or $H_2O$ vapor pressure) is not included in standard Curtis-Godson scaling theory, it must be treated as an independent parameter since the vapor pressure determines the self-broadening of lines and the strength of the self-continuum. The effective relative humidity $\widetilde{\rho}$ is defined in terms of an effective $H_2O$ specific humidity $\widetilde{q}$ and saturation specific humidity $\widetilde{q}_s$ along the path:

$$\widetilde{\rho} = \frac{\widetilde{q}}{\widetilde{q}_s} \tag{4.261}$$

$$\widetilde{q} = \frac{g\,W}{p_2 - p_1} \tag{4.262}$$

$$\widetilde{q}_s = \frac{\epsilon \, e_s(\widetilde{T}_p)}{\widetilde{P} - (1-\epsilon) e_s(\widetilde{T}_p)} \tag{4.263}$$

$$\widetilde{P} = \frac{p_0 \, U}{W} \tag{4.264}$$

where $e_s(T)$ is the saturation vapor pressure at temperature $T$, $\widetilde{P}$ is an effective pressure, and $\epsilon = 0.622$ is the ratio of gas constants for air and water vapor.

The window term $A_w(p_1, p_2)$ requires a special provision for the different path parameters for the lines and continuum. Let

$$\begin{aligned} \widetilde{A}_w(i) &= \text{absorptivity for path parameters } i\text{, lines and continuum} \\ \widetilde{A}'_w(i) &= \text{absorptivity for path parameters } i\text{, lines only} \end{aligned} \tag{4.265}$$

The set of parameters for the line absorption in the window region are:

$$l_w = \left[\widetilde{U_w}, \widetilde{P_w}, T_e, \widetilde{T}_p, \widetilde{\rho}\right] \tag{4.266}$$

The set of scaling parameters that determine the continuum absorption in the window are:

$$c_w = \left[U', \widetilde{P_w}, T_e, \widetilde{T}_p, \widetilde{\rho}\right] \tag{4.267}$$

For the continuum, the pressure-weighted path length is calculated using:

$$U' = \frac{\epsilon}{\widetilde{q}} \frac{C_s(\bar{\nu}, T_{ref})}{C_s(\bar{\nu}, \widetilde{T}_p)} U_c \tag{4.268}$$

where $T_{ref} = 296K$ is a reference temperature, $\bar{\nu}$ is a suitably chosen wavenumber inside the window, $U_c$ is the self-continuum path length, and $C_s(\nu, T)$ is the self continuum absorption coefficient. The self-continuum path length may be approximated by

$$U_c = \int_{p_1}^{p_2} \frac{q}{\epsilon} \frac{p}{p_0} \frac{C_s(\bar{\nu}, T)}{C_s(\bar{\nu}, T_{ref})} \, dW(p) \tag{4.269}$$

The lines-only absorptivity can be written in terms of a line transmission factor $L(i)$ and an asymptotic absorptivity $A_{w,\infty}$ in the limit of a black-body atmosphere. $A_{w,\infty}$ is a function only of $T_e$ [Ramanathan and Downey, 1986]. The relationship is

$$\widetilde{A}'_w(i) = A_{w,\infty}[1 - L(i)] \tag{4.270}$$

Define an effective continuum transmission $C(i)$ by setting

$$\widetilde{A}_w(i) = A_{w,\infty}[1 - L(i)C(i)] \tag{4.271}$$

We approximate the window absorptivity by:

$$A_w(p_1, p_2) \simeq A_{w,\infty}[1 - L(l_w)C(c_w)] \tag{4.272}$$

This approximation for $A_w(p_1, p_2)$ can be cast entirely in terms of the absorptivities defined in equation 4.265. From equations 4.270 and 4.271, the line and continuum transmission are:

$$\begin{aligned} L(l_w) &= 1 - \frac{\widetilde{A}'_w(l_w)}{A_{w,\infty}} \\ C(c_w) &= \frac{A_{w,\infty} - \widetilde{A}_w(c_w)}{A_{w,\infty} - \widetilde{A}'_w(c_w)} \end{aligned} \tag{4.273}$$

In the presence of stratospheric volcanic aerosols, the expressions for the absorptivity become:

$$\begin{aligned} A_{nw}(p_1,p_2) &\simeq A_{nw,\infty}\left[1-\left(1-\frac{\widetilde{A}_{nw}(l_{nw})}{A_{nw,\infty}}\right)\mathcal{T}^{nw}_{H_2SO_4}\right] \\ A_{w}(p_1,p_2) &\simeq A_{w,\infty}[1-L(l_w)C(c_w)\mathcal{T}^{w}_{H_2SO_4}] \end{aligned} \tag{4.274}$$

The volcanic transmission factor is

$$\mathcal{T}^{b}_{H_2SO_4} = \bar{\mathcal{T}}^{b}_{H_2SO_4} = \exp\left(-D\,\kappa_{b,volc}\,W_{volc}\right) \tag{4.275}$$

where $D = 1.66$ is the diffusivity factor, $\kappa_{b,volc}$ is an effective specific extinction for the band, and $W_{volc}$ is the mass path of the volcanic aerosols. The extinction $\kappa_{b,volc}$ has been adjusted iteratively to reproduce the heating rates calculated using the spectral bands in the original [Ramanathan and Downey, 1986] parameterization. This completes the set of approximations used to calculate the absorptivity (and by extension the emissivity).

### 4.9.3 Trace gas parameterizations

**Methane.** The radiative effects of methane are represented by the last term in (4.241). We re-write this in terms of the absorptivity due to methane as

$$\begin{aligned} \int_{1170}^{1500}(1-\mathcal{T}_{CH_4}\mathcal{T}^3_{N_2O}\mathcal{T}_{H_2O}\mathcal{T}^5_{H_2SO_4})F(B_\nu)d\nu &= \int(1-\mathcal{T}_{H_2O}\mathcal{T}^{nw}_{H_2SO_4})F(B_\nu)d\nu + \\ \int\mathcal{A}_{CH_4}\mathcal{T}_{H_2O}\mathcal{T}^5_{H_2SO_4}F(B_\nu)d\nu &+ \int\mathcal{A}^3_{N_2O}\mathcal{T}_{CH_4}\mathcal{T}_{H_2O}\mathcal{T}^5_{H_2SO_4}F(B_\nu)d\nu \end{aligned} \tag{4.276}$$

Note that this expression also incorporates the absorptance due to the 7.7 micron band of nitrous oxide as well. The first term is due to the rotation band of water vapor and is already accounted for in the CAM 3.0 radiation model by the parameterization described in Ramanathan and Downey [1986]. The second term in (4.276) accounts for the absorptance due to the 7.7 micron band of methane. The spectroscopic parameters are from Donner and Ramanathan [1980]. In terms of the broad band approximation we have,

$$\int\mathcal{A}_{CH_4}\mathcal{T}_{H_2O}\mathcal{T}^5_{H_2SO_4}F(B_\nu)d\nu \approx A_{CH_4}\bar{T}_{H_2O}\bar{T}^5_{H_2SO_4}F(B_{\bar{\nu}}) \tag{4.277}$$

where according to (4.235),

$$A_{CH_4} = 6.00444\sqrt{T_p}\ln\left\{1+\frac{u}{\sqrt{4+u(1+1/\beta)}}\right\} \tag{4.278}$$

where $T_p$ is a path weighted temperature,

$$T_p = \frac{\int T(p)dp}{\int dp} \tag{4.279}$$

The dimensionless path length is,

$$u = \frac{D\;8.60957\times10^4}{g}\int\frac{\mu_{CH_4}}{\sqrt{T}}dp \tag{4.280}$$

and the mean line width factor is,

$$\beta = 2.94449 \frac{\int \frac{1}{T}\left(\frac{P}{P_0}\right)\mu_{CH_4} dp}{\int \frac{1}{\sqrt{T}}\mu_{CH_4} dp} \tag{4.281}$$

where $\mu_{CH_4}$ is the mass mixing ratio of methane, $T$ is the local layer temperature in Kelvin and $P$ is the pressure in Pascals, and $P_0$ is $1 \times 10^5$ Pa. $D$ is a diffusivity factor of 1.66. The water vapor overlap factor for this spectral region is,

$$\bar{T}_{H_2O} = \exp(-U_{H_2O}) \tag{4.282}$$

where,

$$U_{H_2O} = D \int \mu_{H_2O} \left(\frac{P}{P_0}\right) \frac{dp}{g} \tag{4.283}$$

and $\mu_{H_2O}$ is the mass mixing ratio of water vapor.

**Nitrous Oxide.** For nitrous oxide there are three absorption bands of interest: 589, 1168 and 1285 cm$^{-1}$ bands. The radiative effects of the 1285 cm$^{-1}$ band is given by the last term in (4.276),

$$\int \mathcal{A}^3_{N_2O}\mathcal{T}_{CH_4}\mathcal{T}_{H_2O}\mathcal{T}^5_{H_2SO_4}F(B_\nu)d\nu \approx A^3_{N_2O}\bar{T}_{CH_4}\bar{T}_{H_2O}\bar{T}^5_{H_2SO_4}F(B_{\bar{\nu}}) \tag{4.284}$$

The absorptance for the 1285 cm$^{-1}$ $N_2O$ band is given by

$$A^3_{N_2O} = 2.35558\sqrt{T_p}\ln\left\{1 + \frac{u^3_0}{\sqrt{4 + u^3_0(1 + 1/\beta^3_0)}} + \frac{u^3_1}{\sqrt{4 + u^3_1(1 + 1/\beta^3_1)}}\right\} \tag{4.285}$$

where $u^3_0$, $\beta^3_0$ account for the fundamental transition, while $u^3_1$, $\beta^3_1$ account for the first "hot" band transition. These parameters are defined as

$$u^3_0 = D\ 1.02346 \times 10^5 \int \frac{\mu_{N_2O}}{\sqrt{T}}\frac{dp}{g} \tag{4.286}$$

and,

$$\beta^3_0 = 19.399 \frac{\int \frac{1}{\sqrt{T}}\left(\frac{P}{P_0}\right) du_0}{\int du^3_0} \tag{4.287}$$

While the "hot" band parameters are defined as

$$u^3_1 = D\ 2.06646 \times 10^5 \int \frac{1}{\sqrt{T}} e^{-847.36/T}\mu_{N_2O}\frac{dp}{g} \tag{4.288}$$

and,

$$\beta^3_1 = 19.399 \frac{\int \frac{1}{\sqrt{T}}\left(\frac{P}{P_0}\right) du^3_1}{\int du^3_1} \tag{4.289}$$

The overlap factors in (4.284) due to water vapor is the same factor defined by (4.282), while the overlap due to methane is obtained by using the definition of the transmission factor in terms of the equivalent width [Ramanathan, 1976].

$$\bar{T}_{CH_4} = e^{-A_{CH_4}/2A_0} \tag{4.290}$$

Substitution of (4.278) into (4.284) leads to,

$$\bar{T}_{CH_4} = \frac{1}{1 + 0.02\frac{u}{\sqrt{4+u(1+1/\beta)}}} \tag{4.291}$$

where $u$ and $\beta$ are given by (4.280) and (4.281), respectively, and the 0.02 factor is an empirical constant to match the overlap effect obtained from narrow band model benchmark calculations. This factor can physically be justified as accounting for the fact that the entire methane band does not overlap the $N_2O$ band.

The 1168 cm$^{-1}$ $N_2O$ band system is represented by the seventh term on the RHS of (4.241). This term can be re-written as

$$\int_{1120}^{1170} (1 - \mathcal{T}^4_{CFC12}\mathcal{T}_{H_2O}\mathcal{T}^4_{H_2SO_4}\mathcal{T}^2_{N_2O})F(B_\nu)d\nu = \int (1 - \mathcal{T}_{H_2O}\mathcal{T}^w_{H_2SO_4})F(B_\nu)d\nu +$$

$$\int \mathcal{A}^4_{CFC12}\mathcal{T}_{H_2O}\mathcal{T}^4_{H_2SO_4}F(B_\nu)d\nu + \int \mathcal{A}^2_{N_2O}\mathcal{T}^4_{CFC12}\mathcal{T}_{H_2O}\mathcal{T}^4_{H_2SO_4}F(B_\nu)d\nu \tag{4.292}$$

where the last term accounts for the 1168 cm$^{-1}$ $N_2O$ band. For the broad band formulation this expression becomes,

$$\int \mathcal{A}^2_{N_2O}\mathcal{T}^4_{CFC12}\mathcal{T}_{H_2O}\mathcal{T}^4_{H_2SO_4}F(B_\nu)d\nu \approx A^2_{N_2O}\bar{T}^4_{CFC12}\bar{T}_{H_2O}\bar{T}^4_{H_2SO_4}F(B_{\bar{\nu}}) \tag{4.293}$$

The band absorptance for the 1168 cm$^{-1}$ $N_2O$ band is given by

$$A^2_{N_2O} = 2.54034\sqrt{T_p}\ln\left\{1 + \frac{u^2_0}{\sqrt{4 + u^2_0(1 + 1/\beta^2_0}}\right\} \tag{4.294}$$

where the fundamental band path length and mean line parameters can be simply expressed in terms of the parameters defined for the 1285 cm$^{-1}$ band (eq. 4.286-4.287).

$$u^2_0 = 0.0333767u^3_0 \tag{4.295}$$

and,

$$\beta^2_0 = 0.982143\beta^3_0 \tag{4.296}$$

Note that the 1168 cm$^{-1}$ band does not include a "hot" band transition. The overlap by water vapor includes the effects of water vapor rotation lines, the so called "e-type" and "p-type" continua (e.g. Roberts et al. [1976]). The combined effect of these three absorption features is,

$$\bar{T}_{H_2O} = \bar{T}_l\bar{T}_e\bar{T}_p \tag{4.297}$$

where the contribution by line absorption is modeled by a Malkmus model formulation,

$$\bar{T}_l = \exp\left\{-\delta_1\bar{\Pi}\left(\sqrt{1+\delta_2\frac{\bar{u}_l}{\bar{\Pi}}}-1\right)\right\} \tag{4.298}$$

where $\delta_1$ and $\delta_2$ are coefficients that are obtained by fitting (4.298) to the averaged transmission from a 10 cm$^{-1}$ narrow band Malkmus. The path length $\bar{u}_l$ is,

$$\bar{u}_l = D\,\bar{\Phi}\int \rho_w\frac{dP}{g} \tag{4.299}$$

and,

$$\bar{\Pi} = \left(\frac{P}{P_0}\right)\left(\frac{\bar{\Psi}}{\bar{\Phi}}\right), \tag{4.300}$$

where $\bar{\Phi}$ and $\bar{\Psi}$ account for the temperature dependence of the spectroscopic parameters [Rodgers and Walshaw, 1966]

$$\bar{\Psi} = e^{-\alpha|T_p-250|-\beta|T_p-250|^2} \tag{4.301}$$

$$\bar{\Phi} = e^{-\alpha'|T_p-250|-\beta'|T_p-250|^2} \tag{4.302}$$

The coefficients for various spectral intervals are given in Table 4.3. The transmission due to the e-type continuum is given by

$$\bar{T}_e = e^{-\delta_3\bar{u}_e} \tag{4.303}$$

where the path length is defined as

$$\bar{u}_e = \frac{D}{P_0\varepsilon g}\int e^{1800(\frac{1}{T}-\frac{1}{296})}w_{H_2O}^2 P dP \tag{4.304}$$

The p-type continuum is represented by

$$T_p = e^{-\delta_4\bar{u}_p} \tag{4.305}$$

where,

$$\bar{u}_p = \frac{D}{gP_0}\int e^{1800(\frac{1}{T}-\frac{1}{296})}w_{H_2O} P dP \tag{4.306}$$

The factors $\delta_1$, $\delta_2$, $\delta_3$ and $\delta_4$ are listed for specific spectral intervals in Table 4.4.

The final $N_2O$ band centered at 589 cm$^{-1}$ is represented by the first term on the RHS of (4.241),

$$\int_{500}^{750}(1-\mathcal{T}^1_{CO_2}\mathcal{T}^1_{N_2O}\mathcal{T}_{H_2O}\mathcal{T}^1_{H_2SO_4})F(B_\nu)d\nu =$$

$$\int(1-\mathcal{T}^1_{CO_2}\mathcal{T}_{H_2O}\mathcal{T}^1_{H_2SO_4})F(B_\nu)d\nu + \int \mathcal{A}^1_{N_2O}\mathcal{T}^1_{CO_2}\mathcal{T}_{H_2O}\mathcal{T}^1_{H_2SO_4}F(B_\nu)d\nu \tag{4.307}$$

Table 4.3: Coefficients for the Temperature Dependence Factors in (4.301) and (4.302).

| Index | $\nu_1 - \nu_2$ | $\alpha$ | $\beta$ | $\alpha'$ | $\beta'$ |
|---|---|---|---|---|---|
| 1 | 750 - 820 | 2.9129e-2 | -1.3139e-4 | 3.0857e-2 | -1.3512e-4 |
| 2 | 820 - 880 | 2.4101e-2 | -5.5688e-5 | 2.3524e-2 | -6.8320e-5 |
| 3 | 880 - 900 | 1.9821e-2 | -4.6380e-5 | 1.7310e-2 | -3.2609e-5 |
| 4 | 900 - 1000 | 2.6904e-2 | -8.0362e-5 | 2.6661e-2 | -1.0228e-5 |
| 5 | 1000 - 1120 | 2.9458e-2 | -1.0115e-4 | 2.8074e-2 | -9.5743e-5 |
| 6 | 1120 - 1170 | 1.9892e-2 | -8.8061e-5 | 2.2915e-2 | -1.0304e-4 |

Table 4.4: Coefficients for the broad-band water vapor overlap transmission factors.

| Index | $\nu_1 - \nu_2$ | $\delta_1$ | $\delta_2$ | $\delta_3$ | $\delta_4$ |
|---|---|---|---|---|---|
| 1 | 750 - 820 | 0.0468556 | 14.4832 | 26.1891 | 0.0261782 |
| 2 | 820 - 880 | 0.0397454 | 4.30242 | 18.4476 | 0.0369516 |
| 3 | 880 - 900 | 0.0407664 | 5.23523 | 15.3633 | 0.0307266 |
| 4 | 900 - 1000 | 0.0304380 | 3.25342 | 12.1927 | 0.0243854 |
| 5 | 1000 - 1120 | 0.0540398 | 0.698935 | 9.14992 | 0.0182932 |
| 6 | 1120 - 1170 | 0.0321962 | 16.5599 | 8.07092 | 0.0161418 |

where the last term in (4.307) represents the radiative effects of the 589 cm$^{-1}$ $N_2O$ band,

$$\int \mathcal{A}^1_{N_2O}\mathcal{T}^1_{CO_2}\mathcal{T}_{H_2O}\mathcal{T}^1_{H_2SO_4}F(B_\nu)d\nu \approx A^1_{N_2O}\bar{T}^1_{CO_2}\bar{T}_{H_2O}\bar{T}^1_{H_2SO_4}F(B_{\bar{\nu}}) \tag{4.308}$$

The absorptance for this band includes both the fundamental and hot band transitions,

$$A^1_{N_2O} = 2.65581\sqrt{T_p}\ln\left\{1 + \frac{u^1_0}{\sqrt{4 + u^1_0(1 + 1/\beta^1_0)}} + \frac{u^1_1}{\sqrt{4 + u^1_1(1 + 1/\beta^1_1)}}\right\} \tag{4.309}$$

where the path lengths for this band can also be defined in terms of the 1285 cm$^{-1}$ band path length and mean lines parameters (4.286 - 4.289),

$$u^1_0 = 0.100090u^3_0 \tag{4.310}$$

and,

$$\beta^1_0 = 0.964282\beta^3_0 \tag{4.311}$$

and,

$$u^1_1 = 0.0992746u^3_1 \tag{4.312}$$

and,

$$\beta^1_1 = 0.964282\beta^3_1 \tag{4.313}$$

The overlap effect of water vapor is given by the transmission factor for the 500 to 800 cm$^{-1}$ spectral region defined by Ramanathan and Downey [1986] in their Table A2. This expression is thus consistent with the transmission factor for this spectral region employed for the water vapor formulation of the first term on the right hand side of (4.307). The overlap factor due to the $CO_2$ bands near 589 cm$^{-1}$ is obtained from the formulation in Kiehl and Briegleb [1991],

$$\bar{T}^1_{CO_2} = \frac{1}{1 + 0.2\frac{u_{CO_2}}{\sqrt{4+u_{CO_2}(1+1/\beta_{CO_2})}}} \tag{4.314}$$

where the functional form is obtained in the same manner as the transmission factor for $CH_4$ was determined in (4.290). The 0.2 factor is empirically determined by comparing (4.314) with results from 5 cm$^{-1}$ Malkmus narrow band calculations. The path length parameters are given by

$$u_{CO_2} = \frac{D\ 4.9411 \times 10^4(1 - e^{-960/T})^3}{\sqrt{T_p}}e^{-960/T}\int w_{CO_2}\frac{dP}{g} \tag{4.315}$$

and,

$$\beta_{CO_2} = \frac{5.3228}{\sqrt{T_p}}\left\{\frac{P}{P_0} + 5 \times e^{-3}\sqrt{\frac{T}{250}\frac{T}{300}}\right\} \tag{4.316}$$

**CFCs.** The effects of both CFC11 and CFC12 are included by using the approach of Ramanathan et al. [1985]. Thus, the band absorptance of the CFCs is given by

$$A_{CFC} = \Delta\nu \left(1 - e^{-D\frac{S}{\Delta\nu}u_{CFC}}\right) \tag{4.317}$$

where $\Delta\nu$ is the width of the CFC absorption band, $S$ is the band strength, $u_{CFC}$ is the abundance of CFC (g cm$^{-2}$),

$$u_{CFC} = \int \mu_{CFC}\frac{dp}{g} \tag{4.318}$$

where $\mu_{CFC}$ is the mass mixing ratio of either CFC11 or CFC12. $D$ is the diffusivity factor. In the linear limit $D = 2$, since (4.317) deviates slightly from the pure linear limit we let $D = 1.8$. We account for the radiative effects of four bands due to CFC11 and four bands due to CFC12. The band parameters used in (4.317) for these eighth bands are given in Table 4.5.

The contribution by these CFC absorption bands is accounted for by the following terms in (4.241).

$$\int_{750}^{820} (1 - \mathcal{T}^1_{CFC11}\mathcal{T}_{H_2O}\mathcal{T}^*_{H_2SO_4})F(B_\nu)d\nu = \int (1 - \mathcal{T}_{H_2O}\mathcal{T}^{nw}_{H_2SO_4})F(B_\nu)d\nu + \int \mathcal{A}^1_{CFC11}\mathcal{T}_{H_2O}\mathcal{T}^*_{H_2SO_4}F(B_\nu)d\nu \quad (4.319)$$

$$\int_{820}^{880} (1 - \mathcal{T}^2_{CFC11}\mathcal{T}_{H_2O}\mathcal{T}^3_{H_2SO_4})F(B_\nu)d\nu = \int (1 - \mathcal{T}_{H_2O}\mathcal{T}^{w}_{H_2SO_4})F(B_\nu)d\nu + \int \mathcal{A}^2_{CFC11}\mathcal{T}_{H_2O}\mathcal{T}^3_{H_2SO_4}F(B_\nu)d\nu \quad (4.320)$$

$$\int_{880}^{900} (1 - \mathcal{T}^1_{CFC12}\mathcal{T}_{H_2O}\mathcal{T}^3_{H_2SO_4})F(B_\nu)d\nu = \int (1 - \mathcal{T}_{H_2O}\mathcal{T}^{w}_{H_2SO_4})F(B_\nu)d\nu + \int \mathcal{A}^1_{CFC12}\mathcal{T}_{H_2O}\mathcal{T}^3_{H_2SO_4}F(B_\nu)d\nu \quad (4.321)$$

$$\begin{aligned}\int_{900}^{1000} (1 - \mathcal{T}^2_{CO_2}\mathcal{T}_{H_2O}\mathcal{T}^3_{H_2SO_4}\mathcal{T}^3_{CFC11}\mathcal{T}^2_{CFC12})F(B_\nu)d\nu &= \int (1 - \mathcal{T}_{H_2O}\mathcal{T}^{w}_{H_2SO_4})F(B_\nu)d\nu \\ + \int \mathcal{A}^2_{CFC12}\mathcal{T}_{H_2O}\mathcal{T}^3_{H_2SO_4}F(B_\nu)d\nu &+ \int \mathcal{A}^3_{CFC11}\mathcal{T}_{H_2O}\mathcal{T}^3_{H_2SO_4}\mathcal{T}^2_{CFC12}F(B_\nu)d\nu \quad (4.322) \\ &+ \int \mathcal{A}^2_{CO_2}\mathcal{T}_{H_2O}\mathcal{T}^3_{H_2SO_4}\mathcal{T}^3_{CFC11}\mathcal{T}^2_{CFC12}F(B_\nu)d\nu\end{aligned}$$

$$\begin{aligned}\int_{1000}^{1120} (1 - \mathcal{T}^3_{CO_2}\mathcal{T}_{O_3}\mathcal{T}_{H_2O}\mathcal{T}^4_{H_2SO_4}\mathcal{T}^4_{CFC11}\mathcal{T}^3_{CFC12})F(B_\nu)d\nu &= \int (1 - \mathcal{T}_{H_2O}\mathcal{T}^{w}_{H_2SO_4})F(B_\nu)d\nu \\ + \int \mathcal{A}_{O_3}\mathcal{T}_{H_2O}\mathcal{T}^4_{H_2SO_4}F(B_\nu)d\nu &+ \int \mathcal{A}^3_{CO_2}\mathcal{T}_{O_3}\mathcal{T}_{H_2O}\mathcal{T}^4_{H_2SO_4}\mathcal{T}^4_{CFC11}\mathcal{T}^3_{CFC12}F(B_\nu)d\nu \\ + \int \mathcal{A}^4_{CFC11}\mathcal{T}_{O_3}\mathcal{T}_{H_2O}\mathcal{T}^4_{H_2SO_4}F(B_\nu)d\nu &+ \int \mathcal{A}^3_{CFC12}\mathcal{T}_{O_3}\mathcal{T}_{H_2O}\mathcal{T}^4_{H_2SO_4}F(B_\nu)d\nu \quad (4.323)\end{aligned}$$

For the 798 cm$^{-1}$ CFC11 band, the absorption effect is given by the second term on the right hand side of (4.319),

$$\int \mathcal{A}^1_{CFC11}\mathcal{T}_{H_2O}\mathcal{T}^*_{H_2SO_4}F(B_\nu)d\nu \approx A^1_{CFC11}\bar{T}_{H_2O}\bar{T}^*_{H_2SO_4}F(B_{\bar{\nu}}) \quad (4.324)$$

where the band absorptance for the CFC is given by (4.317) and the overlap factor due to water vapor is given by (4.297) using the index 1 factors from Tables 4.3 and 4.4. Similarly, the 846 cm$^{-1}$ CFC11 band is represented by the second term on the RHS of (4.320),

$$\int \mathcal{A}^2_{CFC11}\mathcal{T}_{H_2O}\mathcal{T}^3_{H_2SO_4}F(B_\nu)d\nu \approx A^2_{CFC11}\bar{T}_{H_2O}\bar{T}^3_{H_2SO_4}F(B_{\bar{\nu}}) \quad (4.325)$$

where the $H_2O$ overlap factor is given by index 2 in Tables 4.3 and 4.4. The 933 cm$^{-1}$ CFC11

Table 4.5: Band Parameters for the CFCs transmission factors.

| Band Number | Band Center ($cm^{-1}$) | $\Delta\nu$ ($cm^{-1}$) | $S/\Delta\nu$ ($cm^2$ $gm^{-1}$) |
|---|---|---|---|
| | CFC11 | | |
| 1[1] | 798 | 50 | 54.09 |
| 2[2] | 846 | 60 | 5130.03 |
| 3[1] | 933 | 60 | 175.005 |
| 4[2] | 1085 | 100 | 1202.18 |
| | CFC12 | | |
| 1[1] | 889 | 45 | 1272.35 |
| 2[2] | 923 | 50 | 5786.73 |
| 3[2] | 1102 | 80 | 2873.51 |
| 4[2] | 1161 | 70 | 2085.59 |

[1] Data are from Kagann et al. [1983].
[2] Data are from Varanasi and Chudamani [1988].

band is given by the third term on the RHS of (4.322),

$$\int \mathcal{A}^3_{CFC11}\mathcal{T}_{H_2O}\mathcal{T}^3_{H_2SO_4}\mathcal{T}^2_{CFC12}F(B_\nu)d\nu \approx A^3_{CFC11}\bar{T}_{H_2O}\bar{T}^3_{H_2SO_4}T^2_{CFC12}F(B_{\bar{\nu}}) \tag{4.326}$$

where the $H_2O$ overlap factor is defined as index 4 in Tables 4.3 and 4.4, and the CFC12 transmission factor is obtained from (4.317). The final CFC11 band centered at 1085 $cm^{-1}$ is represented by the fourth term on the RHS of (4.323),

$$\int \mathcal{A}^4_{CFC11}\mathcal{T}_{O_3}\mathcal{T}_{H_2O}\mathcal{T}^4_{H_2SO_4}F(B_\nu)d\nu \approx A^4_{CFC11}\bar{T}_{O_3}\bar{T}_{H_2O}\bar{T}^4_{H_2SO_4}F(B_{\bar{\nu}}) \tag{4.327}$$

where the transmission due to the 9.6 micron ozone band is defined similar to (4.314) for $CO_2$ as

$$\bar{T}_{O_3} = \frac{1}{1 + \sum_{i=1}^{2} \frac{u^i_{O_3}}{\sqrt{4 + u^i_{O_3}(1 + 1/\beta^i_{O_3})}}} \tag{4.328}$$

where the path lengths are defined in Ramanathan and Dickinson [1979]. The $H_2O$ overlap factor is defined by index 5 in Tables 4.3 and 4.4.

For the 889 $cm^{-1}$ CFC12 band the absorption is defined by the second term in (4.321) as

$$\int \mathcal{A}^1_{CFC12}\mathcal{T}_{H_2O}\mathcal{T}^3_{H_2SO_4}F(B_\nu)d\nu \approx A^1_{CFC12}\bar{T}_{H_2O}\bar{T}^3_{H_2SO_4}F(B_{\bar{\nu}}) \tag{4.329}$$

where the $H_2O$ overlap factor is defined by index 3 of Tables 4.3 and 4.4, and the CFC absorptance is given by (4.317). The 923 $cm^{-1}$ CFC12 band is described by the second term in

(4.322),

$$\int \mathcal{A}^2_{CFC12}\mathcal{T}_{H_2O}\mathcal{T}^3_{H_2SO_4}F(B_\nu)d\nu \approx A^2_{CFC12}\bar{T}_{H_2O}\bar{T}^3_{H_2SO_4}F(B_{\bar{\nu}}) \tag{4.330}$$

where the $H_2O$ overlap is defined as index 4 in Tables 4.3 and 4.4. The 1102 cm$^{-1}$ CFC12 band is represented by the last term on the RHS of (4.323),

$$\int \mathcal{A}^3_{CFC12}\mathcal{T}_{O_3}\mathcal{T}_{H_2O}\mathcal{T}^4_{H_2SO_4}F(B_\nu)d\nu \approx A^3_{CFC12}\bar{T}_{O_3}\bar{T}_{H_2O}\bar{T}^4_{H_2SO_4}F(B_{\bar{\nu}}) \tag{4.331}$$

where the transmission by ozone is described by (4.328) and the $H_2O$ overlap factor is represented by index 5 in Tables 4.3 and 4.4. The final CFC12 band at 1161 cm$^{-1}$ is represented by the second term on the RHS of (4.292),

$$\int \mathcal{A}^4_{CFC12}\mathcal{T}_{H_2O}\mathcal{T}^4_{H_2SO_4}F(B_\nu)d\nu \approx A^4_{CFC12}\bar{T}_{H_2O}\bar{T}^4_{H_2SO_4}F(B_{\bar{\nu}}) \tag{4.332}$$

where the $H_2O$ overlap factor is defined as index 6 in Tables 4.3 and 4.4.

**Minor $CO_2$ Bands.** There are two minor bands of carbon dioxide that were added to the CCM3 longwave model. These bands play a minor role in the present day radiative budget, but are very important for high levels of $CO_2$, such as during the Archean. The first band we consider is centered at 961 cm$^{-1}$. The radiative contribution of this band is represented by the last term in (4.322),

$$\int \mathcal{A}^2_{CO_2}\mathcal{T}_{H_2O}\mathcal{T}^3_{H_2SO_4}\mathcal{T}^3_{CFC11}\mathcal{T}^2_{CFC12}F(B_\nu)d\nu \approx A^2_{CO_2}\bar{T}_{H_2O}\bar{T}^3_{H_2SO_4}\bar{T}^3_{CFC11}\bar{T}^2_{CFC12}F(B_{\bar{\nu}}) \tag{4.333}$$

where the transmission factors for water vapor, CFC11 and CFC12 are defined in the previous section for the 900 to 1000 cm$^{-1}$ spectral interval. The absorptance due to $CO_2$ is given by

$$A^2_{CO_2} = 3.8443\sqrt{T_p}\ln\left\{1+\sum_{i=1}^{3}\frac{u_i}{\sqrt{4+u_i(1+1/\beta_i)}}\right\} \tag{4.334}$$

where the path length parameters are defined as

$$\begin{aligned} u_1 &= 3.88984\times10^3\alpha(T_p)we^{-1997.6/T} && (4.335)\\ u_1 &= 3.88984\times10^3\alpha(T_p)we^{-1997.6/T} && (4.336)\\ u_3 &= 6.50642\times10^3\alpha(T_p)we^{-2989.7/T} && (4.337)\end{aligned}$$

and the pressure parameter is,

$$\begin{aligned} \beta_1 &= 2.97558\left(\frac{P}{P_0}\right)\frac{1}{\sqrt{T}} && (4.338)\\ \beta_2 &= \beta_1 && (4.339)\\ \beta_3 &= 2\beta_1 && (4.340)\end{aligned}$$

and,

$$\alpha(T_p) = \frac{\left(1 - e^{-1360.0/T_p}\right)^3}{\sqrt{T_p}} \tag{4.341}$$

The $CO_2$ band centered at 1064 cm$^{-1}$ is represented by the third term on the RHS of (4.323),

$$\int \mathcal{A}^3_{CO_2} \mathcal{T}_{O_3} \mathcal{T}_{H_2O} \mathcal{T}^4_{H_2SO_4} \mathcal{T}^4_{CFC11} \mathcal{T}^3_{CFC12} F(B_\nu) d\nu \approx A^3_{CO_2} \bar{T}_{O_3} \bar{T}_{H_2O} \bar{T}^4_{H_2SO_4} \bar{T}^4_{CFC11} \bar{T}^3_{CFC12} F(B_{\bar{\nu}}) \tag{4.342}$$

where the transmission factors due to ozone, water vapor, CFC11 and CFC12 are defined in the previous section. The absorptance due to the 1064 cm$^{-1}$ $CO_2$ band is given by

$$A^3_{CO_2} = 3.8443\sqrt{T_p} \ln \left\{ 1 + \sum_{i=1}^{3} \frac{u_i}{\sqrt{4 + u_i(1 + 1/\beta_i)}} \right\} \tag{4.343}$$

where the dimensionless path length is defined as

$$u_1 = 3.42217 \times 10^3 \alpha(T_p) w e^{-1849.7/T} \tag{4.344}$$
$$u_2 = 6.02454 \times 10^3 \alpha(T_p) w e^{-2782.1/T} \tag{4.345}$$
$$u_3 = 5.53143 \times 10^3 \alpha(T_p) w e^{-3723.2/T} \tag{4.346}$$

where

$$\alpha(T_p) = \frac{\left(1 - e^{-1540.0/T_p}\right)^3}{\sqrt{T_p}} \tag{4.347}$$

The pressure factor, $\beta_1$, for (4.343) is the same as defined in (4.338), while the other factors are,

$$\beta_2 = 2\beta_1 \tag{4.348}$$
$$\beta_3 = \beta_2 \tag{4.349}$$

In the above expressions, $w$ is the column mass abundance of $CO_2$,

$$w = \int \mu_{CO_2} \frac{dP}{g} = \frac{\mu_{CO_2}}{g} \Delta P \tag{4.350}$$

where $\mu_{CO_2}$ is the mass mixing ratio of $CO_2$ (assumed constant).

### 4.9.4 Mixing ratio of trace gases

The mixing ratios of methane, nitrous oxide, CFC11 and CFC12 are specified as zonally averaged quantities. The stratospheric mixing ratios of these various gases do vary with latitude. This is to mimic the effects of stratospheric circulation on these tracers. The exact latitude dependence of the mixing ratio scale height was based on information from a two dimensional chemical model (S. Solomon, personal communication). In the troposphere the gases are assumed to be well mixed,

$$\begin{aligned} \mu^0_{CH_4} &= 0.55241 w_{CH_4} && (4.351)\\ \mu^0_{N_2O} &= 1.51913 w_{N_2O} && (4.352)\\ \mu^0_{CFC11} &= 4.69548 w_{CFC11} && (4.353)\\ \mu^0_{CFC12} &= 4.14307 w_{CFC12} && (4.354) \end{aligned}$$

where $w$ denotes the volume mixing ratio of these gases. The CAM 3.0 employs volume mixing ratios for the year 1992 based on IPCC [1995], $w_{CH_4} = 1.714$ *ppmv*, $w_{N_2O} = 0.311$ *ppmv*, $w_{CFC11} = 0.280$ *ppbv* and $w_{CFC12} = 0.503$ *ppbv*. The pressure level (mb) of the tropopause is defined as

$$p_{trop} = 250.0 - 150.0 \cos^2 \phi \qquad (4.355)$$

For $p \leq p_{trop}$, the stratospheric mixing ratios are defined as

$$\begin{aligned} \mu_{CH_4} &= \mu^0_{CH_4} \left(\frac{p}{p_{trop}}\right)^{X_{CH_4}} && (4.356)\\ \mu_{N_2O} &= \mu^0_{N_2O} \left(\frac{p}{p_{trop}}\right)^{X_{N_2O}} && (4.357)\\ \mu_{CFC11} &= \mu^0_{CFC11} \left(\frac{p}{p_{trop}}\right)^{X_{CFC11}} && (4.358)\\ \mu_{CFC12} &= \mu^0_{CFC12} \left(\frac{p}{p_{trop}}\right)^{X_{CFC12}} && (4.359) \end{aligned}$$

where the mixing ratio scale heights are defined as

$$\left.\begin{aligned} X_{CH_4} &= 0.2353\\ X_{N_2O} &= 0.3478 + 0.00116\,|\phi|\\ X_{CFC11} &= 0.7273 + 0.00606\,|\phi|\\ X_{CFC12} &= 0.4000 + 0.00222\,|\phi| \end{aligned}\right\} |\phi| \leq 45 \qquad (4.360)$$

and,

$$\left.\begin{aligned} X_{CH_4} &= 0.2353 + 0.22549\,|\phi|\\ X_{N_2O} &= 0.4000 + 0.01333\,|\phi|\\ X_{CFC11} &= 1.0000 + 0.01333\,|\phi|\\ X_{CFC12} &= 0.5000 + 0.02444\,|\phi| \end{aligned}\right\} |\phi| \geq 45 \qquad (4.361)$$

where $\phi$ is latitude in degrees.

### 4.9.5 Cloud emissivity

The clouds in CAM 3.0 are gray bodies with emissivities that depend on cloud phase, condensed water path, and the effective radius of ice particles. The cloud emissivity is defined as

$$\epsilon_{cld} = 1 - e^{-D\kappa_{abs} CWP} \qquad (4.362)$$

where $D$ is a diffusivity factor set to 1.66, $\kappa_{abs}$ is the longwave absorption coefficient ($m^2 g^{-1}$), and CWP is the cloud water path ($gm^{-2}$). The absorption coefficient is defined as

$$\kappa_{abs} = \kappa_l (1 - f_{ice}) + \kappa_i f_{ice} \tag{4.363}$$

where $\kappa_l$ is the longwave absorption coefficient for liquid cloud water and has a value of 0.090361, such that $D\kappa_l$ is 0.15. $\kappa_i$ is the absorption coefficient for ice clouds and is based on a broad band fit to the emissivity given by Ebert and Curry's formulation,

$$\kappa_i = 0.005 + \frac{1}{r_{ei}}. \tag{4.364}$$

### 4.9.6 Numerical algorithms and cloud overlap

The treatment of cloud overlap follows Collins [2001]. The new parameterizations can treat random, maximum, or an arbitrary combination of maximum and random overlap between clouds. This scheme replaces the treatment in CCM3, which was an exact treatment for random overlap of plane-parallel infinitely-thin gray-body clouds. The new method is an exact treatment for arbitrary overlap among the same type of clouds. It is therefore more accurate than the original matrix method of Manabe and Strickler [1964] and improved variants of it [Raisanen, 1998; Li, 2000].

If longwave scattering is omitted, the upwelling and downwelling longwave fluxes are solutions to uncoupled ordinary differential equations [Goody and Yung, 1989]. The emission from clouds is calculated using the Stefan-Boltzmann law applied to the temperatures at the cloud boundaries. The cloud boundaries correspond to the interfaces of the model layers. This approximation greatly simplifies the mathematical form of the flux solutions since the clouds can be treated as boundary conditions for the differential equations. The approximation becomes more accurate as the clouds become more optically thick.

The solutions are formulated in terms of the same conversion of vertical cloud distributions to binary cloud profiles used for the shortwave calculations (p. 111). First consider the flux boundary conditions for a maximum-overlap region $j$. The downward flux at the upper boundary of the region is spatially heterogeneous and has terms contributed by all the binary configurations above the region. Similarly, the upward flux at the lower boundary of the region has terms contributed by all the binary configurations below the region. The fluxes within the region are area-weighted sums of the fluxes calculated for all possible combinations of these boundary terms and the cloud configurations within the region. Fortunately the arithmetic can be simplified because the solutions to the longwave equations are linear in the boundary conditions. Therefore the downward (upward) fluxes can be computed by summing the solutions for each configuration in the region for a single boundary condition given by the area-averaged fluxes at the region interfaces denoted by $\bar{F}^{\downarrow}(i_{j,\min})$ ($\bar{F}^{\uparrow}(i_{j,\max})$). The mathematics is explained in Collins [2001]. In the absorptivity-emissivity method, the boundary conditions are included in the solution using the emissivity array. In the standard formulation [Manabe and Möller, 1961; Ramanathan and Downey, 1986] used in CAM 3.0, this array is only defined for boundary conditions at the top of the model domain for computational economy. It is not possible to treat arbitrary flux boundary conditions inside the domain (e.g., $\bar{F}^{\downarrow}(i_{j,\min})$) using the emissivity array. However, the flux boundary conditions $\bar{F}^{\downarrow}(i_{j,\min})$ and $\bar{F}^{\uparrow}(i_{j,\max})$ are mathematically equivalent to the fluxes from a single "pseudo" cloud deck above and below the region, respectively. The pseudo clouds have unit area and occupy a single model layer. The vertical positions and emissivities of these clouds are chosen so that the net area-mean fluxes incident on the top and bottom of the region equal $\bar{F}^{\downarrow}(i_{j,\min})$ and $\bar{F}^{\uparrow}(i_{j,\max})$. With the introduction of the pseudo clouds, the fluxes inside each maximum-overlap region can be calculated using the standard absorptivity-emissivity formulation.

The total upward and downward mean fluxes at a layer $i$ within a maximum-overlap region $j$ are given by:

$$
\begin{aligned}
\bar{F}^{\uparrow}(i) &= \sum_{k_j=1}^{n_j+1} \tilde{A}_{j,k_j} \bar{F}[k_j]^{\uparrow}(i) \\
\bar{F}^{\downarrow}(i) &= \sum_{k_j=1}^{n_j+1} \tilde{A}_{j,k_j} \bar{F}[k_j]^{\downarrow}(i)
\end{aligned} \tag{4.365}
$$

where $\bar{F}[k_j]^{\uparrow}(i)$ and $\bar{F}[k_j]^{\downarrow}(i)$ are the upward and downwelling fluxes for the cloud configuration $\tilde{\mathcal{C}}_{j,k_j}$. The symbols required to write these fluxes are defined in Table 4.6.

Table 4.6: Definition of terms in fluxes.

| | |
|---|---|
| $\sigma$ | Stefan-Boltzmann constant |
| $p$ | pressure |
| $p_t(i)$ | pressure at top of layer $i$ |
| $p_b(i)$ | pressure at bottom of layer $i$ ($p_b(i) > p_t(i)$) |
| $T(p)$ | temperature at pressure $p$ |
| $B(p)$ | $\sigma T^4(p)$ |
| $i^{\downarrow}_{p,j}$ | layer containing pseudo cloud for $\bar{F}^{\downarrow}(i_{j,\min})$ b.c. |
| $i^{\uparrow}_{p,j}$ | layer containing pseudo cloud for $\bar{F}^{\uparrow}(i_{j,\max})$ b.c. |
| $\epsilon_{cld}(i)$ | emissivity of cloud in layer $i$ |
| $\epsilon_{p,j}(i)$ | emissivity of pseudo clouds at $i = i^{\downarrow}_{p,j}$ and $i^{\uparrow}_{p,j}$ |
| $\alpha(p, p')$ | clear-sky absorptivity from pressure $p'$ to $p$ |
| $F^{\downarrow}_{clr}(i)$ | downwelling clear-sky flux at layer $i$ |
| $F^{\uparrow}_{clr}(i)$ | upwelling clear-sky flux at layer $i$ |
| $t^{\uparrow\downarrow}_{j,k_j}(i)$ | weights for up/downwelling clear-sky flux at layer $i$ |
| $T^{\uparrow\downarrow}_{j,k_j}(i, i')$ | weights for up/downwelling flux at layer $i$ from cloud at $i'$ |

The downward and upward fluxes for each configuration can be derived by iterating the longwave equations from TOA and the surface to the layer $i$. At each iteration, the solutions are advanced between successive cloud layers. The final form of the fluxes in configuration $\tilde{\mathcal{C}}_{j,k_j}$

is:

$$
\begin{aligned}
\bar{F}[k_j]^{\uparrow}(i) &= F^{\uparrow}_{clr}(i)t^{\uparrow}_{j,k_j}(i) + \\
&\sum_{i'=i}^{N}\left\{B\left(p_t(i')\right) - \int_{p_t(i)}^{p_t(i')}\alpha(p_t(i),p')\frac{dB(p')}{dp'}dp'\right\}T^{\uparrow}_{j,k_j}(i,i')
\end{aligned} \tag{4.366}
$$

$$
\begin{aligned}
\bar{F}[k_j]^{\downarrow}(i) &= F^{\downarrow}_{clr}(i)t^{\downarrow}_{j,k_j}(i) + \\
&\sum_{i'=1}^{i}\left\{B\left(p_b(i')\right) + \int_{p_b(i')}^{p_b(i)}\alpha(p_b(i),p')\frac{dB(p')}{dp'}dp'\right\}T^{\downarrow}_{j,k_j}(i,i')
\end{aligned} \tag{4.367}
$$

The clear-sky and cloudy-sky weights are:

$$t^{\uparrow}_{j,k_j}(i) = \prod_{l=i}^{N}\left[1-\tilde{\epsilon}_{j,k_j}(l)\right] \tag{4.368}$$

$$t^{\downarrow}_{j,k_j}(i) = \prod_{l=1}^{i}\left[1-\tilde{\epsilon}_{j,k_j}(l)\right] \tag{4.369}$$

$$T^{\uparrow}_{j,k_j}(i,i') = \tilde{\epsilon}_{j,k_j}(i')\prod_{l=i}^{i'-1}\left[1-\tilde{\epsilon}_{j,k_j}(l)\right] \tag{4.370}$$

$$T^{\downarrow}_{j,k_j}(i,i') = \tilde{\epsilon}_{j,k_j}(i')\prod_{l=i'+1}^{i}\left[1-\tilde{\epsilon}_{j,k_j}(l)\right] \tag{4.371}$$

$$\tilde{\epsilon}_{j,k_j}(l) = \begin{cases} \epsilon_{cld}(l)\tilde{\mathcal{C}}_{j,k_j}(l) & \text{if } i_{j,\min} \le l \le i_{j,\max} \\ \epsilon_{p,j}(i^{\downarrow}_{p,j}) & \text{if } l = i^{\downarrow}_{p,j} \\ \epsilon_{p,j}(i^{\uparrow}_{p,j}) & \text{if } l = i^{\uparrow}_{p,j} \\ 0 & \text{otherwise} \end{cases} \tag{4.372}$$

The longwave atmospheric heating rate is obtained from

$$Q_{\ell w}(p_k) = \frac{g}{c_p}\frac{\bar{F}^{\uparrow}(k+1) - \bar{F}^{\downarrow}(k+1) - \bar{F}^{\uparrow}(k) + \bar{F}^{\downarrow}(k)}{p_{k+1}-p_k}. \tag{4.373}$$

which is added to the nonlinear term ($Q$) in the thermodynamic equation.

The full calculation of longwave radiation (which includes heating rates as well as boundary fluxes) is computationally expensive. Therefore, modifications to the longwave scheme were developed to improve its efficiency for the diurnal framework. For illustration, consider the clear-sky fluxes defined in (4.229) and (4.230). Well over 90% of the longwave computational cost involves evaluating the absorptivity $\alpha$ and emissivity $\epsilon$. To reduce this computational burden, $\alpha$ and $\epsilon$ are computed at a user defined frequency that is set to every 12 model hours in the standard configuration, while longwave heating rates are computed at the diurnal cycle frequency of once every model hour.

Calculation of $\alpha$ and $\epsilon$ with a period longer than the evaluation of the longwave heating rates neglects the dependence of these quantities on variations in temperature, water vapor, and ozone. However, variations in radiative fluxes due to changes in cloud amount are fully

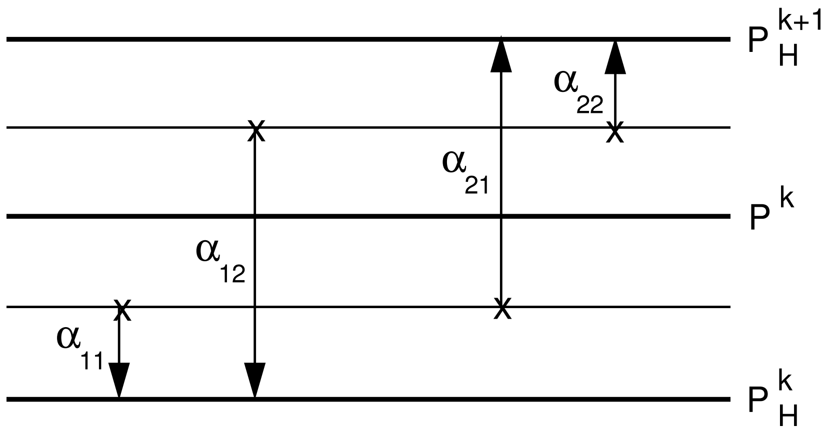


Figure 4.3: Subdivision of model layers for radiation flux calculation

accounted for at each radiation calculation, which is regarded to be the dominant effect on diurnal time scales. The dominant effect on the heating rates of changes in temperature occurs through the Planck function and is accounted for with this method.

The continuous equations for the longwave calculations require a sophisticated vertical finite–differencing scheme due to the integral term $\int \alpha dB$ in Equations (4.229)–(4.230). The reason for the additional care in evaluating this integral arises from the nonlinear behavior of $\alpha$ across a given model layer. For example, if the flux at interface $p_k$ is required, an integral of the form $\int_{p_s}^{p_k} \alpha(p', p_k) dB(p')$ must be evaluated. For the nearest layer to level $p_k$, the following terms will arise:

$$\int_{p_{k+1}}^{p_k} \alpha(p', p_k) dB(p') = \frac{[\alpha(p_{k+1}, p_k) + \alpha(p_k, p_k)]}{2} \left[B(p_k) - B(p_{k+1})\right], \tag{4.374}$$

employing the trapezoidal rule. The problem arises with the second absorptivity $\alpha(p_k, p_k)$, since this term is zero. It is also known that $\alpha$ is nearly exponential in form within a layer. Thus, to accurately account for the variation of $\alpha(p, p')$ across a layer, many more grid points are required than are available in CAM 3.0. The nearest layer must, therefore, be subdivided and $\alpha$ must be evaluated across the subdivided layers. The algorithm that is employed in is to use a trapezoid method for all layers except the nearest layer. For the nearest layer a subdivision, as illustrated in Figure 4.3, is employed.

For the upward flux, the nearest layer contribution to the integral is evaluated from

$$\int_{p_H^k}^{p_H^{k+1}} \alpha dB(p') = \alpha_{22}\left[B(p_H^{k+1}) - B(p^k)\right] + \alpha_{21}\left[B(p^k) - B(p_H^k)\right], \tag{4.375}$$

while for the downward flux, the integral is evaluated according to

$$\int_{p_H^{k+1}}^{p_H^k} \alpha dB(p') = \alpha_{11}\left[B(p^k) - B(p_H^k)\right] + \alpha_{12}\left[B(p_H^{k+1}) - B(p^k)\right]. \tag{4.376}$$

The $\alpha_{ij},\ i = 1, 2;\ j = 1, 2$, are absorptivities evaluated for the subdivided paths shown in Figure 4.3. The path–length dependence for the absorptivities arises from the dependence on the absorptance $A(p, p')$ [*e.g.,* Eq. (4.373)]. Temperatures are known at model levels. Temperatures at layer interfaces are determined through linear interpolation in $\log p$ between layer midpoint temperatures. Thus, $B(p_k) = \sigma_B T_k^4$ can be evaluated at all required levels. The most involved calculation arises from the evaluation of the fraction of layers shown in Figure 4.3. In general, the absorptance of a layer can require the evaluation of the following path lengths:

$$\xi(p_k, p_{k+1}) = f(\overline{T})\overline{p}\Delta p, \tag{4.377}$$

and

$$u(p_k, p_{k+1}) = g(\overline{T})\Delta p, \tag{4.378}$$

and

$$\beta(p_k, p_{k+1}) = h(\overline{T})\overline{p}, \tag{4.379}$$

where $f$, $g$, and $h$ are functions of temperature due to band parameters (see Kiehl and Ramanathan [1983], and $\overline{T}$ is an absorber mass–weighted mean temperature.

These path lengths are used extensively in the evaluation of $A_{O_3}$ [Ramanathan and Dickinson, 1979] and $A_{CO_2}$ [Kiehl and Briegleb, 1991] and the trace gases. But path lengths dependent on both $p^2$ (*i.e.* $\xi$) and $p$ (*i.e.* $u$) are also needed in calculating the water–vapor absorptivity, $\alpha_{H_2O}$ [Ramanathan and Downey, 1986]. To account for the subdivided layer, a fractional layer amount must be multiplied by $\xi$ and $u$, *e.g.*

$$\overline{\xi}_{11} = \xi(p_H^k p_H^{k+1}) \times UINPL(1,k), \tag{4.380}$$

$$\overline{u}_{11} = u(p_H^k, p_H^{k+1}) \times WINPL(1,k), \tag{4.381}$$

and

$$\overline{\beta}_{11} = \beta(p_H^k, p_H^{k+1}) \times PINPL(1,k), \tag{4.382}$$

where $UINPL$, $WINPL$, and $PINPL$ are factors to account for the fractional subdivided layer amount. These quantities are derived for the case where the mixing ratio is assumed to be constant within a given layer ($CO_2$ and $H_2O$). For ozone, the mixing ratio is assumed to interpolate linearly in physical thickness; thus, another fractional layer amount $ZINPL$ is required for evaluating $A_{O_3}(p, p')$ across subdivided layers.

Consider the subdivided path for $\alpha_{22}$; the total path length from $p_H^k$ to $p_H^{k+1}$ for the $p^2$ path length will be

$$\xi(p_H^k, p_H^{k+1}) \approx \overline{p}_H \left[p_H^k - p_H^{k+1}\right], \tag{4.383}$$

where $\overline{p}_H \equiv \frac{p_H^k + p_H^{k+1}}{2}$. The total layer path length is, therefore, proportional to

$$\xi(p_H^k, p_H^{k+1}) \approx \frac{1}{2}(\left(p_H^k\right)^2 - \left(p_H^{k+1}\right)^2). \tag{4.384}$$

The path length $\xi$ for $\alpha_{22}$ requires the mean pressure

$$\overline{p}_{22} \approx \frac{1}{2}\left\{\frac{p^k + p_H^{k+1}}{2} + p_H^{k+1}\right\}, \tag{4.385}$$

and the pressure difference

$$\Delta p_{22} \approx \frac{p^k + p_H^{k+1}}{2} - p_H^{k+1}. \tag{4.386}$$

Therefore, the path $\xi_{22}$ is

$$\xi_{22} \approx \overline{p}_{22}\,\Delta p_{22} = \frac{1}{2}\left\{\left(\frac{p^k + p_H^{k+1}}{2}\right)^2 - \left(p_H^{k+1}\right)^2\right\}. \tag{4.387}$$

The fractional path length is obtained by normalizing this by $\xi(p_H^k, p_H^{k+1})$,

$$UINPL(2,k) = DAF3(k)\left\{\left(\frac{p^k + p_H^{k+1}}{2}\right)^2 - \left(p_H^{k+1}\right)^2\right\}, \tag{4.388}$$

where

$$DAF3(k) = \frac{1}{\left(p_H^k\right)^2 - \left(p_H^{k+1}\right)^2}. \tag{4.389}$$

Similar reasoning leads to the following expressions for the remaining fractional path lengths, for $\alpha_{21}$,

$$UINPL(3,k) = DAF3(k)\left\{\left(\frac{p^k + p_H^k}{2}\right)^2 - \left(p_H^{k+1}\right)^2\right\}, \tag{4.390}$$

for $\alpha_{11}$,

$$UINPL(1,k) = DAF3(k)\left\{\left(p_H^k\right)^2 - \left(\frac{p^k + p_H^k}{2}\right)^2\right\}, \tag{4.391}$$

and for $\alpha_{12}$,

$$UINPL(4,k) = DAF3(k)\left\{\left(p_H^k\right)^2 - \left(\frac{p^k + p_H^{k+1}}{2}\right)^2\right\}. \tag{4.392}$$

The $UINPL$ are fractional layer amounts for path length that scale as $p^2$, *i.e.*, $\overline{\xi}_{ij}$.

For variables that scale linearly in $p$, *e.g.* $\overline{u}_{ij}$, the following fractional layer amounts are used:

$$WINPL(1,k) = DAF4(k)\left\{\frac{p_H^k - p^k}{2}\right\}, \tag{4.393}$$

$$WINPL(2,k) = DAF4(k)\left\{\frac{p^k - p_H^{k+1}}{2}\right\}, \tag{4.394}$$

$$WINPL(3,k) = DAF4(k)\left\{\left(\frac{p_H^k + p^k}{2}\right) - p_H^{k+1}\right\}, \tag{4.395}$$

$$WINPL(4,k) = DAF4(k)\left\{p_H^k - \left(p_H^{k+1} + p^k 2\right)\right\}, \tag{4.396}$$

where

$$DAF4(k) = \frac{1}{p_H^k - p_H^{k+1}}. \tag{4.397}$$

These fractional layer amounts are directly analogous to the $UINPL$, but since $\overline{u}$ is linear in $p$, the squared terms are not present.

The variable $\overline{\beta}_{ij}$ requires a mean pressure for the subdivided layer. These are

$$PINPL(1,k) = \frac{1}{2}\left\{\frac{p^k + p_H^k}{2} + p_H^k\right\}, \tag{4.398}$$

$$PINPL(2,k) = \frac{1}{2}\left\{\frac{p^k + p_H^{k+1}}{2} + p_h^{k+1}\right\}, \tag{4.399}$$

$$PINPL(3,k) = \frac{1}{2}\left\{\frac{p^k + p_H^k}{2} + p_H^{k+1}\right\}, \tag{4.400}$$

$$PINPL(4,k) = \frac{1}{2}\left\{\frac{p^k + p_H^{k+1}}{2} + p_H^k\right\}. \tag{4.401}$$

Finally, fractional layer amounts for ozone path lengths are needed, since ozone is interpolated linearly in physical thickness. These are given by

$$ZINPL(1,k) = \frac{1}{2}\frac{\ln\left(\frac{p_H^k}{p_k}\right)}{\ln\left(\frac{p_H^k}{p_H^{k+1}}\right)}, \tag{4.402}$$

$$ZINPL(2,k) = \frac{1}{2}\frac{\ln\left(\frac{p^k}{p_H^{k+1}}\right)}{\ln\left(\frac{p_H^k}{p_H^{k+1}}\right)}, \tag{4.403}$$

$$ZINPL(3,k) = ZINPL(1,k) + 2ZINPL(2,k), \tag{4.404}$$

$$ZINPL(4,k) = ZINPL(2,k) + 2ZINPL(1,k). \tag{4.405}$$

## 4.10 Surface Exchange Formulations

The surface exchange of heat, moisture and momentum between the atmosphere and land, ocean or ice surfaces are treated with a bulk exchange formulation. We present a description of each surface exchange separately. Although the functional forms of the exchange relations are identical, we present the descriptions of these components as developed and represented in the various subroutines in CAM 3.0. The differences in the exchange expressions are predominantly in the definition of roughness lengths and exchange coefficients. The description of surface exchange over ocean follows from Bryan et al. [1996], and the surface exchange over sea ice is discussed in chapter 6. Over lakes, exchanges are computed by a lake model embedded in the land surface model described in the following section.

### 4.10.1 Land

In CAM 3.0, the NCAR Land Surface Model (LSM) [Bonan, 1996] has been replaced by the Community Land Model CLM2 [Bonan et al., 2002]. This new model includes components treating hydrological and biogeochemical processes, dynamic vegetation, and biogeophysics. Because of the increased complexity of this new model and since a complete description is available online, users of CAM 3.0 interested in CLM should consult this documentation at `http://www.cgd.ucar.edu/tss/clm/`. A discussion is provided here only of the component of CLM which controls surface exchange processes.

Land surface fluxes of momentum, sensible heat, and latent heat are calculated from Monin-Obukhov similarity theory applied to the surface (i.e. constant flux) layer. The zonal $\tau_x$ and meridional $\tau_y$ momentum fluxes (kg m$^{-1}$s$^{-2}$), sensible heat $H$ (W m$^{-2}$) and water vapor $E$ (kg m$^{-2}$s$^{-1}$) fluxes between the surface and the lowest model level $z_1$ are:

$$\tau_x = -\rho_1\overline{(u'w')} \quad = -\rho_1 u_*^2(u_1/V_a) = \rho_1\frac{u_s-u_1}{r_{am}} \tag{4.406}$$

$$\tau_y = -\rho_1\overline{(v'w')} \quad = -\rho_1 u_*^2(v_1/V_a) = \rho_1\frac{v_s-v_1}{r_{am}} \tag{4.407}$$

$$H = \quad \rho_1 c_p\overline{(w'\theta')} = -\rho_1 c_p u_*\theta_* \quad = \rho_1 c_p\frac{\theta_s-\theta_1}{r_{ah}} \tag{4.408}$$

$$E = \quad \rho_1\overline{(w'q')} \quad = -\rho_1 u_* q_* \quad = \rho_1\frac{q_s-q_1}{r_{aw}} \tag{4.409}$$

$$r_{am} = V_a/u_*^2 \tag{4.410}$$

$$r_{ah} = (\theta_1-\theta_s)/u_*\theta_* \tag{4.411}$$

$$r_{aw} = (q_1-q_s)/u_*q_* \tag{4.412}$$

where $\rho_1$, $u_1$, $v_1$, $\theta_1$ and $q_1$ are the density (kg m$^{-3}$), zonal wind (m s$^{-1}$), meridional wind (m s$^{-1}$), air potential temperature (K), and specific humidity (kg kg$^{-1}$) at the lowest model level. By definition, the surface winds $u_s$ and $v_s$ equal zero. The symbol $\theta_1$ represents temperature, and $q_1$ is specific humidity at surface. The terms $r_{am}$, $r_{ah}$, and $r_{aw}$ are the aerodynamic resistances (s m$^{-1}$) for momentum, sensible heat, and water vapor between the lowest model level at height $z_1$ and the surface at height $z_{0m}+d$ [$z_{0h}+d$]. Here $z_{0m}$ [$z_{0h}$] is the roughness length (m) for momentum [scalar] fluxes, and $d$ is the displacement height (m).

For the vegetated fraction of the grid, $\theta_s = T_{af}$ and $q_s = q_{af}$, where $T_{af}$ and $q_{af}$ are the air temperature and specific humidity within canopy space. For the non-vegetated fraction, $\theta_s = T_g$ and $q_s = q_g$, where $T_g$ and $q_g$ are the air temperature and specific humidity at ground surface. These terms are described by Dai et al. [2001].

### Roughness lengths and zero-plane displacement

The aerodynamic roughness $z_{0m}$ is used for wind, while the thermal roughness $z_{0h}$ is used for heat and water vapor. In general, $z_{0m}$ is different from $z_{0h}$, because the transfer of momentum is affected by pressure fluctuations in the turbulent waves behind the roughness elements, while for heat and water vapor transfer no such dynamical mechanism exists. Rather, heat and water vapor must ultimately be transferred by molecular diffusion across the interfacial sublayer. Over bare soil and snow cover, the simple relation from Zilitinkevich [1970] can be used [Zeng and Dickinson, 1998]:

$$\ln\frac{z_{0m}}{z_{0h}} = a\left(\frac{u_* z_{0m}}{\nu}\right)^{0.45} \tag{4.413}$$

$$a = 0.13 \tag{4.414}$$

$$\nu = 1.5\times10^{-5}\mathrm{m}^2\mathrm{s}^{-1} \tag{4.415}$$

Over canopy, the application of energy balance

$$R_n - H - L_v E = 0 \tag{4.416}$$

(where $R_n$ is the net radiation absorbed by the canopy) is equivalent to the use of different $z_{0m}$ versus $z_{0h}$ over bare soil, and hence thermal roughness is not needed over canopy [Zeng et al., 1998].

The roughness $z_{0m}$ is proportional to canopy height, and is also affected by fractional vegetation cover, leaf area index, and leaf shapes. The roughness is derived from the simple relationship $z_{0m} = 0.07\, h_c$, where $h_c$ is the canopy height. Similarly, the zero-plane displacement height $d$ is proportional to canopy height, and is also affected by fractional vegetation cover, leaf area index, and leaf shapes. The simple relationship $d/h_c = 2/3$ is used to obtain the height.

**Monin-Obukhov similarity theory**

**(1) Turbulence scaling parameters**

A length scale (the Monin-Obukhov length) $L$ is defined by

$$L = \frac{\theta_v u_*^2}{k g \theta_{v*}} \tag{4.417}$$

where $k$ is the von Kàrman constant, and $g$ is the gravitational acceleration. $L > 0$ indicates stable conditions, $L < 0$ indicates unstable conditions, and $L = \infty$ applies to neutral conditions. The virtual potential temperature $\theta_v$ is defined by

$$\theta_v = \theta_1(1 + 0.61 q_1) = T_a \left(\frac{p_s}{p_l}\right)^{R/c_p} (1 + 0.61 q_1) \tag{4.418}$$

where $T_1$ and $q_1$ are the air temperature and specific humidity at height $z_1$ respectively, $\theta_1$ is the atmospheric potential temperature, $p_l$ is the atmospheric pressure, and $p_s$ is the surface pressure. The surface friction velocity $u_*$ is defined by

$$u_*^2 = [\overline{u'w'}^2 + \overline{v'w'}^2]^{1/2} \tag{4.419}$$

The temperature scale $\theta_*$ and $\theta_{*v}$ and a humidity scale $q_*$ are defined by

$$\theta_* = -\overline{w'\theta'}/u_* \tag{4.420}$$

$$q_* = -\overline{w'q'}/u_* \tag{4.421}$$

$$\begin{aligned} \theta_{v*} &= -\overline{w'\theta_v'}/u_* \\ &\approx -(\overline{w'\theta'} + 0.61\overline{\theta}\,\overline{w'q'})/u_* \\ &= \theta_* + 0.61\overline{\theta} q_* \end{aligned} \tag{4.422}$$

(where the mean temperature $\overline{\theta}$ serves as a reference temperature in this linearized form of $\theta_v$ ).

The stability parameter is defined as

$$\varsigma = \frac{z_1 - d}{L} \quad , \tag{4.423}$$

with the restriction that $-100 \leqslant \varsigma \leqslant 2$. The scalar wind speed is defined as

$$V_a^2 = u_1^2 + v_1^2 + U_c^2 \tag{4.424}$$

$$U_c = \begin{cases} 0.1\ \mathrm{ms}^{-1} & \text{, if } \varsigma \geqslant 0 \text{ (stable)} \\ \beta w_* = \beta \left( z_i \frac{g}{\theta_v} \theta_{v*} u_* \right)^{1/3} & \text{, if } \varsigma < 0 \text{ (unstable)}. \end{cases} \tag{4.425}$$

Here $w_*$ is the convective velocity scale, $z_i$ is the convective boundary layer height, and $\beta = 1$. The value of $z_i$ is taken as 1000 m

**(2) Flux-gradient relations [Zeng et al., 1998]**

The flux-gradient relations are given by:

$$\frac{k(z_1 - d)}{\theta_*} \frac{\partial \theta}{\partial z} = \phi_h(\varsigma) \tag{4.426}$$

$$\frac{k(z_1 - d)}{q_*} \frac{\partial q}{\partial z} = \phi_q(\varsigma) \tag{4.427}$$

$$\phi_h = \phi_q \tag{4.428}$$

$$\phi_m(\varsigma) = \begin{cases} (1 - 16\varsigma)^{-1/4} & \text{for } \varsigma < 0 \\ 1 + 5\varsigma & \text{for } 0 < \varsigma < 1 \end{cases} \tag{4.429}$$

$$\phi_h(\varsigma) = \begin{cases} (1 - 16\varsigma)^{-1/2} & \text{for } \varsigma < 0 \\ 1 + 5\varsigma & \text{for } 0 < \varsigma < 1 \end{cases} \tag{4.430}$$

Under very unstable conditions, the flux-gradient relations are taken from Kader and Yaglom [1990]:

$$\phi_m = 0.7k^{2/3}(-\varsigma)^{1/3} \tag{4.431}$$

$$\phi_h = 0.9k^{4/3}(-\varsigma)^{-1/3} \tag{4.432}$$

To ensure the functions $\phi_m(\varsigma)$ and $\phi_h(\varsigma)$ are continuous, the simplest approach (i.e., without considering any transition regions) is to match the above equations at $\varsigma_m = -1.574$ for $\phi_m(\varsigma)$ and $\varsigma_h = -0.465$ for $\phi_h(\varsigma)$ .

Under very stable conditions (i.e., $\varsigma > 1$ ), the relations are taken from Holtslag et al. [1990]:

$$\phi_m = \phi_h = 5 + \varsigma \tag{4.433}$$

**(3) Integral forms of the flux-gradient relations**

Integration of the wind profile yields:

$$V_a = \frac{u_*}{k} f_M(\varsigma) \tag{4.434}$$

$$f_M(\varsigma) = \left\{ \left[ \ln\left(\frac{\varsigma_m L}{z_{0m}}\right) - \psi_m(\varsigma_m) \right] + 1.14[(-\varsigma)^{1/3} - (-\varsigma_m)^{1/3}] \right\}, \quad \varsigma < \varsigma_m = -1.574 \tag{4.434a}$$

$$f_M(\varsigma) = \left[ \ln\left(\frac{z_1 - d}{z_{0m}}\right) - \psi_m(\varsigma) + \psi_m\left(\frac{z_{0m}}{L}\right) \right], \quad \varsigma_m < \varsigma < 0 \tag{4.434b}$$

$$f_M(\varsigma) = \left[ \ln\left(\frac{z_1 - d}{z_{0m}}\right) + 5\varsigma \right], \quad 0 < \varsigma < 1 \tag{4.434c}$$

$$f_M(\varsigma) = \left\{ \left[ \ln\left(\frac{L}{z_{0m}}\right) + 5 \right] + [5\ln(\varsigma) + \varsigma - 1] \right\}, \quad \varsigma > 1 \tag{4.434d}$$

Integration of the potential temperature profile yields:

$$\theta_1 - \theta_s = \frac{\theta_*}{k} f_T(\varsigma) \tag{4.435}$$

$$f_T(\varsigma) = \left\{ \left[ \ln\left(\frac{\varsigma_h L}{z_{0h}}\right) - \psi_h(\varsigma_h) \right] + 0.8[(-\varsigma_h)^{-1/3} - (-\varsigma)^{-1/3}] \right\}, \quad \varsigma < \varsigma_h = -0.465 \tag{4.435a}$$

$$f_T(\varsigma) = \left[ \ln\left(\frac{z_1 - d}{z_{0h}}\right) - \psi_h(\varsigma) + \psi_h\left(\frac{z_{0h}}{L}\right) \right], \qquad \varsigma_h < \varsigma < 0 \tag{4.435b}$$

$$f_T(\varsigma) = \left[ \ln\left(\frac{z_1 - d}{z_{0h}}\right) + 5\varsigma \right], \qquad 0 < \varsigma < 1 \tag{4.435c}$$

$$f_T(\varsigma) = \left\{ \left[ \ln\left(\frac{L}{z_{0h}}\right) + 5 \right] + [5\ln(\varsigma) + \varsigma - 1] \right\}, \qquad \varsigma > 1 \tag{4.435d}$$

The expressions for the specific humidity profiles are the same as those for potential temperature except that $(\theta_1 - \theta_s)$, $\theta_*$ and $z_{0h}$ are replaced by $(q_1 - q_s)$, $q_*$ and $z_{0q}$ respectively. The stability functions for $\varsigma < 0$ are

$$\psi_m = 2\ln\left(\frac{1+\chi}{2}\right) + \ln\left(\frac{1+\chi^2}{2}\right) - 2\tan^{-1}\chi + \frac{\pi}{2} \tag{4.436}$$

$$\psi_h = \psi_q = 2\ln\left(\frac{1+\chi^2}{2}\right) \tag{4.437}$$

where

$$\chi = (1 - 16\varsigma)^{1/4} \tag{4.438}$$

Note that the CLM code contains extra terms involving $z_{0m}/\varsigma$, $z_{0h}/\varsigma$, and $z_{0q}/\varsigma$ for completeness. These terms are very small most of the time and hence are omitted in Eqs. 4.434 and 4.435.

In addition to the momentum, sensible heat, and latent heat fluxes, land surface albedos and upward longwave radiation are needed for the atmospheric radiation calculations. Surface albedos depend on the solar zenith angle, the amount of leaf and stem material present, their optical properties, and the optical properties of snow and soil. The upward longwave radiation is the difference between the incident and absorbed fluxes. These and other aspects of the land surface fluxes have been described by Dai et al. [2001].

### 4.10.2 Ocean

The bulk formulas used to determine the turbulent fluxes of momentum (stress), water (evaporation, or latent heat), and sensible heat into the atmosphere over ocean surfaces are

$$(\boldsymbol{\tau}, E, H) = \rho_A \, |\Delta\, \boldsymbol{v}| \, (C_D \Delta\, \boldsymbol{v}, C_E \Delta\, q, C_p C_H \Delta\theta), \tag{4.439}$$

where $\rho_A$ is atmospheric surface density and $C_p$ is the specific heat. Since CAM 3.0 does not allow for motion of the ocean surface, the velocity difference between surface and atmosphere is $\Delta\, \boldsymbol{v} = \boldsymbol{v}_A$, the velocity of the lowest model level. The potential temperature difference is $\Delta\theta = \theta_A - T_s$, where $T_s$ is the surface temperature. The specific humidity difference is $\Delta q = q_A - q_s(T_s)$, where $q_s(T_s)$ is the saturation specific humidity at the sea-surface temperature.

In (4.439), the transfer coefficients between the ocean surface and the atmosphere are computed at a height $Z_A$ and are functions of the stability, $\zeta$:

$$C_{(D,E,H)} = \kappa^2 \left[ \ln\left(\frac{Z_A}{Z_{0m}}\right) - \psi_m \right]^{-1} \left[ \ln\left(\frac{Z_A}{Z_{0(m,e,h)}}\right) - \psi_{(m,s,s)} \right]^{-1} \tag{4.440}$$

where $\kappa = 0.4$ is von Kármán's constant and $Z_{0(m,e,h)}$ is the roughness length for momentum, evaporation, or heat, respectively. The integrated flux profiles, $\psi_m$ for momentum and $\psi_s$ for scalars, under stable conditions ($\zeta > 0$) are

$$\psi_m(\zeta) = \psi_s(\zeta) = -5\zeta. \tag{4.441}$$

For unstable conditions ($\zeta < 0$), the flux profiles are

$$\begin{aligned} \psi_m(\zeta) =& 2\ln[0.5(1+X)] + \ln[0.5(1+X^2)] \\ & - 2\tan^{-1} X + 0.5\pi, \qquad (4.442) \\ \psi_s(\zeta) =& 2\ln[0.5(1+X^2)], \qquad (4.443) \\ X =& (1-16\zeta)^{1/4}. \qquad (4.444) \end{aligned}$$

The stability parameter used in (4.441)–(4.444) is

$$\zeta = \frac{\kappa\, g\, Z_A}{u^{*2}} \left( \frac{\theta^*}{\theta_v} + \frac{Q^*}{(\epsilon^{-1} + q_A)} \right), \tag{4.445}$$

where the virtual potential temperature is $\theta_v = \theta_A(1 + \epsilon q_A)$; $q_A$ and $\theta_A$ are the lowest level atmospheric humidity and potential temperature, respectively; and $\epsilon = 0.606$. The turbulent velocity scales in (4.445) are

$$\begin{aligned} u^* =& C_D^{1/2} |\Delta \boldsymbol{v}|, \\ (Q^*, \theta^*) =& C_{(E,H)} \frac{|\Delta \boldsymbol{v}|}{u^*} (\Delta q, \Delta\theta). \qquad (4.446) \end{aligned}$$

Over oceans, $Z_{0e} = 9.5 \times 10^{-5}$ m under all conditions and $Z_{0h} = 2.2 \times 10^{-9}$ m for $\zeta > 0$, $Z_{0h} = 4.9 \times 10^{-5}$ m for $\zeta \leq 0$, which are given in Large and Pond [1982]. The momentum roughness length depends on the wind speed evaluated at 10 m as

$$\begin{aligned} Z_{om} =& 10 \exp\left[ -\kappa \left( \frac{c_4}{U_{10}} + c_5 + c_6 U_{10} \right)^{-1} \right], \\ U_{10} =& U_A \left[ 1 + \frac{\sqrt{C_{10}^N}}{\kappa} \ln\left( \frac{Z_A}{10} - \psi_m \right) \right]^{-1}, \qquad (4.447) \end{aligned}$$

where $c_4 = 0.0027$ m s$^{-1}$, $c_5 = 0.000142$, $c_6 = 0.0000764$ m$^{-1}$ s, and the required drag coefficient at 10-m height and neutral stability is $C_{10}^N = c_4 U_{10}^{-1} + c_5 + c_6 U_{10}$ as given by Large et al. [1994].

The transfer coefficients in (4.439) and (4.440) depend on the stability following (4.441)–(4.444), which itself depends on the surface fluxes (4.445) and (4.446). The transfer coefficients also depend on the momentum roughness, which itself varies with the surface fluxes over oceans (4.447). The above system of equations is solved by iteration.

### 4.10.3 Sea Ice

The fluxes between the atmosphere and sea ice are described in detail in chapter 6.

## 4.11 Vertical Diffusion and Boundary Layer Processes

The vertical diffusion parameterization in CAM 3.0 provides the interface to the turbulence parameterization, computes the molecular diffusivities (if necessary) and finally computes the tendencies of the input variables. The diffusion equations are actually solved implicitly, so the tendencies are computed from the difference between the final and initial profiles.

In the near future, the gravity wave parameterization will also be called from within the vertical diffusion. This will allow the turbulent and, especially, the molecular diffusivity to be passed to the gravity wave parameterization to damp vertically propagating waves. The gravity wave parameterization may return additional diffusivities and tendencies to be applied before the actual diffusion is applied.

As in CCM2 and CCM3, the turbulence parameterization in CAM 3.0 includes computation of diffusivities for the free atmosphere, based on the gradient Richardson number, and an explicit, non-local Atmospheric Boundary Layer (ABL) parameterization. The ABL parameterization includes a determination of the boundary layer depth. In practice, the free atmosphere diffusivities are calculated first at all levels. The ABL scheme then determines the ABL depth and diffusivities and replaces the free atmosphere values for all levels within the ABL, returning both the updated diffusivities and the non-local transport terms. The implementation of the ABL parameterization in CCM2 is discussed in [Holtslag and Boville, 1993], while the formalism only is discussed here. Following the ABL scheme, molecular diffusivities are computed if the model top extends above $\sim$90 km (0.1 Pa).

As described in Boville and Bretherton [2003], a general vertical diffusion parameterization can be written in terms of the divergence of diffusive fluxes:

$$\frac{\partial}{\partial t}(u, v, q) = -\frac{1}{\rho}\frac{\partial}{\partial z}(F_u, F_v, F_q) \tag{4.448}$$

$$\frac{\partial}{\partial t}s = -\frac{1}{\rho}\frac{\partial}{\partial z}F_H + D \tag{4.449}$$

where $s = c_p T + gz$ is the dry static energy, $z$ is the geopotential height above the local surface (does not include the surface elevation) and $D$ is the heating rate due to the dissipation of resolved kinetic energy in the diffusion process. The diffusive fluxes are defined as:

$$F_{u,v} = -\rho K_m \frac{\partial}{\partial z}(u, v), \tag{4.450}$$

$$F_{q,H} = -\rho K_{q,H} \frac{\partial}{\partial z}(q, s) + \rho K^t_{q,H}\gamma_{q,H}. \tag{4.451}$$

The viscosity $K_m$ and diffusivities $K_{q,H}$ are the sums of: turbulent components $K^t_{m,q,H}$, which dominate below the mesopause; and molecular components $K_{m,q,H}$, which dominate above 120 km. The turbulent diffusivities are the sum of two components, free atmosphere and boundary layer diffusivities, defined below. In the future, these terms also may include effective diffusivities from the gravity wave parameterization. The non-local transport terms $\gamma_{q,H}$ are given by the ABL parameterization. Note that $F_q$, as defined in (4.451) and implemented in CAM 3.0, does not include the term which causes diffusive separation of constituents of differing molecular weights. The molecular diffusion in CAM 3.0 is currently incomplete and should be used with caution. The molecular viscosity and diffusivities are all currently defined as $3.55 \times 10^{-7} T^{2/3}/\rho$. A more complete form, allowing separation of constituents, will be implemented later.

The kinetic energy dissipation term $D$ in (4.449) is determined by forming the equation for total energy from (4.448–4.449):

$$\frac{\partial E}{\partial t} = u\frac{\partial u}{\partial t} + v\frac{\partial v}{\partial t} + \frac{\partial s}{\partial t} \tag{4.452}$$

$$= -\frac{1}{\rho}\left(u\frac{\partial F_u}{\partial z} + v\frac{\partial F_v}{\partial z} + \frac{\partial F_H}{\partial z}\right) + D \tag{4.453}$$

$$= -\frac{1}{\rho}\left(\frac{\partial F_{KE}}{\partial z} + \frac{\partial F_H}{\partial z}\right). \tag{4.454}$$

The diffusive kinetic energy flux in (4.454) is

$$F_{KE} \equiv uF_u + vF_v \tag{4.455}$$

and the kinetic energy dissipation is

$$D \equiv -\frac{1}{\rho}\left(F_u\frac{\partial u}{\partial z} + F_v\frac{\partial v}{\partial z}\right). \tag{4.456}$$

To show that $D$ is positive definite, we use (4.450) to expand for $F_u$ and $F_v$:

$$D = (K_m^t + K_m^m)\left[\left(\frac{\partial u}{\partial z}\right)^2 + \left(\frac{\partial v}{\partial z}\right)^2\right] \geq 0. \tag{4.457}$$

We show that energy is conserved in the column by integrating (4.454) in the vertical, from the surface ($z = 0$), to the top of the model ($z = z_{top}$):

$$\int_0^{z_{top}} \rho\frac{\partial E}{\partial t}dz = (F_{KE} + F_H)|_{z_{top}}^0. \tag{4.458}$$

Therefore, the vertically integrated energy will only change because of the boundary fluxes of energy, of which only the surface heat flux, $F_H(z = 0)$, is usually nonzero. It is typically assumed that the surface wind vanishes, even over oceans and sea ice, giving $F_{KE}(z = 0) = 0$. Then, the surface stress $F_{u,v}(z = 0)$ does not change the total energy in the column, but does result in kinetic energy dissipation and heating near the surface (see below) For coupled models, nonzero surface velocities can be accommodated by including $F_{KE}$ on both sides of the surface interface.

### 4.11.1 Free atmosphere turbulent diffusivities

The free atmospheric turbulent diffusivities are typically taken as functions of length scales $\ell_c$ and local vertical gradients of wind and virtual potential temperature, *e.g.*

$$K_c = {\ell_c}^2 S F_c(Ri). \tag{4.459}$$

Here $S$ is the local shear, defined by

$$S = \left| \frac{\partial \boldsymbol{V}}{\partial z} \right|, \tag{4.460}$$

and the mixing length $\ell_c$ is generally given by

$$\frac{1}{\ell_c} = \frac{1}{kz} + \frac{1}{\lambda_c}, \tag{4.461}$$

where $k$ is the Von Karman constant, and $\lambda_c$ is the so-called asymptotic length scale, taken to be 30 m above the ABL. Since the lowest model level is always greater than 30 m in depth, $\ell_c$ is simply set to 30 m in CAM 3.0. Furthermore, $F_c(Ri)$ denotes a functional dependence of $K_c$ on the gradient Richardson number:

$$Ri = \frac{g}{\theta_v} \frac{\partial \theta_v / \partial z}{S^2}, \tag{4.462}$$

where $\theta_v$ is the virtual potential temperature,

$$\theta_v = \theta \left[ 1 + \left( \frac{R_v}{R} - 1 \right) q \right]. \tag{4.463}$$

For simplicity, in the free atmosphere, we specify the same stability functions $F_c$ for all $c$. For unstable conditions ($Ri < 0$) we choose

$$F_c(Ri) = (1 - 18Ri)^{1/2}, \tag{4.464}$$

and for stable conditions ($Ri > 0$) we use.

$$F_c(Ri) = \frac{1}{1 + 10Ri\,(1 + 8Ri)}, \tag{4.465}$$

This means that no distinction is made between turbulent vertical diffusion of heat, scalars and momentum outside the boundary layer. However, separate coefficient arrays are maintained and other parameterizations (such as gravity wave drag) may provide distinct diffusivities. We also note the the turbulent diffusivity is the same for all constituents, even within the ABL. However, the molecular diffusivities differ for each constituent since they depend on it's molecular weight.

### 4.11.2 "Non-local" atmospheric boundary layer scheme

The free atmosphere turbulent diffusivities, described above, are an example of the local diffusion approach. In such an approach, the turbulent flux of a quantity is proportional to the local gradient of that quantity (*e.g.* (4.450)–(4.451)). In addition, the eddy diffusivity depends on local gradients of mean wind and mean virtual temperature (see (4.459)). These are reasonable assumptions when the length scale of the largest turbulent eddies is smaller than the size of the domain over which the turbulence extends. In the Atmospheric Boundary Layer (ABL) this is typically true for neutral and stable conditions only. For unstable and convective conditions, however, the largest transporting eddies may have a size similar to the boundary layer height itself, and the flux can be counter to the local gradient [Deardorff, 1972; Holtslag and Moeng, 1991]. In such conditions a local diffusion approach is no longer appropriate, and the eddy diffusivity is better represented with turbulent properties characteristic of the ABL. We will refer to such an approach as non-local diffusion.

To account for "non-local" transport by convective turbulence in the ABL, the local diffusion term for constituent $c$ is modified as in (4.451):

$$\overline{w'C'} = -K_c \left( \frac{\partial C}{\partial z} - \gamma_c \right) , \tag{4.466}$$

where $K_c$ is the non-local eddy diffusivity for the quantity of interest. The term $\gamma_c$ is a "non-local" transport term and reflects non-local transport due to dry convection. Eq. (4.466) applies to static energy, water vapor, and passive scalars. No countergradient term is applied to the wind components, so (4.450) does not contain these terms. For stable and neutral conditions the non-local term is not relevant for any of the quantities. The eddy diffusivity formalism is, however, modified for all conditions.

In the non-local diffusion scheme the eddy diffusivity is given by

$$K_c = k \; w_t \; z \left( 1 - \frac{z}{h} \right)^2 , \tag{4.467}$$

where $w_t$ is a turbulent velocity scale and $h$ is the boundary layer height. Equation (4.467) applies for heat, water vapor and passive scalars. The eddy diffusivity of momentum $K_m$, is also defined as (4.467) but with $w_t$ replaced by another velocity scale $w_m$. With proper formulation of $w_t$ (or $w_m$) and $h$, it can be shown that equation (4.467) behaves well from very stable to very unstable conditions in horizontally homogeneous and quasi-stationary conditions. For unstable conditions $w_t$ and $w_m$ are proportional to the so-called convective velocity scale $w_*$, while for neutral and stable conditions $w_t$ and $w_m$ are proportional to the friction velocity $u_*$.

The major advantage of the present approach over the local eddy diffusivity approach is that large eddy transport in the ABL is accounted for and entrainment effects are treated implicitly. Above the ABL, $\gamma_c = 0$ so (4.466) reduces to a local form with $K_c$ given by (4.459). Near the top of the ABL we use the maximum of the values by (4.459) and (4.467), although (4.467) almost always gives the larger value in practice.

The non-local transport term in (4.466), $\gamma_c$, represents non-local influences on the mixing by turbulence [Deardorff, 1972]. As such, this term is small in stable conditions, and is therefore neglected under these conditions. For unstable conditions, however, most heat and moisture transport is achieved by turbulent eddies with sizes on the order of the depth $h$ of the ABL. In such cases, a formulation for $\gamma_c$ consistent with the eddy formulation of (4.466) is given by

$$\gamma_c = a \frac{w_* (\overline{w'C'})_s}{{w_m}^2 h} , \tag{4.468}$$

where $a$ is a constant and $(\overline{w'C'})_s$ is the surface flux (in kinematic units) of the transported scalar. The form of (4.468) is similar to the one proposed in Holtslag and Moeng [1991]. The non-local correction vanishes under neutral conditions, for which $w_* = 0$.

The formulations of the eddy-diffusivity and the non-local terms are dependent on the boundary layer height $h$. The CCM2 configuration of this non-local scheme made use of a traditional approach to estimating the boundary layer depth by assuming a constant value for the bulk

Richardson number across the boundary layer depth so that $h$ was iteratively determined using

$$h = \frac{Ri_{cr}\,\{u(h)^2 + v(h)^2\}}{(g/\theta_s)\,(\theta_v(h) - \theta_s)}\ , \tag{4.469}$$

where $Ri_{cr}$ is a critical bulk Richardson number for the ABL; $u(h)$ and $v(h)$ are the horizontal velocity components at $h$; $g/\theta_s$ is the buoyancy parameter and $\theta_v(h)$ is the virtual temperature at $h$. The quantity $\theta_s$ is a measure of the surface air temperature, which under unstable conditions was given by

$$\theta_s = \theta_v\,(z_s) + b\,\frac{(\overline{w'\theta_v'})_s}{w_m}\ , \tag{4.470}$$

where $b$ is a constant, $(\overline{w'\theta_v'})_s$ is the virtual heat flux at the surface, $\theta_v\,(z_s)$ is a virtual temperature in the atmospheric surface layer (nominally 10 m), $b\ (\overline{w'\theta_v'})_s/w_m$ represents a temperature excess (a measure of the strength of convective thermals in the lower part of the ABL) and unstable conditions are determined by $(\overline{w'\theta_v'})_s > 0$. The quantity $\theta_v\,(z_s)$ was calculated from the temperature and moisture of the first model level and of the surface by applying the procedure in Geleyn [1988]. The value of the critical bulk Richardson number $Ri_{cr}$ in (4.469), which generally depends on the vertical resolution of the model, was chosen as $Ri_{cr} = 0.5$ for the CCM2.

Vogelezang and Holtslag [1996] have recently studied the suitability of this formulation in the context of field observations, large-eddy simulations [Moeng and Sullivan, 1994], and an $E - \epsilon$ turbulence closure model [Duynkerke, 1988]. They propose a revised formulation which combines shear production in the outer region of the boundary layer with surface friction, where the Richardson number estimate is based on the differences in wind and virtual temperature between the top of the ABL and a lower height that is well outside the surface layer (*i.e.* 20 m - 80 m). In addition to providing more realistic estimates of boundary layer depth, the revised formulation provides a smoother transition between stable and neutral boundary layers. Consequently, CAM 3.0 employs the Vogelezang and Holtslag [1996] formulation for estimating the atmospheric boundary layer height, which can be written as

$$h = z_s + \frac{Ri_{cr}\,\{(u(h) - u_{SL})^2 + (v(h) - v_{SL})^2 + \mathcal{B}u_*^2\}}{(g/\theta_{SL})\,(\theta_v(h) - \theta_{SL})}. \tag{4.471}$$

The quantities $u_{SL}$, $v_{SL}$, and $\theta_{SL}$ represent the horizontal wind components and virtual potential temperature just above the surface layer (nominally $0.1h$). In practice, the lowest model level values for these quantities are used to iteratively determine $h$ for all stability conditions, where the critical Richardson number, $Ri_{cr}$, is assumed to be 0.3. The disposable parameter $\mathcal{B}$ has been experimentally determined to be equal to 100 (see Vogelezang and Holtslag [1996]). The computation starts by calculating the bulk Richardson number $Ri$ between the level of $\theta_{SL}$ and subsequent higher levels of the model. Once $Ri$ exceeds the critical value, the value of $h$ is derived by linear interpolation between the level with $Ri > Ri_{cr}$ and the level below.

Using the calculated value for $h$ and the surface fluxes, we calculate the velocity scales, the eddy diffusivities with (4.467), and the countergradient terms with (4.468), for each of the transported constituents. Subsequently, the new profiles for $\theta$, $q$, $u$, and $v$ are calculated using an implicit diffusion formulation.

The turbulent velocity scale of (4.467) depends primarily on the relative height $z/h$ ($h$ is boundary layer height), and the stability within the ABL. Here stability is defined with respect to the surface virtual heat flux $(\overline{w'\theta_v'})_s$. Secondly, the velocity scales are also generally dependent on the specific quantity of interest. We will assume that the velocity scales for mixing of passive scalars and specific humidity are equal to the one for heat, denoted by $w_t$. For the wind components, the velocity scale is different and denoted by $w_m$. The specification of $w_t$ and $w_m$ is given in detail by Troen and Mahrt [1986]. Holtslag et al. [1990] have rewritten the velocity scale, in terms of the more widely accepted profile functions of Dyer [1974], and have given a new formulation for very stable conditions. Below we follow the latter approach.

For stable ($(\overline{w'\theta_v'})_s < 0$) and neutral surface conditions ($(\overline{w'\theta_v'})_s = 0$), the velocity scale for scalar transport is

$$w_t = \frac{u_*}{\phi_h} \ , \tag{4.472}$$

where $u_*$ is the friction velocity defined by

$$u_* = \left[(\overline{u'w'})_s^2 + (\overline{v'w'})_s^2\right]^{1/4} . \tag{4.473}$$

Furthermore, $\phi_h$ is the dimensionless vertical temperature gradient given by Dyer [1974],

$$\phi_h = 1 + 5\frac{z}{L} \ , \tag{4.474}$$

for $0 \le z/L \le 1$. Here $L$ is the Obukhov length, defined by

$$L = \frac{-u_*^3}{k(g/\theta_{v0})(\overline{w'\theta_v'})_0}. \tag{4.475}$$

For $z/L > 1$,

$$\phi_h = 5 + \frac{z}{L} \ , \tag{4.476}$$

which matches (4.474) for $z/L = 1$. Equation (4.476) is a simple means to prevent $\phi_h$ from becoming too large (and $K_c$ too small) in very stable conditions. In stable conditions, the exchange coefficients for heat and momentum are often found to be similar. Therefore we may use $w_m$=$w_t$.

For unstable conditions $(\overline{w'\theta_v'})_s > 0$, we have that $w_t$ and $w_m$ differ in the surface layer ($z/h \le 0.1$) and in the outer layer of the ABL ($z/h > 0.1$). For the surface layer, $w_t$ is given by (4.472) with

$$\phi_h = \left(1 - 15\frac{z}{L}\right)^{-1/2} \ . \tag{4.477}$$

Similarly, $w_m$ is written as

$$w_m = \frac{u_*}{\phi_m} \ , \tag{4.478}$$

where $\phi_m$ is the dimensionless wind gradient given by

$$\phi_m = \left(1 - 15\frac{z}{L}\right)^{-1/3} \ . \tag{4.479}$$

In the surface layer, the scalar flux is normally given by

$$(\overline{w'c'})_0 = -\frac{ku_*z}{\phi_h}\left(\frac{\partial C}{\partial z}\right) \ . \tag{4.480}$$

Comparison with (4.466) and (4.467) shows that, in the surface layer, we should have $a = 0$ in (4.468) for consistency.

For the outer layer, $w_t$ and $w_m$ are given by

$$w_t = w_m/Pr \ , \tag{4.481}$$

where

$$w_m = \left(u_*^3 + c_1 w_*^3\right)^{1/3} \ , \tag{4.482}$$

and

$$w_* = \left((g/\theta_{v0}) \ (\overline{w'\theta_v'})_0 h\right)^{1/3} \tag{4.483}$$

is the convective velocity scale. Furthermore, $Pr$ is the turbulent Prandtl number and $c_1$ is a constant. The latter is obtained by evaluating the dimensionless vertical wind gradient $\phi_m$ by (4.479) at the top of the surface layer, as discussed by Troen and Mahrt [1986]. This results in $c_1 = 0.6$. For very unstable conditions ($h \gg -L$ or $w_*/u_* \gg 0$), it can be shown with (4.481) that $w_m$ is proportional to 0.85 $w_*$, while for the neutral case $w_m = u_*$. The turbulent Prandtl number $Pr$ ($= K_m/K_h = w_m/w_t$) of (4.481) is evaluated from

$$Pr = \frac{\phi_h}{\phi_m} \ \left(\frac{z}{L}\right) + ak\frac{z}{h}\frac{w_*}{w_m} \tag{4.484}$$

for $z = 0.1h$. Equation (4.484) arises from matching (4.466), (4.467), (4.468), and (4.480) at the top of the surface layer. As in Troen and Mahrt we assume that $Pr$ is independent of height in the unstable outer layer. Its value decreases from $Pr = 1$ for the neutral case ($z/L = 0$ and $w_* = 0$), to $Pr = 0.6$ for $w_*/u_* \simeq 10$ in very unstable conditions.

In very unstable conditions, the countergradient term of (4.468) approaches

$$\gamma_c = d\frac{\overline{wC_0}}{w_* h} \ , \tag{4.485}$$

where $d \simeq a/0.85^2$, because for very unstable conditions we obtain $w_m \simeq 0.85 w_*$. Since typically $d \simeq 10$ Troen and Mahrt [1986], we have $a = 7.2$. Similarly, the temperature excess of (4.470) reads in this limit as $d(\overline{w'\theta_v'})_0/w_*$. This leads to $b$ ($= 0.85\ d$) $= 8.5$ in (4.470).

Finally, using the velocity scales described above, the flux equation (4.466) is continuous in relative height ($z/h$) and in the boundary layer stability parameter ($h/L$ or $w_*/u_*$).

### 4.11.3 Discretization of the vertical diffusion equations

In CAM 3.0, as in previous version of the CCM, (4.448–4.451) are cast in pressure coordinates, using

$$dp = -\rho g dz, \tag{4.486}$$

and discretized in a time-split form using an Euler backward time step. Before describing the numerical solution of the diffusion equations, we define a compact notation for the discrete equations. For an arbitrary variable $\psi$, let a subscript denote a discrete time level, with current step $\psi_n$ and next step $\psi_{n+1}$. The model has $L$ layers in the vertical, with indexes running from top to bottom. Let $\psi^k$ denote a layer midpoint quantity and let $\psi^{k-}$ denote the value on the upper interface of layer $k$ while $\psi^{k+}$ denotes the value on the lower interface. The relevant quantities, used below, are then:

$$
\begin{aligned}
\psi^{k+} &= (\psi^k + \psi^{k+1})/2, \quad k \in (1, 2, 3, ..., L-1) \\
\psi^{k-} &= (\psi^{k-1} + \psi^k)/2, \quad k \in (2, 3, 4..., L) \\
\delta^k \psi &= \psi^{k+} - \psi^{k-}, \\
\delta^{k+} \psi &= \psi^{k+1} - \psi^k, \\
\delta^{k-} \psi &= \psi^k - \psi^{k-1}, \\
\psi_{n+} &= (\psi_n + \psi_{n+1})/2, \\
\delta_n \psi &= \psi_{n+1} - \psi_n, \\
\delta t &= t_{n+1} - t_n, \\
\Delta^{k,l} &= 1, \ k = l, \\
&= 0, \ k \neq l.
\end{aligned}
\tag{4.487}
$$

Like the continuous equations, the discrete equations are required to conserve momentum, total energy and constituents. The discrete forms of (4.448–4.449) are:

$$
\frac{\delta_n (u, v, q)^k}{\delta t} = g \frac{\delta^k F_{u,v,q}}{\delta^k p} \tag{4.488}
$$

$$
\frac{\delta_n s^k}{\delta t} = g \frac{\delta^k F_H}{\delta^k p} + D^k. \tag{4.489}
$$

For interior interfaces, $1 \leq k \leq L-1$,

$$
F^{k+}_{u,v} = \left(g\rho^2 K_m\right)^{k+}_n \frac{\delta^{k+}(u,v)_{n+1}}{\delta^{k+} p} \tag{4.490}
$$

$$
\begin{aligned}
F^{k+}_{q,H} &= \left(g\rho^2 K_{q,H}\right)^{k+}_n \frac{\delta^{k+}(u,v)_{n+1}}{\delta^{k+} p} \\
&+ \left(\rho K^t_{q,H} \gamma_{q,H}\right)^{k+}_n .
\end{aligned}
\tag{4.491}
$$

Surface fluxes $F^{L+}_{u,v,q,H}$ are provided explicitly at time $n$ by separate surface models for land, ocean, and sea ice while the top boundary fluxes are usually $F^{1-}_{u,v,q,H} = 0$. The turbulent diffusion coefficients $K^t_{m,q,H}$ and non-local transport terms $\gamma_{q,H}$ are calculated for time $n$ by the turbulence model described above, which is identical to CCM3. The molecular diffusion coefficients, described earlier, are only included if the model top is above $\sim 90$ km, in which case nonzero top boundary fluxes may be included for heat and some constituents.

The free atmosphere turbulent diffusivities $K^{k+}_n$, given by (4.459–4.465), are discretized as

$$
K^{k+}_n = K^{k+}_N \cdot F_c\big(R^{k+}_I\big) \geq 0.01. \tag{4.492}
$$

The stability function is:

$$
F_c(R_I) = \begin{cases} 1/\left(1 + 10 R_I [1 + 8 R_I]\right) & \text{for } R_I \geq 0 \text{ (stable)}, \\ \sqrt{1 - 18 R_I} & \text{for } R_I < 0 \text{ (unstable)}, \end{cases} \tag{4.493}
$$

The neutral $K_N$ is calculated by

$$K_N^{k+} = \ell^2 \frac{\left[\left(\delta^{k+}u_n\right)^2 + \left(\delta^{k+}v_n\right)^2\right]^{1/2}}{\delta^{k+}z_n}, \tag{4.494}$$

with $\ell = 30$ m. The Richardson number in the free atmosphere is calculated from

$$R_I^{k+} = \frac{g}{\theta_v^{k+}} \times \frac{\delta^{k+}z_n\delta^{k+}\theta_v}{\left(\delta^{k+}u_n\right)^2 + \left(\delta^{k+}v_n\right)^2} \tag{4.495}$$

where

$$\theta_v^k = \theta_n^k \left(1.0 + \left(\frac{R_v}{R} - 1\right) q_n^k\right). \tag{4.496}$$

Similarly to the continuous form (4.456), $D^k$ is determined by separating the kinetic energy change over a time step into the kinetic energy flux divergence and the kinetic energy dissipation. The discrete system is required to conserve energy exactly:

$$\begin{aligned}\sum_{k=1}^{L} \left[(u_{n+1}^k)^2 + (v_{n+1}^k)^2 + s_{n+1}^k\right] \delta^k p = \\ \sum_{k=1}^{L} \left[(u_n^k)^2 + (v_n^k)^2 + s_n^k\right] \delta^k p + \delta t(F_H^{L+} + F_H^{1-}),\end{aligned} \tag{4.497}$$

where we have assumed zero boundary fluxes for kinetic energy. This leads to

$$D^k = \frac{g}{2\delta^k p}(d_u^{k+} + d_u^{k-} + d_v^{k+} + d_v^{k-}) \tag{4.498}$$

$$d_{u,v}^{k+} = \delta^{k+}(u,v)_{n+}F_{u,v}^{k+}, \quad 1 \leq k \leq L-1 \tag{4.499}$$

$$d_{u,v}^{L+} = -2(u,v)_{n+}^L F_{u,v}^{L+} \tag{4.500}$$

According to (4.498), the internal dissipation of kinetic energy in each layer $D^k$ is the average of the dissipation on the bounding interfaces $d_{u,v}^{k\pm}$, given by (4.499) and (4.500). Expanding (4.499) using (4.490) and recalling that $u_{n+} = (u_{n+1} + u_n)/2$,

$$d_u^{k+} = \frac{\left(g\rho^2 K_m\right)^{k+}}{2\delta^{k+}p} \left[\left(\delta^{k+}u_{n+1}\right)^2 + \delta^{k+}u_{n+1}\delta^{k+}u_n\right], \tag{4.501}$$

for $1 \leq k \leq L-1$ and similarly for $d_v^{k+}$. The discrete kinetic energy dissipation is not positive definite, because the last term in (4.501) is the product of the vertical difference of momentum at two time levels. Although $d_{u,v}^{k+}$ will almost always be $> 0$, values $\leq 0$ may occur occasionally. The kinetic energy dissipation at the surface is

$$d_{u,v}^{L+} = -\left[(u,v)_{n+1}^L + (u,v)_n^L\right] F_{u,v}^{L+}. \tag{4.502}$$

Since the surface stress is opposed to the bottom level wind, the surface layer is heated by the frictional dissipation. However, $d_{u,v}^{L+}$ is not guaranteed to be positive, since it involves the bottom level wind at two time levels.

Note that it has been assumed that the pressure does not change within the vertical diffusion, even though there are boundary fluxes of constituents, including water. This assumption has been made in all versions of the CCM and is still made in CAM 3.0. This assumption will be removed in a future version of CAM 3.0, since the implied horizontal fluxes of dry air, to compensate for the boundary flux of water, cause implied fluxes of other constituents.

### 4.11.4 Solution of the vertical diffusion equations

A series of time-split operators is actually defined by (4.488–4.491) and (4.498–4.500). Once the diffusivities ($K_{m,q,H}$) and the non-local transport terms ($\gamma_{q,H}$) have been determined, the solution of (4.488–4.491), proceeds in several steps.

1. update the $q$ and $s$ profiles using $\gamma_{q,H}$;
2. update the bottom level values of $u$, $v$, $q$ and $s$ using the surface fluxes;
3. invert (4.488) and (4.490) for $u, v_{n+1}$;
4. compute $D$ and use to update the $s$ profile;
5. invert (4.488,4.489) and (4.491) for $s_{n+1}$ and $q_{n+1}$;

Note that since all parameterizations in CAM 3.0 return tendencies rather than modified profiles, the actual quantities returned by the vertical diffusion are $\delta_n(u,v,s,q)/\delta t$.

The non-local transport terms, $\gamma_{q,H}$, given by (4.468), cannot be treated implicitly because they depend on the surface flux, the boundary layer depth and the velocity scale, but not explicitly on the profile of the transported quantity. Therefore, application of $\gamma_q$ is not guaranteed to give a positive value for $q$ and negative values may not be removed by the subsequent implicit diffusion step. This problem is not strictly numerical; it arises under highly non-stationary conditions for which the ABL formulation is not strictly applicable. In practice, we evaluate

$$q_{n*} = q_n + \frac{g\delta t}{\delta^k p}\delta^k \left[\rho K_q^t \gamma_q\right]_n \tag{4.503}$$

and check the $q_{n*}$ profile for negative values (actually for $q^k_{n*} < q_{min}$, where $q_{min}$ may be $> 0$). If any negative values are found, we set $q_{n*} = q_n$ for that constituent profile (but not for other constituents at the same point).

Equations (4.488–4.491) constitute a set of four tridiagonal systems of the form

$$-A^k \psi^{k+1}_{n+1} + B^k \psi^k_{n+1} - C^k \psi^{k-1}_{n+1} = \psi^k_{n\prime}, \tag{4.504}$$

where $\psi_{n\prime}$ indicates $u$, $v$, $q$, or $s$ after updating from time $n$ values with the nonlocal and boundary fluxes. The super-diagonal ($A^k$), diagonal ($B^k$) and sub-diagonal ($C^k$) elements of (4.504) are:

$$A^k = \frac{1}{\delta^k p}\frac{\delta t}{\delta^{k+} p}\left(g^2\rho^2 K\right)^{k+}_n, \tag{4.505}$$

$$B^k = 1 + A^k + C^k, \tag{4.506}$$

$$C^k = \frac{1}{\delta^k p}\frac{\delta t}{\delta^{k-} p}\left(g^2\rho^2 K\right)^{k-}_n. \tag{4.507}$$

The solution of (4.504) has the form

$$\psi^k_{n+1} = E^k \psi^{k-1}_{n+1} + F^k, \tag{4.508}$$

or,

$$\psi_{n+1}^{k+1} = E^{k+1}\psi_{n+1}^{k} + F^{k+1}. \tag{4.509}$$

Substituting (4.509) into (4.504),

$$\psi_{n+1}^{k} = \frac{C^k}{B^k - A^k E^{k+1}}\psi_{n+1}^{k-1} + \frac{\psi_{n\prime}^{k} + A^k F^{k+1}}{B^k - A^k E^{k+1}}. \tag{4.510}$$

Comparing (4.508) and (4.510), we find

$$E^k = \frac{C^k}{B^k - A^k E^{k+1}}, \quad L > k > 1, \tag{4.511}$$

$$F^k = \frac{\psi_{n\prime}^{k} + A^k F^{k+1}}{B^k - A^k E^{k+1}}, \quad L > k > 1. \tag{4.512}$$

The terms $E^k$ and $F^k$ can be determined upward from $k = L$, using the boundary conditions

$$E^{L+1} = F^{L+1} = A^L = 0. \tag{4.513}$$

Finally, (4.510) can be solved downward for $\psi_{n+1}^{k}$, using the boundary condition

$$C^1 = 0 \Rightarrow E^1 = 0. \tag{4.514}$$

CCM1-3 used the same solution method, but with the order of the solution reversed, which merely requires writing (4.509) for $\psi_{n+1}^{k-1}$ instead of $\psi_{n+1}^{k+1}$. The order used here is particularly convenient because the turbulent diffusivities for heat and all constituents are the same but their molecular diffusivities are not. Since the terms in (4.511-4.512) are determined from the bottom upward, it is only necessary to recalculate $A^k$, $C^k$, $E^k$ and $1/(B^k - A^k E^{k+1})$ for each constituent within the region where molecular diffusion is important. Note that including the diffusive separation term for constituents (which will be in the next version of CAM 3.0) adds additional terms to the definitions of $A^k$, $B^k$, and $C_k$, but does not otherwise change the solution method.

### 4.11.5 Discrete equations for $s$, $T$, and $z$

The dry static energy at step $n$ and level $k$ is

$$s_n^k = c_p^d T_n^k + g z^k, \tag{4.515}$$

which can be calculated from $T_n$ by integrating the hydrostatic equation using the perfect gas law.

$$gz \equiv \Phi = \Phi_s + \int_{p_s}^{p} RT\, d\ln p', \tag{4.516}$$

where $\Phi$ is the geopotential, $\Phi_s$ is the geopotential at the Earth's surface and $p_s$ is the surface pressure. A fairly arbitrary discretization of (4.516) can be represented using a triangular hydrostatic matrix $H^{kl}$,

$$\Phi^k = \Phi_s + \sum_{l=L}^{k} R^l H^{kl} T^l. \tag{4.517}$$

Note that (4.517) is often written in terms of the virtual temperature $T_v = TR/R^d$. The apparent gas constant $R$ includes the effect of water vapor and is defined as

$$R = R^d + (R^w - R^d)q, \tag{4.518}$$

where $R^d$ is the apparent gas constant for dry air and $R^w$ is the gas constant for water vapor.

Using (4.517) in (4.515), we have

$$\begin{aligned} s_n^k &= c_p^d T_n^k + \sum_{l=L}^{k} R^l H^{kl} T_n^l, & (4.519) \\ &= \left(c_p^d + R^k H^{kk}\right) T_n^k + \Phi_n^{k+}. & (4.520) \end{aligned}$$

The interface geopotential in (4.520) is defined as

$$\Phi^{k+} = \sum_{l=L}^{k+1} R^k H^{kl} T^l, \tag{4.521}$$

and $R^k$ is evaluated from (4.518), using $q_n^k$. Although the correct boundary condition on (4.521) is $\Phi_{L+} = \Phi_s$, within the parameterization suite it is usually sufficient to take $\Phi_{L+} = 0$.

The definition of the hydrostatic matrix $H$ depends on the numerical method used in the dynamics and is subject to constraints from energy and mass conservation. The definitions of $H$ for the three dynamical methods used in CAM 3.0 are given in the dynamics descriptions.

After $s_n$ is modified by diabatic heating in a time split process, the new $s_{n+1} = s_n + Q_n \delta t$ can be converted into $T_{n+1}$ and $\Phi_{n+1}$ using (4.520):

$$\begin{aligned} s_{n+1}^k &= \left(c_p^d + R^k H^{kk}\right) T_{n+1}^k + \Phi_{n+1}^{k+} & (4.522) \\ T_{n+1}^k &= \left(s_{n+1}^k - \Phi_{n+1}^{k+}\right) \left(c_p + R^k H^{kk}\right)^{-1} & (4.523) \end{aligned}$$

with $R^k$ evaluated from using $q_{n+1}^k$. Once $H$ is defined, (4.521) and (4.523) can be solved for $T_{n+1}$ and $\Phi_{n+1}$ from the bottom up. Since the latter must normally recalculated if $T$ is modified, calculating $T$ and $\Phi$ from $s$ involves the same amount of computation as calculating $\Phi$ and $s$ from $T$.

## 4.12 Sulfur Chemistry

It is also possible to set CAM to predict sulfate aerosols. These aerosols can be run as passive (non-interacting) constituents, or the model can be set to allow sulfate to interact with the radiative transfer formulation. The CAM 3.0 release of the model allows only the direct radiative effect of the aerosols, although it is a straightforward modification of the model to allow indirect effects as well.

The formulation for the parameterization follows closely that described in Barth et al. [2000] and Rasch et al. [2000]. The module was used to examine the influence of sulfate aerosols on the atmospheric radiation budget in Kiehl et al. [2000] The standard emission inventory used for prognostic aerosols is not the same as that used to produce the climatological prescribed sulfate aerosols described in section 4.8.3.

The sulfur chemistry represented in the model includes emissions, transport, gas and aqueous reactions, and wet and dry deposition of DMS, $SO_2$, $SO_4^{2-}$, and $H_2O_2$. Sources and sinks represented in the description of the sulfur cycle include emissions of DMS and anthropogenic sulfur, gas-phase oxidation of DMS and $SO_2$, gas-phase production and destruction of $H_2O_2$, aqueous-phase oxidation of S(IV) by $H_2O_2$ and $O_3$, dry deposition of $H_2O_2$, $SO_2$, and aerosol sulfate, and wet deposition of $H_2O_2$, $SO_2$, and aerosol sulfate.

Transport processes of trace gases and aerosols include resolved-scale advection and subgrid-scale convection and diffusion. The convective transport of trace gases and aerosols is performed on the interstitial fraction of these species in the cloudy volume and the fraction of dissolved material in the cloud drops that do not undergo microphysical transformation to precipitation. The species can be can be detrained at higher levels in the model by the convective processes.

### 4.12.1 Emissions

Emissions of sulfur species in the model include anthropogenic emissions of $SO_2$ and $SO_4^{2-}$ and oceanic emissions of DMS; volcanic and biomass burning sources currently are excluded. Anthropogenic emissions come from the Smith et al. [2001] inventory. The seasonally averaged emissions data were provided at the surface and at 100 m and above to accommodate emissions from industry stacks

The anthropogenic emissions are assumed to be 98% by mole $SO_2$ and 2% $SO_4^{2-}$. Since the emissions inventory supplied data at two levels and the height of the interface between the bottom two model levels was generally above 100 m (average height was ∼120 m), we apportioned a fraction of the emissions data from above 100 m to the bottom level of the model. The fraction into the bottom level was determined as

$$\frac{zi(1) - 100}{zi(2) - 100},$$

where $zi(1)$ is the height of the top of the lowest level of the model and $zi(2)$ is the height of the top of the second lowest level of the model.

The emissions of DMS were obtained from the biogenic sulfur emissions inventory of Kettle et al. [1999].

### 4.12.2 Chemical Reactions

The order of the chemistry calculations is as follows. The aqueous chemistry is performed after the cloud water mixing ratio is determined. The new $H_2O_2$, $SO_2$, and $SO_4^{2-}$ concentrations are then used for the gas chemistry calculations. The modified $H_2O_2$, $SO_2$, and $SO_4^{2-}$ concentrations then are used in the wet deposition calculation. After the chemistry and wet deposition are calculated, transport through subgrid convective cores is determined for the interstitial fraction of each species (because of their high solubility, sulfate aerosols are not convectively transported). Because a centered time step is used, a time filter couples the concentrations from the odd and even time step integrations. Then the emissions and dry deposition calculations are performed.

The reactions used for the sulfur cycle are described in Table 4.7.

Table 4.7: Reactions Included in the Global Sulfur Model

| | | | | $k_{298}$[1] | $\frac{E}{R}$ | Reference[2] |
|---|---|---|---|---|---|---|
| *Gas Chemistry* | | | | | | |
| (R1) | $SO_2$+ OH + M | $\rightarrow$ | $SO_4^{2-}$+ M | $k_o$=3.0$\times$ $10^{-31}(\frac{T}{300})^{-3.3}$ <br> $k_\infty$=1.5$\times$ $10^{-12}$ | | NASA97 |
| (R2) | DMS + OH | $\rightarrow$ | $\alpha SO_2$+ (1 - $\alpha$) MSA[3] | | | Y90 |
| (R3) | DMS + $NO_3$ | $\rightarrow$ | $SO_2$+ $HNO_3$ | 1.0$\times$ $10^{-12}$ | 500. | NASA97 |
| (R4) | $HO_2$+ $HO_2$ | $\rightarrow$ | $H_2O_2$+ $O_2$ | 8.6$\times$ $10^{-12}$ | -590. | NASA97 |
| (R5) | $H_2O_2$+ h$\nu$ | $\rightarrow$ | 2OH | see text | | |
| (R6) | $H_2O_2$+ OH | $\rightarrow$ | $HO_2$+ $H_2O$ | 1.7$\times$ $10^{-12}$ | 160. | NASA97 |
| *Aqueous Chemistry* | | | | | | |
| (R7) | $HSO_3^-$+ $H_2O_2$ | $\rightarrow$ | $SO_4^{2-}$+ $2H^+$+ $H_2O$ | 2.7$\times$ $10^7$ [4] | 4750. | HC85 |
| (R8) | $HSO_3^-$+ $O_3$ | $\rightarrow$ | $SO_4^{2-}$+ $H^+$+ $O_2$ | 3.7$\times$ $10^5$ | 5300. | HC85 |
| (R9) | $SO_3^{2-}$+ $O_3$ | $\rightarrow$ | $SO_4^{2-}$+ $O_2$ | 1.5$\times$ $10^9$ | 5280. | HC85 |
| *Equilibrium Reactions* | | | | | | |
| (R10) | $H_2O_2$(g) | $\rightleftharpoons$ | $H_2O_2$(aq) | 7.4$\times$ $10^4$ | -6621. | LK86 |
| (R11) | $O_3$(g) | $\rightleftharpoons$ | $O_3$(aq) | 1.15$\times$ $10^{-2}$ | -2560. | NBS65 |
| (R12) | $SO_2$(g) | $\rightleftharpoons$ | $SO_2$ (aq) | 1.23 | -3120. | NBS65 |
| (R13) | $H_2SO_3$ | $\rightleftharpoons$ | $HSO_3^-$+ $H^+$ | 1.3$\times$ $10^{-2}$ | -2015. | M82 |
| (R14) | $HSO_3^-$ | $\rightleftharpoons$ | $SO_3^{2-}$+ $H^+$ | 6.3$\times$ $10^{-8}$ | -1505. | M82 |

## Gas-Phase Reactions

Oxidation of $SO_2$ to form sulfate, oxidation of DMS to form $SO_2$, and production and destruction of $H_2O_2$ are represented in the model.

In R1, it is assumed that the $SO_2$ + OH reaction is the rate-limiting step of the multistep process of forming aerosol sulfate. Concentrations of short-lived radicals OH, $NO_3$, and $HO_2$ are prescribed using three-dimensional, monthly averaged concentrations obtained from the Intermediate Model of Global Evolution of Species (IMAGES) [Müller and Brasseur, 1995]. The diurnal variation of these oxidants is not included in our calculations, but instead, the diurnally averaged value is used at each time step. The rate coefficient for (R2) follows Benkovitz et al. [1994], who followed the work of Yin et al. [1990*b*,*a*]. The rate of $H_2O_2$ photolysis is determined via a look-up table method where the photolysis rate depends on the diurnally averaged zenith angle and the height of the grid point, assuming that the albedo for ultraviolet radiation is 0.3. Because R4 is nonlinear and the diurnally averaged rate of reaction does not equal the reaction rate of diurnally averaged $HO_2$ mixing ratios, the $HO_2$ mixing ratios are adjusted by the amount of daylight at any given latitude. The rates of the sulfur reactions are determined by the effective

[1]Units for first order reactions are $s^{-1}$, for the second-order gas reactions are $molecules^{-1}$ $cm^3$ $s^{-1}$, for the third-order gas reactions $molecules^{-2}$ $cm^6$ $s^{-1}$, and for the second-order aqueous reactions are $M^{-1}$ $s^{-1}$. Units for solubility constants are M $atm^{-1}$, and units for dissociation constants are M. Reaction rates are of the form $k = k_{298}\exp[-\frac{E}{R}(\frac{1}{T} - \frac{1}{298})]$ unless otherwise noted.

[2]NASA97, Demore et al. [1997]; Y90, Yin et al. [1990*b*,*a*]; HC85, Hoffmann and Calvert [1985]; LK86, Lind and Kok [1986]; NBS65, National Bureau of Standards [1965]; and M82, Maahs [1982].

[3]Here $k = \frac{Te^{-234/T}+8.46\times10^{-10}e^{7230/T}+2.68\times10^{-10}e^{7810/T}}{1.04\times10^{11}T+88.1e^{7460/T}}$.

[4]Here $k = \frac{k_{298}\exp[-\frac{E}{R}(\frac{1}{T}-\frac{1}{298})][H^+]}{1+13[H^+]}$.

first-order rate coefficient and using a quasi-steady state approximation [Hesstvedt et al., 1978]. The $H_2O_2$ concentration determined from the gas-phase reactions is calculated using an Euler forward approximation.

### Aqueous-Phase Reactions

Oxidation of aqueous $SO_2$ by $O_3$ and $H_2O_2$ to form $SO_4^{2-}$ aerosol is included in the model (Table 4.7). The concentrations of $O_3$ are prescribed using three-dimensional, monthly averaged concentrations obtained from the IMAGES model. Prescribed species ($O_3$, OH, $HO_2$, and $NO_3$) are set according to the linearly interpolated concentration for the location of the grid point and the time of year.

The pH of the drops is determined diagnostically assuming an $NH_4^+$ to $SO_4^{2-}$ molar ratio of 1.0.

$$[H^+] = [HSO_3^-] + [SO_4^{2-}].$$

The liquid water content in a grid cell is determined by combining the resolved-scale cloud water mixing ratio that is predicted, the subgrid-scale deep convective and shallow convective cloud water mixing ratios, and the resolved-scale rain mixing ratio that is diagnosed from the precipitation rate using a mass-weighted fall speed, which is determined assuming a Marshall Palmer size distribution for rain. $SO_2$ and $H_2O_2$ are depleted and $SO_4^{2-}$ is produced only in the cloudy region of the grid box. The grid box concentration of these species is found by multiplying the cloudy region concentration times the cloud fraction and the clear air concentration times the fraction of clear air in the grid box.

Because the rate of S(IV) ($= SO_2 \cdot H_2O + HSO_3^- + SO_3^{2-}$) oxidation by $O_3$ depends on the pH of the drops, the aqueous-phase reactions are evaluated using a 2-min time step with an Euler forward numerical approximation. At the end of each 2-min time step the hydrogen ion concentration is recalculated so that the influence of pH on S(IV) oxidation is captured.

## 4.12.3 Wet Deposition

The wet deposition rates are calculated separately for gases and aerosols. Cloud water and rain mixing ratios from both the resolved clouds and the subgrid-scale clouds are determined for the cloudy volume in each grid column. Trace gases are scavenged only by the liquid hydrometeors, whereas aerosols can also be scavenged by snow.

The fraction of a trace gas that is in the liquid water is determined through each species' Henry's law coefficient, which is temperature- and/or pH-dependent. At any particular level in the model the flux of the dissolved trace gas in the precipitation entering the grid cell from above is found. The trace gas is reequilibrated with the current model level's properties. Then the flux of the dissolved trace gas exiting the model level is determined. The rate of wet deposition is found from the flux divergence, maintaining mass conservation.

The wet deposition of aerosols is performed in a similar flux method. Any layer in the model can undergo both below-cloud and in-cloud scavenging.

The *below-cloud scavenging* follows Dana and Hales [1976] and Balkanski et al. [1993]. It is assumed that both rain and snow, which has graupel-like characteristics (and therefore characteristics similar to rain), scavenge the aerosol below cloud. Removal is assumed to take place by a first-order loss process. That is,

$$L_{W,bc} = 0.1Pq$$

where $L_{W,bc}$ is the loss rate by below-cloud scavenging, 0.1 is the collection efficiency, $P$ is the precipitation flux expressed in mm $h^{-1}$, and $q$ is the species mass mixing ratio.

*In-cloud scavenging* is performed assuming that the some fraction (currently 30%) of the aerosol reside in the cloud water. That fraction is then removed in proportion to the fraction of cloud water that is converted to rain through coalescence and accretion processes. This fraction of the aerosol is removed through wet deposition.

Evaporation of rain is accounted for in the wet deposition rate calculation by releasing a proportionate mass of aerosol to the atmosphere (i.e., if 10% of the precipitation evaporates, then 10% of the sulfate aerosol is released back to the air). This last assumption could lead to an overestimate of sulfate mixing ratios in the air [Barth et al., 1992] because the number of drops that completely evaporate (and therefore the amount of sulfate aerosol released from the drop to the air) is not necessarily proportional to the mass of rain that evaporates.

### 4.12.4 Dry Deposition

In Barth et al. [2000] we used of dry deposition similar to that described by Benkovitz et al. [1994]. The deposition velocity of $SO_2$ is determined following the series resistance method outlined by Wesely [1989] where the deposition velocity is inversely proportional to the sum of the aerodynamic resistance, the resistance to transport across the atmospheric sublayer in contact with surface elements, and the surface resistance. The aerodynamic and sublayer resistances are determined using boundary layer meteorological parameters. The surface resistance is found through a parameterization outlined by Wesely [1989].

We are in the process of integrating this calculation with the surface process characterization produced by the Common Land Model (CLM). When complete, the internal consistency of the parameterization will be much improved.

In the meantime, we have chosen to prescribe our deposition velocities following Feichter et al. [1996]. For $SO_2$ we use 0.6 cm/s for land, 0.8 cm/s over ocean, and 0.1 cm/s over ice and snow. Deposition velocities for $SO_4^{2-}$ are set to 0.2cm/s everywhere.

## 4.13 Prognostic Greenhouse Gases

The principal greenhouse gases whose longwave radiative effects are included in CAM 3.0 are $H_2O$, $CO_2$, $O_3$, $CH_4$, $N_2O$, CFC11, and CFC12. The prediction of water vapor is described elsewhere in this chapter, and $CO_2$ is assumed to be well mixed. Monthly $O_3$ fields are specified as input, as described in chapter 7. The radiative effects of the other four greenhouse gases ($CH_4$, $N_2O$, CFC11, and CFC12) may be included in CAM 3.0 through specified concentration distributions [Kiehl et al., 1998] or prognostic concentrations [Boville et al., 2001].

The specified distributions are globally uniform in the troposphere. Above a latitudinally and seasonally specified tropopause height, the distributions are zonally symmetric and decrease upward, with a separate latitude-dependent scale height for each gas.

Prognostic distributions are computed following Boville et al. [2001]. Transport equations for the four gases are included, and losses have been parameterized by specified zonally symmetric loss frequencies: $\partial q/\partial t = -\alpha(y,z,t)q$. Monthly averaged loss frequencies, $\alpha$, are obtained from the two-dimensional model of Garcia and Solomon [1994].

We have chosen to specify globally uniform surface concentrations of the four gases, rather than their surface fluxes. The surface sources are imperfectly known, particularly for $CH_4$ and $N_2O$ in preindustrial times. Even given constant sources and reasonable initial conditions, obtaining equilibrium values for the loading of these gases in the atmosphere can take many years. CAM 3.0 was designed for tropospheric simulation with relatively coarse vertical resolution in the upper troposphere and lower stratosphere. It is likely that the rate of transport into the stratosphere will be misrepresented, leading to erroneous loading and radiative forcing if surface fluxes are specified. Specifying surface concentrations has the advantage that we do not need to worry much about the atmospheric lifetime. However, we cannot examine observed features such as the interhemispheric gradient of the trace gases. For climate change experiments, the specified surface concentrations are varied but the stratospheric loss frequencies are not.

Oxidation of $CH_4$ is an important source of water vapor in the stratosphere, contributing about half of the ambient mixing ratio over much of the stratosphere. Although $CH_4$ is not generally oxidized directly into water vapor, this is not a bad approximation, as shown by Le Texier et al. [1988]. In CAM 3.0, it is assumed that the water vapor (volume mixing ratio) source is twice the $CH_4$ sink. This approach was also taken by Mote et al. [1993] for middle atmosphere studies with an earlier version of the CCM. This part of the water budget is of some importance in climate change studies, because the atmospheric $CH_4$ concentrations have increased rapidly with time and this increase is projected to continue into the next century (e.g., Alcamo et al. [1995]) The representation of stratospheric water vapor in CAM 3.0 is necessarily crude, since there are few levels above the tropopause. However, the model is capable of capturing the main features of the $CH_4$ and water distributions.

# Chapter 5

# Slab Ocean Model

The Slab Ocean Model (SOM) configuration enables a simple but tightly coupled ocean modeling component combined with a thermodynamic sea ice component based on the CCSM3 sea ice model. This configuration of the atmospheric model allows for a fully-interactive treatment of surface exchange processes in the CAM 3.0. The ocean prognostic variable is the mixed layer temperature $T_o$, while the thermodynamic sea ice model treats snow depth, surface temperature, ice thickness, ice fractional coverage, and internal energy at four layers for a single thickness category. The ocean mixed layer contains an internal heat source $Q$ (also called a $Q$ flux), whose values are generally specified by a CAM control run, representing seasonal deep water exchange and horizontal ocean heat transport. For example, using prescribed sea surface temperatures and sea ice distributions, the net surface energy flux over the ocean surface can be evaluated to yield the heat source $Q$. Additional exchange of heat occurs between the ocean mixed layer and the sea ice model during ice formation and ice melt. To ensure the CAM 3.0 SOM sea ice simulation compares well to the observed ice distribution, and to moderate sea ice changes in climate change experiments, the $Q$ flux term is adjusted under the ice in a globally conserving manner.

## 5.1 Open Ocean Component

The general formulation for the open ocean slab model is taken from Hansen et al. [1984], although we have modified it to allow for a fractional sea ice coverage. The governing equation for ocean mixed layer temperature $T_o$ is:

$$\rho_o C_o h_o \frac{\partial T_o}{\partial t} = (1 - A)F + Q + AF_{oi} + (1 - A)F_{frz} \tag{5.1}$$

where $T_o$ is the ocean mixed layer temperature, $\rho_o$ is the density of ocean water, $C_o$ is the heat capacity of ocean water, $h_o$ is the annual mean ocean mixed layer depth (m), $A$ is the fraction of the ocean covered by sea ice, $F$ is the net atmosphere to ocean heat flux (Wm$^{-2}$), $Q$ is the internal ocean mixed layer heat flux (Wm$^{-2}$), simulating deep water heat exchange and ocean transport, $F_{oi}$ is the heat exchanged with the sea ice (Wm$^{-2}$) (including solar radiation transmitted through the ice, see Eq. 6.39) and $F_{frz}$ is the heat gained when sea ice grows over open water (Wm$^{-2}$). $\rho_o$ and $C_o$ are constants (see Table 5.1 for values of the constants), and the nomenclature is such that all right-hand-side fluxes are positive down.

Table 5.1: Constants for the Slab Ocean Model

| **Temperatures** |
|---|
| $T_f = -1.8$ °C |
| **Ocean** |
| $\rho_o = 1.026 \times 10^3$ kg m$^{-3}$<br>$C_o = 3.93 \times 10^3$ J kg$^{-1}$ K$^{-1}$ |
| **Ice** |
| $L_i = 3.014 \times 10^8$ J m$^{-3}$ |

The geographic structure of ocean mixed layer depth $h_o$ is specified from Levitus [1982]. Monthly mean mixed layer depths are determined using this dataset's standard measure of salinity $\sigma_t = (\rho_S - 1) \cdot 10^3$ ($\rho_S$ is the density of sea water for a specified salinity, temperature, and atmospheric pressure) where the equality $\sigma_t(h_o) - \sigma_t(\text{surface}) = .125$ is satisfied on a $1° \times 1°$ grid. These data are then averaged to the standard CAM 3.0 grid (all data falling within a CAM 3.0 grid box are equally weighted), horizontally smoothed 10 times using a 1-2-1 smoother, and capped at 200m (to prevent excessively long adjustment times in coupled atmosphere ocean experiments). The resulting mixed layer depths in the tropics are generally shallow (10m-30m) while at high latitudes in both hemispheres there are large seasonal variations (from 10m up to the 200m maximum). The annually-averaged geographically-varying mixed layer depth, which is used for purposes related to energy conservation, is produced by averaging the monthly mean values.

The geographic distribution of the internal heat source $Q$ is generally specified on a monthly basis using a control CAM 3.0 integration as described below. During a SOM numerical integration $Q$ is linearly interpolated between monthly values (taken as mid month) to the appropriate model time step. The energy fluxes associated with ice formation and ice melt ($F_{frz}$ and $F_{mlt}$ respectively) are explicitly predicted.

The net atmosphere-to-ocean heat flux in the absence of sea ice, $F$, is defined as:

$$F = FS - FL - SH - LH \tag{5.2}$$

where $FS$ is the net solar flux absorbed by the ocean mixed layer, $FL$ is the net longwave energy flux of the ocean surface to the atmosphere, $SH$ is the sensible heat flux from the ocean to the atmosphere, and $LH$ is the latent heat flux from the ocean to the atmosphere. The surface temperature used in evaluating these fluxes is $T_o$.

The evolution of the mixed-layer temperature field, $T_o$, is evaluated using an explicit forward time step. At iteration $n$ the required information to advance the forecast include $T_o^n, h_o, F^n, Q^n$, and $A^n$, where $h_o$ is time invariant and $Q^n$ is linearly interpolated in time between prescribed mid-monthly values. It is assumed that the exchange between the ocean mixed layer and the atmosphere occurs faster than deep adjustments. Hence, the first adjustment to $T_o$ is evaluated as:

$$T_o^{(n+1)'} = T_o^n + \frac{(1 - A^n)F^n}{\rho_o C_o h_o}\Delta t \tag{5.3}$$

where $\Delta t$ is the model time step. We note that $A^n$ is computed from the fraction of the total

CAM 3.0 grid box that is not covered by land, since only ocean and sea ice covered portion of the grid cell are considered for the SOM configuration:

$$A^n = \frac{icefrac^n}{(1 - landfrac)} \tag{5.4}$$

where $icefrac$ is the fraction of ice in the CAM 3.0 grid cell and $landfrac$ is the fraction of land in the CAM 3.0 grid box.

The $Q^n$ flux is then adjusted since it is possible (using monthly specified values of $Q$) to introduce a non-physical cooling of the mixed layer when its temperature is at the freezing point. Therefore, if $Q^n > 0$ and $T_o^{(n+1)'} < 0°C$, then

$$Q^{n'} = Q^n f_T \tag{5.5}$$

where $f_T = (T_f - T_o^{(n+1)'})/T_f$, and $T_f$ is the ocean freezing temperature of -1.8°C (where $T_o$ is expressed in units of °C). This adjustment smoothly reduces the loss of heat from the mixed layer (if any) to zero as its temperature approaches the specified freezing point of sea water.

To ensure that the predicted SOM sea ice distribution compares favorably with the control simulation, and is bounded against unchecked growth or loss for atmospheric conditions significantly different from present day, an additional adjustment to $Q$ under sea ice is applied:

$$Q^{n''} = Q^{n'} + [A^n f(h_i) q_{hem}] \tag{5.6}$$

where

$$\begin{aligned} f(h_i) &= h_i/(1 + h_i) \;\; q_{hem} < 0 \\ f(h_i) &= 1/(1 + h_i) \;\; q_{hem} > 0 \end{aligned} \tag{5.7}$$

$h_i$ is the local ice thickness, and $q_{hem}$ is a tuning constant which may have different values for the Northern and Southern hemispheres. The coefficient $A^n$ ensures this adjustment only occurs under sea ice covered ocean. The function $f(h_i)$ is empirical, and is designed to ensure that the hemispheric adjustments asymptote properly for very small and very large values of ice thickness. For present-day climate simulations the values of $q_{hem}$ which yield good control sea ice distributions are $+15W/m^2$ and -10$W/m^2$ for the Northern and Southern hemispheres respectively.

The adjusted $Q^n$ ($Q^{n''}$) is then used to update all ocean points due to deep ocean heat exchange and transport as:

$$T_o^{(n+1)''} = T_o^{(n+1)'} - \frac{Q^{n''} + A^n F_{oi}^n}{(\rho_o C_o h_o)} \Delta t \tag{5.8}$$

where $F_{oi}^n$ is the energy flux associated with any ice melt and shortwave radiation transmitted through the sea ice from the previous time step.

The quantity $F_{frz}^n$ is nonzero only if the temperature of the slab ocean falls below the freezing point:

$$F_{frz}^{n+1} = (\rho_o C_o h_o) max(T_f - T_o^{(n+1)''}, 0)/\Delta t \tag{5.9}$$

If $F_{frz}^{n+1}$ is nonzero, new ice forms over the ice-free portion of the grid cell and $T_o^{n+1}$ is returned to the freezing temperature:

$$T_o^{(n+1)''} = max(T_o^{(n+1)''}, T_f) \tag{5.10}$$

A renormalization is necessary to ensure energy is conserved when $Q$ is adjusted as described above. We distinguish warm ocean as those points for which $T_o > 0°$C. An adjustment for warm ocean points is computed after all modifications to $Q$ are completed. Let $Q_o$ be the original unadjusted $Q$, and let $< Q_o >$ be the global (area weighted) mean. The final (total) $Q$ applied to warm ocean points is:

$$Q''' = Q'' + [(< Q_o > - < Q'' >)(A_o/A_w)] \tag{5.11}$$

where $A_o$ is the global area over all ocean, and $A_w$ the corresponding area over warm ocean. Taking the global mean of the bracketed quantity (which is zero over non-warm oceans) results in a multiplicative factor $(A_w/A_o)$. Thus, $< Q''' >=< Q_o >$, satisfying global energy conservation of $Q$ for every time step. In practice, the bracket term adjustment is applied to warm ocean points after the Q redistribution is completed.

## 5.2 Thermodynamic Sea Ice Model

After the slab ocean component computes the atmosphere-ocean heat fluxes and updates $T_o$ and $F_{frz}$, the thermodynamic sea ice model takes the latter two variables as input and computes the atmosphere-ice and ocean-ice heat fluxes and advances the state of the sea ice, including snow depth, surface temperature, ice thickness, ice fractional coverage, and internal energy profile in the ice. The physics of the sea ice component model in CAM 3.0 are discussed in detail in the next chapter.

## 5.3 Evaluation of the Ocean $Q$ Flux

The ocean $Q$ flux is generally evaluated using a CAM 3.0 control simulation driven by prescribed sea surface temperature and sea ice distributions. Let

$$F_{net} = FS - FL - LH - SH \tag{5.12}$$

over ocean (regardless of whether the ocean surface is open or ice covered), for each of 12 ensemble mean months (n=1,...,12). The Q flux distribution for each month n is then evaluated: (note that here we use the CAM 3.0 sign convention on the Q flux).

$$Q = Q_{ocean} - Q_{ice} - F_{net} \tag{5.13}$$

where:

$$Q_{ocean} = (\rho_o C_o h_o / \texttt{daysmonth}(m))\{(1 - A(m+1))T_o(m+1) - (1 - A(m-1))T_o(m-1)\} \tag{5.14}$$

$$Q_{ice} = L_i \{A(m+1)h_i(m+1) - A(m-1)h_i(m-1)\}/\texttt{daysmonth}(m) \tag{5.15}$$

where `daysmonth` is the number of days in each month, $L_i$ is the latent heat of fusion for ice, and $h_i$ is the regionally specified ice thickness. We then define an annual average using the monthly mean data:

$$\overline{Q} = \sum_{m=1,12} \texttt{daysmonth}(m) Q(m)/365 \tag{5.16}$$

By definition

$$\overline{Q_{ocean}} = 0 \tag{5.17}$$

$$\overline{Q_{ice}} = 0 \tag{5.18}$$

so that

$$\overline{Q} = -\overline{F_{net}} \tag{5.19}$$

Since $F_{net}$ is the monthly mean flux into the ocean directly from the control, $Q$ must be constrained to ensure that the actual $Q$ applied in the SOM configuration has the same annual mean as $-\overline{F_{net}}$. Otherwise, the application of the $Q$ flux would introduce a source or sink of heat with respect to the control.

The actual $Q$ applied in the SOM configuration is based on linear interpolation between monthly means, taken as midpoints. Since the months have different lengths, in general the annual mean of the $Q$ flux applied to the SOM *will not* equal $-\overline{F_{net}}$. Thus, we must define another annual mean, based on the time interpolated $Q$, to ensure that the SOM applied Q has the identical annual mean as the fluxes $F_{net}$ from the control run.

# Chapter 6

# Sea Ice Thermodynamics

This chapter describes the physics of the sea ice thermodynamics beginning with basic assumptions and followed by a description of the fundamental equations, various parameterization, and numerical approximations. The philosophy behind the design of the sea ice formulation of CAM 3.0 is to use the same physics, where possible, as in the sea ice model within CCSM, which is known as CSIM for community sea ice model. The sea ice formulation in CAM 3.0 uses parameterizations from CSIM for predicting snow depth, brine pockets, internal shortwave radiative transfer, surface albedo, ice-atmosphere drag, and surface exchange fluxes. The full CSIM is described in detail in an NCAR technical note by Briegleb et al. [2002]. The pieces of CSIM that are also used in CAM 3.0 (without the flux coupler) are described here.

The features of the sea ice model that are used in CAM 3.0 depend on the boundary conditions over ice-free ocean. If sea surface temperatures (SSTs) are prescribed, then sea ice concentration and thickness are also prescribed. In this case, the primary function of the sea ice model in CAM 3.0 is to compute surface fluxes. However, if the slab ocean model is employed, sea ice thickness and concentration are computed within CAM 3.0. These two types of surface boundary conditions within CAM 3.0 will be referred to as uncoupled and coupled in this chapter.

## 6.1 Basic assumptions

When CAM 3.0 is run uncoupled (i.e., without an ocean model), sea ice thickness and concentration must be specified. Sea ice concentrations are known with reasonable accuracy owing to satellite microwave instruments and ship observations. However, no adequate measurements of thickness exist to produce a comprehensive dataset. Therefore, when ice thickness must be specified, the thickness of the ice covered portion of the grid cell is fixed in space and time at 2 m in the Northern Hemisphere and 0.5 m in the Southern Hemisphere. Ice concentrations are interpolated from monthly input data, which may vary in space and time.[1]

For either coupled or uncoupled integrations, snow depth on sea ice is prognostic as snow accumulates when precipitation falls as snow, and it melts when allowed by the surface energy balance. For uncoupled simulations only, the maximum snow depth is fixed at 0.5 m. Rain has no effect on sea ice or snow on sea ice in the model.

[1] Mid-month concentrations are input and then interpolated to daily values. The input data are constructed to correctly recover the observed monthly means value using the method of Taylor et al. [2001]

## 6.2 Fundamental Equations

The method for computing the surface turbulent heat and radiative exchange, evaporative flux, and surface drag is integrally coupled with the formulation of heat transfer through the sea ice and snow. The equation governing vertical heat transfer in the ice and snow, which allows for internal absorption of penetrating solar radiation, is

$$\rho c \frac{\partial T}{\partial t} = \left( \frac{\partial}{\partial z} k \frac{\partial T}{\partial z} + Q_{SW} \right) \tag{6.1}$$

where $\rho$ is the density, $c$ is the heat capacity, $T$ is the temperature, $k$ is the thermal conductivity, $Q_{SW}$ is shortwave radiative heating, $z$ is the vertical coordinate, and $t$ is time. Note that $\rho$, $c$, and $k$ differ for snow and sea ice, and also the latter two depend on temperature and salinity within the sea ice to account for the behavior of brine pockets.

The boundary condition for the heat equation at the surface is

$$F_{TOP}(T_s) = F_{SW} - I_{SW} + F_{LW} + F_{SH} + F_{LH} + k\frac{dT}{dz} \tag{6.2}$$

where $T_s$ is the surface temperature, $F_{SW}$ is the absorbed shortwave flux, $I_{SW}$ is the shortwave flux that penetrates into the ice interior, $F_{LW}$ is the net longwave flux, $F_{SH}$ is the sensible heat flux, and $F_{LH}$ is the latent heat flux. All fluxes are taken as positive down. If $F_{TOP}(T_s = 0) \geq 0$, then the surface is assumed to be melting and a temperature boundary conditions (i.e., $T_s = 0$) is used for the upper boundary with Eq. 6.1. However if $F_{TOP}(T_s = 0) < 0$ in Eq. 6.2, then the surface is assumed to be freezing and a flux boundary condition is used for Eq. 6.1, and Eqs. 6.1 and 6.2 are solved simultaneously with $F_{TOP}(T_s) = 0$ in the latter.

Snow melt and accumulation is computed from

$$\rho_s \frac{dh_s}{dt} = \frac{-F_{TOP}}{L_i} + \frac{F_{LH}}{L_i + L_v} + F_{SNW} \tag{6.3}$$

where $h_s$ is the snow depth, $\rho_s$ is the snow density, $L_i$ and $L_v$ are the latent heats of fusion and vaporization, and $F_{SNW}$ is the snowfall rate (see Table 6.1 for values of constants).

When CAM 3.0 is coupled to the mixed layer ocean and the sea ice is snow-free, sea ice surface melt is computed from

$$\frac{dh_i}{dt} = \frac{F_{TOP}}{q} + \frac{F_{LH}}{-q + \rho_i L_v} \tag{6.4}$$

where $h_i$ is the ice thickness, $\rho_i$ is the ice density, and $q$ is the energy of melting of sea ice ($q < 0$ by definition, see section 6.6 on brine pockets). Basal growth or melt is computed from

$$\frac{dh_i}{dt} = \frac{F_{BOT}}{q} - \frac{k}{q}\frac{dT}{dz} \tag{6.5}$$

where $F_{BOT}$ is the heat flux from the ocean to the ice (see section 6.5). Finally an equation is needed to describe the evolution of the ice concentration $A$:

$$\frac{dA}{dt} = \mathcal{A} \tag{6.6}$$

where $\mathcal{A}$ accounts for new ice formation over open water and lateral melt (see section 6.7)

Parameterizations of albedo, surface fluxes, brine pockets, and shortwave radiative transfer within the sea ice are given next. Finally, the numerical solution to Eq. 6.1 is described. Numerical methods for Eqs. 6.2 –6.6 are straight-forward and hence are not described here.

Table 6.1: List of Physical Constants

| Symbol | Description | Value |
|---|---|---|
| $\rho_s$ | Density of snow | 330 kg m$^{-3}$ |
| $\rho_i$ | Density of ice | 917 kg m$^{-3}$ |
| $\rho_o$ | Density of surface ocean water | 1026 kg m$^{-3}$ |
| $C_p$ | Specific heat of atmosphere dry | 1005 J kg$^{-1}$ K$^{-1}$ |
| $C_{pwv}$ | Specific heat of atmosphere water | 1810 J kg$^{-1}$ K$^{-1}$ |
| $C_o$ | Specific heat of ocean water | 3996 J kg$^{-1}$ K$^{-1}$ |
| $c_s$ | Specific heat of snow | 0 J kg$^{-1}$ K$^{-1}$ |
| $c_o$ | Specific heat of fresh ice | 2054 J kg$^{-1}$ K$^{-1}$ |
| $z_i$ | Aerodynamic roughness of ice | 5.0x10$^{-4}$ m |
| $z_{ref}$ | Reference height for bulk fluxes | 10 m |
| $q_1(ice)$ | saturation specific humidity constant | 11637800 |
| $q_2(ice)$ | saturation specific humidity constant | 5897.8 |
| $k_s$ | Thermal conductivity of snow | 0.31 W m$^{-1}$ K$^{-1}$ |
| $k_o$ | Thermal conductivity of fresh ice | 2.0340 W m$^{-1}$ K$^{-1}$ |
| $\beta$ | Thermal conductivity ice constant | 0.1172 W m$^{-1}$ ppt$^{-1}$ |
| $L_i$ | Latent heat of fusion of ice | 3.340x10$^{5}$ J kg$^{-1}$ |
| $L_v$ | Latent heat of vaporization | 2.501x10$^{6}$ J kg$^{-1}$ |
| $T_{melt}$ | Melting temperature of top surface | 0 °C |
| $\mu$ | Ocean freezing temperature constant | 0.054 °C ppt$^{-1}$ |
| $\sigma_{sb}$ | Stefan-Boltzmann constant | 5.67x10$^{-8}$ W m$^{-2}$ K$^{-4}$ |
| $\varepsilon$ | Ice emissivity | 0.95 |
| $\kappa_{vs}$ | Ice SW visible extinction coefficient | 1.4 m$^{-1}$ |
| $\kappa_{ni}$ | Ice SW near-ir extinction coefficient | 17.6 m$^{-1}$ |

NOTE: CSIM in CAM 3.0 uses the shared constants defined in Appendix A.

## 6.3 Snow and Ice Albedo

The albedo depends upon spectral band, snow thickness, ice thickness and surface temperature. Snow and ice spectral albedos (visible = $vs$, wavelengths $< 0.7\mu m$ and near-infrared = $ni$, wavelengths $> 0.7\mu m$) are distinguished, as both snow and ice spectral reflectivities are significantly higher in the $vs$ band than in the $ni$ band. This two-band separation represents the basic spectral dependence. The near-infrared spectral structure, with generally decreasing reflectivity with increasing wavelength [Ebert and Curry, 1993] is ignored. The zenith angle dependence of snow and ice is ignored [Ebert and Curry, 1993; Grenfell et al., 1994], and hence there is no distinction between downwelling direct and diffuse shortwave radiation. The approximations made for the albedo are further described by Briegleb et al. [2002].

Here we ignore the dependence of snow albedo on age, but retain the melting/non-melting distinction and thickness dependence. Dry snow spectral albedos are:

$$\begin{aligned} \alpha^s_{vsdf}(dry) =& 0.96 \\ \alpha^s_{nidf}(dry) =& 0.68 \end{aligned}. \tag{6.7}$$

To represent melting snow albedos, the surface temperature is used. Springtime warming produces a rapid transition from sub-zero to melting temperatures, while late fall values transition more slowly to sub-zero conditions. This is approximated by a temperature dependence out to $-1°$C. If $T_s \geq -1°$C, then

$$\begin{aligned} \Delta T_s =& T_s + 1.0 \\ \alpha^s_{vsdf}(melt) =& \alpha^s_{vsdf}(dry) - 0.10\Delta T_s \\ \alpha^s_{nidf}(melt) =& \alpha^s_{nidf}(dry) - 0.15\Delta T_s \end{aligned}. \tag{6.8}$$

For bare non-melting sea ice thicker than 0.5 m, as is the case for all sea ice prescribed in CAM 3.0, the albedos are

$$\begin{aligned} \alpha_{vsdf}(dry) =& 0.73 \\ \alpha_{nidf}(dry) =& 0.33 \end{aligned}. \tag{6.9}$$

For bare melting sea ice, melt ponds can significantly lower the area averaged albedo. This effect is crudely approximated by the following temperature dependence:

$$\begin{aligned} \alpha_{vsdf}(melt) =& \alpha_{vsdf}(dry) - 0.075\Delta T_s \\ \alpha_{nidf}(melt) =& \alpha_{nidf}(dry) - 0.075\Delta T_s \end{aligned} \tag{6.10}$$

for $T_s \geq -1°$C.

The horizontal fraction of surface covered with snow is assumed to be

$$f_s = \frac{h_s}{h_s + 0.02}. \tag{6.11}$$

Finally, combining ice and snow albedos by averaging over the horizontal coverage results in

$$\begin{aligned} \alpha_{vsdf} =& \alpha_{vsdf}(1 - f_s) + f_s\alpha^s_{vsdf} \\ \alpha_{nidf} =& \alpha_{nidf}(1 - f_s) + f_s\alpha^s_{nidf} \end{aligned}. \tag{6.12}$$

The same equations applies for direct albedos.

## 6.4 Ice to Atmosphere Flux Exchange

Atmospheric states and downwelling fluxes, along with surface states and properties, are used to compute atmosphere-ice shortwave and longwave fluxes, stress, sensible and latent heat fluxes. Surface states are temperature $T_s$ and albedos $\alpha_{vsdr}$, $\alpha_{vsdf}$, $\alpha_{nidr}$, $\alpha_{nidf}$ (see section 6.3), while surface properties are longwave emissivity $\varepsilon$ and aerodynamic roughness $z_i$ (note that these properties in general vary with ice thickness, but are here assumed constant). Additionally, certain flux temperature derivatives required for the ice temperature calculation are computed, as well as a reference diagnostic surface air temperature.

The following formulas are for the absorbed shortwave fluxes and upwelling longwave flux:

$$
\begin{aligned}
F_{SWvs} =& F_{SWvsdr}(1-\alpha_{vsdr}) + F_{SWvsdf}(1-\alpha_{vsdf}) \\
F_{SWni} =& F_{SWnidr}(1-\alpha_{nidr}) + F_{SWnidf}(1-\alpha_{nidf}) \\
F_{SW} =& F_{SWvsn} + F_{SWnin} \\
F_{LWUP} =& -\varepsilon\sigma_{sb}T_s^4 + (1-\varepsilon)F_{LWDN}
\end{aligned}
\tag{6.13}
$$

for $T_s$ in Kelvin and $\sigma_{sb}$ denotes the Stefan-Boltzmann constant. The downwelling shortwave flux and albedos distinguish between visible ($vs, \lambda < 0.7\mu m$), near-infrared ($ni, \lambda > 0.7\mu m$), direct ($dr$) and diffuse ($df$) radiation for each category. Note that the upwelling longwave flux has a reflected component from the downwelling longwave whenever $\varepsilon < 1$.

For stress components $\tau_{ax}$ and $\tau_{ay}$ and sensible and latent heat fluxes the following bulk formulas are used [Bryan et al., 1996]:

$$
\begin{aligned}
\tau_{ax} =& \rho_a r_m u^* u_a \\
\tau_{ay} =& \rho_a r_m u^* v_a \\
F_{SH} =& \rho_a c_a r_h u^* \left(\theta_a - T_s\right) \\
F_{LH} =& \rho_a (L_i + L_v) r_e u^* \left(q_a - \overline{q}^*\right).
\end{aligned}
\tag{6.14}
$$

The quantities from the lowest layer of the atmosphere include wind components $u_a$ and $v_a$, the density of air $\rho_a$, the potential temperature $\theta_a$, and the specific humidity $q_a$. The surface saturation specific humidity is

$$
\overline{q}^* = (q_1/\rho_a)e^{-q_2/T_s} \tag{6.15}
$$

where the values of $q_1$ and $q_2$ were kindly supplied by Xubin Zeng of the University of Arizona. The specific heat of the air in the lowest layer is evaluated from

$$
\begin{aligned}
c_a =& C_p(1 + C_{pvir}\overline{q}^*) \\
C_{pvir} =& (C_{pwv}/C_p) - 1
\end{aligned}
\tag{6.16}
$$

where specific heat of dry air and water vapor are $C_p$ and $C_{pwv}$, respectively. Values for the exchange coefficients for momentum, sensible and latent heat $r_{m,h,e}$ and the friction velocity $u^*$ require further consideration.

The bulk formulas are based on Monin-Obukhov similarity theory. Among boundary layer scalings, this is the most well tested [Large, 1998]. It is based on the assumption that in the surface layer (typically the lowest tenth of the atmospheric boundary layer), but away from the surface roughness elements, only the distance from the boundary and the surface kinematic fluxes are important in the turbulent exchange. The fundamental turbulence scales that are formed from these quantities are the friction velocity $u^*$, the temperature and moisture fluctuations $\theta^*$ and $q^*$ respectively, and the Monin-Obukhov length scale $L$:

$$
\begin{aligned}
u^* =& r_m V_{mag} \\
\theta^* =& r_h(\theta_a - T_s) \\
q^* =& r_e(q_a - \overline{q}^*)) \\
L =& u^{*3}/(\kappa F)
\end{aligned}
\tag{6.17}
$$

with

$$V_{mag} = \max(1.0, \sqrt{u_a^2 + v_a^2}), \tag{6.18}$$

to prevent zero or small fluxes under quiescent wind conditions, $\kappa$ is von Karman's constant (0.4), and $F$ is the buoyancy flux, defined as:

$$F = \frac{u^*}{g}\left[\frac{\theta^*}{\theta_v} + \frac{q^*}{z_v^{-1} + q_a}\right] \tag{6.19}$$

with g the gravitational acceleration and the virtual potential temperature $\theta_v = \theta_a(1 + z_v q_a)$ where $z_v = \rho_{wv}/\rho_a - 1$.

Similarity theory holds that the vertical gradients of mean horizontal wind, potential temperature and specific humidity are universal functions of stability parameter $\zeta = z/L$, where $z$ is height above the surface ($\zeta$ is positive for a stable surface layer and negative for an unstable surface layer). These universal similarity functions are determined from observations in the atmospheric boundary layer [Hogstrom, 1988] though no single form is widely accepted. Integrals of the vertical gradient relations result in the familiar logarithmic mean profiles, from which the exchange coefficients can be defined, where $\zeta = z_a/L$:

$$\begin{aligned}
r_m =& r_0\left\{1 + \frac{r_0}{\kappa}\left[\ln(z_a/z_{ref}) - \chi_m(\zeta)\right]\right\}^{-1} \\
r_h =& r_0\left\{1 + \frac{r_0}{\kappa}\left[\ln(z_a/z_{ref}) - \chi_h(\zeta)\right]\right\}^{-1} \\
r_e =& r_h
\end{aligned} \tag{6.20}$$

with the neutral coefficient

$$r_0 = \frac{\kappa}{ln(z_{ref}/z_i)}. \tag{6.21}$$

The flux profile functions (integrals of the similarity functions mentioned above) for momentum $m$ and heat/moisture $h$ are:

$$\chi_m(\zeta) = \chi_h(\zeta) = -5\zeta \tag{6.22}$$

for stable conditions ($\zeta > 0$). For unstable conditions ($\zeta < 0$):

$$\chi_m(\zeta) = \ln\{(1 + X(2 + X))(1 + X^2)/8\} - 2\tan^{-1}(X) + 0.5\pi \tag{6.23}$$

$$\chi_h(\zeta) = 2\ln\{(1 + X^2)/2\} \tag{6.24}$$

with

$$X = \left\{\max((1 - 16\zeta)^{1/2}), 1\right\}^{1/2}. \tag{6.25}$$

The stability parameter $\zeta$ is a function of the turbulent scales and thus the fluxes, so an iterative solution is necessary. The coefficients are initialized with their neutral value $r_0$, from which the turbulent scales, stability, and then flux profile functions can be evaluated. This order is repeated for five iterations to ensure convergence to an acceptable solution.

The surface temperature derivatives required by the ice temperature calculation are evaluated as:

$$\frac{dF_{LWUP}}{dT_s} = -4\varepsilon\sigma_{sb}T_s^3 \tag{6.26}$$
$$\frac{dF_{SH}}{dT_s} = -\rho_a c_a r_h u^* \tag{6.27}$$
$$\frac{dF_{LH}}{dT_s} = -\rho_a L_s r_e u^* \frac{d\overline{q}^*(T_s)}{dT_s} \tag{6.28}$$

where the small temperature dependencies of $c_a$, the exchange coefficients $r_h$ and $r_e$ and velocity scale $u^*$ are ignored.

For diagnostic purposes, an air temperature ($T_{REF}$) at the reference height of $z_{2m} = 2m$ is computed, making use of the stability and momentum/sensible heat exchange coefficients. Defining $b_m = \kappa/r_m$, and $b_h = \kappa/r_h$, we have:

$$\begin{aligned} \ln_m &= \ln\{(1 + z_{2m}/z_a)(e^{b_m} - 1)\} \\ \ln_h &= \ln\{(1 + z_{2m}/z_a)(e^{b_m - b_h} - 1)\}. \end{aligned} \tag{6.29}$$

For stable conditions ($\zeta > 0$)

$$f_{int} = (\ln_m - (z_{2m}/z_a)(b_m - b_h))/b_h \tag{6.30}$$

and for unstable conditions ($\zeta < 0$)

$$f_{int} = (\ln_m - \ln_h)/b_h \tag{6.31}$$

where $f_{int}$ is bounded by 0 and 1. The resulting reference temperature is:

$$T_{ref} = T_s + (T_a - T_s)f_{int}. \tag{6.32}$$

## 6.5 Ice to Ocean Flux Exchange

This section is only relevant when CAM 3.0 is coupled to a slab ocean. When sea ice is present, only a fraction of the melting potential from heat stored in the ocean actually reaches the ice at the base and side. The melting potential is

$$F_{max} = -h_o\rho_o C_o(T_o - T_f) \tag{6.33}$$

where $h_o$, $\rho_o$, $C_o$, and $T_o$ are the ocean layer thickness, density, heat capacity, and temperature and $T_f$ is the freezing temperature of the layer (assumed to be -1.8$^o$C).

Usually only a fraction of $F_{max}$ is available to melt ice at the base and side, and these fractions are determined from boundary-layer theories at the ice-ocean interfaces. However, it is critical that the sum of the fractions never exceeds one, otherwise ice formation might become unstable. Hence we compute the upper-limit partitioning of $F_{max}$, even though these amounts are rarely reached. The partitioning assumes $F_{oi}$ is dominated by shortwave radiation and that shortwave radiation absorbed in the ocean surface layer above the mean ice thickness causes side melting and below it causes basal melting:

$$
\begin{aligned}
f_{bot} =& Re^{-h/\zeta_1} + (1-R)e^{-h/\zeta_2} \\
f_{sid} =& 1 - f_{bot}
\end{aligned}
\tag{6.34}
$$

where $R = 0.68$, $\zeta_1 = 1.2\ m^{-1}$, $\zeta_2 = 28\ m^{-1}$ [Paulson and Simpson] and $f_{bot}$ and $f_{sid}$ are the fractions of bottom and side melt flux available, respectively. Thus the maximum fluxes available for melt are $f_{bot}F_{oi}$ and $f_{sid}F_{oi}$. The actual amount used for bottom melting, $F_{BOT}$, is based on boundary layer theory of McPhee [1992]:

$$
F_{BOT} = max(-\rho_o C_o c_h u^*(T_o - T_f), f_{bot}F_{max})
\tag{6.35}
$$

where the empirical drag coefficient $c_h$=0.006 and the skin friction speed $u^* = 1$ cm/s [Steele, 1995].

The heat flux for lateral melt is the product of the vertically-summed, thickness-weighted energy of melting of snow and ice $E_{tot}$ with the interfacial melting rate $M_a$ and the total floe perimeter $p_f$ per unit floe area $A_f$. The interfacial melting rate is taken from the empirical expression of Maykut and Perovich [1987] based on Marginal Ice Zone Experiment observations: $M_a = m_1(T_o - T_f)^{m_2}$, where $m_1 = 1.6 \times 10^{-6}$m s$^{-1}$ deg$^{m_2}$ and $m_2 = 1.36$. The lead-ice perimeter depends on the ice floe distribution and geometry. For a mean floe diameter $d$ and number of floes $n_f$, $p_f = n_f \pi d$ and the floe area $A_f = \eta_{lm} d^2$ [Rothrock and Thorndike, 1984]. Thus the heat flux for lateral melt is $E_{tot}(p_f/A_f)M_a$, so that the actual amount used is:

$$
F_{SID} = max(\frac{E_{tot}\pi}{\eta_{lm} d} m_1(T_o - T_f)^{m_2}, f_{sid}F_{max})
\tag{6.36}
$$

where $\eta_{lm} = 0.66$ [Rothrock and Thorndike, 1984]. Based partially on tuning and partially on the results of floe distribution measurements, the mean floe diameter of $d$=300 m was chosen. The ice area, volume, snow volume, and ice energy are all reduced by side melt in time $\Delta t$ by the fraction $R_{side} = |\frac{F_{SID}\Delta t}{E_{tot}}|$.

The heat flux that is actually used by the ice model is then:

$$
F_{BOT} + F_{SID} \leq F_{max}.
\tag{6.37}
$$

The net flux exchanged between ocean and ice $F_{oi}$ also includes the shortwave flux transmitted to the ocean through sea ice

$$
F_{SWo} = I_{0vs}e^{-\kappa_{vs}h} + I_{0ni}e^{-\kappa_{ni}h}
\tag{6.38}
$$

(see Eq. 6.45). Hence

$$
F_{oi} = F_{SWo} + F_{BOT} + F_{SID}.
\tag{6.39}
$$

## 6.6 Brine Pockets and Internal Energy of Sea Ice

Shortwave radiative heating within the sea ice and conduction warms the sea ice and opens brine pockets, melting the ice internally and storing latent heat. This storage of latent heat is accounted for explicitly by using a heat capacity and thermal conductivity that depend on temperature and salinity following the work of Maykut and Untersteiner [1971] and Bitz and Lipscomb [1999]. The equation for the heat capacity for sea ice $c$ was first postulated by Untersteiner [1961] and then later derived from first principles by Ono [1967]:

$$c(T, S) = c_o + \frac{L_i \mu S}{T^2}, \tag{6.40}$$

where $c_o$ is the heat capacity for fresh ice, $S$ is the sea ice salinity, $T$ is the temperature, and $\mu$ is an empirical constant relating the freezing temperature of sea water linearly to its salinity ($T_f = -\mu S$).

Equation 6.40 can be multiplied by the sea ice density and integrated to give the amount of energy $Q$ required to raise the temperature of a unit volume of sea ice from $T$ to $T'$:

$$Q(S, T, T') = \rho_i c_o (T' - T) - \rho_i L_o \mu S \left( \frac{1}{T'} - \frac{1}{T} \right). \tag{6.41}$$

If we take $T'$ to be the melting temperature of ice with salinity $S$, then at $T'$ sea ice consists entirely of brine; that is, the brine pockets have grown to encompass the entire mass of ice. The amount of energy needed to melt a unit volume of sea ice of salinity $S$ at temperature $T$, resulting in meltwater at $T_f$, is equal to

$$q(S, T) = \rho_i c_o (-\mu S - T) + \rho_i L_o \left( 1 + \frac{\mu S}{T} \right). \tag{6.42}$$

$q$ is referred to as the *energy of melting* of sea ice, and it appears in Eqs. 6.4 and 6.5.

The thermal conductivity for sea ice $k$ is

$$k(S, T) = k_o + \frac{\beta S}{T} \tag{6.43}$$

where $k_o$ and $\beta$ are empirical constants from Untersteiner [1961].

The vertical salinity profile is prescribed based on the work of Maykut and Untersteiner [1971] to be

$$S(w) = 1.6 \left[ 1 - \cos\left( \pi w^{\frac{0.407}{0.573 + w}} \right) \right] \tag{6.44}$$

with the normalized coordinate $w = z/h$. This results in a profile that varies from 0 ppt at ice surface increasing to 3.2 ppt at ice base. Snow is assumed fresh.

Shortwave radiative heating within the sea ice $Q_{SW}$ is equal to the vertical gradient of the radiative transfer within the sea ice:

$$Q_{SW} = -\frac{d}{dz} \{ I_{0vs} e^{-\kappa_{vs} z} + I_{0ni} e^{-\kappa_{ni} z} \} \tag{6.45}$$

where $I_{0vs}$ and $I_{0ni}$, the visible and near infrared radiation fluxes that penetrate the surface, are reduced according to Beer's law with the sea ice spectral extinction coefficients $\kappa_{vs}$ and $\kappa_{ni}$, respectively. For simplicity no shortwave radiation is allowed to penetrate through snow and all of the near-infrared radiation and 30% of the visible radiation is assumed to be absorbed at the surface of sea ice (Gary Maykut, personal communication):

$$I_{0vs} = 0.70 F_{SWvsn}(1 - f_s) \tag{6.46}$$
$$I_{0ni} = 0.0 \tag{6.47}$$

where $f_s$ is the horizontal fraction of surface covered by snow (see Eq. 6.11).

## 6.7 Open-Water Growth and Ice Concentration Evolution

When coupled to a mixed layer ocean, the ice model must account for new ice growth over open water and other processes that alter the lateral sea ice coverage. New ice growth occurs whenever the surface layer in the ocean is at the freezing temperature and the fluxes would draw additional heat out of the ocean (see Eq. 5.1). In this case the additional heat comes from freezing sea water, as the ocean cannot supercool in this model. Hence

$$q_f \frac{\partial h_{new}}{\partial t} = F_{frz}\,(1 - A) \tag{6.48}$$

where $q_f$ is the energy of melting for new ice growth (assuming the salinity is 4psu and the new ice temperature is -1.8$^o$C), $h_{new}$ is the thickness of the new ice, and $F_{frz}$ is the additional heat lost by slab ocean once it reaching the freezing point (see section 5.1). When new ice grows over open water, it is recombined with the rest of the ice in the grid cell by first reshaping the new ice volume so its thickness is at least 15 cm - this recreates ice-free ocean if the thickness was below 15 cm. Then the new ice is added to the old ice in the grid cell and a new thickness and concentration are computed by conserving ice volume.

In motionless sea ice model, such as this one, open water is not created by deformation as in nature, and hence the ice concentration would tend to 0 or 100% unless open water production is parameterized somehow. A typical method is to assume the ice thickness on a subgrid-scale is linearly distributed between 0 and $2h$, so that when ice melts vertically, it also reduces the concentration:

$$\left(A - \frac{\partial A}{\partial t}\right)^2 = \frac{A^2}{h_i}\left(h - \frac{\partial h_i}{\partial t}\right) \tag{6.49}$$

The ice concentration is also reduced by a lateral heat flux from the ocean (see Eq. 6.36):

$$\frac{\partial A}{\partial t} = A \frac{F_{SID}}{E_{TOT}} \tag{6.50}$$

although it is typically only a small contribution to the concentration tendency.

It is not possible to combine Eqs. 6.48–6.50 to make a single analytic expression for $\mathcal{A}$ in Eq. 6.6. Instead the model using time splitting to solve the three equations independently.

## 6.8 Snow-Ice Conversion

Snow to ice conversion occurs if the snow layer overlying the sea ice becomes thick enough to depress the snow-ice interface below freeboard (the ocean surface). This process is only accounted for when CAM 3.0 is coupled to a mixed layer ocean, otherwise the snow depth is merely capped at 0.5 m. The interface height is:

$$z_{int} = h - (\rho_s h_s + \rho_i h)/\rho_o. \tag{6.51}$$

If $z_{int} < 0$, then an amount of snow equal to $-z_{int}\rho_i/\rho_s$ is removed from the snow layer and added to the ice. It is assumed that ocean water floods the depressed snow, and then converts it into ice of thickness $-z_{int}$. The energy of melting of the newly formed ice is: $q_{flood} = q_s\rho_i/\rho_s$. Note that such conversion is assumed to occur with no heat or salt exchange with the ocean.

## 6.9 Numerics

The heat content change within the sea ice over the time interval $t$ to $t'$ corresponding to temperatures $T$ and $T'$, respectively, allowing for temperature dependent heat capacity, thermal conduction (see section 6.6) and internal absorption of penetrating solar radiation, is given by:

$$\int_T^{T'} \rho_i c dT = \rho_i c_o (T' - T)\left(1 + \frac{L_i \mu S}{c_o T' T}\right) = \int_t^{t'} \left(\frac{\partial}{\partial z} k \frac{\partial T}{\partial z} + Q_{SW}\right) dt \tag{6.52}$$

The heat equation is discretized using a backwards-Euler, space-centered scheme. Using a staggered grid with $T_l$ representing the layer temperature and $k_l$ representing conductivity at the layer interfaces, for interior layers we have

$$\rho_i c_o (T_l^{m+1} - T_l^m)\left(1 + \frac{L_i \mu S_l}{c_o T_l^{m+1} T_l^m}\right) = \frac{\Delta t}{\Delta h^m}\left(k_{l+1}^m \frac{T_{l+1}^{m+1} - T_l^{m+1}}{\Delta h^m} - k_l^m \frac{T_l^{m+1} - T_{l-1}^{m+1}}{\Delta h^m} + I_l^m\right), \tag{6.53}$$

where $\Delta h^m = h^m/L$, the conductivity is

$$k_l^m = k\left(\frac{S_l + S_{l+1}}{2}, \frac{T_l^m + T_{l+1}^m}{2}\right), \tag{6.54}$$

and the absorbed solar radiation is

$$I_l^m = I_{0vs}(e^{-\kappa_{vs} l \Delta h^m} - e^{-\kappa_{vs}(l+1)\Delta h^m}) + I_{0ni}(e^{-\kappa_{ni} l \Delta h^m} - e^{-\kappa_{ni}(l+1)\Delta h^m}). \tag{6.55}$$

See Figure 6.1 for a diagram on the vertical level structure.

For a purely implicit backward scheme, $k$ should be evaluated at the $m+1$ time level. However, when $k$ is evaluated at time level $m$, experiments show that the solution is stable and converges to the same solution one gets when evaluating $k$ at $m+1$.

The discrete heat equation for the surface layers is modified slightly from Eq. 6.53 to maintain second-order accuracy for $\partial T/\partial z$. The equation for the bottom layer ($l = L$) is

$$\begin{aligned} &\rho_i c_o (T_L^{m+1} - T_L^m)\left(1 + \frac{L_i \mu S_L}{c_o T_L^{m+1} T_L^m}\right) = \\ &\frac{\Delta t}{\Delta h^m}\left(3k_{L+1}\frac{T_b - T_L^{m+1}}{\Delta h^m} - \frac{1}{3}k_{L+1}\frac{T_b - T_{L-1}^{m+1}}{\Delta h^m} - k_L^m \frac{T_L^{m+1} - T_{L-1}^{m+1}}{\Delta h^m} + I_L^m\right), \end{aligned} \tag{6.56}$$

where the $L+1$ interface in contact with the underlying ocean is assumed to be at temperature $T_b = -1.8$°C, and where the conductivity is simply $k_{L+1} = k(S_b, T_b)$. The equations for the top surface depend on the surface conditions, of which there are four possibilities, as outlined in Table 6.2.

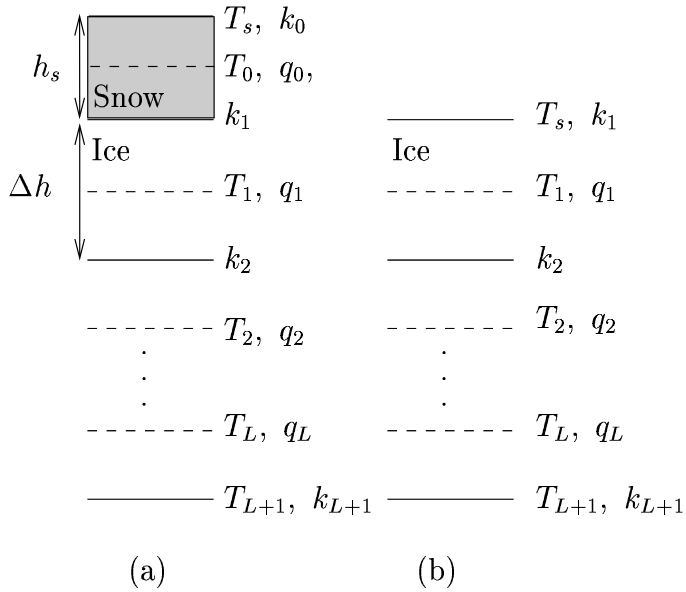


Figure 6.1: Vertical grid of the sea ice (a) when snow is present and (b) when the ice is snow free; $\Delta h$ is the thickness of an ice layer and $h_s$ is the thickness of the snow layer. The surface temperature in either case is $T_s$. Modified from Bitz and Lipscomb [1999].

Table 6.2: Top Surface Boundary Cases

| | snow accumulated | melting |
|---|---|---|
| case I | yes | no |
| case II | no | no |
| case III | yes | yes |
| case IV | no | yes |

### 6.9.1 Case I: Snow accumulated with no melting

The discrete heat equation for the uppermost layer (i.e, the snow layer) is

$$\rho_s c_s (T_0^{m+1} - T_0^m) = \frac{\Delta t}{h_s^m}\left[k_1^m \frac{T_1^{m+1} - T_0^{m+1}}{(\Delta h^m + h_s^m)/2} - \alpha k_s \frac{T_0^{m+1} - T_s^{m+1}}{h_s^m} - \beta k_s \frac{T_1^{m+1} - T_s^{m+1}}{h_s^m}\right]. \quad (6.57)$$

The heat equation solver is formulated for the general case where the heat capacity of snow $c_s$ may be specified, although it is taken to be 0. The parameters $\alpha$ and $\beta$ are defined to give second-order accurate spatial differencing for $\partial T/\partial z$ across the changing layer spacing at the snow/ice boundary;

$$\begin{aligned}\alpha &= \frac{h_s^m + \Delta h^m/2}{h_s^m/2}\ \frac{2}{h_s^m + \Delta h^m} h_s^m \\ \beta &= \frac{-h_s^m/2}{h_s^m + \Delta h^m/2}\ \frac{2}{h_s^m + \Delta h^m} h_s^m.\end{aligned} \quad (6.58)$$

The conductivity at the snow–ice interface is found by equating conductive fluxes above and below the interface;

$$k_1^m = \frac{2k_s k(S_1, T_1^m)}{h_s^m k(S_1, T_1^m) + \Delta h^m k_s} \frac{h_s^m + \Delta h^m}{2}. \tag{6.59}$$

Because $T_s$ is below melting, a flux boundary condition is used, and an additional equation is required in the coupled set:

$$F_o(T_s^{m+1}) + \alpha k_s \frac{T_0^{m+1} - T_s^{m+1}}{h_s^m} + \beta k_s \frac{T_1^{m+1} - T_s^{m+1}}{h_s^m} = 0, \tag{6.60}$$

where $F_o(T_s^{m+1})$ is the sum of all terms on the right-hand side of Eq. 6.2 except $k\partial T/\partial z$. The net surface flux $F_o(T_s^{m+1})$ is approximated as linear in $T_s^{m+1}$; thus

$$F_o(T_s^{m+1}) \sim F_o(T_s^m) + \left.\frac{\partial F_o}{\partial T_s}\right|_{T_s^m} (T_s^{m+1} - T_s^m). \tag{6.61}$$

with

$$\left.\frac{\partial F_o}{\partial T_s}\right|_{T_s^m} = \left.\frac{\partial F_{LWUP}}{\partial T_s}\right|_{T_s^m} + \left.\frac{\partial F_{SH}}{\partial T_s}\right|_{T_s^m} + \left.\frac{\partial F_{LH}}{\partial T_s}\right|_{T_s^m} \tag{6.62}$$

To simplify our set of equations, we define

$$\hat{c}_l^{m+1} = \rho_i \left( c_o + \frac{L_i \mu S}{T_l^{m+1} T_l^m} \right), \tag{6.63}$$

where the hat implies that $\hat{c}_l^{m+1}$ depends on $T_l^m$ as well as on $T_l^{m+1}$, and

$$\chi_l^{m+1} = \frac{\Delta t}{\Delta h^m} \frac{1}{\hat{c}_l^{m+1}}. \tag{6.64}$$

Also, let

$$k_l = \frac{k_l^m}{\Delta h^m}. \tag{6.65}$$

for $l \geq 2$ and

$$k_0 = \frac{k_s}{h_s^m} \tag{6.66}$$

$$k_1 = \frac{k_1^m}{(\Delta h^m + h_s^m)/2} \tag{6.67}$$

and suppress the index $m$ for $I_l^m$, so that for interior layers ($l = 1...L-1$),

$$T_l^{m+1} - T_l^m = \chi_l^{m+1} \left[ k_{l+1}(T_{l+1}^{m+1} - T_l^{m+1}) - k_l(T_l^{m+1} - T_{l-1}^{m+1}) + I_l \right] \tag{6.68}$$

and at the bottom layer

$$\begin{aligned} T_L^{m+1} - T_L^m = \chi_L^{m+1} \Bigg[ & 3k_b(T_b - T_L^{m+1}) - \frac{1}{3} k_b(T_b - T_{L-1}^{m+1}) \\ & - k_L(T_L^{m+1} - T_{L-1}^{m+1}) + I_L \Bigg] \end{aligned} \tag{6.69}$$

where $k_b = k_{L+1}/\Delta h^m$. The equation describing the snow layer is written

$$\rho_s c_s (T_0^{m+1} - T_0^m) = \frac{\Delta t}{h_s^m}\left[k_1(T_1^{m+1} - T_0^{m+1}) - \alpha k_0 (T_0^{m+1} - T_s^{m+1}) - \beta k_0 (T_1^{m+1} - T_s^{m+1})\right]. \quad (6.70)$$

Finally, the flux boundary condition becomes

$$F_o(T_s^m) + \left.\frac{\partial F_o}{\partial T_s}\right|_{T_s^m} (T_s^{m+1} - T_s^m) = -\alpha k_0 (T_0^{m+1} - T_s^{m+1}) - \beta k_0 (T_1^{m+1} - T_s^{m+1}). \quad (6.71)$$

The complete set of coupled equations for case I can be written with all of the terms that explicitly depend on temperature at the $m+1$ time step gathered on the right-hand side:

$$\begin{aligned}
-F_o(T_s^m) + \left.\frac{\partial F_o}{\partial T_s}\right|_{T_s^m} T_s^m &= T_s^{m+1}\left(\left.\frac{\partial F_o}{\partial T_s}\right|_{T_s^m} - \alpha k_0 - \beta k_0\right) \\
&\quad + T_0^{m+1}\alpha k_0 + T_1^{m+1}\beta k_0 \\
\rho_s c_s T_0^m &= T_s^{m+1}\left(-\frac{\Delta t}{h_s^m}\right)(\alpha k_0 + \beta k_0) \\
&\quad + T_0^{m+1}\left(\rho_s c_s + \frac{\Delta t}{h_s^m}(\alpha k_0 + k_1)\right) \\
&\quad + T_1^{m+1}\frac{\Delta t}{h_s^m}(\beta k_0 - k_1) \\
T_l^m + \chi_l^{m+1} I_l &= T_{l-1}^{m+1}(-\chi_l^{m+1} k_l) \\
&\quad + T_l^{m+1}(1 + \chi_l^{m+1} k_l + \chi_l^{m+1} k_{l+1}) \\
&\quad + T_{l+1}^{m+1}(-\chi_l^{m+1} k_{l+1}) \\
T_L^m + \chi_L^{m+1} I_L + \frac{8}{3}\chi_L^{m+1} k_b T_b &= T_{L-1}^{m+1}\left(-\frac{1}{3}\chi_L^{m+1} k_b - \chi_L^{m+1} k_L\right) \\
&\quad + T_L^{m+1}(1 + 3\chi_L^{m+1} k_b + \chi_L^{m+1} k_L).
\end{aligned} \quad (6.72)$$

These equations are subsequently related to the following abbreviated form

$$\begin{aligned}
r_s &= T_s^{m+1} b_s + T_0^{m+1} c_s + T_1^{m+1} d_s \\
r_0 &= T_s^{m+1} a_0 + T_0^{m+1} b_0 + T_1^{m+1} c_0 \\
r_1 &= T_0^{m+1} a_1 + T_1^{m+1} b_1 + T_2^{m+1} c_1 \\
&\vdots \\
r_L &= T_{L-1}^{m+1} a_L + T_L^{m+1} b_L.
\end{aligned} \quad (6.73)$$

The first two rows can be combined to eliminate the coefficient on $T_1^{m+1}$ in the first row, allowing the set to be written in tridiagonal form:

$$r = \begin{bmatrix} r_s c_0 - r_0 d_s \\ r_0 \\ r_1 \\ \vdots \end{bmatrix} \quad A = \begin{bmatrix} b_s c_0 - a_0 d_s & c_s c_0 - b_0 d_s & & \\ a_0 & b_0 & c_0 & \\ & a_1 & b_1 & c_1 \\ & & & \ddots \end{bmatrix} \quad T = \begin{bmatrix} T_s^{m+1} \\ T_0^{m+1} \\ T_1^{m+1} \\ \vdots \end{bmatrix}. \quad (6.74)$$

Because the matrix A depends on $\chi_l^{m+1}$, which in turn depends on $T_l^{m+1}$, the system of equations is solved iteratively. An initial guess is used for the temperature dependence of $\chi_l^{m+1}$, and then $\chi_l^{m+1}$ is updated successively after each iteration. Under most conditions the method approaches a solution in less than four iterations with a maximum error tolerance of $\Delta T_{err}$ for $T_l$ with an initial guess of $T_l^{m+1} = T_l^m$.

### 6.9.2 Case II: Snow free with no melting

Nearly the same method applies when the ice is snow free, except one less equation is needed to describe the evolution of the temperature profile. The equation for the uppermost ice layer is written

$$\begin{aligned} &\rho_i c_o (T_1^{m+1} - T_1^m)\left(1 + \frac{L_i \mu S_1}{c_o T_1^{m+1} T_1^m}\right) \\ &\quad = \frac{\Delta t}{\Delta h^m}\left(k_2^m \frac{T_2^{m+1} - T_1^{m+1}}{\Delta h^m} - 3k_1^m \frac{T_1^{m+1} - T_s^{m+1}}{\Delta h^m} + \frac{1}{3}k_1^m \frac{T_2^{m+1} - T_s^{m+1}}{\Delta h^m} + I_1^m\right), \end{aligned} \tag{6.75}$$

where $k_1^m = k(S_1, T_1^m)$. After the definitions from Eqs. 6.63–6.65 are applied, Eq. 6.75 becomes

$$T_1^{m+1} - T_1^m = \chi_1^{m+1}\left[k_2(T_2^{m+1} - T_1^{m+1}) - 3k_1(T_1^{m+1} - T_s^{m+1}) + \frac{1}{3}k_1(T_2^{m+1} - T_s^{m+1}) + I_1^m\right]. \tag{6.76}$$

The flux boundary condition follows after linearizing $F_o(T_s^{m+1})$ in $T_s^{m+1}$:

$$F_o(T_s^m) + \left.\frac{\partial F_o}{\partial T_s}\right|_{T_s^m}(T_s^{m+1} - T_s^m) = -3k_1(T_1^{m+1} - T_s^{m+1}) + \frac{1}{3}k_1(T_2^{m+1} - T_s^{m+1}). \tag{6.77}$$

The complete set of coupled equation includes Eqs. 6.72 for layers 2 to L with the following two equations for the surface and upper ice layer:

$$\begin{aligned} -F_o(T_s^m) + \left.\frac{\partial F_o}{\partial T_s}\right|_{T_s^m} T_s^m &= T_s^{m+1}\left(\left.\frac{\partial F_o}{\partial T_s}\right|_{T_s^m} - k_1\frac{8}{3}\right) + T_1^{m+1}3k_1 + T_2^{m+1}(-k_1/3) \\ T_1^m + \chi_1^{m+1}I_1^m &= T_s^{m+1}\left(-\chi_1^{m+1}k_1\frac{8}{3}\right) \\ &\quad + T_1^{m+1}(1 + \chi_1^{m+1}k_2 + 3\chi_1^{m+1}k_1) \\ &\quad + T_2^{m+1}(-\chi_1^{m+1}k_2 - \frac{1}{3}\chi_1^{m+1}k_1), \end{aligned} \tag{6.78}$$

which can be written

$$\begin{aligned} r_s &= T_s^{m+1}b_s + T_1^{m+1}c_s + T_2^{m+1}d_s \\ r_1 &= T_s^{m+1}a_1 + T_1^{m+1}b_1 + T_2^{m+1}c_1. \end{aligned} \tag{6.79}$$

These two equations can be combined to eliminate the coefficient on $T_2^{m+1}$, allowing the set to be written in tridiagonal form:

$$r = \begin{bmatrix} r_s c_1 - r_1 d_s \\ r_1 \\ r_2 \\ \vdots \end{bmatrix} \qquad A = \begin{bmatrix} b_s c_1 - a_1 d_s & c_s c_1 - b_1 d_s & & \\ a_1 & b_1 & c_1 & \\ & a_2 & b_2 & c_2 \\ & & & \ddots \end{bmatrix} \qquad T = \begin{bmatrix} T_s^{m+1} \\ T_1^{m+1} \\ T_2^{m+1} \\ \vdots \end{bmatrix}. \tag{6.80}$$

As for case I, this system of equations must be solved iteratively.

### 6.9.3 Case III: Snow accumulated with melting

Case III describes melting conditions in the presence of a snow layer at the surface. Here a temperature boundary condition is used, which simplifies the solution because the first row in Eqs. 6.72 is not needed and $T_s = T_{melt} = 0°\mathrm{C}$ in the second row. Hence the complete set of coupled equations is identical to Eqs. 6.72 for layers 1 to L, with the addition of an equation for the snow layer,

$$\rho_s c_s T_0^m + T_{melt}\frac{\Delta t}{h_s}(\alpha+\beta)k_0 = T_0^{m+1}\left[\rho_s c_s + \frac{\Delta t}{h_s}(k_1+\alpha k_0)\right] - T_1^{m+1}\frac{\Delta t}{h_s}(k_1-\beta k_0). \tag{6.81}$$

This set of equations can be written in tridiagonal form, without the need to eliminate any terms, as was required in cases I and II. However, the solution must still be iterated.

### 6.9.4 Case IV: No snow with melting

Like case III, case IV describes melting conditions, but here the sea ice is snow free. Hence, the first two rows of Eqs. 6.72 are not needed, and $T_s = T_{melt}$ for $l = 1$. The set of coupled equations comprises those from Eqs. 6.72 for layers 2 to L and the following equation for layer 1:

$$T_1^m + \chi_1^{m+1} I_1^m + T_{melt}\chi_1^{m+1} k_1 \frac{8}{3} = T_1^{m+1}\left(1 + \chi_1^{m+1}k_2 + 3\chi_1^{m+1}k_1\right) + T_2^{m+1}\left(-\chi_1^{m+1}k_2 - \frac{1}{3}\chi_1^{m+1}k_1\right). \tag{6.82}$$

As in case III, this set of equations can immediately be written in the tridiagonal form and solved iteratively.

### 6.9.5 Temperature Adjustment Due to Melt/Growth

The energy of melting of the ice and snow layers needs to be adjusted when the layer spacing changes after growth/melt, evaporation/sublimation, and flooding (see Figure 6.2). This calculation is only made when CAM 3.0 is coupled to a mixed layer ocean. The adjusted energy of melting is

$$q_l' = \begin{cases} \sum_{k=1}^{L} w_{k,1}q_k - q_{\mathrm{flood}}\frac{z_{int}}{\Delta h'}; & l = 1 \\ \sum_{k=1}^{L} w_{k,l}q_k; & 1 < l < L, \\ \sum_{k=1}^{L} w_{k,L}q_k + q_b \max(\frac{\delta h|_{\mathrm{basal}}}{\Delta h'}, 0); & l = L \end{cases} \tag{6.83}$$

where $w_{k,l}$ are weights computed from the relative overlap of layer $l$ with each layer $k$ from the old layer spacing and $\Delta h'$ is the new layer spacing.

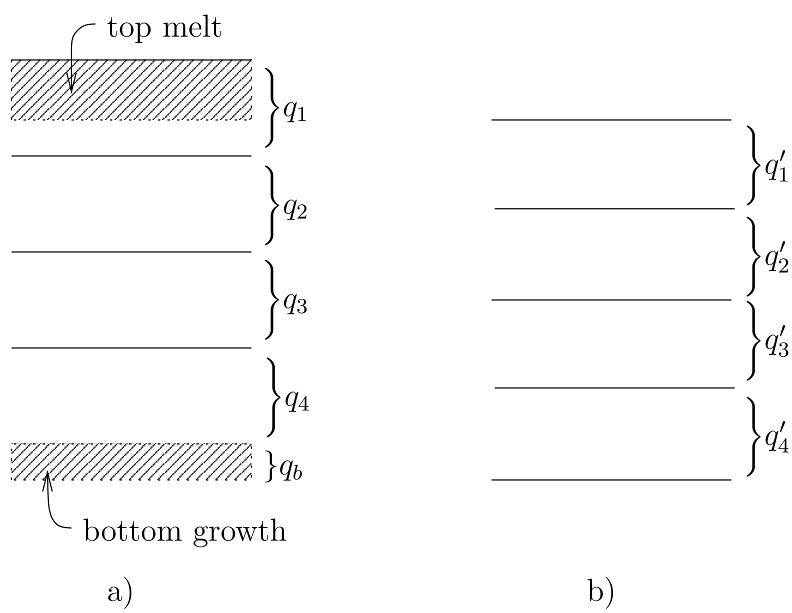


Figure 6.2: Diagram showing energy content before (a) and after (b) changing the layer spacing for an ice model with four vertical layers that experiences melt at the top surface and growth at the bottom surface. From Bitz [2000]

# Chapter 7

# Initial and Boundary Data

## 7.1 Initial Data

In this section, we describe how the time integration is started from data consistent with the spectral truncation. The land surface model requires its own initial data, as described by Bonan [1996]. The basic initial data for the model consist of values of $u, v, T, q, \Pi$, and $\Phi_s$ on the Gaussian grid at time $t = 0$. From these, $U, V, T'$, and $\Pi$ are computed on the grid using (3.11), and (3.49). The Fourier coefficients of these variables $U^m, V^m, T'^m, \Pi^m$, and $\Phi_s^m$ are determined via an FFT subroutine (3.149), and the spherical harmonic coefficients $T_n'^m, \Pi_n^m$, and $(\Phi_s)_n^m$ are determined by Gaussian quadrature (3.150). The relative vorticity $\zeta$ and divergence $\delta$ spherical harmonic coefficients are determined directly from the Fourier coefficients $U^m$ and $V^m$ using the relations,

$$\zeta = \frac{1}{a(1-\mu^2)} \frac{\partial V}{\partial \lambda} - \frac{1}{a} \frac{\partial U}{\partial \mu}, \tag{7.1}$$

$$\delta = \frac{1}{a(1-\mu^2)} \frac{\partial U}{\partial \lambda} + \frac{1}{a} \frac{\partial V}{\partial \mu}. \tag{7.2}$$

The relative vorticity and divergence coefficients are obtained by Gaussian quadrature directly, using (3.154) for the $\lambda$–derivative terms and (3.157) for the $\mu$–derivatives.

Once the spectral coefficients of the prognostic variables are available, the grid–point values of $\zeta, \delta, T', \Pi$, and $\Phi_s$ may be calculated from (3.180), the gradient $\nabla\Pi$ from (3.183) and (3.184), and $U$ and $V$ from (3.189) and (3.190). The absolute vorticity $\eta$ is determined from the relative vorticity $\zeta$ by adding the appropriate associated Legendre function for $f$ (3.117). This process gives grid–point fields for all variables, including the surface geopotential, that are consistent with the spectral truncation even if the original grid–point data were not. These grid–point values are then convectively adjusted (including the mass and negative moisture corrections).

The first time step of the model is forward semi–implicit rather than centered semi–implicit, so only variables at $t = 0$ are needed. The model performs this forward step by setting the variables at time $t = -\Delta t$ equal to those at $t = 0$ and by temporarily dividing $2\Delta t$ by 2 for this time step only. This is done so that formally the code and the centered prognostic equations of chapter 3 also describe this first forward step and no additional code is needed for this special step. The model loops through as indicated sequentially in chapter 3. The time step $2\Delta t$ is set to its original value before beginning the second time step.

## 7.2 Boundary Data

In addition to the initial grid–point values described in the previous section, the model also requires lower boundary conditions. The required data are surface temperature ($T_s$) at each ocean point, the surface geopotential at each point, and a flag at each point to indicate whether the point is land, ocean, or sea ice. The land surface model requires its own boundary data, as described by Bonan [1996]. A surface temperature and three subsurface temperatures must also be provided at non-ocean points.

For the uncoupled configuration of the model, a seasonally varying sea–surface temperature, and sea–ice concentration dataset is used to prescribe the time evolution of these surface quantities. This dataset prescribes analyzed monthly mid-point mean values of SST and ice concentration for the period 1950 through 2001. The dataset is a blended product, using the global HadISST OI dataset prior to 1981 and the Smith/Reynolds EOF dataset post-1981 (see Hurrell, 2002). In addition to the analyzed time series, a composite of the annual cycle for the period 1981-2001 is also available in the form of a mean "climatological" dataset. The sea–surface temperature and sea ice concentrations are updated every time step by the model at each grid point using linear interpolation in time. The mid-month values have been evaluated in such a way that this linear time interpolation reproduces the mid-month values.

Earlier versions of the global atmospheric model (the CCM series) included a simple land-ocean-sea ice mask to define the underlying surface of the model. It is well known that fluxes of fresh water, heat, and momentum between the atmosphere and underlying surface are strongly affected by surface type. The CAM 3.0 provides a much more accurate representation of flux exchanges from coastal boundaries, island regions, and ice edges by including a fractional specification for land, ice, and ocean. That is, the area occupied by these surface types is described as a fractional portion of the atmospheric grid box. This fractional specification provides a mechanism to account for flux differences due to sub-grid inhomogeneity of surface types.

In CAM 3.0 each atmospheric grid box is partitioned into three surface types: land, sea ice, and ocean. Land fraction is assigned at model initialization and is considered fixed throughout the model run. Ice concentration data is provided by the external time varying dataset described above, with new values determined by linear interpolation at the beginning of every time-step. Any remaining fraction of a grid box not already partitioned into land or ice is regarded as ocean.

Surface fluxes are then calculated separately for each surface type, weighted by the appropriate fractional area, and then summed to provide a mean value for a grid box:

$$F_{\psi_T} = a_i \, F_{\psi_i} + a_o \, F_{\psi_o} + a_l \, F_{\psi_l} \ , \tag{7.3}$$

where $F$ denotes the surface flux of the arbitrary scalar quantity $\psi$, $a$ denotes fractional area, and the subscripts $T, i, o$, and $l$ respectively denote the total, ice, ocean, and land components of the fluxes. For each time-step the aggregated grid box fluxes are passed to the atmosphere and all flux arrays which have been used for the accumulations are reset to zero in preparation for the next time-step. The fractional land values for CAM 3.0 were calculated from Navy 10-Min Global Elevation Data. An area preserving binning algorithm was used to interpolate from the high-resolution Navy dataset to standard model resolutions.

The radiation parameterization requires monthly mean ozone volume mixing ratios to be specified as a function of the latitude grid, 23 vertical pressure levels, and time. The ozone path lengths are evaluated from the mixing–ratio data. The path lengths are interpolated to the model $\eta$–layer interfaces for use in the radiation calculation. As with the sea–surface temperatures, the seasonal version assigns the monthly averages to the mid–month date and updates them every 12 hours via linear interpolation. The actual mixing ratios used in the standard version were derived by Chervin [1986] from analysis of Dütsch [1986].

The sub-grid scale standard deviation of surface orography is specified in the following manner. The variance is first evaluated from the global Navy $10'$ topographic height data over an intermediate grid (*e.g.* $2^\circ \times 2^\circ$ grid for T42 and lower resolutions, $1.67^\circ \times 1.67^\circ$ for T63, and $1.0^\circ \times 1.0^\circ$ for T106 resolution) and is assumed to be isotropic. Once computed on the appropriate grid, the standard deviations are binned to the CAM 3.0 grid (*i.e.,* all values whose latitude and longitude centers fall within each grid box are averaged together). Finally, the standard deviation is smoothed twice with a 1–2–1 spatial filter. Values over ocean are set to zero.

# Appendix A

# Physical Constants

Following the American Meteorological Society convention, the model uses the International System of Units (SI) (see August 1974 *Bulletin of the American Meteorological Society*, **Vol. 55**, No. 8, pp. 926-930).

| | | | |
|---|---|---|---|
| $a$ | $=$ | $6.37122 \times 10^6$ m | Radius of earth |
| $g$ | $=$ | $9.80616$ m s$^{-2}$ | Acceleration due to gravity |
| $\pi$ | $=$ | $3.14159265358979323846$ | Pi |
| $t_s$ | $=$ | $86164.0$ s | Earth's sidereal day |
| $\Omega$ | $=$ | $2 * \pi / t_s$ [s$^{-1}$] | Earth's angular velocity |
| $\sigma_B$ | $=$ | $5.67 \times 10^{-8}$ W m$^{-2}$ K$^{-4}$ | Stefan − Boltzmann constant |
| $k$ | $=$ | $1.38065 \times 10^{-23}$ JK$^{-1}$ | Boltzmann constant |
| $N$ | $=$ | $6.02214 \times 10^{26}$ | Avogadro's number |
| $R^*$ | $=$ | $k\,N$ [JK$^{-1}$] | Universal gas constant |
| $m_{air}$ | $=$ | $28.966$ kg | Molecular weight of dry air |
| $R$ | $=$ | $R^*/m_{air}$ [J kg$^{-1}$ K$^{-1}$] | Gas constant for dry air |
| $m_v$ | $=$ | $18.016$ kg | Molecular weight of water vapor |
| $R_v$ | $=$ | $R^*/m_v$ [J kg$^{-1}$ K$^{-1}$] | Gas constant for water vapor |
| $c_p$ | $=$ | $1.00464 \times 10^3$ J kg$^{-1}$ K$^{-1}$ | Specific heat of dry air at constant pressure |
| $\kappa$ | $=$ | $2/5$ | Von Karman constant |
| $z_{vir}$ | $=$ | $R_v/R - 1$ | Ratio of gas constants for water vapor and dry air |
| $L_v$ | $=$ | $2.501 \times 10^6$ J kg$^{-1}$ | Latent heat of vaporization |
| $L_i$ | $=$ | $3.337 \times 10^5$ J kg$^{-1}$ | Latent heat of fusion |
| $\rho_{H_2O}$ | $=$ | $1.0 \times 10^3$ kg m$^{-3}$ | Density of liquid water |
| $c_{pv}$ | $=$ | $1.81 \times 10^3$ J kg$^{-1}$ K$^{-1}$ | Specific heat of water vapor at constant pressure |
| $T_{melt}$ | $=$ | $273.16$ °K | Melting point of ice |
| $p_{std}$ | $=$ | $1.01325 \times 10^5$ Pa | Standard pressure |
| $\rho_{air}$ | $=$ | $p_{std}/(R\,T_{melt})$ [kgm$^{-3}$] | Density of dry air at standard pressure/temperature |

The model code defines these constants to the stated accuracy. We do not mean to imply that these constants are known to this accuracy nor that the low-order digits are significant to the physical approximations employed.

# Appendix B

# Acronyms

| | |
|---|---|
| ABL | Atmospheric Boundary Layer |
| AMIP | Atmospheric Model Intercomparison Project |
| AMWG | Atmospheric Model Working Group |
| BATS | Biosphere-Atmosphere Transfer Scheme |
| CAM | Community Atmosphere Model |
| CAPE | Convectively Available Potential Energy |
| CCM | Community Climate Model |
| CCN | Cloud Condensation Nucleus |
| CCSM | Community Climate System Model |
| CFC | Chloro-Fluoro Carbon |
| CFL | Courant-Friedrichs-Levy Condition |
| CGD | NCAR Climate and Global Dynamics Division |
| CGS | Centimeters/grams/seconds |
| CKD | Clough-Kneizys-Davies |
| CLM | Community Land Model |
| CMS | (NCAR) Climate Modeling Section |
| CSIM | Community Sea-Ice Model |
| CWP | Condensed Water Path |
| DAO | (NASA Goddard) Data Assimilation Office |
| DAS | Data Assimilation System |
| DISORT | DIScrete-Ordinate method Radiative Transfer |
| ECMWF | European Centre for Medium Range Forecasts |
| EOF | Empirical Orthogonal Function |
| FASCODE | FASt atmosphere Signature Code |
| FFSL | Flux-Form Semi-Lagrangian Transport |
| FFT | Fast Fourier Transform |
| FV/fv | Finite Volume |
| GCM | General Circulation Model |
| GENLN | General Line-by-line Atmospheric Transmittance and Radiance Model |
| GEOS | Goddard Earth Observing System |
| GFDL | Geophysical Fluid Dynamics Laboratory |
| GSFC | Goddard Space Flight Center |
| GMT | Greenwich Mean Time |

| | |
|---|---|
| HadISST | Hadley Centre for Climate Prediction and Research SST |
| HITRAN | High-resolution Transmission Molecular Absorption Database |
| ICA | Independent Column Approximation |
| IPCC | International Panel on Climate Change |
| KNMI | Royal Netherlands Meteorological Institute |
| LBL | Line by line |
| LCL | Lifting condensation level |
| LSM | Land Surface Model |
| MATCH | Model for Atmospheric Transport and Chemistry |
| M/R | Maximum/Random overlap |
| NASA | National Space Administration |
| NCAR | National Center for Atmospheric Research |
| NCEP | National Center for Environmental Prediction |
| NOAA | National Oceanographic and Atmospheric Administration |
| NWP | Numerical Weather Prediction |
| OI | Optimal Interpolation |
| OPAC | Optical Properties of Aerosols and Clouds |
| PBL | Planetary Boundary Layer |
| PCMDI | Program for Climate Model Diagnosis and Intercomparison |
| PPM | Piece-wise Parabolic Method |
| RHS | Right Hand Side |
| RMS | Root-mean Square |
| SCMO | Sufficient Condition for Monotonicity |
| SI | International System of Units |
| SOM | Slab Ocean Model |
| SST | Sea-surface temperature |
| TOA | Top Of Atmosphere |
| TOM | Top Of Model |
| UCAR | University Corporation for Atmospheric Research |
| WKB | Wentzel-Kramer-Brillouin approximation |

# Appendix C

# Resolution and dycore-dependent parameters

The following adjustable parameters differ between various dynamical cores and model resolutions in CAM 3.0.

Table C.1: Resolution and dycore-dependent parameters

| Parameter | FV | T85 | T42 | T31 | Description |
|---|---|---|---|---|---|
| $q_{ic,warm}$ | 8.e-4 | 4.e-4 | 4.e-4 | 4.e-4 | threshold for autoconversion of warm ice |
| $q_{ic,cold}$ | 11.e-6 | 16.e-6 | 5.e-6 | 3.e-6 | threshold for autoconversion of cold ice |
| $k_{e,strat}$ | 5.e-6 | 5.e-6 | 10.e-6 | 10.e-6 | stratiform precipitation evaporation efficiency parameter |
| $RH_{\min}^{low}$ | .91 | .91 | .90 | .88 | minimum RH threshold for low stable clouds |
| $RH_{\min}^{high}$ | .80 | .70 | .80 | .80 | minimum RH threshold for high stable clouds |
| $k_{1,shallow}$ | 0.04 | 0.07 | 0.07 | 0.07 | parameter for shallow convection cloud fraction |
| $k_{1,deep}$ | 0.10 | 0.14 | 0.14 | 0.14 | parameter for deep convection cloud fraction |
| $p_{mid}$ | 750.e2 | 250.e2 | 750.e2 | 750.e2 | top of area defined to be mid-level cloud |
| $c_{0,shallow}$ | 1.0e-4 | 1.0e-4 | 2.0e-4 | 5.0e-4 | shallow convection precip production efficiency parameter |
| $c_{0,deep}$ | 3.5E-3 | 4.0E-3 | 3.0E-3 | 2.0E-3 | deep convection precipitation production efficiency parameter |
| $k_{e,conv}$ | 1.0E-6 | 1.0E-6 | 3.0E-6 | 3.0E-6 | convective precipitation evaporation efficiency parameter |
| dif4 | N/A | 1.0e15 | 1.0e16 | 2.0e16 | horizontal diffusion coefficient |

# Bibliography


Alcamo, J., A. Bouwman, J. Edmonds, A. Grubler, T. Morita, and A. Sugandhy, An evaluation of the ipcc is92 emission scenarios, in *Climate Change 1994: Radiative Forcing of Climate Change and an Evaluation of the IPCC IS92 Emission Scenarios*, edited by J. Houghton, 247–304, Cambridge University Press, 1995.

Ammann, C. M., G. A. Meehl, W. M. Washington, and C. S. Zender, A monthly and latitudinally varying volcanic forcing dataset in simulations of 20th century climate, *Geophys. Res. Lett.*, *30* **(12)**, DOI 1029/2003GL016875, 2003, article no. 1657.

Anderson, G. P., S. A. Clough, F. X. Kneizys, J. H. Chetwynd, and E. P. Shettle, AFGL atmospheric constituent profiles (0-120 km), Technical Report AFGL-TR-86-0110, AFGL (OPI), Hanscom AFB, MA. 01736, 1986.

Anthes, R. A., Summary of workshop on the NCAR Community Climate/forecast Models 14–26 July 1985, Boulder, Colorado, *Bull. Am. Meteorol. Soc.*, *67*, 94–198, 1986.

Arakawa, A., and V. R. Lamb, A potential enstrophy and energy conserving scheme for the shallow-water equations, *Mon. Wea. Rev.*, *109*, 18–36, 1981.

Asselin, R., Frequency filter for time integrations, *Mon. Wea. Rev.*, *100*, 487–490, 1972.

Austin, P., Y. Wang, R. Pincus, and V. Kujala, Precipitation in stratocumulus clouds: Observational and modeling results, *J. Atmos. Sci.*, *52*, 2329–2352, 1995.

Baede, A. P. M., M. Jarraud, and U. Cubasch, Adiabatic formulation and organization of ECMWF's model, Technical Report 15, ECMWF, Reading, U.K., 1979.

Baker, M. B., Variability in concentrations of cloud condensation nuclei in the marine cloud-topped boundary layer, *Tellus*, *45B*, 458–472, 1993.

Balkanski, Y. J., D. J. Jacob, G. M. Gardner, W. C. Graustein, and K. K. Turekian, Transport and residence times of tropospheric aerosols inferred from a global three-dimensional simulation of $^{210}$Pb, *J. Geophys. Res.*, *98*, 20,573–20,586, 1993.

Barth, M. C., D. A. Hegg, and P. V. Hobbs, Numerical modeling of cloud and precipitation chemistry associated with two rainbands and some comparisons with observations, *J. Geophys. Res.*, *97*, 5825–5845, 1992.

Barth, M. C., P. J. Rasch, J. T. Kiehl, C. M. Benkovitz, and S. E. Schwartz, Sulfur chemistry in the National Center for Atmospheric Research Community Climate Model: Description, evaluation, features and sensitivity to aqueous chemistry, *J. Geophys. Res.*, *105*, 1387–1415, 2000.

Bates, J. R., F. H. M. Semazzi, R. W. Higgins, and S. R. Barros, Integration of the shallow water equations on the sphere using a vector semi-Lagrangian scheme with a multigrid solver, *Mon. Wea. Rev.*, *118*, 1615–1627, 1990.

Bath, L., J. Rosinski, and J. Olson, User's Guide to NCAR CCM2, Technical Report NCAR/TN-379+IA, National Center for Atmospheric Research, Boulder, CO, 156 pp., 1992.

Bath, L. M., M. A. Dias, D. L. Williamson, G. S. Williamson, and R. J. Wolski, User's Guide to NCAR CCM1, Technical Report NCAR/TN-286+IA, National Center for Atmospheric Research, Boulder, CO, 173 pp., 1987.

Benkovitz, C. M., C. M. Berkowitz, R. C. Easter, S. Nemesure, R. Wagener, and S. E. Schwartz, Sulfate over the North Atlantic and adjacent continental regions: Evaluation for October and November 1986 using a three-dimensional model driven by observation-derived meteorology, *jgr*, *99*, 20,725–20,756, 1994.

Berger, A. L., Long-term variations of daily insolation and quaternary climatic changes, *J. Atmos. Sci.*, *35*, 2362–2367, 1978.

Betts, A. K., Parametric interpretation of trade-wind cumulus budget studies, *J. Atmos. Sci.*, *32*, 1934–1945, 1975.

Bitz, C. M., Documentation of a lagrangian sea ice thickness distribution model with energy-conserving thermodynamics, Technical report, U. of Washington APL-UW TM 4–99, 2000.

Bitz, C. M., and W. H. Lipscomb, An energy-conserving thermodynamic model of sea ice, *J. Geophys. Res.*, *104*, 15669–15677, 1999.

Blanchard, D. C., and A. H. Woodcock, Production, concentration, and vertical distribution of the sea salt aerosol, *Annals New York Acad. Sci.*, *338*, 330–347, 1980.

Bonan, G. B., A land surface model (LSM version 1.0) for ecological, hydrological, and atmospheric studies: Technical description and user's guide, Technical Report NCAR/TN-417+STR, National Center for Atmospheric Research, Boulder, CO, 150 pp., 1996.

Bonan, G. B., K. W. Oleson, M. Vertenstein, S. Levis, X. Zeng, Y. Dai, R. E. Dickinson, , and Z.-L. Yang, The land surface climatology of the Community Land Model coupled to the NCAR Community Climate Model, *J. Climate*, *15*, 3123–3149, 2002.

Bourke, W., B. McAvaney, K. Puri, and R. Thurling, Global modeling of atmospheric flow by spectral methods, in *Methods in Computational Physics*, Vol. 17, 267–324, Academic Press, New York, 1977.

Boville, B. A., and C. S. Bretherton, Heating and dissipation in the NCAR community atmosphere model, *J. Climate*, *16*, 3877–3887, 2003.

Boville, B. A., J. T. Kiehl, P. J. Rasch, and F. O. Bryan, Improvements to the ncar csm-1 for transient climate simulations, *J. Climate*, *14*, 164–179, 2001.

Briegleb, B. P., Delta-Eddington approximation for solar radiation in the NCAR Community Climate Model, *J. Geophys. Res.*, *97*, 7603–7612, 1992.

Briegleb, B. P., C. M. Bitz, E. C. Hunke, W. H. Lipscomb, and J. L. Schramm, Description of the community climate system model version 2 sea ice model, Technical report, National Center for Atmospheric Research, http://www.ccsm.ucar.edu/models/ice-csim4, 2002.

Bryan, F. O., B. G. Kauffman, W. G. Large, and P. R. Gent, The NCAR CSM Flux Coupler, Technical Report NCAR/TN-424+STR, National Center for Atmospheric Research, Boulder, Colorado, 58 pp., 1996.

Cess, R. D., Nuclear war: Illustrative effects of atmospheric smoke and dust upon solar radiation, *Clim. Change*, *7*, 237–251, 1985.

Chen, C., and W. R. Cotton, The physics of the marine stratocumulus-capped mixed layer, *J. Atmos. Sci.*, *44* **(50)**, 2951–2977, 1987.

Chervin, R. M., Interannual variability and seasonal climate predictability, *J. Atmos. Sci.*, *43*, 233–251, 1986.

Clough, S. A., F. X. Kneizys, and R. W. Davies, Line shape and the water vapor continuum, *Atmos. Res.*, *23*, 229–241, 1989.

Clough, S. A., M. J. Iacono, and J. L. Moncet, Line-by-line calculations of atmospheric fluxes and cooling rates – Application to water vapor, *J. Geophys. Res.*, *97*, 15761–15785, 1992.

Coakley, J. A., R. D. Cess, and F. B. Yurevich, The effect of tropospheric aerosols on the Earth's radiation budget: A parameterization for climate models, *J. Atmos. Sci.*, *40*, 116–138, 1983.

Colella, P., and P. R. Woodward, The piecewise parabolic method (ppm) for gas-dynamical simulations, *J. Comp. Phys.*, *54*, 174–201, 1984.

Collins, W. D., A global signature of enhanced shortwave absorption by clouds, *J. Geophys. Res.*, *103*, 31669–31679, 1998.

Collins, W. D., Parameterization of generalized cloud overlap for radiative calculations in general circulation models, *J. Atmos. Sci.*, *58*, 3224–3242, 2001.

Collins, W. D., P. J. Rasch, B. E. Eaton, B. Khattatov, J.-F. Lamarque, and C. S. Zender, Simulating aerosols using a chemical transport model with assimilation of satellite aerosol retrievals: Methodology for INDOEX, *J. Geophys. Res.*, *106*, 7313–7336, 2001.

Collins, W. D., J. K. Hackney, and D. P. Edwards, A new parameterization for infrared emission and absorption by water vapor in the National Center for Atmospheric Research Community Atmosphere Model, *J. Geophys. Res.*, *107* **(D22)**, 2002*a*.

Collins, W. D., P. J. Rasch, B. E. Eaton, D. W. Fillmore, J. T. Kiehl, T. C. Beck, and C. S. Zender, Simulation of aerosol distributions and radiative forcing for INDOEX: Regional climate impacts, *J. Geophys. Res.*, *107*, DOI 10.1029/2001JD001365, 2002*b*, article no. 8028.

Cooke, W. F., C. Liousse, H. Cachier, and J. Feichter, Construction of a 1 degrees x 1 degrees fossil fuel emission data set for carbonaceous aerosol and implementation and radiative impact in the ECHAM4 model, *J. Geophys. Res.*, *104*, 22137–22162, 1999.

Côté, J., and A. Staniforth, A two-time-level semi-Lagrangian semi-implicit scheme for spectral models, *Mon. Wea. Rev.*, *116*, 2003–2012, 1988.

Curtis, A. R., Contribution to a discussion of 'A statistical model for water vapour absorption' by R. M. Goody, *Q. J. R. Meteorol. Soc.*, *78*, 638–640, 1952.

Dai, Y., X. Zeng, R. E. Dickinson, and coauthors, The Common Land Model: Documentation and User's Guide, `http://climate.eas.gatech.edu/dai/clmdoc.pdf`, 2001.

Daley, R., C. Girard, J. Henderson, and I. Simmonds, Short-term forecasting with a multi-level spectral primitive equation model. Part I—model formulation, *Atmosphere*, *14*, 98–116, 1976.

Dana, T. M., and J. M. Hales, Statistical aspects of the washout of polydisperse aerosols, *Atmos. Environ.*, *10*, 45–50, 1976.

Deardorff, J. W., Parameterization of the planetary boundary layer for use in general circulation models, *Mon. Wea. Rev.*, *100*, 93–106, 1972.

Demore, W. B., S. P. Sander, C. J. Howard, A. R. Ravishankara, D. M. Golden, C. E. Kolb, R. F. Hampson, M. J. Kurylo, and M. J. Molina, Chemical kinetics and photochemical data for use in stratospheric modeling: Evaluation number 12, Technical Report JPL Publ. 97-4, JPL, 266 pp., 1997.

Dickinson, R. E., A. Henderson-Sellers, P. J. Kennedy, and M. F. Wilson, Biosphere-atmosphere transfer scheme (BATS) for the NCAR Community Climate Model, Technical Report NCAR/TN-275+STR, National Center for Atmospheric Research, Boulder, Colorado, 69 pp., 1987.

Donner, L., and V. Ramanathan, Methane and nitrous oxide: Their effects on the terrestrial climate, *J. Atmos. Sci.*, *37*, 119–124, 1980.

Dütsch, H. U., Vertical ozone distribution on a global scale, *Pure Appl. Geophys.*, *116*, 511–529, 1986.

Duynkerke, P. G., Application of the E-$\epsilon$ turbulence closure model to the neutral and stable atmospheric boundary layer, *J. Atmos. Sci.*, *45*, 865–880, 1988.

Dyer, A. J., A review of flux-profile relationships, *Boundary Layer Meteorol.*, *7*, 363–372, 1974.

Ebert, E. E., and J. A. Curry, A parameterization of ice cloud optical properties for climate models, *J. Geophys. Res.*, *97*, 3831–3836, 1992.

Ebert, E. E., and J. A. Curry, An intermediate one-dimensional thermodynamic sea ice model for investigating ice-atmosphere interactions, *J. Geophys. Res.*, *98*, 10085–10109, 1993.

Edwards, D. P., GENLN2: A general line-by-line atmospheric transmittance and radiance model, Technical Report NCAR/TN-367+STR, NCAR, P.O. Box 3000, Boulder, Colorado, 80307–3000, 147 pp., January, 1992.

Feichter, J., E. Kjellström, H. Rodhe, F. Dentener, J. Lelieveld, and G.-J. Roelofs, Simulation of the tropospheric sulfur cycle in a global climate model, *Atmos. Environ.*, *30* **(10)**, 1693–1707, 1996.

Garcia, R. R., and S. Solomon, A new numerical model of the middle atmosphere. part ii: Ozone and related species, *J. Geophys. Res.*, *99*, 12937–12951, 1994.

Geleyn, J.-F., Interpolation of wind, temperature and humidity values from model levels to the height of measurement, *Tellus, Series A (Dynamic Meteorology and Oceanography)*, *40A*, 347–351, 1988.

Godson, W. L., The evaluation of infra-red radiative fluxes due to atmospheric water vapour, *Q. J. R. Meteorol. Soc.*, *79*, 367–379, 1953.

Goody, R. M., and Y. L. Yung, *Atmospheric Radiation.* Oxford Univ. Press, New York, 2nd edition, 1989, 519 pp.

Grenfell, T. C., S. G. Warren, and P. C. Mullen, Reflection of solar radiation by the antarctic snow surface at ultraviolet, visible, and near-infrared wavelengths, *J. Geophys. Res.*, *99*, 18669–18684, 1994.

Hack, J. J., Parameterization of moist convection in the National Center for Atmospheric Research Community Climate Model (CCM2), *J. Geophys. Res.*, *99*, 5551–5568, 1994.

Hack, J. J., L. M. Bath, G. W. Williamson, and B. A. Boville, Modifications and enhancements to the NCAR Community Climate Model (CCM1), Technical Report NCAR/TN-336+STR, National Center for Atmospheric Research, Boulder, Colorado, 97 pp., 1989.

Hack, J. J., B. A. Boville, B. P. Briegleb, J. T. Kiehl, P. J. Rasch, and D. L. Williamson, Description of the NCAR Community Climate Model (CCM2), Technical Report NCAR/TN-382+STR, National Center for Atmospheric Research, 120 pp., 1993.

Hansen, J., A. Lacis, D. Rind, G. Russell, P. Stone, I. Fung, R. Ruedy, and J. Lerner, Climate sensitivity: Analysis of feedback mechanisms, in *Climate Processes and Climate Sensitivity*, edited by J. E. Hansen, and T. Takahashi, 130–163, Amer. Geophys. Union, Washington, D.C., 1984.

Held, I. M., and M. J. Suarez, A proposal for the intercomparison of the dynamical cores of atmospheric general circulation models, *Bull. Am. Meteorol. Soc.*, *75*, 1825–1830, 1994.

Hess, M., P. Koepke, and I. Schult, Optical properties of aerosols and clouds: the software package OPAC, *Bull. Am. Meteorol. Soc.*, *79*, 831–844, 1998.

Hesstvedt, E., O. Hov, and I. S. A. Isaksen, Quasi-steady-state approximation in air pollution modeling: Comparison of two numerical schemes of oxidant prediction, *International Journal of Chemical Kinetics*, *10*, 971–994, 1978.

Hildebrand, F. B., *Introduction to Numerical Analysis*. McGraw-Hill, New York, New York, 1956, 511 pp.

Hoffmann, M. R., and J. G. Calvert, Chemical transportation modules for Eulerian acid deposition models, vol. II, The aqueous-phase chemistry, Rep. EPA/600/3-85/017, Environ. Prot. Agency, Research Triangle Park, N. C., 1985.

Hogstrom, U., Non-dimensional wind and temperature profiles in the atmospheric surface layer: a re-evaluation, *Boundary Layer Meteorol.*, *42*, 55–78, 1988.

Holtslag, A. A. M., and B. A. Boville, Local versus nonlocal boundary-layer diffusion in a global climate model, *J. Climate*, *6*, 1825–1842, 1993.

Holtslag, A. A. M., E. I. F. deBruijn, and H.-L. Pan, A high resolution air mass transformation model for short-range weather forecasting, *Mon. Wea. Rev.*, *118*, 1561–1575, 1990.

Holtslag, A. A. M., and C.-H. Moeng, Eddy diffusivity and countergradient transport in the convective atmospheric boundary layer, *J. Atmos. Sci.*, *48*, 1690–1698, 1991.

Hortal, M. 1999. Aspects of the numerics of the ECMWF model. in *Proceedings of ECMWF Seminar: Recent developments in numerical methods for atmospheric modelling, 7–11 September 1998*, 127–143*,* .

Hsu, Y.-J. G., and A. Arakawa, Numerical modeling of the atmosphere with an isentropic vertical coordinate, *Mon. Wea. Rev.*, *118*, 1933–1959, 1990.

IPCC, *Climate Change, 1994 : Radiative Forcing of Climate Change and an Evaluation of the IPCC IS92 emission Scenarios.* Cambridge University Press, 1995, ed., John T. Houghton.

Joseph, J. H., W. J. Wiscombe, and J. A. Weinman, The delta-Eddington approximation for radiative flux transfer, *J. Atmos. Sci.*, *33*, 2452–2459, 1976.

Kader, B. A., and A. M. Yaglom, Mean fields and fluctuation moments in unstably stratified turbulent boundary layers, *J. Fluid Mech.*, *212*, 637–662, 1990.

Kagann, R. H., J. W. Elkins, and R. L. Sams, Absolute band strengths of halocarbons F-11 and F-12 in the 8- to 16-$\mu$m region, *J. Geophys. Res.*, *88*, 1427–1432, 1983.

Kalnay, E., M. Kanamitsu, R. Kistler, W. Collins, D. Deaven, L. Gandin, M. Iredell, S. Saha, G. White, J. Woollen, Y. Zhu, M. Chelliah, W. Ebisuzaki, W. Higgins, J. Janowiak, K. C. Mo, C. Ropelewski, J. Wang, A. Leetmaa, R. Reynolds, R. Jenne, and D. Joseph, The NCEP/NCAR 40-year reanalysis project, *Bull. Am. Meteorol. Soc.*, *77*, 437–471, 1996.

Kasahara, A., Various vertical coordinate systems used for numerical weather prediction, *Mon. Wea. Rev.*, *102*, 509–522, 1974.

Kessler, E., *On the distribution and continuity of water substance in atmospheric circulations*. Amer. Meteor. Soc., Boston, Mass., 1969.

Kettle, A. J., M. O. Andreae, D. Amouroux, and T. W. Andreae, A global database of sea surface dimethylsulfide (DMS) measurements and a procedure to predict sea surface DMs as a function of latitude, longitude, and month, *Glob. Biogeochem. Cycles*, *13*, 399–444, 1999.

Kiehl, J. T., and B. P. Briegleb, A new parameterization of the absorptance due to the 15 $\mu$m band system of carbon dioxide, *J. Geophys. Res.*, *96*, 9013–9019, 1991.

Kiehl, J. T., and B. P. Briegleb, The relative roles of sulfate aerosols and greenhouse gases in climate forcing, *Science*, *260*, 311–314, 1993.

Kiehl, J. T., J. J. Hack, and B. P. Briegleb, The simulated Earth radiation budget of the National Center for Atmospheric Research Community Climate Model CCM2 and comparisons with the Earth Radiation Budget Experiment (ERBE), *J. Geophys. Res.*, *99*, 20815–20827, 1994.

Kiehl, J. T., J. Hack, G. Bonan, B. Boville, B. Briegleb, D. Williamson, and P. Rasch, Description of the NCAR Community Climate Model (CCM3), Technical Report NCAR/TN-420+STR, National Center for Atmospheric Research, Boulder, Colorado, 152 pp., 1996.

Kiehl, J. T., J. J. Hack, G. B. Bonan, B. B. Boville, D. L. Williamson, and P. J. Rasch, The National Center for Atmospheric Research Community Climate Model: CCM3, *J. Climate*, *11*, 1131–1149, 1998.

Kiehl, J. T., T. L. Schneider, P. J. Rasch, M. Barth, and J. Wong, Radiative forcing due to sulfate aerosols from simulations with the National Center for Atmospheric Research Community Climate Model, Version 3, *J. Geophys. Res.*, , 1441—1457, 2000.

Kiehl, J. T., and V. Ramanathan, $CO_2$ radiative parameterization used in climate models: comparison with narrow band models and with laboratory data, *J. Geophys. Res.*, *88*, 5191–5202, 1983.

Kiehl, J. T., and V. Ramanathan, Comparison of cloud forcing derived from the Earth Radiation Budget Experiment with that simulated by the NCAR Community Climate Model, *J. Geophys. Res.*, *95*, 11679–11698, 1990.

Klein, S. A., and D. L. Hartmann, The seasonal cycle of low stratiform clouds, *J. Climate*, *6*, 1587–1606, 1993.

Kluzek, E. B., M. Vertenstein, and B. E. Eaton, User's Guide to NCAR CAM2.0, Technical report, National Center for Atmospheric Research, Boulder, Colorado, `http://www.ccsm.ucar.edu/models/atm-cam/UsersGuide/cover.html`, 2002.

Kristjánsson, J. E., and J. Kristiansen, Impact of a new scheme for optical properties of ice crystals on climates of two gcms, *J. Geophys. Res.*, *105*, 10063–10079, 2000.

Lacis, A. A., and V. Oinas, A description of the correlated k distribution method for modeling nongray gaseous absorption, thermal emission, and multiple scattering in vertically inhomogeneous atmospheres, *J. Geophys. Res.*, *96*, 9027–9063, 1991.

Large, W. G., Ocean modeling and parameterization, in *Modeling and parameterizing the ocean planetary boundary layer*, edited by E.P.Chassignet, and J. (eds.), 81–120, Kluwer Academic Publishers, 1998, Printed in the Netherlands.

Large, W. G., J. C. McWilliams, and S. C. Doney, Oceanic vertical mixing: A review and a model with a nonlocal boundary layer parameterization, *Rev. Geophys.*, *32*, 363–403, 1994.

Large, W. G., and S. Pond, Sensible and latent heat flux measurements over the ocean, *J. Phys. Oceanogr.*, *12*, 464–482, 1982.

Lawrence, M. G., and P. J. Crutzen, The impact of cloud particle gravitational settling on soluble trace gas distributions, *Tellus*, *50B*, 263—289, 1998.

Le Texier, H., S. Solomon, and R. R. Garcia, Role of molecular hydrogen and methane oxidation in the water vapor budget of the stratosphere, *Q. J. R. Meteorol. Soc.*, *114*, 281–295, 1988.

Lean, J., J. Beer, and R. S. Bradley, Reconstruction of solar irradiance since 1610: Implications for climate change, *Geophys. Res. Lett.*, *22*, 3195–3198, 1995.

Levitus, S., Climatological atlas of the world ocean, Technical Report NOAA Professional Paper 13, National Oceanic and Atmospheric Administration, 1982.

Levkov, L., B. Rockel, H. Kapitza, and E. Raschke, 3D mesoscale numerical studies of cirrus and stratus clouds by their time and space evolution, *Beitr. Phys. Atmosph.*, *65*, 35–58, 1992.

Li, J., Accounting for overlap of fractional cloud in infrared radiation, *Q. J. R. Meteorol. Soc.*, *126*, 3325–3342, 2000.

Lin, S.-J., W. C. Chao, Y. C. Sud, and G. K. Walker, A class of the van leer-type transport schemes and its applications to the moisture transport in a general circulation model, *Mon. Wea. Rev.*, *122*, 1575–1593, 1994.

Lin, S.-J., and R. B. Rood, Multidimensional flux form semi-lagrangian transport schemes, *Mon. Wea. Rev.*, *124*, 2046–2070, 1996.

Lin, S.-J., and R. B. Rood, An explicit flux-form semi-lagrangian shallow water model on the sphere, *Q. J. R. Meteorol. Soc.*, *123*, 2531–2533, 1997.

Lin, Y.-L., R. R. Farley, and H. D. Orville, Bulk parameterization of the snow field in a cloud model, *J. Clim. Appl. Meteorol.*, *22*, 1065–1092, 1983.

Lind, J. A., and G. L. Kok, Henry's law determination for aqueous solutions of hydrogen peroxide, methyl hydroperoxide, and peroxyacetic acid, *J. Geophys. Res.*, *91*, 7889–7896, 1986.

Liousse, C., J. E. Penner, C. Chuang, J. J. Walton, H. Eddleman, and H. Cachier, A global three-dimensional model study of carbonaceous aerosols, *J. Geophys. Res.*, *101*, 19411–19432, 1996.

Locatelli, J. D., and P. V. Hobbs, Fall speeds and masses of solid precipitation particles, *J. Geophys. Res.*, *79*, 2185–2197, 1974.

Lohmann, U., and E. Roeckner, Design and performance of a new cloud microphysics scheme developed for the ECHAM general circulation model, *Climate Dynamics*, *12*, 557–572, 1996.

Lord, S. J., W. C. Chao, and A. Arakawa, Interaction of a cumulus cloud ensemble with the large-scale environment. part iv: The discrete model, *J. Atmos. Sci.*, *39*, 104–113, 1982.

Maahs, H. G. 1982. Sulfur dioxide/water equilibrium between 0° and 50°C: An examination of data at low concentrations. in *Heterogeneous Atmospheric Chemistry, Geophys. Monogr. Ser.*, volume 26, 273, Washington, D. C. AGU.

Machenhauer, B., The spectral method, in *Numerical Methods Used in Atmospheric Models*, World Meteorological Organization, Geneva, Switzerland, 1979.

Machenhauer, B. 1998. MPI workshop on conservative transport schemes. in *Report No. 265,* . Max-planck-Institute for Meteorology.

Mahowald, N., C. Luo, J. delCorral, and C. Zender, Interannual variability in atmospheric mineral aerosols from a 22-year model simulation and observational data, *J. Geophys. Res.*, 2003.

Manabe, S., Climate and the ocean circulation: 1. The atmospheric circulation and the hydrology of the earth's surface, *Mon. Wea. Rev.*, *97*, 739–774, 1969.

Manabe, S., and F. Möller, On the radiative equilibrium and heat balance of the atmosphere, *Mon. Wea. Rev.*, *89*, 503–562, 1961.

Manabe, S., and R. Strickler, Thermal equilibrium of the atmosphere with a convective adjustment, *J. Atmos. Sci.*, *21*, 361–385, 1964.

Maykut, G. A., and D. Perovich, The role of shortwave radiation in the summer decay of a sea ice cover, *J. Geophys. Res.*, *92*, 7032–7044, 1987.

Maykut, G. A., and N. Untersteiner, Some results from a time-dependent thermodynamic model of sea ice, *J. Geophys. Res.*, *76*, 1550–1575, 1971.

McAvaney, B. J., W. Bourke, and K. Puri, A global spectral model for simulation of the general circulation, *J. Atmos. Sci.*, *35*, 1557–1583, 1978.

McPhee, M. G., Turbulent heat flux in the upper ocean under sea ice, *J. Geophys. Res.*, *97*, 5365–5379, 1992.

Moeng, C.-H., and P. P. Sullivan, A comparison of shear- and buoyancy-driven planetary boundary layer flows, *J. Atmos. Sci.*, *51*, 999–1022, 1994.

Mote, P. W., J. R. Holton, J. M. Russell, and B. A. Boville, A comparison of observed (haloe) and modeled (ccm2) methane and stratospheric water vapor, *grl*, *20*, 1419—1422, 1993.

Müller, J.-F., and G. P. Brasseur, IMAGES: A three-dimensional chemical transport model of the global troposphere, *jgr*, *100*, 16445—16490, 1995.

National Bureau of Standards, Selected values of chemical thermodynamic properties, 1, Tech. Note 270-1, National Bureau of Standards, Gaithersburg, Md., 1965.

Ono, N., Specific heat and heat of fusion of sea ice, in *Physics of Snow and Ice*, Vol. I, edited by H. Oura, 599–610, Institute of Low Temperature Science, Hokkaido, Japan, 1967.

Orszag, S. A., Fourier series on spheres, *Mon. Wea. Rev.*, *106*, 405–412, 1974.

Paulson, C. A., and J. J. Simpson, Irradiance measurements in the upper ocean, *J. Phys. Oceanogr*, *7*, 952–956.

Raisanen, P., Effective longwave cloud fraction and maximum-random overlap of clouds: A problem and a solution, *Mon. Wea. Rev.*, *126*, 3336–3340, 1998.

Ramanathan, V., Radiative transfer within the Earth's troposphere and stratosphere: A simplified radiative-convective model, *J. Atmos. Sci.*, *33*, 1330–1346, 1976.

Ramanathan, V., and R. E. Dickinson, The role of stratospheric ozone in the zonal and seasonal radiative energy balance of the Earth-troposphere system, *J. Atmos. Sci.*, *36*, 1084–1104, 1979.

Ramanathan, V., and P. Downey, A nonisothermal emissivity and absorptivity formulation for water vapor, *J. Geophys. Res.*, *91*, 8649–8666, 1986.

Ramanathan, V., R. J. Cicerone, H. B. Singh, and J. T. Kiehl, Trace gas trends and their potential role in climate change, *J. Geophys. Res.*, *90*, 5547–5566, 1985.

Ramaswamy, V., and S. M. Freidenreich, Solar radiative line-by-line determination of water vapor absorption and water cloud extinction in inhomogeneous atmospheres, *J. Geophys. Res.*, *96*, 9133–9157, 1991.

Rasch, P. J., B. A. Boville, and G. P. Brasseur, A three-dimensional general circulation model with coupled chemistry for the middle atmosphere, *J. Geophys. Res.*, *100*, 9041–9071, 1995.

Rasch, P. J., N. M. Mahowald, and B. E. Eaton, Representations of transport, convection, and the hydrologic cycle in chemical transport models: Implications for the modeling of short-lived and soluble species, *J. Geophys. Res.*, *102*, 28127–28138, 1997.

Rasch, P. J., M. C. Barth, J. T. Kiehl, S. E. Schwartz, and C. M. Benkovitz, A description of the global sulfur cycle and its controlling processes in the National Center for Atmospheric Research Community Climate Model, Version 3, *J. Geophys. Res.*, *105*, 1367–1385, 2000.

Rasch, P. J., and J. E. Kristjánsson, A comparison of the CCM3 model climate using diagnosed and predicted condensate parameterizations, *J. Climate*, *11*, 1587—1614, 1998.

Rasch, P. J., and M. G. Lawrence. 1998. Recent developments in transport methods at ncar. in *MPI workshop on conservative transport methods*, 93*Report No. 265.,* , Hamburg, Germany. Max Planck Institute for Meteorology.

Rasch, P. J., and D. L. Williamson, On shape-preserving interpolation and semi-Lagrangian transport, *SIAM J. Sci. Stat. Comput.*, *11*, 656–687, 1990.

Ringler, T. D., R. P. Heikes, , and D. A. Randall, Modeling the atmospheric general circulation using a spherical geodesic grid: A new class of dynamical cores, *Mon. Wea. Rev.*, *128*, 2471–2490, 2000.

Ritchie, H., and M. Tanguay, A comparison of spatially averaged Eulerian and semi-Lagrangian treatments of mountains, *Mon. Wea. Rev.*, *124*, 167–181, 1996.

Robert, A. J., The integration of a low order spectral form of the primitive meteorological equations, *J. Meteorol. Soc. Japan*, *44*, 237–245, 1966.

Roberts, R. E., J. E. A. Salby, and L. M. Biberman, Infrared continuum absorption by atmospheric water vapor in the 8–12 $\mu$m window, *Appl. Opt.*, *15*, 2085–2090, 1976.

Rodgers, C. D., and C. D. Walshaw, The computation of infra-red cooling rate in planetary atmospheres, *Q. J. R. Meteorol. Soc.*, *92*, 67–92, 1966.

Rothman, L. S., A. Goldman, J. R. Gillis, R. R. Gamache, H. M. Pickett, R. L. Poynter, N. Husson, and A. Chedin, AFGL trace gas compilation – 1982 version, *Appl. Opt.*, *22*, 1616–1627, 1983.

Rothman, L. S., A. Barbe, D. C. Benner, L. R. Brown, C. Camy-Peyret, M. R. Carleer, K. Chance, C. Clerbaux, V. Dana, V. M. Devi, A. Fayt, J.-M. Flaud, R. R. Gamache, A. Goldman, D. Jacquemart, K. W. Jucks, W. J. Lafferty, J.-Y. Mandin, S. T. Massie, V. Nemtchinov, D. A. Newnham, A. Perrin, C. P. Rinsland, J. Schroeder, K. M. Smith, M. A. H. Smith, K. Tang, R. A. Toth, J. V. Auwera, P. Varanasi, and K. Yoshino, The HITRAN molecular spectroscopic database: Edition of 2000 including updates of 2001, *J. Quant. Spectrosc. Radiat. Transfer*, *82*, 2003.

Rothrock, D. A., and A. S. Thorndike, Measuring the sea ice floe size distribution, *J. Geophys. Res.*, *89*, 6477–6486, 1984.

Sangster, W. E., A meteorological coordinate system in which the Earth's surface is a coordinate surface, Ph.D. thesis, University of Chicago, Department of Geophysical Sciences, 1960.

Sato, R. K., L. M. Bath, D. L. Williamson, and G. S. Williamson, User's guide to NCAR CCMOB, Technical Report NCAR/TN-211+IA, National Center for Atmospheric Research, Boulder, Colorado, 133 pp., 1983.

Simmons, A. J., and D. M. Burridge, An energy and angular momentum conserving vertical finite-difference scheme and hybrid vertical coordinates, *Mon. Wea. Rev.*, *109*, 758–766, 1981.

Simmons, A. J., and R. Strüfing, An energy and angular-momentum conserving finite-difference scheme, hybrid coordinates and medium-range weather prediction, Technical Report ECMWF Report No. 28, European Centre for Medium–Range Weather Forecasts, Reading, U.K., 68 pp., 1981.

Simmons, A. J., and R. Strüfing, Numerical forecasts of stratospheric warming events using a model with hybrid vertical coordinate, *Q. J. R. Meteorol. Soc.*, *109*, 81–111, 1983.

Slingo, A., A GCM parameterization for the shortwave radiative properties of clouds, *J. Atmos. Sci.*, *46*, 1419–1427, 1989.

Slingo, J. M., The development and verification of a cloud prediction scheme for the ECMWF model, *Q. J. R. Meteorol. Soc.*, *113*, 899–927, 1987.

Smith, S. J., H. Pitcher, and T. M. L. Wigley, Global and regional anthropogenic sulfur dioxide emissions, *Glob. Biogeochem. Cycles*, *29*, 99–119, 2001.

Stamnes, K., S. C. Tsay, W. Wiscombe, and K. Jayaweera, A numerically stable algorithm for discrete-ordinate-method radiative transfer in multiple scattering and emitting layered media, *Appl. Opt.*, *27*, 2502–2509, 1988.

Starr, V. P., A quasi-lagrangian system of hydrodynamical equations, *J. Meteor.*, *2*, 227–237, 1945.

Steele, M., Sea ice melting and floe geometry in a simple ice–ocean model, *J. Geophys. Res.*, *97*, 17,729–17,738, 1995.

Stenchikov, G. L., I. Kirchner, A. Robock, H. F. Graf, J. C. Antuna, R. G. Grainger, A. Lambert, and L. Thomason, Radiative forcing from the 1991 Mount Pinatubo volcanic eruption, *J. Geophys. Res.*, *103*, 13837–13857, 1998.

Stowe, L. L., A. M. Ignatov, and R. R. Singh, Development, validation, and potential enhancements to the second-generation operational aerosol product at the National Environmental Satellite, Data, and Information Service of the National Oceanic and Atmospheric Administration, *J. Geophys. Res.*, *102*, 16889–16910, 1997.

Suarez, M. J., and L. L. Takacs, Documentation of the aries/geos dynamical core: Version 2, Technical Report Technical Memorandum 104 606 Vol. 5, NASA, 1995.

Sundqvist, H., Parameterization of condensation and associated clouds in models for weather prediction and general circulation simulation, in *Physically-based Modeling and Simulation of Climate and Climate Change*, Vol. 1, edited by M. E. Schlesinger, 433–461, Kluwer Academic, 1988.

Taylor, K. E., D. Williamson, and F. Zwiers. 2001. Amip ii sea surface temperature and sea ice concentration boundary conditions. http://www-pcmdi.llnl.gov/amip/AMIP2EXPDSN/BCS/amip2bcs.html 23 June 1997 (revised 6 April 2001).

Temperton, C., Treatment of the Coriolis terms in semi-Lagrangian spectral models, in *Atmospheric and Ocean Modelling. The André J. Robert Memorial Volume*, edited by C. Lin, R. Laprise,, and H. Ritchie, 293–302, Canadian Meteorological and Oceanographic Society, Ottawa, Canada, 1997.

Temperton, C., M. Hortal, and A. Simmons, A two-time-level semi-Lagrangian global spectral model, *Q. J. R. Meteorol. Soc.*, *127*, 111–127, 2001.

Tripoli, G. J., and W. R. Cotton, A numerical investigation of several factors contributing to the observed variable intensity of deep convection over south Florida, *J. Appl. Meteorol.*, *19*, 1037–1063, 1980.

Troen, I., and L. Mahrt, A simple model of the atmospheric boundary layer; sensitivity to surface evaporation, *Boundary Layer Meteorol.*, *37*, 129–148, 1986.

Twomey, S. A., M. Piepgrass, and T. L. Wolfe, An assessment of the impact of pollution on global cloud albedo, *Tellus*, *36*, 356–366, 1984.

Untersteiner, N., On the mass and heat budget of Arctic sea ice, *Arch. Meteorol. Geophys. Bioklimatol., A*, *12*, 151–182, 1961.

Varanasi, P., and S. Chudamani, Infrared intensities of some chlorofluorocarbons capable of perturbing the global climate, *J. Geophys. Res.*, *93*, 1666–1668, 1988.

Vogelezang, D. H. P., and A. A. M. Holtslag, Evaluation and model impacts of alternative boundary-layer height formulations, *Boundary Layer Meteorol.*, *81*, 245–269, 1996.

Washington, W. M., Documentation for the Community Climate Model (CCM), Version ∅, Technical Report NTIS No. PB82 194192, National Center for Atmospheric Research, Boulder, Colorado, 1982.

Wesely, M. L., Parameterization of surface resistances to gaseous dry deposition in regional-scale numerical models, *Atmos. Environ.*, *23*, 1293–1304, 1989.

Williamson, D. L., Description of NCAR Community Climate Model (CCM0B), Technical Report NCAR/TN-210+STR, National Center for Atmospheric Research, Boulder, Colorado, NTIS No. PB83 23106888, 88 pp., 1983.

Williamson, D. L., Time-split versus process-split coupling of parameterizations and dynamical core, *Mon. Wea. Rev.*, *130*, 2024–2041, 2002.

Williamson, D. L., L. M. Bath, R. K. Sato, T. A. Mayer, and M. L. Kuhn, Documentation of NCAR CCM0B program modules, Technical Report NCAR/TN-212+IA, National Center for Atmospheric Research, Boulder, Colorado, NTIS No. PB83 263996, 198 pp., 1983.

Williamson, D. L., J. T. Kiehl, V. Ramanathan, R. E. Dickinson, and J. J. Hack, Description of NCAR Community Climate Model (CCM1), Technical Report NCAR/TN-285+STR, National Center for Atmospheric Research, Boulder, Colorado, 112 pp., 1987.

Williamson, D. L., and J. G. Olson, Climate simulations with a semi-Lagrangian version of the NCAR Community Climate Model, *Mon. Wea. Rev.*, *122*, 1594–1610, 1994.

Williamson, D. L., and P. J. Rasch, Two-dimensional semi-Lagrangian transport with shape-preserving interpolation, *Mon. Wea. Rev.*, *117*, 102–129, 1989.

Williamson, D. L., and J. M. Rosinski, Accuracy of reduced grid calculations, *Q. J. R. Meteorol. Soc.*, *126*, 1619–1640, 2000.

Williamson, D. L., and G. S. Williamson, Circulation statistics from January and July simulations with the NCAR Community Climate Model (CCM0B), Technical Report NCAR/TN-224+STR,, National Center for Atmospheric Research, Boulder, Colorado, NTIS No. PB85 165637/AS, 112 pp., 1984.

Williamson, G. S., CCM2 datasets and circulation statistics, Technical Report NCAR/TN-391+STR, National Center for Atmospheric Research, Boulder, Colorado, 85 pp., 1993.

Williamson, G. S., and D. L. Williamson, Circulation statistics from seasonal and perpetual January and July simulations with the NCAR Community Climate Model (CCM1): R15, Technical Report NCAR/TN-302+STR, National Center for Atmospheric Research, Boulder, Colorado, 199 pp., 1987.

Wiscombe, W. J., and J. W. Evans, Exponential-sum fitting of radiative transmission functions, *J. Comput. Phys.*, *24*, 416–444, 1977.

Xu, K.-M., and S. K. Krueger, Evaluation of cloudiness parameterizations using a cumulus ensemble model, *Mon. Wea. Rev.*, *119*, 342–367, 1991.

Yanai, M., S. Esbensen, and J.-H. Chu, Determination of bulk properties of tropical cloud clusters from large-scale heat and moisture budgets, *J. Atmos. Sci.*, *30*, 611–627, 1973.

Yin, F., D. Grosjean, and J. H. Seinfeld, Photooxidation of dimethyl sulfide and dimethyl disulfide, I, Mechanism development, *J. Atmos. Chem.*, *11*, 309–364, 1990*a*.

Yin, F., D. Grosjean, R. C. Flagan, and J. H. Seinfeld, Photooxidation of dimethyl sulfide and dimethyl disulfide, II, Mechanism evaluation, *J. Atmos. Chem.*, *11*, 365–399, 1990*b*.

Zender, C. S., H. Bian, and D. Newman, The mineral Dust Entrainment And Deposition (DEAD) model: Description and 1990's dust climatology, *J. Geophys. Res.*, *108*, 2003.

Zeng, X., and R. E. Dickinson, Effect of surface sublayer on surface skin temperature and fluxes, *J. Climate*, *11*, 537–550, 1998.

Zeng, X., M. Zhao, and R. E. Dickinson, Intercomparison of bulk aerodynamic algorithms for the computation of sea surface fluxes using TOGA COARE and TAO data, *J. Climate*, *11*, 2628–2644, 1998.

Zhang, G. J., and N. A. McFarlane, Sensitivity of climate simulations to the parameterization of cumulus convection in the Canadian Climate Centre general circulation model, *Atmosphere-Ocean*, *33*, 407–446, 1995.

Zhang, M., W. Lin, C. S. Bretherton, J. J. Hack, and P. J. Rasch, A modified formulation of fractional stratiform condensation rate in the NCAR community atmospheric model CAM2, *J. Geophys. Res.*, *108* **(D1)**, 2003.

Zilitinkevich, S. S., *Dynamics of the Atmospheric Boundary Layer*. Gidrometeoizdat, Leningrad, 1970, 292 pp.